Quantum Optics Experiments in a Microstructured Ion Trap

Dissertation

zur Erlangung des Doktorgrades Dr. rer. nat.

der Fakultät für Naturwissenschaften der Universität Ulm

vorgelegt von

Ulrich Georg Poschinger

aus Berlin

Tag der Promotion: 15.2.2011

2010

ulm university universität ulm

Amtierender Dekan: Prof. Dr. Axel Groß

Erstgutachter: Prof. Dr. Ferdinand Schmidt-Kaler

Zweitgutachter: Prof. Dr. Johannes Hecker Denschlag

Hiermit erkläre ich, Ulrich Poschinger, dass ich die vorliegende Dissertation *Quantum Optics Experiments in a Microstructured Ion Trap* selbstständig angefertigt und keine anderen als die angegebenen Quellen und Hilfsmittel benutzt sowie die wörtlich und inhaltlich übernommenen Stellen als solche kenntlich gemacht und die Satzung der Universität Ulm zur Sicherung guter wissenschaftlicher Praxis beachtet habe.

Ulrich Poschinger
Ulm, den 12. November 2010

The work described in this thesis was carried out at the

Universität Ulm
Institut für Quanteninformationsverarbeitung
Albert-Einstein-Allee 11
D-89069 Ulm

Funding from the EU within the research programs
MICROTRAP, SCALA, AQUTE and the MRTN EMALI,
and from the DFG within the framework SFB/TRR21
is gratefully acknowledged.

Extraordinary rains pretty generally fall after great battles.
-Plutarch

Abstract

This dissertation describes a prototype experiment aiming at the realization of scalable quantum information. The essential feature is the usage of a novel microstructured ion trap derived from the Paul trap. It allows for storing and manipulating a large number of ions, as compared to conventional linear Paul traps. This thesis describes how the way is paved towards the realization of quantum information experiments in this ion trap. An analysis of the electrostatic properties of the ion trap is presented, which is laying the foundation for understanding the limits of confinement stability and effects beyond standard Paul trap behavior. The focus of this work lies on the realization and characterization of single and dual qubit operations, which are achieved by means of (semiclassical) atom-light interaction. In our experiment, the qubit is implemented in the Zeeman sublevels of the ion's ground state, i.e. in the *spin* of the bright electron of a $^{40}Ca^{+}$ ion. The main body of this thesis then describes the realization of the necessary steps of preparation, manipulation and readout of this qubit. The preparation includes optical pumping and cooling close to the motional quantum ground state by means of sideband cooling. Several possible techniques for these steps are tested and analyzed. Coherent manipulations are carried out by means of stimulated Raman transitions. Here, a strong emphasis is put on the characterization of the various decoherence mechanisms, which are dominated by the motional excitation of the ion due to thermalization of the ion with the trap electrodes, and by imperfections in the ion-laser interactions. As by-product of the latter investigation, a new measurement scheme for the experimental determination of atomic dipole matrix elements is presented. Finally, experimental results on the preparation of Schrödinger Cat states and on the tomography of a single ion's motional state are presented. It is also described how Schrödinger Cat states can be used as a measurement tool for the ultraprecise monitoring of a single ion's phase space trajectory, where deviations from the Lamb-Dicke limit dynamics are seen.

Zusammenfassung

Diese Dissertation behandelt die grundlegenden Schritte eines Prototyp-Experiments welches auf die Realisierung skalierbarer Quanteninformation abzielt. Das entscheidende Merkmal liegt in der Verwendung einer neuartigen mikrostrukturierten Ionenfalle, welche auf der bekannten Paulfalle basiert. Verglichen mit konventionellen Paulfallen erlaubt diese die Speicherung und Manipulation einer grösseren Anzahl von Ionen. Diese Arbeit beschreibt wie der Weg zur Realisierung von Quanteninformationsexperimenten in dieser Ionenfalle geebnet wird. Zuerst wird eine detaillierte Analyse der elektrostatischen Eigenschaften der verwendeten Ionenfalle präsentiert, was ein grundlegendes Verständnis der Einschlusseigenschaften und möglicher Effekte jenseites des idealen Verhaltens ermöglicht. Der Fokus dieser Arbeit liegt bei der Realisierung und Charakterisierung von Operationen mit einem und zwei Qubits, welche mit Hilfe der (semiklassischen) Atom-Licht Wechselwirkung ausgefhrt werden. In unserem Experiment wird das Qubit in den Zeeman-Unterzuständen des elektronischen Grundzustands des Ions kodiert, also im *Spin* des Leuchtelektrons eines $^{40}Ca^{+}$ Ions. Der Hauptteil dieser Arbeit umfasst die Realisierung der nötigen Verfahrensschritte Präparation, Manipulation und Auslese dieser Art von Qubit. Die Präparation umfasst optisches Pumpen und Kühlen nahe an den quantenmechanischen Grundzustand der Bewegung. Mehrere mögliche Techniken dafür werden getestet und analysiert. Kohärente Manipulationen werden mithilfe stimulierter Ramanübergänge ausgeführt. Hier wird eine starke Betonung auf die Charakterisierung der verschiedenen Dekohärenzprozesse gelegt, die von der Anregung der Ionenbewegung durch Thermalisierung mit der Umgebung und Imperfektionen bei der Ionen-Licht-Wechselwirkung dominiert werden. Als Nebenprodukt des letzteren wird ein neues Messverfahren zur Bestimmung atomarer Dipolmatrixelemente präsentiert. Zuletzt werden experimentelle Ergebnisse zur Präparation eines Schrödinger-Katzenzustands und zur Tomographie des Bewegungszustandes eines einzelnen Ions gezeigt. Es wird ebenfalls demonstriert, wie Schrödinger-Katzenzustände benutzt werden können um die Phasenraumtrajektorie eines einzelnen ions mit hoher Genauigkeit zu verfolgen, wobei auch Abweichungen vom Lamb-Dicke Regime beobachtet werden.

Contents

1. Introduction **1**

2. Theoretical Foundations **9**
2.1. Laser-Ion Interactions 9
2.1.1. The Two-Level System: Dynamics 9
2.1.2. The Two-Level System: Coupling Matrix Elements 13
2.1.3. Including the Motional Degrees of Freedom: Laser Cooling 15
2.1.4. Including the Motional Degrees of Freedom: The Resolved Sideband Regime 19
2.1.5. Multilevel Systems Interacting with Multiple Laser Fields: Optical Pumping 23
2.1.6. Multilevel Systems Interacting with Off-Resonant Laser Fields: Stimulated Raman Transitions and Decoherence Effects 29
2.2. Linear Segmented Paul Traps 33
2.2.1. Confinement Mechanism 33
2.2.2. Vibrational Modes of Ion Crystals 37

3. Experimental Setup **41**
3.1. The Trap, Vacuum Vessel and the Ovens 41
3.2. Laser Systems 42
3.2.1. 423 nm and 375 nm for Photoionization 43
3.2.2. 397 nm for Doppler Cooling, Ion Detection and Optical Pumping . . . 44
3.2.3. 854 nm and 866 nm for Repumping and Quenching 46
3.2.4. 729 nm for Electron Shelving 47
3.2.5. 397 nm for Stimulated Raman Transitions 50
3.3. Imaging and Detection 54
3.4. Trap Voltage Supplies 54
3.5. Quantizing Magnetic Field 56
3.6. Experimental Control System 56

4. Implementation of the Spin Qubit **59**
4.1. A Brief Survey of Trapped Ion Qubit Types 59
4.2. Basic Qubit Operations 61
4.2.1. State Discrimination by Fluorescence Counting 61
4.2.2. Spectroscopy on the Quadrupole Transition 66
4.2.3. Coherent Dynamics on the Quadrupole Transition 68

4.2.4. Qubit Preparation . . . 73
4.2.5. Qubit Reset . . . 77
4.3. 3D Heating Rate Measurement by Fluorescence Observation . . . 80
4.4. Qubit Readout via Electron Shelving . . . 82
4.5. Stimulated Raman Transitions . . . 88
4.5.1. Raman Spectroscopy and Single Qubit Rotations . . . 88
4.6. Sideband Cooling and Phonon Distribution Measurements . . . 94
4.7. Coherence and Decoherence of the Spin Qubit . . . 102

5. Trap Characteristics **113**
5.1. Electrostatic Potentials . . . 113
5.2. Micromotion Compensation . . . 119

6. Determination of Atomic Matrix Elements with Off-Resonant Radiation **127**
6.1. Motivation . . . 127
6.2. Basic Idea of the Measurement Procedure . . . 127
6.3. Measurement of the Scattering Rates . . . 130
6.4. Measurement of the Raman Detuning . . . 131
6.5. Measurement of the AC Stark Shift . . . 131
6.6. Robustness against Experimental Imperfections . . . 134
6.7. Extraction of the Scattering Parameters and Error Analysis . . . 136
6.8. Final Results . . . 138
6.9. Additional Error Sources . . . 139
6.10. Complete Measurement by Measuring Absolute Stark Shifts . . . 140

7. Motional State Tomography **145**
7.1. The Method . . . 145
7.2. The Measurement Scheme . . . 147

8. Preparation and Characterization of Schrödinger Cat States **153**
8.1. Preparation of a Schrödinger Cat State of a Single Ion . . . 153
8.2. Temperature Dependence and Quantum Effects . . . 161
8.3. Phonon Distribution Dynamics . . . 163
8.4. The Wavepacket Beating Scheme . . . 169

9. Measurements with Two-Ion Crystals **177**
9.1. Stability and Read-out . . . 177
9.2. Localization and Alignment in a Standing Wave . . . 180
9.3. Spectroscopy and Cooling . . . 186
9.4. Coherent Manipulations . . . 190
9.5. A Two-Ion Schrödinger Cat . . . 195

10. Conclusion and Outlook **203**
10.1. Conclusion . . . 203

10.2. Open Questions 204
10.3. Outlook 205

A. Adiabatic Elimination on the Master Equation **207**

B. Trap Voltage Supply Electronics **211**

C. Advanced Reconstruction Technique for Phonon Number Distributions **219**

D. Tomography Method for States with Entanglement of Spin and Motion **223**

E. Coherently Driven Ion Crystals **227**
E.1. Driving the Internal State 227
E.2. Driving the Motion 228

F. Atomic Properties of Calcium **231**

G. Publications **233**
G.1. Journal Publications 233
G.2. Talks 234
G.3. Posters 234

List of Figures

1.1. Progress in ion-trap quantum computing 2
1.2. Illustration of the limited scalability in linear Paul traps 4

2.1. Doppler cooling 16
2.2. Product Hilbert space for a two-level system and a harmonic oscillator 20
2.3. Motional matrix elements 21
2.4. Simulated Rabi oscillations on carrier and first order sideband for different temperatures and Lamb-Dicke factors 24
2.5. Sideband cooling scheme 25
2.6. Dephasing of Rabi oscillations 26
2.7. Level scheme for the pumping problem 27
2.8. Continuous pumping rates in a four-level system 28
2.9. Optimum depump Rabi frequency versus excitation Rabi frequency 29
2.10. Excitation suppression and broadening in a three- and four-level system . . . 30
2.11. Level scheme for off-resonant interactions 31
2.12. Basic types of Paul traps 33
2.13. Mechanism for confinement in a quadrupolar rf potential 35
2.14. Regions of stability for different trap geometries 36

3.1. Trap layout and picture 42
3.2. General beam geometry 43
3.3. Optical setup for the laser at 397 nm for Doppler cooling 44
3.4. Optical setup of the laser at 866 nm and 854 nm 46
3.5. Optical setup of the 729 nm laser 47
3.6. 729 nm AOM characterization 48
3.7. Optical setup for the laser at 397 nm for off-resonant coherent manipulations 50
3.8. Characterization of the switching EOM 51
3.9. rf network for the supply of the AOMs in the Raman beamline 52
3.10. Setup for imaging and fluorescence detection 55
3.11. Experimental control system 57

4.1. Complete level scheme of $^{40}Ca^{+}$ 60
4.2. Fluorescence histogram 62
4.3. Fluorescence discrimination errors for different count rates 63
4.4. Spectroscopy on the $S_{1/2}$ to $P_{1/2}$ transition 65
4.5. Detailed level scheme of the quadrupole transition 66

4.6. Accessible quadrupole transitions . . . 67
4.7. Spectroscopy on the quadrupole transition . . . 68
4.8. Coherent dynamics on the quadrupole transition . . . 69
4.9. Effective Rabi frequency distribution . . . 70
4.10. Gauge of the Rabi frequency on the quadrupole transition . . . 71
4.11. Two different schemes for optical pumping . . . 73
4.12. Optical pumping on the quadrupole transition . . . 74
4.13. Measurement of spurious polarization components . . . 75
4.14. Quenching of the $D_{5/2}$ state . . . 78
4.15. Quenching of the $D_{3/2}$ state . . . 79
4.16. Fluorescence heating rate measurement . . . 80
4.17. Scheme of the RAP process . . . 82
4.18. Rapid adiabatic passage pulse . . . 83
4.19. RAP efficiency versus peak Rabi frequency for different chirp ranges . . . 84
4.20. Robustness of the shelving process with respect to frequency errors . . . 85
4.21. Parasitic shelving . . . 86
4.22. Spectroscopy on the orthogonal Raman transition . . . 89
4.23. Spectroscopy on the collinear Raman transition . . . 90
4.24. Coherent dynamics on the collinear Raman transition . . . 92
4.25. Coherent versus incoherent effects on the Raman transition . . . 93
4.26. Two different schemes for sideband cooling . . . 94
4.27. Raman spectra with and without sideband cooling . . . 95
4.28. Coherent dynamics on the blue sideband after sideband cooling . . . 96
4.29. Cosine transform of blue sideband Rabi oscillations . . . 97
4.30. Coherent dynamics on the orthogonal Raman transition after sideband cooling 98
4.31. Results of the heating rate measurement . . . 99
4.32. Calculated phonon removal times for different red sideband transitions . . . 100
4.33. T_2^* measurement on various transitions . . . 102
4.34. T_2 measurement on various transitions . . . 103
4.35. Sample results from the spin echo contrast measurement . . . 105
4.36. Laser induced dephasing mechanisms . . . 106
4.37. Spin-echo contrast versus decohering pulse time . . . 107
4.38. Resulting decoherence rate coefficients . . . 108
4.39. Investigation of the intensity-fluctuation induced decoherence process . . . 110

5.1. Trap layout for electrostatic field simulation . . . 113
5.2. Electrostatic axial confinement potentials . . . 115
5.3. Radial potential cuts . . . 116
5.4. Radial confinement strength along the trap axis . . . 118
5.5. Off-site spectroscopy . . . 119
5.6. Micromotion compensation by fluorescence measurement . . . 122
5.7. Modulation index along the trap axis . . . 124
5.8. Micromotion induced phonon lasing effect . . . 125

6.1. Relevant levels and transitions for the lifetime measurement scheme 128
6.2. Raw data from the scattering rate measurement 131
6.3. Comparison of theoretical and experimental error bars 132
6.4. Spin flip curves 133
6.5. Fluorescence calibration of the wavemeter 134
6.6. Example Stark shift measurement 135
6.7. Stark shift measurement accuracy 136
6.8. Calibration by means of the Stark shift 137
6.9. Error ellipsoid for the scattering rates 138
6.10. Level scheme for absolute Stark shift measurement 141
6.11. Measurement scheme for the absolute Stark shift 142
6.12. Measurement scheme for the absolute Stark shift 143

7.1. The complete tomography measurement 148
7.2. Resulting phonon distributions 149
7.3. Resulting density matrix 150

8.1. Illustration of the spin-dependent light force 154
8.2. Analogy between the Schrödinger cat experiment and a Mach-Zehnder interferometer 158
8.3. Entanglement-induced contrast loss for the Schrödinger cat state 159
8.4. Groundstate versus thermal signals 161
8.5. Classical and quantum mechanical trajectories 163
8.6. Reconstructed phonon distributions 164
8.7. Reconstructed phonon distributions with fits to coherent state distributions . 165
8.8. Results from the phonon distribution measurements 166
8.9. Decoherence rate versus displacement 167
8.10. Quantum jumps during sideband Rabi oscillations 168
8.11. Schematic of the wavepacket beating experiment 169
8.12. Measurement results for the wavepacket beating scheme 170
8.13. Measured signals from the wavepacket beating scheme 171
8.14. Contrast and carrier off-resonance 172
8.15. Measured particle trajectory 173
8.16. Cat states with varying parity 174

9.1. Fluorescence histogram of two ions 178
9.2. Shelving of two ions 179
9.3. Localization measurement samples 181
9.4. Localization measurement result 182
9.5. Fluorescence autocorrelation 183
9.6. Raman spectrum of two ions 186
9.7. Sideband cooling of two ions 189
9.8. Rabi oscillations of two ions 190

9.9. Balanced Rabi oscillations of two ions 191
9.10. Camera-based read-out of a two ion crystal 192
9.11. Histograms resulting from the two-ion readout 192
9.12. Independent readout of two-ion Rabi oscillations 193
9.13. PMT data of two-ion Rabi oscillations 194
9.14. Schrödinger cat state schematic with two ions 195
9.15. Schrödinger cat state creation with two ions 196
9.16. Parameters describing the quantum dynamics of two ions 199
9.17. Beat between displacement and squeezing 201

B.1. Voltage generation stage 212
B.2. Buffer and adding stage 213
B.3. Transistor buffer stage 213
B.4. Heating rate measurements for different buffer stages 214
B.5. Design of the scalable trap voltage supply 215
B.6. Data flow within the FPGA subsystem 216

C.1. Determination of confidence interval for an occupation probability 220

1. Introduction

The reason for the late discovery of quantum mechanics is that genuine quantum phenomena are hardly observed in our everyday life. Even though the stability of atoms, nuclei and condensed matter objects - without which we would not even exist - originates from quantum mechanics, essential quantum concepts like superposition states and entanglement appear to be counterintuitive. They still lead to philosophical objections against the theory. Because of this, quantum mechanics was not even fully accepted by some of its inventors, like Albert Einstein or Erwin Schrödinger. However, it is up to now the only theory which could withstand every experimental test with tremendous success. The last decades have seen a paradigm shift from the pure investigation of quantum phenomena and tests of the theory to the *usage* of quantum mechanics for technological applications. There are already devices which play crucial roles in the modern world which heavily rely on quantum mechanics, e.g. semiconductor microelectronics or the laser. Applications of the pure quantum effects mentioned above, however, remain scarce. Nevertheless, a large number of promising proposals, an impressive number of stunning experimental demonstrations and even some commercial products show that the application of fundamental quantum mechanics is currently one the most exciting fields of research. This field can be roughly subdivided into the areas of quantum information, quantum simulation, quantum communication and quantum metrology. Quantum information is based on the idea of using entanglement as a computational resource, which promises a tremendous increase in computational efficiency for certain problems. The idea behind quantum simulation is to use the ability to control tailored quantum systems to model real-life systems which are still not completely understood, like e.g. high-temperature superconductors. Quantum communication makes use of fundamental ideas like the no-cloning theorem to provide absolutely safe information transfer. Finally, quantum metrology attempts to increase the measurement accuracy for natural constants by means of entanglement enhancement are even to construct more accurate sensors, like SQUIDS for magnetic fields.
Both the late discovery of these effects and the difficulty of their usage can be explained by the fact that they are obscured by the complexity of systems consisting of many degrees of freedom. If we consider a small system of interest, superposition states within this system are destroyed by the interaction with many degrees of freedom from the surrounding environment, a process which is called decoherence. This transfer of information from the small system to the outside world, which is a model for the measurement process, provides at least a partial explanation for the projection postulate. Ironically, entanglement is difficult to observe because of - entanglement: Coherences within the system of interest effectively decay because the interaction with the environmental degrees of freedom lead to mutual entanglement. This in turn reduces the quantum coherence within the system, such that the

fundamental concepts of classical physics, i.e. causality, locality and reality are restored on the macroscopic scale.

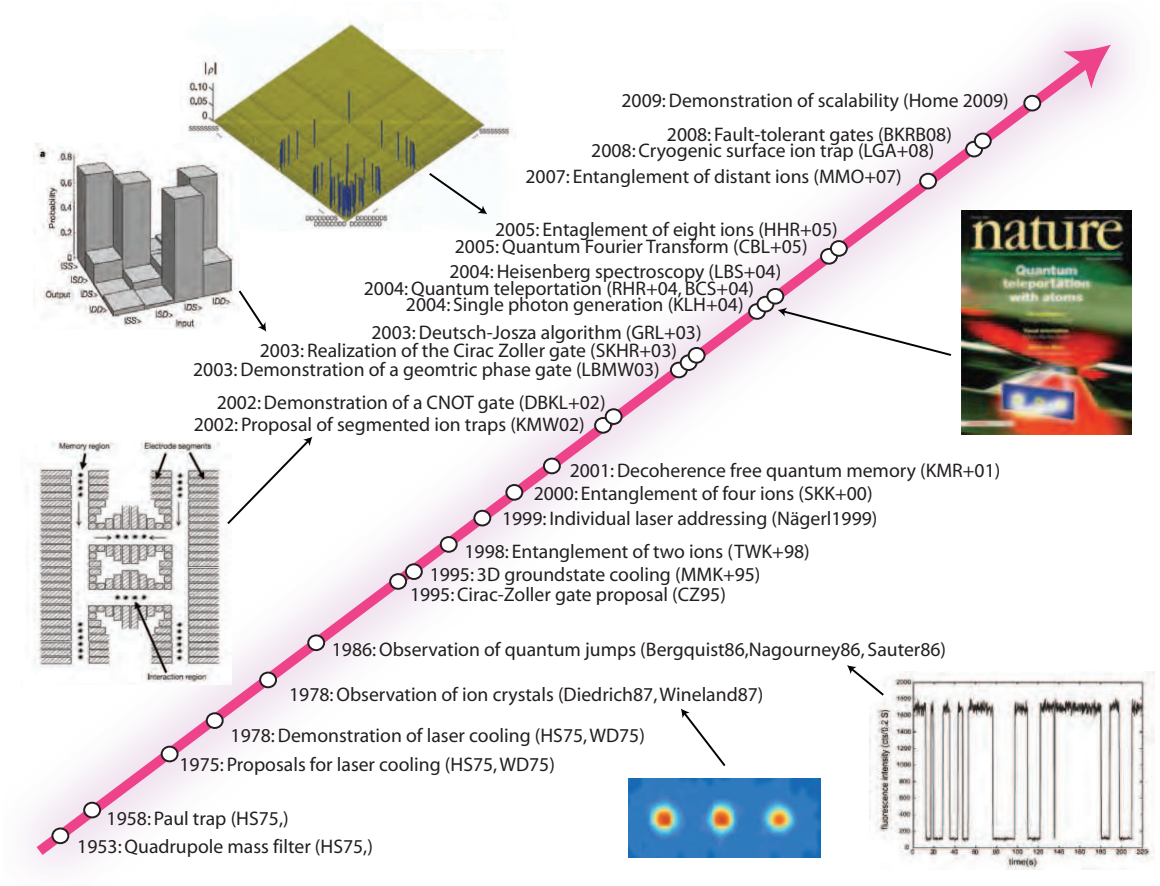

Figure 1.1.: Milestones in ion-trap quantum computing..

The ability to investigate, control and utilize quantum systems thus relies on the ability to isolate small systems sufficiently from the outside world and to provide techniques for controlled quantum state manipulations and measurements. Today, the best possible technical realizations of this are traps for charged atomic particles, i.e. *ion traps*. These come basically in two flavors, namely *Paul traps*, where a combination of static and rapidly alternating electric fields is used to provide confinement in free space, or *Penning traps*, which use static electric and magnetic fields to accomplish this task. Despite the very successful history of Penning traps, Paul traps have shown to be a better suited tool to realize some of the ideas mentioned above. An overview of the milestones of quantum physics with Paul traps is shown in Fig. 1.1, where the selection reflects the personal opinion of the author. The basic physical idea of the Paul trap, namely to provide stable confinement in two spa-

tial dimensions by means of ponderomotive forces, initially led to its original use as a mass spectrometer, for which it is actually still employed for today. However, it was recognized that also stable confinement in three spatial directions is possible, which allowed for studies on isolated single atomic particles. With the advent of laser-cooling, it became possible to bring these particles completely to rest, enabling a large number of fundamental experiments, which even the founding fathers of quantum mechanics would have never dreamed of. As the trapped ions are isolated from massive objects, the suitable means to exert control and obtain information is light. As lasers are monochromatic and coherent, they provide the ideal tool for cooling, manipulation and read-out of the ions. If the atomic species which is used has at least two (meta)stable energy levels, between which population can be transferred by means of laser light, it represents a carrier of binary quantum information, a *qubit*. The figures define the value of any quantum information register: The number of qubits that can be stored and manipulated, the timescales on which decoherence occurs and the speed of the information processing steps, i.e. the *quantum gates*. In particular, the latter has to beat the decoherence timescale. Despite the successful demonstration of all necessary steps to realize a quantum information processor based on a Paul trap, the limiting issue for actual application is the scalability to a large enough number of qubits. The current state of the art is the demonstration of complete control over a number of eight ion qubits, which is unlikely to be overtrumped on the basis of conventional technology. A number of problems arise if one attempts to store a large number of ions in a single linear Paul trap: First, the required strength of radial confinement to maintain the ions aligned along a string increases with the number of ions. Second, the decrease of the minimum distance between two qubits for larger numbers of ions makes the ion addressing more and more difficult. Third, the addressing of motional modes in frequency space also becomes a challenge for many ions, as the number of motional modes increases linearly, leading to spectral crowding. To make this point clear, these statements are illustrated in Fig. 1.2.

Several ways to circumvent these scalability problems have been proposed and partially realized:

- **Atom-photon networking**
  It has been successfully demonstrated that groups of up to eight ions can be fully controlled in a single linear Paul trap. Thus, one could simply operate several of such traps. This brings up the necessity to transfer quantum information between the different sub-processors, i.e. the nodes of the quantum network. The natural candidate as information carrier is of course the photon, which has a long tradition as a carrier of quantum information. This scheme has been originally proposed in [Cir97]. The scheme only works if a deterministic mapping of quantum information from atomic to photonic qubits can be performed, for which cavity QED delivers the most suitable physical realization. A successful demonstration of this mapping with neutral atoms has been performed in [Wil07]. The combination of ion traps and high-finesse cavities has already led to a deterministic single photon generation from ions [Kel04], the combination of these techniques however still remains an experimental challenge. An alternative method to provide the desired coupling between photons and

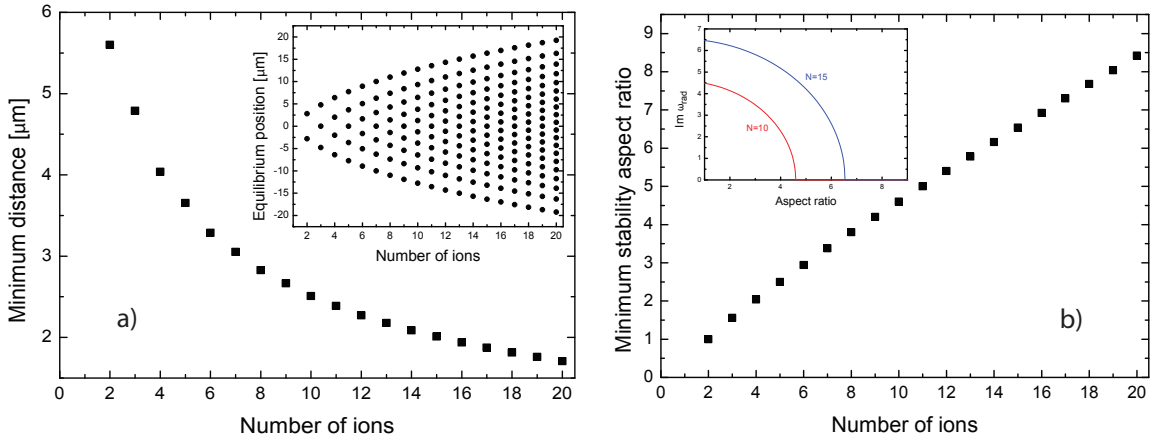

Figure 1.2.: Illustration of the limited scalability in linear Paul traps: **a)** shows how the minimum ion distance decreases as more and more ions are stored in a trap (example parameters assumed here are a trap frequency of 1 MHz and the mass of $^{40}Ca^{+}$ ions). The inset shows the equilibrium positions of the ions, also demonstrating the increasing inhomogeneity of the string for larger ions numbers. The scaling behavior is found to be $\Delta z_{min} \propto N^{-0.56}$ [Jam98]. **b)** shows how the radial confinement has to be increased for stable operation with larger numbers of ions. The minimum trap aspect ratio is ω_{rad}/ω_{ax} yielding a linear ion string is plotted against the ion number. The inset shows how the instability occurs for decreased radial confinement, see Sec. 2.2.

atoms is a free-space configuration with strong focusing [Tey09]. Another alternative is not to use light, but charge excitations in metal wires to transfer the qubit information over distances [Dan09].

- **Probabilistic entanglement**
  A tremendous experimental simplification is achieved if the requirement of deterministic coupling in the previously mentioned scheme, i.e. unit efficiency of qubit conversion, is dropped. The price to be paid is that the computation scheme becomes probabilistic. A possible realization was proposed in [Dua04b], with the key idea of making use of emitted photons as *heralds* for entanglement. After a certain number of attempts, one would therefore know that ions at remote locations are in a given entangled state. This state can then be used as a resource for quantum computation without the necessity of further quantum information transfer, e.g. in the spirit of the cluster state computation scheme proposed in [Rau01]. The scheme has recently been realized for two ions [Moe07], but the future prospects remain questionable because of the low suc-

cess rates for entanglement and the unfavorable scaling behavior for more than two qubits. However, a hybrid approach where cavities are used to enhance the photon collection efficiencies might still be a very promising candidate for large-scale quantum computation.

- **Laserless quantum computing**
  The necessity of ultra-stable laser sources in unfavorable wavelength ranges, with high demands on power and stability, represents one of the greatest obstacles for the commercial use of quantum computation. Also, some of the scalability limits listed above arise due to the requirement of well-defined interactions between ions and laser light. Furthermore, frequency and intensity fluctuations and scattering represent unavoidable decoherence sources, which is carefully investigated in this thesis. A partial relief from these difficulties would be to place an ion string in a strong magnetic field gradient, which breaks translational symmetry such that the conservation of momentum does not hold anymore. Thus, a coupling between qubit state and external degrees of freedom can be achieved without short wavelength laser radiation, and thereby enables the coupling of the internal states of distant ions. This was originally proposed in [Min01], and the selective addressing of different ions in a magnetic field gradient has been demonstrated in [Joh09], along with the observation of a signature of magnetic-field induced coupling between radio-frequency and motion.

- **Fast gates on large ion arrays**
  According to a gate proposal from 2003 [GR03], ultrafast laser pulses with durations much shorter than the radiative lifetime of an excited state pertaining to a dipole transition can be used for coherent population transfer. The momentum kick accompanying the photon absorption can then be used to mediate the gate by conditional pick-up of geometric phases as in the conventional geometric phase gate [Lei03b]. It was realized in Ref. [Dua04a] that due to the fact that the total gate time can be shorter than the vibrational period of the ions, only local oscillations are excited and the errors that occur from parasitic coupling to spectator ions is strongly reduced. It was found in Ref. [Zhu06a] that the experimental effort can be reduced with the application of quantum control techniques, and it is shown in Ref. [Zhu06b] that the usage of radial vibrational modes instead of the axial ones yields major experimental advantages. Radial mode entangling gates based on conventional cw-laser radiation have been demonstrated in Ref. [Kim09], and entangling gates with pulse trains comprised of ultrashort laser pulses were accomplished in Ref. [Hay10].

- **Multiplexed trap architectures**
  A way to overcome the limits for the manipulation of large ion crystals is the usage of multiplexed trap structures. The idea is to use more complicated electrode geometries making up an *array* of miniature Paul traps, where smaller groups of ions can be stored and manipulated easily. In order to make use of the full number of ions as qubits, ions must be shuttled between the different trap sites. This approach was first presented in [Kie02], and in the following years several groups have made attempts to

fabricate and use microstructured segmented Paul traps. Shuttling and splitting operations have been successfully demonstrated [Row02]. Variations in the geometry such as surface traps [Sei06], T-junction traps with three layers [Hen06] and semiconductor traps [Sti06] have been successfully used. Two main issues determine the usability of these segmented traps for a future quantum computer: The first is the feasibility and scalability of the fabrication process, which led to the strong interest in surface and semiconductor traps, as one hopes that it is possible to adapt well-established fabrication techniques from the semiconductor industry for the production of arbitrarily complicated structures. Second, as the trap structures become smaller and more complex, the behavior of trapped ions will deviate more from ideal harmonically confined particles. Especially the heating rate from the motional ground state increases and micromotion compensation and optical access become more difficult. Because of this, up to date more conventional microchip trap made out of gold-coated ceramic arranged in a 3D geometry have been more successful, although they are more difficult to fabricate. However, several experiments utilizing surface traps are catching up [Lab08]. Another advantage of surface traps is their dimensionality: Structures which allow for rearranging the order of ion crystals can be fabricated more easily. Recently, high-fidelity shuttling over an X-junction in a 3D geometry has been demonstrated [Bla09]. The most tremendous challenge for microstructured traps certainly is the largely enhanced heating rate, which scales as r^{-4} with respect to the minimum distance r of an ion to the most nearby surface [Des06]. A possible solution to this is to utilize other ion species for sympathetic cooling [Hom09], which however largely increases the experimental overhead.

In this thesis, we employ the last of the presented approaches. We describe the effort towards utilizing a microstructured trap with a linear 3D geometry for scalable quantum logic. The manuscript is organized as follows: In chapter 2, we lay the theoretical foundations in a way such that the thesis is mostly self-contained. We introduce the basics of atom-light interactions, which are extended step by step to include motional degrees of freedom, dissipation and far-off-resonant laser beams. We also give a theoretical account on the operation principles of Paul traps, which is generalized for the treatment of arbitrary trap structures. In chapter 3, we present the experimental setup which was partially created, enhanced and optimized throughout the course of this dissertation. Technicalities are avoided as much as possible, emphasis is put on the experimental limitations arising from technological issues, and on the usability as a reference manual for future work on the experiment. In chapter 4, we describe how the experimental apparatus is used to establish a qubit based on a trapped ion. Basic qubit operations such as initialization, readout and coherent manipulation are described in detail, along with measurement results on cooling and heating of trapped ions and an exhaustive study of decoherence effects. The next chapter 5 describes how elaborate numerical tools are used to shed light on the properties of our microtrap. It presents a precise calculation of the trap potentials, which are used to infer secular frequencies. Measured trap frequencies are then compared to experimental values. Furthermore, the compensation of micromotion in our trap is explained. Chapter 6 presents a novel measurement method for

atomic dipole matrix elements, i.e. transition lifetimes. This method is based on the methods developed for handling the spin qubit. First results indicate that the method might be used for attaining a comparable or even better accuracy than conventional methods. In chapter 7, we perform a tomographic measurement of the quantum state of a motional mode of a single trapped ion, which lays the foundation for envisaged experiments in the field of quantum thermodynamics. Chapter 8 gives a detailed account on the experimental preparation and manipulation of Schrödinger cat states of a single ion, i.e. on the entanglement between spin and motional degrees of freedom. These measurements represent a crucial step for the realization of two-qubit gates for quantum computation. Chapter 9 shows various measurement results on two-ion crystals, providing an essential step towards quantum computation and scalability. In chapter 10, we conclude the thesis and give an outlook on future perspectives. Some rather detailed matter is presented in appendices: Appendix A shows a method to obtain a dissipative quantum mechanical equation of motion for an effective two-level system exposed to off-resonant laser fields. Appendix C describes how phonon number distributions can be reconstructed from the coherent dynamics of a laser-driven ion. In appendix B, we give an account on the trap voltage supply electronics, which represents a key technology for the realization of scalable quantum information with segmented microchip ion traps. Finally, appendix D deals with theoretical considerations on quantum state tomography schemes superior and more powerful than the one used in chapter 7.

2. Theoretical Foundations

In this chapter, we intend to provide the theoretical foundation for the classical and quantum dynamics of trapped ion in a mostly self-contained way. After starting from the dynamics of a laser-driven two-level system including dissipation in Sec. 2.1.1, we establish a necessary link to fundamental atomic physics to explain how laser beam parameters have to set to control the interaction with the ion in Sec. 2.1.2. We then include motional effects to the laser-driven dynamics both semiclassically in Sec. 2.1.3 and on the quantum level in Sec. 2.1.4. Sec. 2.1.5 treats dissipative effects in multilevel systems, while Sec. 2.1.6 gives a generalized framework for coherent and incoherent effects in multilevel systems interacting with multiple off-resonant lasers. Finally, Sec. 2.2 gives a basic account on Paul-trap theory which is present with an emphasis on applicability for general trap geometries.

2.1. Laser-Ion Interactions

This section treats some general and specific aspects of the interaction between light and atoms. As a starting point, the dynamics of a two-level system is treated, with an emphasis on how it can be used for basic single qubit operations and the observation of resonance fluorescence. For understanding how the laser polarization affects the couplings in a multilevel system, we give expressions for the coupling matrix elements for the cases of electric dipole and quadrupole transitions. We then include the motional degree of freedom in order to explain how laser cooling in both the regimes of unresolved and resolved sidebands works. Finally, we give a framework for the treatment of multilevel atoms in multiple laser fields in the presence of spontaneous emission. This enables a rigorous derivation of the relevant parameters for driving stimulated Raman transitions, which is of crucial importance in the following chapters.

2.1.1. The Two-Level System: Dynamics

We consider two electronic levels of an atom, referred to as ground state $|g\rangle$ and excited state $|e\rangle$. The atom is placed in a laser beam, which is described as a monochromatic electric field propagating in direction x:

$$\vec{E}(t) = \vec{E}_0 \cos(kx - \omega_l t + \phi). \tag{2.1}$$

The prefactor $\vec{E}_0 = E_0\vec{\epsilon}$ gives the amplitude and polarization of the laser beam. Due to the fact that the atom is localized within a small fraction of the optical wavelength, we set the spatial phase kx of the wave to be constant which can be absorbed in the optical phase ϕ. This approximation is to be dropped in Sec. 2.1.4. The Schödinger picture Hamiltonian is

written as the sum of the atomic Hamiltonian $\hat{H}_0$ setting the energies of the two states, and the interaction Hamiltonian $\hat{H}_i(t)$ coupling the states via the light field:

$$\begin{aligned} \hat{H} &= \hat{H}_0 + \hat{H}_i \\ \hat{H}_0 &= E_g\hat{P}_g + E_e\hat{P}_e = \hbar\omega_{ge}\hat{\sigma}_z \\ \hat{H}_i(t) &= V_{ge}(t)\hat{\sigma}^+ + \text{h.c.}\,, \end{aligned} \tag{2.2}$$

where

$$\begin{aligned} \hat{P}_g &= |g\rangle\langle g| \\ \hat{P}_e &= |e\rangle\langle e| \\ \hat{\sigma}^+ &= |g\rangle\langle e| \\ \hat{\sigma}_z &= -\hat{P}_g + \hat{P}_e \end{aligned} \tag{2.3}$$

and E_g and E_e are the energies of the atomic levels and $\omega_{ge} = (E_e - E_g)/\hbar$. Different mechanisms for the coupling between the light wave and the atom exist, see Sec. 2.1.2 below. For the moment, we just assume a given coupling matrix element $V_{ge}(t)$ containing the electric field $\vec{E}(t)$ between ground and excited state, which allows us to write down the time dependent Schrödinger equation in matrix notation:

$$\begin{aligned} |\Psi\rangle &= c_g|g\rangle + c_e|e\rangle \\ i\hbar\frac{d}{dt}|\Psi\rangle &= \hat{H}|\Psi\rangle \\ \Rightarrow i\hbar\frac{d}{dt}\begin{pmatrix} c_g \\ c_e \end{pmatrix} &= \begin{pmatrix} E_g & V_{ge}(t) \\ V_{ge}^*(t) & E_e \end{pmatrix}\begin{pmatrix} c_g \\ c_e \end{pmatrix}. \end{aligned} \tag{2.4}$$

The off-diagonal coupling matrix element

$$V_{ge}(t) = E_0\cos(\omega_l t + \phi)M_{ge}(\vec{\epsilon}) \tag{2.5}$$

is comprised of the electric field amplitude, the oscillation at the laser frequency ω_l and a polarization dependent matrix element. With the definitions

$$\begin{aligned} \omega_{eg} &= (E_e - E_g)/\hbar \\ \delta &= \omega_l - \omega_{eg} \\ \Omega &= E_0 M_{ge}/\hbar, \end{aligned} \tag{2.6}$$

where Ω is called the *Rabi frequency* and δ is the *detuning* from resonance, we can transform the Hamiltonian in a frame rotating at ω_{eg} according to

$$\hat{H}' = \hat{U}^\dagger\hat{H}\hat{U} - i\hbar\dot{\hat{U}}^\dagger\hat{U} \tag{2.7}$$

with

$$\hat{U} = e^{iE_g t/\hbar}|g\rangle\langle g| + e^{iE_e t/\hbar}|e\rangle\langle e|. \tag{2.8}$$

and $\cos(\omega_l t + \phi) = (e^{i(\omega_l t+\phi)} + e^{-i(\omega_l t+\phi)})/2$, we obtain a new representation of Eq. 2.4:

$$\Rightarrow i\frac{d}{dt}\begin{pmatrix} c_g \\ c_e \end{pmatrix} = \begin{pmatrix} 0 & \Omega e^{i\delta t} \\ \Omega^* e^{-i\delta t} & 0 \end{pmatrix}\begin{pmatrix} c_g \\ c_e \end{pmatrix}, \tag{2.9}$$

where terms oscillating at the sum of laser frequency and the atomic transition frequency, $\omega_l + \omega_{eg}$ were omitted. This is the rotating wave approximation (RWA), which is justified by the fact that the sum frequency is in the 10^{15} Hz range for optical transitions, whereas the timescales of interest are on the order of microseconds, such that the fast oscillations average out upon integration of the Schrödinger equation. Note that the laser phase ϕ has been absorbed in the Rabi frequency in Eq. 2.9. Another unitary transformation of the type defined by Eqs. 2.8 and 2.8 with respect to the frame rotating at the detuning δ leads to the following convenient representation of the Schrödinger equation:

$$\Rightarrow i\frac{d}{dt}\begin{pmatrix} c_g \\ c_e \end{pmatrix} = \frac{1}{2}\begin{pmatrix} -\delta & \Omega \\ \Omega^* & \delta \end{pmatrix}\begin{pmatrix} c_g \\ c_e \end{pmatrix}, \tag{2.10}$$

which has a time-independent Hamiltonian for constant Ω and δ. Hence, it can be straightforwardly integrated to give the propagator

$$\hat{U}(t) = \begin{pmatrix} \cos(\tilde{\Omega}t/2) - i\frac{\delta}{\tilde{\Omega}}\sin(\tilde{\Omega}t/2) & i\frac{\Omega}{\tilde{\Omega}}\sin(\tilde{\Omega}t/2) \\ i\frac{\Omega^*}{\tilde{\Omega}}\sin(\Omega t/2) & \cos(\tilde{\Omega}t/2) + i\frac{\delta}{\tilde{\Omega}}\sin(\tilde{\Omega}t/2) \end{pmatrix}, \tag{2.11}$$

where $\tilde{\Omega} = \sqrt{\Omega^2 + \delta^2}$ is the off-resonant Rabi frequency, at which population is transferred back and forth between ground and excited state. Note that the coefficients c_g, c_e still pick up a phase of $\pm\delta t/2$ during time t which is not contained in Eq. 2.11 because we transformed into the frame rotating at δ. At resonance, $\delta = 0$, Eq. 2.11 reduces to

$$\hat{U}(t) = \begin{pmatrix} \cos(\Omega t/2) & -ie^{i\phi}\sin(\Omega t/2) \\ -ie^{-i\phi}\sin(\Omega t/2) & \cos(\Omega t/2) \end{pmatrix}. \tag{2.12}$$

In the resonant case, after initially starting in the ground state, the population in the excited state is found to be

$$p_e(t) = |c_e(t)|^2 = \sin^2(\Omega t/2), \tag{2.13}$$

which results in the well-known *Rabi oscillations*. If we now define the *pulse area* to be $\theta = \Omega t$, it can be seen that a pulse with $\theta = \pi$, termed π-pulse, can transfer the population completely from the ground state to the excited state and vice versa. A pulse with $\theta = \pi/2$, termed $\pi/2$-pulse, creates a balanced superposition of ground and excited state upon starting from either ground or excited state. Both types of pulses are elementary building blocks of quantum algorithms.

Note the laser phase ϕ explicitly reappears in Eq. 2.12. Of course, the laser phase cannot be controlled globally, but becomes both controllable and relevant when several propagators of the form Eq. 2.12 are concatenated, corresponding to a sequence of laser pulses with different phases. Another useful picture of this is to see the laser as a stopwatch which is

always running. The first laser pulse then starts another stopwatch, namely the atom. The experimentalist can change the pace of the laser stopwatch and give it sudden kicks, the former corresponding to changing the detuning, the latter to changing the phase directly. Furthermore, the pace of the atomic stopwatch can also be controlled by changing the energy difference between ground and excited state by external control fields, exploiting either Stark- or Zeeman shifts. At every laser pulse following the first one, the relative position of the stopwatch pointers will decide on how the atom reacts on the field. Any uncontrolled external influence on either the laser or the atomic stopwatch will lead to a loss of control over the system, which is called *dephasing*. It is interesting to note that controlling the phase of the atom is only possible if the laser phase is well defined during the whole pulse sequence, therefore the *coherence* of the laser field is of crucial importance. The coherence time τ_c is characterized by the autocorrelation function of the laser field, which is related to the laser bandwidth Δf by the Wiener-Khintchine theorem:

$$\tau_c \Delta f = 1 \tag{2.14}$$

Generally, the laser bandwidth has to be much smaller than the maximum duration of the control pulse sequence.
Vacuum fluctations drive spontaneous decay processes, where the excited state is depleted under emission of a photon. This depletion takes place a rate of

$$\Gamma = \frac{1}{\tau} = \frac{M_{ge}^2 \omega_{ge}^3}{3\pi\epsilon_0 \hbar c^3}. \tag{2.15}$$

In order to include this disspipative process which gives rise to depletion of the excited state and loss of phase coherence of superposition states, we generalize the treatment by describing the system by a density matrix $\hat{\rho}$:

$$\hat{\rho} = \begin{pmatrix} \rho_{gg} & \rho_{ge} \\ \rho_{eg} & \rho_{ee} \end{pmatrix} = \begin{pmatrix} |c_g|^2 & c_g c_e^* \\ c_g^* c_e & |c_e|^2 \end{pmatrix}. \tag{2.16}$$

The Schrdinger equation of motion of the states is straightforwardly extended to the Heisenberg equation of motion for the density matrix:

$$i\hbar\dot{\hat{\rho}} = [\hat{H}, \hat{\rho}]. \tag{2.17}$$

Now the decay from $|e\rangle$ to $|g\rangle$ at rate Γ and the decay of the off-diagonal elements at rate $\Gamma/2$ is empirically included which yields the famous Bloch equations:

$$\begin{aligned} \dot{\rho}_{gg} &= \Gamma\rho_{ee} + \tfrac{i}{2}\Omega\left(\tilde{\rho}_{eg} - \tilde{\rho}_{ge}\right) \\ \dot{\rho}_{ee} &= -\Gamma\rho_{ee} + \tfrac{i}{2}\Omega\left(\tilde{\rho}_{ge} - \tilde{\rho}_{eg}\right) \\ \dot{\tilde{\rho}}_{ge} &= -\left(\left(\Gamma/2 + i\delta\right)\tilde{\rho}_{ge} + \tfrac{i}{2}\Omega\left(\rho_{ee} - \rho_{gg}\right)\right. \\ \dot{\tilde{\rho}}_{eg} &= -\left(\Gamma/2 + -i\delta\right)\tilde{\rho}_{eg} + \tfrac{i}{2}\Omega\left(\rho_{gg} - \rho_{ee}\right) \end{aligned} \tag{2.18}$$

Here $\tilde{\rho}_{ge} = e^{-i\delta t}\rho_{ge}$ and $\tilde{\rho}_{eg} = e^{i\delta t}\rho_{eg}$ are the off-diagonal elements the a frame rotating at the detuning. From the steady-state solution $\dot{\rho}_{ij} = 0$, one obtains the rate at which the two-level atom will emit photons under laser exposure. It is given by the time-averaged population in the excited state times the decay rate:

$$R = \Gamma\overline{\rho_{ee}(t)} = \frac{\Gamma}{2}\frac{\Omega^2}{\Gamma^2 + 2\Omega^2 + 4\delta^2}, \tag{2.19}$$

which gives the familiar Lorentzian lineshape of atomic emission. A generalized version of the Bloch equations is given below in Sec. 2.1.6. One can see that the natural linewidth Γ is broadened if Ω becomes comparable in magnitude, which is called *saturation broadening*. It is convenient to express Eq. 2.19 as

$$R = \frac{\Gamma}{2}S\frac{1}{1 + S + 4\delta^2/\Gamma^2} \tag{2.20}$$

with the *saturation parameter*

$$S = \frac{2\Omega^2}{\Gamma^2}. \tag{2.21}$$

Due to the quadratic dependence on Ω, S can be given in terms of the laser intensity I:

$$S = \frac{12\pi c^2}{\hbar\omega_{ge}^3\Gamma}I. \tag{2.22}$$

ω_{ge} and Γ can be found in atomic data tables [NIS06]. This relation can be directly used to read off the laser power required to saturate a given transition. For laser cooling and fluorescence observation in ion traps, saturation parameters of S =1..10 are typically used.

2.1.2. The Two-Level System: Coupling Matrix Elements

As will be explained in detail in Chapter 4, electric dipole (E1) and electric quadrupole transitions (E2) are of particular interest for the work with Ca^+. The coupling matrix elements for these transitions read

$$\begin{aligned} M_{ge}^{E1} &= e\ \langle g|\vec{\epsilon}\cdot\vec{r}|e\rangle \\ M_{ge}^{E2} &= e\ \langle g|\vec{\epsilon}\cdot(\vec{r}\circ\vec{r})\cdot\vec{k}^{(0)}|e\rangle, \end{aligned} \tag{2.23}$$

where $\vec{\epsilon}$ is the amplitude vector of the electric field, i.e. its polarization, and $\vec{k}^{(0)}$ is the normalized propagation vector of the light wave. A quantizing magnetic field defines the coordinate system up to an arbitrary rotation around the field axis.

By invoking the Wigner-Eckart theorem, one obtains for these matrix elements:

$$\begin{aligned} M_{ge}^{E1} &= \langle g||e\ r\mathcal{C}^{(1)}||e\rangle \sum_{i=x,y,z}\sum_{q=-1}^{+1}\begin{pmatrix} J_g & 1 & J_e \\ -m_g & q & m_e\end{pmatrix} c_i^{(q)}\epsilon_i \\ M_{ge}^{E2} &= \langle g||e\ r^2\mathcal{C}^{(2)}||e\rangle \sum_{i,j=x,y,z}\sum_{q=-2}^{+2}\begin{pmatrix} J_g & 2 & J_e \\ -m_g & q & m_e\end{pmatrix} c_{ij}^{(q)}\epsilon_i k_j^{(0)}, \end{aligned} \tag{2.24}$$

where $c_i^{(q)}, c_{ij}^{(q)}$ are the Racah tensors [Jam98] and $\langle g||\cdot||e\rangle$ denote the reduced matrix elements, respectively. These are unique properties of the electronic transition under consideration and can be inferred from the lifetime of excited states, i.e. the corresponding Einstein coefficients. The matrix elements in round brackets, giving the relative coupling strengths between specific m_J sublevels by a specific polarization component are the Wigner three-j symbols. The important result is that even without the exact knowledge of the electric field strength at the position of the ion and the Einstein coefficients, one is able to calculate the *relative* driving strength of the transitions between the different sublevels within the ground and excited state manifolds. This is of crucial importance for setting up the beam geometry for driving the quadrupole transition , see Sec. 4.2.2, and for driving Raman transitions and exerting spin-dependent forces, see Sec. 4.5 and 8.1. The value of the reduced matrix element, together with the energy difference between ground and excited state, ultimately sets the lifetime of the excited state by Eq. 2.15 when all decay channels to lower lying states are considered. Dipole transitions lead lifetimes on the order of nanoseconds, thus excited states which possess dipolar couplings to lower lying states are not suitable for storing quantum information. By contrast, an excited state which is only connected to lower lying state by a quadrupole transition has a lifetime on the order of seconds and can therefore be used as information carrier.
The polarization vector $\vec{\epsilon}$ determines the transition between the specific Zeeman sublevels which are driven by the laser field. With the quantizing magnetic field along the z-axis, is conveniently expressed in the basis

$$\vec{\epsilon}_-^{(0)} = \frac{1}{\sqrt{2}}\begin{pmatrix}1\\ i\\ 0\end{pmatrix} \quad \vec{\epsilon}_0^{(0)} = \begin{pmatrix}0\\ 0\\ 1\end{pmatrix} \quad \vec{\epsilon}_+^{(0)} = \frac{1}{\sqrt{2}}\begin{pmatrix}-1\\ i\\ 0\end{pmatrix}. \tag{2.25}$$

In the electric dipole case, the $\vec{\epsilon}_-$ component drives $\Delta m_J = -1/2$, the $\vec{\epsilon}_0$ component drives $\Delta m_J = 0$ and the $\vec{\epsilon}_+$ component drives $\Delta m_J = +1/2$ transitions. If we consider a beam propagating at angle θ to the quantizing magnetic field with its polarization at angle ϕ to the $\vec{k} - \vec{B}$ plane, i.e. $\phi = 0$ if $\vec{k} \perp \vec{B} \parallel \vec{\epsilon}$, the polarization components can be expressed as

$$\begin{aligned}
\epsilon_- &= \vec{\epsilon}_-^{(0)} \cdot \vec{\epsilon} = \frac{1}{\sqrt{2}}(i\sin\phi - \cos\theta\cos\phi)\\
\epsilon_0 &= \vec{\epsilon}_0^{(0)} \cdot \vec{\epsilon} = \sin\theta\cos\phi\\
\epsilon_+ &= \vec{\epsilon}_+^{(0)} \cdot \vec{\epsilon} = \frac{1}{\sqrt{2}}(i\sin\phi + \cos\theta\cos\phi).
\end{aligned} \tag{2.26}$$

In general, if we consider a beam with propagating in the direction $\vec{k}$ with polarization components $\epsilon_-^{(k)}, \epsilon_0^{(k)}, \epsilon_+^{(k)}$, and if we assume the magnetic field to be aligned in the y-direction, the polarization vector is transformed by the rotation matrix

$$R = \begin{pmatrix} \cos\theta & \sin\psi\sin\theta & -\sin\theta\cos\psi \\ 0 & \cos\psi & -\sin\psi \\ \sin\theta & \sin\psi\cos\theta & \cos\psi\cos\theta \end{pmatrix}, \tag{2.27}$$

where θ is the azimuth and ψ is the inclination of the k-vector with respect to the coordinate system defined by the magnetic field and the trap axis. The effective polarization components acting on the atomic system can then be obtained by the scalar product

$$\epsilon_p = \bar{\epsilon}_p^{(0)*} \cdot R\bar{\epsilon}^{(k)}. \tag{2.28}$$

2.1.3. Including the Motional Degrees of Freedom: Laser Cooling

In this section, we consider the effect of the spatial phase e^{ikx} which we omitted in the previous section. Due to the fact that quantum mechanically, the ion has to be described by a wavefunction with a finite spatial extension, it 'samples' a portion of the light wave with varying optical phase. Then, a varying phase is imprinted onto the wavefunction, leading to momentum transfer due to the correspondence principle. This coupling between light and motion is important in ion trap experiments for the following reasons:

- The ion has to be strongly localized in phase space. This is achieved by laser cooling, where the coupling between light and motion is used for transferring energy from the ion's motion to the vacuum modes of the electromagnetic field.
- According to the DiVincenzo criteria, one needs to realize quantum gates between at least two ions. Because of the strong localization, the wavefunctions of the ion do not overlap, such that the coupling is only provided by the mutual (classical) Coulomb interaction. The way to realize two-ion quantum gates is then to couple the motion of one ion to the internal degree of the other one, which can be achieved by means of a motion dependent light-matter interaction.

Due to the different physics and the distinct relevance, we treat the cases where the motion is semiclassical and the case when it is quantized separately.

The trajectory of an atom with mass m moving a harmonic potential is simply given by

$$\begin{aligned} x(t) &= \sqrt{\frac{2E}{m\omega^2}} \sin \omega t \\ v(t) &= \sqrt{\frac{2E}{m}} \cos \omega t, \end{aligned} \tag{2.29}$$

where E is the total energy. If we irradiate a laser beam onto the atom, it will fluoresce at a rate given by Eq. 2.20, but in order to incorporate the Doppler effect, we have to replace the detuning as $\delta \to \delta - k_x v(t)$:

$$R(v) = \frac{\Gamma}{2} S \frac{1}{1 + S + 4(\delta - k_x v)^2/\Gamma^2}. \tag{2.30}$$

If the laser is now red-detuned from the transition, i.e. $\delta < 0$, the *absorption* rate will increase if the ion moves antiparallel to the laser beam direction. Shortly after the absorption of a photon, an *emission* process will take the atom back into the ground state. According to momentum conservation, each absorbed photon will change the momentum along the laser

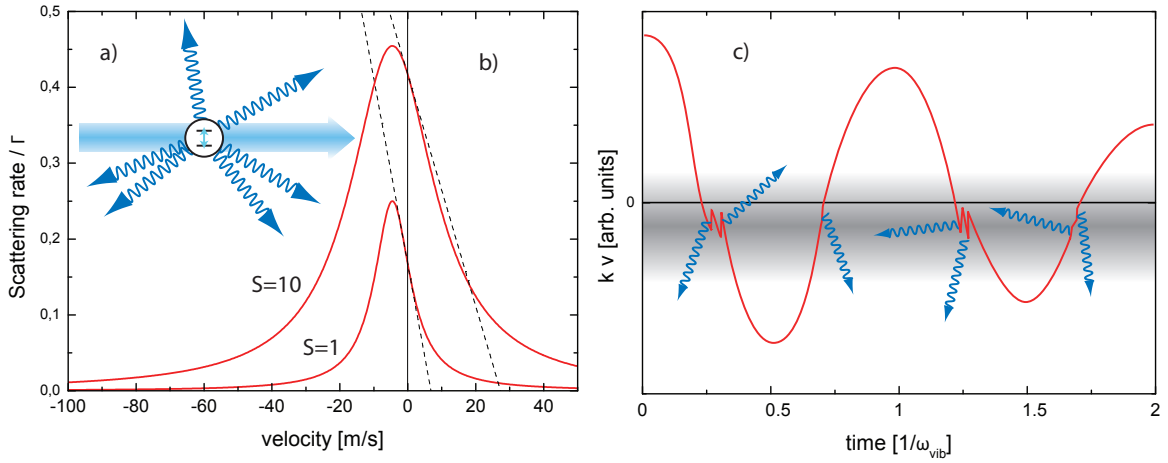

Figure 2.1.: Doppler cooling: **a)** Cartoon of the ion as a two-level system placed in the laser beam and emitting photons. **b)** Photon emission rate from Eq. 2.30 versus velocity for saturation parameters $S = 1$ and $S = 10$ and a detuning of $\delta = -\Gamma/2$. The dashed lines indicate the slope at $v = 0$. Note the curve for multiple saturation has a less steep slope. **c)** Velocity trajectory of an ion oscillating in a harmonic trap at frequency ω_{vib}. The grey shaded area indicates the emission rate as indicated in b). When crossing the resonant region, emission processes take place which decrease the kinetic energy of the oscillation.

beam direction by $\Delta p = \hbar k_l$, but each photon will amount to a momentum kick $\Delta p = \hbar k_{eg}$, where the direction is random [1] such that the net momentum transfer from emission is zero after a number of emission processes. Thus, the laser reduces the overall momentum along the beam direction. In a three-dimensional harmonic potential, the atom possesses three mutually orthogonal components of vibration, which can all be cooled by a single laser beam if the beam direction is not collinear with any of the three modes, which is in contrast to free space cooling in magneto-optical traps where at least four laser beams have to be employed. This is normally the entire explanation the *Doppler cooling* process, however one might wonder if the argument that the momentum kicks due to the emission processes do average out does not break down in the three-dimensional case. The reason why Doppler cooling still works in three dimensions is that the absorption takes place red detuned, whereas the emission takes place on resonance, i.e. $k_l < k_{eg}$. Thus, energy is continuously transferred from the atomic motion to the vacuum light modes. Time-averaged, the cooling can be seen as a dissipative

[1] In a more realistic model, the emission is not completely isotropic due to the presence of a quantizing magnetic field, it rather follows the familiar dipole emission pattern

force

$$F_{cool}(v) = \hbar k_{eq} R(v), \tag{2.31}$$

leading to an energy dissipation rate of

$$\dot{E}_{drift} = \overline{F_{cool}(v) \cdot v} \tag{2.32}$$

This is a drift process, which is counteracted by a diffusion process in momentum space due to the random emission processes. A detailed analysis reveals that optimum Doppler cooling takes place if the detuning just amount half the linewidth $\delta = -\Gamma/2$ and at unity saturation $S = 1$. However, a completely realistic treatment would have to involve the fact that one is dealing with a multilevel system, leakage to other electronic states, the anisotropy of the trap and of the emission pattern, the discrete nature of the emission processes and the micromotion in ion traps, see Sec. 5.2. Quite generally, one finds that the limit for Doppler cooling in ion traps is given by an average number of typically 10..30 motional quanta per mode, depending mostly on the ion species and on the trap secular frequencies. Doppler cooling can be seen as driving the atom to a thermal equilibrium with a reservoir given by the laser, and the equilibrium temperature is given by the transition linewidth. Hence, one will find the atom with a thermal distribution of phonon number after Doppler cooling:

$$p_n = \frac{\bar{n}^n}{(\bar{n}+1)^{n+1}} \quad \text{with} \quad \bar{n} = \frac{k_B T}{\hbar \omega_v} \tag{2.33}$$

Fig. 2.1 shows the photon emission rate versus atomic velocity for different saturation parameters. It can be seen that a finite probability exists that emission processes can take place for $kv > 0$, leading to energy transfer *to* the atom. For low energies, i.e. small velocities, the slope of the emission rate at zero velocity determines the relative weight of cooling and heating processes and therefore sets the final temperature. Thus, narrow atomic lines and small intensities lead to lower final temperatures, but smaller fluorescence rates and cooling rates. This tradeoff is circumvented in ion trap experiments by using small laser power for cooling, but larger power for trapping and fluorescence detection.

In the following, we explain how information about the motional state of a single harmonically confined ion can be extracted from fluorescence rate measurements. We assume a single ion to undergoes classical oscillatory motion along the directions of the motional modes:

$$r_i(t) = A_i \sin(\omega_i t + \phi_i) \qquad i = x, y, z, \tag{2.34}$$

with the amplitudes A_i, frequencies ω_i and relative phases ϕ_i for the three normal modes. In principle one has to average any resulting quantity about the undefined ϕ_i, however as the observation time is much longer than the oscillation periods this is not necessary. The energy stored in the motional modes is given by

$$E_i = A_i^2 m \omega_i^2. \tag{2.35}$$

It should be mentioned here that the equipartition theorem from thermodynamics does not necessarily hold for a single trapped ion, therefore we also do not make use of the notion

of a temperature here. Because we obtain only information about the total energy, we still have to make to approximation that the energy is shared equally among the three motional modes:

$$E_{tot} = \sum_i E_i \approx 3\bar{E} \tag{2.36}$$

For deriving an expression for the fluorescence rate, we take into account that the oscillatory motion acts as to effectively modulate the frequency of the Doppler cooling beam, where the modulation frequency is given by the oscillation frequency and the frequency deviation $\delta_{FM} = \vec{k} \cdot \vec{v}_i^{max}$ is given by

$$\delta_{FM}^{(i)} = A_i \omega_i \frac{\cos\alpha_i}{\lambda} = \sqrt{\frac{2E_{tot}}{3m}} \frac{2\pi \cos\alpha_i}{\lambda}, \tag{2.37}$$

where α_i is the angle that the cooling beam makes with the oscillation vector pertaining to mode i and λ is the cooling beam's wavelength. With the modulation index M_i given by the ratio of frequency deviation and modulation frequency, the relative power of the frequency component which is seen by the ion to have an effective detuning of $\delta_i^{eff} = \delta_0 \pm n\omega_i$ is given by the Bessel coefficient

$$P_n = J_n^2(M_i) \qquad \text{with} \qquad M_i = \sqrt{\frac{2E_{tot}}{3m}} \frac{2\pi \cos\alpha_i}{\omega_i \lambda}. \tag{2.38}$$

For motional frequencies in the MHz range and large thermal excitations of hundreds of phonons, modulation indices $M_i \geq 1$ occur, such that the following approximation for the Bessel coefficient is justified:

$$P_n^{(i)} = \begin{cases} \frac{1}{2M_i} & n \leq M_i \\ 0 & n > M_i \end{cases} \tag{2.39}$$

If the condition holds that the fluorescence observation time is shorter than the timescale at which cooling takes place, we can now use these results together with Eq. 2.30 for the final fluorescence rate:

$$\begin{aligned} R &= \sum_{n_i} \left(\prod_i P_{n_i}^{(i)} \right) \frac{\Gamma}{2} S \frac{1}{1 + S + 4\left(\sum_i n_i \omega_i\right)^2 / \Gamma^2} \\ &\approx \frac{1}{8} \sum_{n_i=0}^{\mathrm{int} M_i} \left(\prod_i \frac{1}{2M_i} \right) \frac{\Gamma S}{2(1+S)} \left(1 - \frac{1}{1+S} \sum_i c_i^2 n_i^2 \right) \\ &\approx R_0 - \sum_{n_i=0}^{\mathrm{int} M_i} \left(\prod_i \frac{1}{2M_i} \right) \frac{\Gamma S}{2(1+S)^2} \sum_i c_i^2 n_i^2, \end{aligned} \tag{2.40}$$

where we additionally assumed $\delta_0 = 0$ for simplicity. Thus the n-summations have been truncated to positive values for symmetry reasons and a second-order Taylor expansion with respect to $c_i^2 n_i^2$ has also been performed in the second line. R_0 as the fluorescence level a

zero motional energy and $c_i = 2\omega_i/\Gamma$ have been introduced. As c_i^2 is assumes values in the 10^{-4} range, the Taylor expansion is clearly justified. Rearranging the correction term yields the fluorescence rate defect

$$\begin{aligned} R_H = R_0 - R &= \left(\prod_i \frac{1}{M_i}\right) \frac{\Gamma S}{2(1+S)^2} \sum_i \sum_{n_i=0}^{\mathrm{int}M_i} c_i^2 n_i^2 \\ &\approx \left(\prod_i \frac{1}{M_i}\right) \frac{\Gamma S}{2(1+S)^2} \frac{1}{3} \left(\prod_i M_i\right) \sum_i c_i^2 M_i^2. \end{aligned} \tag{2.41}$$

In order to obtain a useful expression, we consider that the individual properties of the different motional modes are blurred out in the summation, assume a single effective oscillation frequency $\bar{\omega}$, angle $\bar{\alpha}$ and modulation index $\bar{M}$. The final result for the fluorescence defect rate then reads

$$\begin{aligned} R_H &\approx \frac{\Gamma S}{2(1+S)^2} \bar{c}^2 \bar{M}^2 \\ &= \frac{S}{\Gamma(1+S)^2} \frac{E_{tot}}{3m} \frac{4\pi^2 \cos^2 \bar{\alpha}}{\lambda^2}. \end{aligned} \tag{2.42}$$

For a number d motional modes carrying kinetic energy, which might occur for varying ion numbers or very different heating rates for different modes, the defect rate does not depend on d, because the lower energy per mode in Eq. 2.36 is balanced by the number of modes contributing to the frequency modulation in the first line of Eq. 2.42. Furthermore, note the remarkable fact that the final result Eq. 2.42 is independent of the average trap frequency $\bar{\omega}$.

2.1.4. Including the Motional Degrees of Freedom: The Resolved Sideband Regime

We now treat the case that the linewidth of the atomic transition under consideration Γ is smaller than the vibrational frequency of the trapped ion ω_v. In this case, the quantization of the motion plays an essential role. The ion is confined by a harmonic potential, its motion is therefore the vibration of a harmonic oscillator. Restricting ourselves to one spatial dimension, the Hilbert space of the system is given by the product Hilbert space of the atomic two-level system and the Fock-space of the harmonic oscillator, comprised of equidistant levels separated by the vibrational frequency ω_v. A sketch of the system is shown in Fig. 2.2. We include the Hamiltonian pertaining the harmonic motion of the ion $\hat{H}_m$. In second quantization, we have

$$\begin{aligned} \hat{H}_m &= \hbar\omega_v \left(\hat{a}^\dagger \hat{a} + \frac{1}{2}\right) \\ \hat{x} &= \sqrt{\frac{\hbar}{2m\omega_v}} (\hat{a}^\dagger + \hat{a}), \end{aligned} \tag{2.43}$$

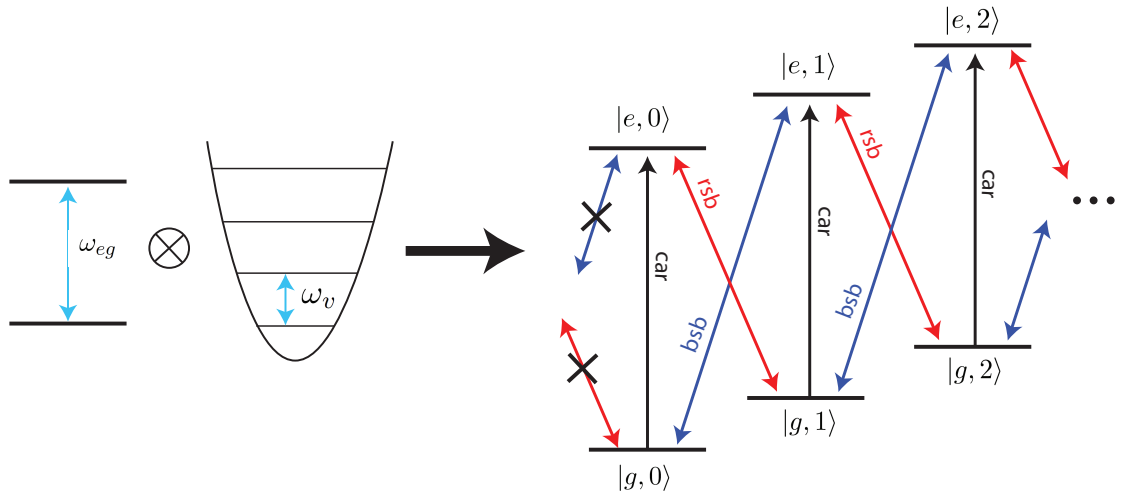

Figure 2.2.: Pictorial view on the product Hilbert space of a two-level system and a harmonic oscillator, together with most important laser-driven transitions. Note that the level $|g,0\rangle$ does not couple to the red sideband, and $|e,0\rangle$ does not couple to the blue sideband.

The coupling Hamilton operator Eq. 2.5 has to be extended by adding the optical phase $k\ x$ associated with the ion's position x along the laser propagation direction:

$$\hat{H}_{ge}(\hat{x},t) = \Omega\ (\hat{\sigma}^+ + \hat{\sigma}^-)\cos(k\hat{x} - \omega_l t + \phi). \tag{2.44}$$

The full Hamiltonian thus reads

$$\begin{aligned}\hat{H} &= \hbar\omega_{ge}\hat{\sigma}_z + \hbar\omega_v\left(\hat{a}^\dagger\hat{a} + \frac{1}{2}\right) \\ &+ \frac{1}{2}\hbar\Omega\left(\hat{\sigma}^+ + \hat{\sigma}^-\right)\left(e^{i(k\sqrt{\frac{\hbar}{2m\omega_v}}(\hat{a}^\dagger+\hat{a})-\omega_l t+\phi)} + e^{-i(k\sqrt{\frac{\hbar}{2m\omega_v}}(\hat{a}^\dagger+\hat{a})-\omega_l t+\phi)}\right).\end{aligned} \tag{2.45}$$

We define the *Lamb-Dicke parameter* to be

$$\eta = k\sqrt{\frac{\hbar}{2m\omega_v}}, \tag{2.46}$$

which is nothing else than the ratio of the extension of the ground state wavefunction of the harmonic oscillator and the laser wavelength, therefore it gives the coupling strength between light and atomic motion. Similarly to the treatment of the simple two-level system,

we transform into the interaction picture with respect to $\hat{H}_0 + \hat{H}_m$:

$$\boxed{\hat{H}_I = \frac{1}{2}\hbar\Omega\left(\hat{\sigma}^+ e^{i(\eta(\hat{a}^\dagger e^{-i\omega_v t}+\hat{a}e^{i\omega_v t})-\delta t+\phi)} + \hat{\sigma}^- e^{-i(\eta(\hat{a}^\dagger e^{-i\omega_v t}+\hat{a}e^{i\omega_v t})-\delta t+\phi)}\right).} \tag{2.47}$$

Here we employed the RWA similar to above and made use of the Campbell-Baker-Haussdorff formula $e^{-i\hbar\omega_v\hat{a}^\dagger\hat{a}t}\hat{a}e^{i\hbar\omega_v\hat{a}^\dagger\hat{a}t} = \hat{a}e^{i\omega_v t}$. Eq. 2.47 is the famous Cirac-Zoller Hamiltonian, [Cir95]. The occurring exponential can be expanded in terms of η:

$$\hat{H}_I = \frac{1}{2}\hbar\Omega\hat{\sigma}^+ e^{-i\delta t+i\phi}\left(1 + i\eta(\hat{a}^\dagger e^{-i\omega_v t} + \hat{a}e^{i\omega_v t}) - \frac{1}{2}\eta^2(\hat{a}^\dagger e^{-i\omega_v t} + \hat{a}e^{i\omega_v t})^2 + ...\right) + \text{h.c.} \tag{2.48}$$

If $\eta \ll 1$ and for low vibrational quantum numbers, which defines the *Lamb-Dicke regime* of laser-ion interactions, we can write

$$\hat{H}_I \approx \frac{1}{2}\hbar\Omega\hat{\sigma}^+ e^{-i\delta t+i\phi}\left(1 + i\eta\hat{a}^\dagger e^{-i\omega_v t} + i\eta\hat{a}e^{i\omega_v t}\right) + \text{h.c.}\,. \tag{2.49}$$

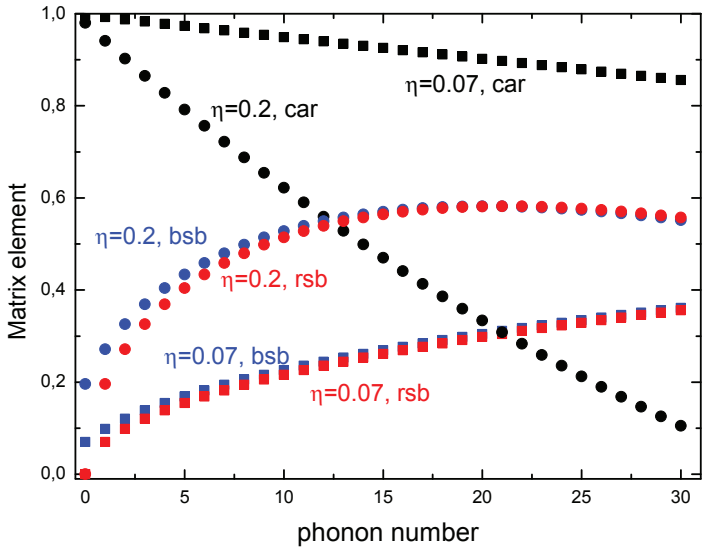

Figure 2.3.: Matrix elements Eq. 2.51 for carrier, red sideband and blue sideband transitions for two different Lamb-Dicke factors. Note that the red sideband and blue sideband matrix elements differ only for small motional quantum numbers.

If now the laser is tuned close to either the atomic transition, $\delta = 0$, or such that is detuned by the vibrational frequency $\delta \pm \omega_v$, the corresponding terms in the bracket of Eq. 2.49 are singled out and the other one can be omitted. The system then almost behaves as a simple two-level system. In the first case, one speaks of the *carrier* transition, where the vibrational quantum number is not changed when a light quantum is absorbed or emitted. In

the second case, we deal with a *sideband* transition, where one vibrational quantum is created ($\delta = +\omega_v$, *blue* sideband, bsb) or annihilated ($\delta = -\omega_v$, *red* sideband, rsb) upon absorption of a photon. Thus, if the Lamb-Dicke regime is attained, the atomic motion can be controlled at the single quantum level. The difference to the simple two-level system is however that the coupling strength, i.e. the Rabi frequency, depends on the vibrational quantum number n. In the carrier case, all transitions $|g,n\rangle \leftrightarrow |e,n\rangle$, and in the sideband case, all transitions $|g,n\rangle \leftrightarrow |e,n\pm 1\rangle$ are driven. The specific Rabi frequencies for a particular n can then be read off Eq. 2.49 by taking the matrix element of the ladder operators with the levels involved in the transition:

$$\begin{aligned} \Omega_{car} &\approx \Omega \\ \Omega_{rsb} &\approx \eta\sqrt{n}\Omega \\ \Omega_{bsb} &\approx \eta\sqrt{n+1}\Omega. \end{aligned} \tag{2.50}$$

Inspection of Eq. 2.50 reveals that the blue sideband can be driven for $n = 0$, whereas the red sideband vanishes, which is of crucial importance for temperature diagnostics. Beyond the Lamb-Dicke regime, one has to consider all higher order sidebands $\Delta n \pm m$, including the fact that an arbitrary number virtual phonons can be exchanged during a transition, i.e. terms such as $\hat{a}\hat{a}^\dagger$ for the carrier transition. The effective Rabi frequencies are then obtained from the matrix element [Cah69]

$$M_{n,n+m} = \langle n+m|e^{ik\hat{x}}|n\rangle = e^{-\eta^2/2}(i\eta)^{|m|}\mathcal{L}_n^{|m|}(\eta^2)\left(\frac{n!}{(n+m)!}\right)^{\mathrm{sign}(m)/2}, \tag{2.51}$$

where $\mathcal{L}_n^{|m|}$ are the associated Laguerre polynomials. The Rabi frequencies are then simply given by

$$\Omega_{n,n+m} = M_{n,n+m}\Omega. \tag{2.52}$$

Matrix elements for the car, rsb and bsb transitions for experimentally relevant Lamb-Dicke factors are depicted in Fig. 2.3. The solution of the time-dependent Schrödinger equation for the two-level system given by the propagator Eq. 2.11 can straightforwardly be extended in the case that the detuning is close to a sideband of any order and if η and Ω are sufficiently small to ignore off-resonant excitation on other transitions. The propagator can be cast into block diagonal form by appropriate ordering of the coefficients when the m-th order sideband is resonantly driven:

$$\begin{aligned} |\Psi\rangle &= \sum_n c_{g,n}|g,n\rangle + \sum_n c_{e,n}|e,n\rangle \\ |\Psi\rangle &\rightarrow \begin{pmatrix} c_{g,0} \\ c_{e,m} \\ c_{g,1} \\ c_{e,1+m} \\ \vdots \end{pmatrix} \end{aligned} \tag{2.53}$$

We then obtain for the propagator:

$$\hat{U}(t) = \begin{pmatrix} x_{0,m} & y_{0,m} & 0 & 0 & \cdots \\ y_{0,m} & x_{0,m} & 0 & 0 & \cdots \\ 0 & 0 & x_{1,m+1} & y_{1,m+1} & \cdots \\ 0 & 0 & y_{1,m+1} & x_{1,m+1} & \cdots \\ \vdots & \vdots & \vdots & \vdots & \ddots \end{pmatrix}, \tag{2.54}$$

with

$$x_{n,m} = \cos(\Omega_{n,m}t/2) \qquad \text{and} \qquad y_{n,m} = ie^{i\phi}\sin(\Omega_{n,m}t/2) \tag{2.55}$$

Analogously to Eq. 2.13, we obtain for the total population in the excited state upon driving Rabi oscillations starting from the ground state:

$$p_e(t) = \sum_n |c_{e,n}(t)|^2 = \sum_n p_n \sin^2(\Omega_{n,n+m}t/2), \tag{2.56}$$

where p_n is the initial phonon probability distribution, which can for example be given by Eq. 2.33.

Fig. 2.4 depicts Rabi oscillations for different thermal states with different mean phonon numbers, where the average over many experiments is plotted. The data is also shown for the same two Lamb-Dicke factors as in Fig. 2.3. One can see that a narrow phonon distribution, i.e. a low temperature, is crucial for driving high-fidelity single qubit rotations if the driving transition is sensitive to the motion.

2.1.5. Multilevel Systems Interacting with Multiple Laser Fields: Optical Pumping

We now extend the treatment of a laser-driven two-level system to an arbitrary number of states, which can be different electronic states or harmonic oscillator levels pertaining to an electronic state due to quantized motion, see Sec. 2.1.4. We also will include spontaneous emission processes in a more rigorous way than in Sec. 2.1.1. The suitable framework for this is a description of the system by a density matrix and utilization of the quantum optical Master equation as the equation of motion:

$$\dot{\hat{\rho}} = -i\left[\hat{H}, \hat{\rho}\right] + \sum_{n,m} \hat{\mathcal{D}}_{nm}(\hat{\rho}). \tag{2.57}$$

where n, m run over the various levels and the *dissipator* $\hat{\mathcal{D}}$

$$\hat{\mathcal{D}}_{nm}(\hat{\rho}) = \Gamma_{nm}\left(\hat{\sigma}^+_{nm}\hat{\rho}\hat{\sigma}^-_{nm} - (\hat{\rho}\hat{\sigma}^-_{nm}\hat{\sigma}^+_{nm} + \hat{\sigma}^-_{nm}\hat{\sigma}^+_{nm}\hat{\rho})/2\right), \tag{2.58}$$

where Γ_{nm} is the spontaneous decay rate associated with the decay channel $n \to m$ and $\hat{\sigma}^+_{nm} = |m\rangle\langle n|$ is the corresponding jump operator. The sum in Eq. 2.57 runs only over

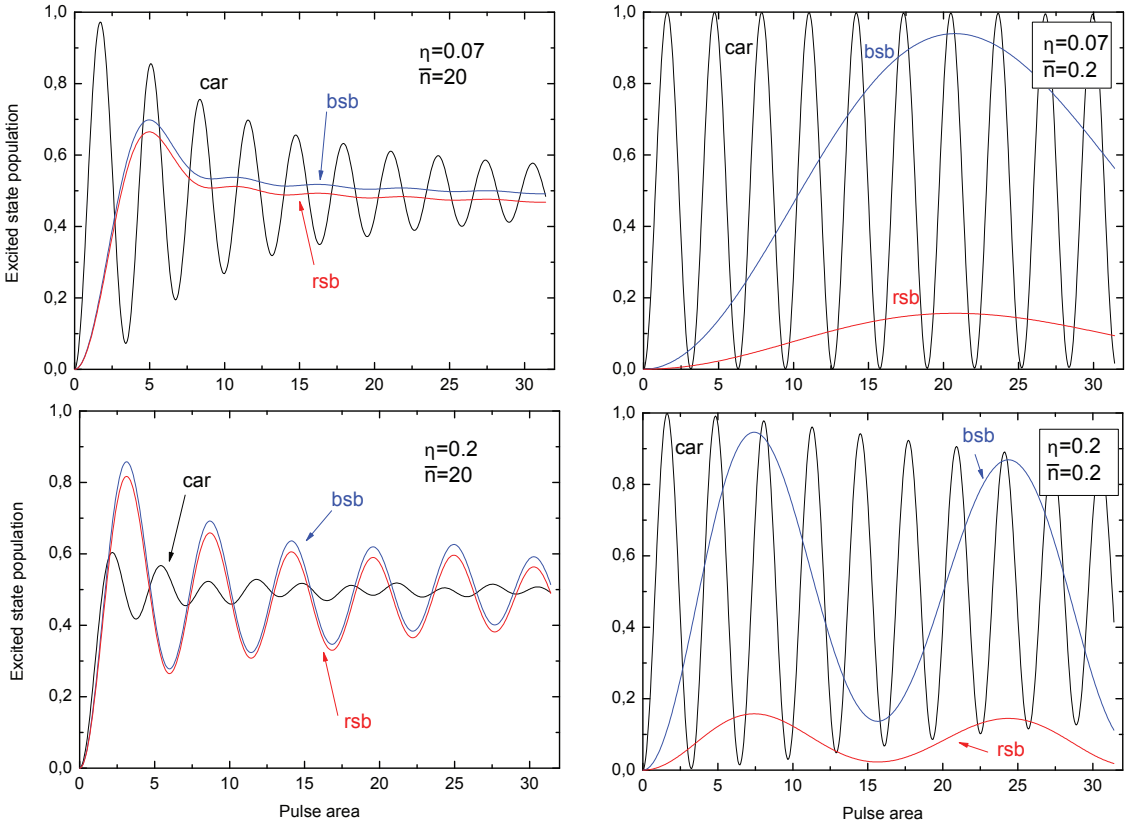

Figure 2.4.: Rabi oscillations on the carrier, bsb and rsb transitions for different mean phonon numbers and Lamb-Dicke factors. **a)** and **c)** show oscillations for $\bar{n} = 20$, corresponding to the situation after Doppler cooling. **b)** and **d)** show oscillations for $\bar{n} = 0.2$, which is a typical result of sideband cooling. **a)** and **b)** are for $\eta = 0.07$, which is realized on the 729 nm quadrupole transition, and **c)** and **d)** are for $\eta = 0.2$, corresponding to the stimulated Raman transition at 397 nm. Note that in contrast to **a)**, the sideband Rabi oscillations in case **c)** dephase less rapidly as the carrier ones. This is due to the plateau of the matrix elements at phonon numbers around 20, see Fig. 2.3.

terms with nonzero Γ_{nm}. Note that $\Gamma_{nm} \neq 0 \Rightarrow \Gamma_{mn} = 0$ and also $\hat{\sigma}^-_{nm}\hat{\sigma}^+_{nm} = \hat{\mathcal{P}}_{nn}$. The Hamiltonian governing the unitary part of the dynamics is generally given by

$$\hat{H} = \sum_n E_n \hat{\mathcal{P}}_n + \frac{\hbar}{2} \sum_l \sum_{nm} (\Omega^{(l)}_{nm} e^{i\omega_l t} \hat{\sigma}^+_{nm} + \text{h.c.}). \tag{2.59}$$

The l-sum runs over the various lasers with frequencies ω_l and Rabi frequencies $\Omega^{(l)}_{nm}$. Note that the nm sum runs only over the transitions between the levels and not over the levels

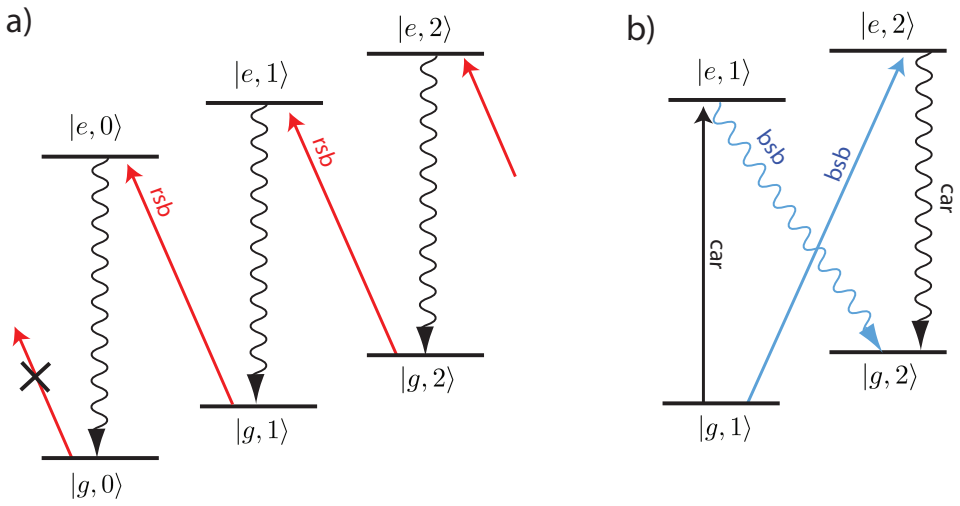

Figure 2.5.: **a)** Cartoon of the sideband cooling scheme, where the motional deexcitation on the red sideband and the dissipative repumping on the carrier transition are indicated. **b)** The two main heating sources counteracting the sideband cooling process: One path is off-resonant excitation on the carrier and subsequent spontaneous emission on the blue sideband, the other one is off-resonant excitation on the blue sideband and decay on the carrier, both leading to the creation of one phonon.

themselves. The lasers are typically tuned close to one particular transition, such that very few terms are actually contained in the sum of Eq. 2.59. This enables one to perform a suitable rotating-wave approximation.
The master equation Eq. 2.57 can be employed for a problem of particular importance for quantum state manipulation with trapped ions, namely the population transfer by frequency-selective optical pumping via a metastable intermediate state. This is illustrated in Fig. 2.7 and is relevant for state initialization and for the dissipative repumping step for sideband cooling. In contrast to conventional optical pumping, where a particular transition is isolated by proper alignment of the polarization of the driving laser, this population transfer process offers an increased degree of control, furthermore it still works if there is no possibility to address specific transitions by means of laser polarization, as it is the case for sideband cooling. The idea is to transfer population coherently from the initial state $|i\rangle$ to an intermediate metastable state $|a\rangle$, this transition is referred to as the *excitation* transition in the following. From this metastable state, the population is transferred to a short-lived intermediate state $|b\rangle$ on the *quench* transition, from where it decays back to either $|i\rangle$ or to the desired final state $|f\rangle$. By repeating this cycle, the probability of *not* ending up in $|f\rangle$ can be in principle pushed to an arbitrarily small value. For example, in the sideband cooling process we have for

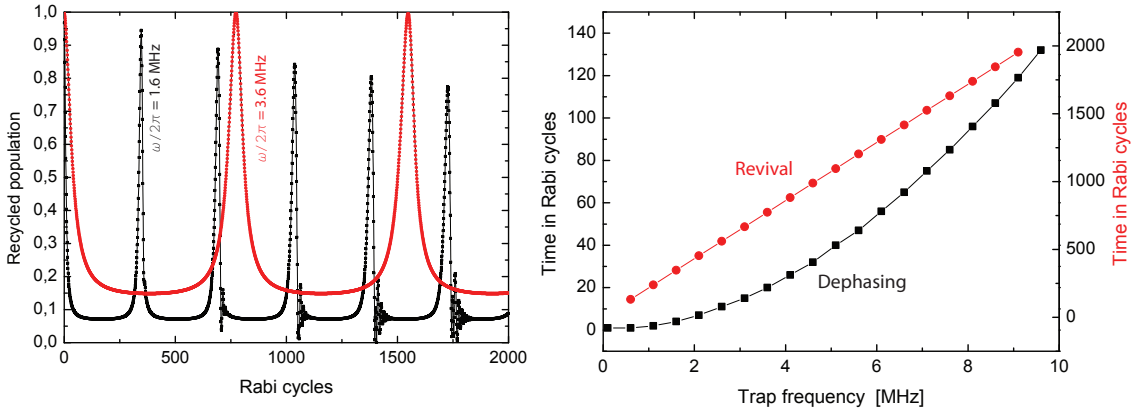

Figure 2.6.: Dephasing study of Rabi oscillations in thermal ensembles. For this example case, the driving wavelength is chosen to 729 nm and the angle of the beam to the oscillation mode is 45^o, corresponding to a typical situation in experiments. For the trap frequency varying between 100 kHz and 10 MHz and a $^{40}Ca^+$ ion, the Lamb-Dicke factor is varying between 0.22 and 0.022. For each trap frequency, a thermal phonon number distribution according to Eqs. 2.33 is assumed. **a)** shows the population in the excited state after driving $2n+1$ π-pulses. The decrease from unity is due to the dephasing occurring at timescale t_{deph}, which is reverted after the revival time t_{rev}. Curves for two different trap frequencies are shown, such that it can be immediately seen that both timescales increase for a tighter trap. **b)** shows t_{deph} and t_{rev} versus trap frequency. t_{deph} increases quadratically with ω_v, whereas t_{rev} grows linearly.

a single phonon removal step $|i\rangle = |g, n\rangle$ and $|f\rangle = |g, n-1\rangle$. The process can be performed either continuously, i.e. the lasers driving the excitation and quench transitions are always switched on, or in a pulsed way, such that the population is first transferred from $|i\rangle$ to $|a\rangle$ by the first laser, and then dumped back to the ground state via $|b\rangle$ by the second laser.

The first scheme acts as to effectively decrease the lifetime of the metastable state $|i\rangle$ [Mar94], increasing the total population transfer rate. However, one is confronted with a tradeoff situation because the lifetime of $|a\rangle$ leads to a less efficient coherent drive of the $|i\rangle \rightarrow |a\rangle$ transition, which requires careful adjustment of Ω_{ab}. This problem is circumvented in the pulsed scheme, which in turn suffers from the drawback that off-resonant excitations $|f\rangle \rightarrow |a\rangle$ might occur for short excitation pulses on $|i\rangle \rightarrow |a\rangle$.

Figs. 2.8,2.9 and 2.10 show a detailed investigation of the continuous pumping process by means of full numerical solution of the master equation Eq. 2.57, revealing some impor-

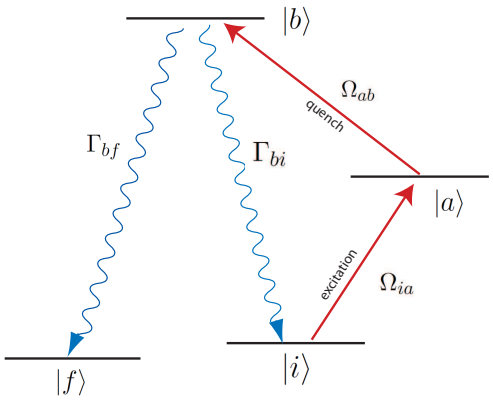

Figure 2.7.: Generic four-level system for the investigation of frequency-selective optical pumping, see text.

tant general aspects some of which appear to be counterintuitive. The case study assumes typical parameters for the $S_{1/2} \rightarrow D_{5/2}$ transition as the narrow excitation transition, the $D_{5/2} \rightarrow P_{3/2}$ as the quench transition and the decay from $P_{3/2}$ back to $S_{1/2}$ with a decay time of 7.7 ns. A branching ratio of 2:1 for the decay back to $|i\rangle$ and $|f\rangle$ is assumed. Fig. 2.8 a) clearly shows that the total transfer rate decreases for strong quench intensities, which can be easily explained by the fact that the strong coupling to a short-lived state perturbs the coherent buildup of population in $|a\rangle$, suppressing the excitation transition in a quantum-Zeno effect-like manner [Ita90]. A quite remarkable feature can be seen in Fig. 2.8 b): the minimum time to reach a 99% transfer efficiency is independent of the excitation strength over a broad range of realistic Rabi frequencies, in contrast to the intuitive guess that the Zeno suppression could be counteracted by simply increasing the excitation Rabi frequency. In the pulsed scheme mentioned above, this time is roughly given by calculating the probability of ending up in the final state after n cycles: $p_n = 1 - b^n$, where b is the branching probability to $|f\rangle$, perfect π-pulses are assumed and the switching and quench times are neglected. Now n is determined such that the desired final state occupation probability is reached. For the 2.5μs example in Fig. 2.8, 99% is attained after only four cycles, such that the pulsed scheme outperforms the continuous one for larger excitation strengths. Not included in the model however is the possibility of off-resonant excitation of parasitic transitions during the excitation step, which might for example be other transitions in the $S_{1/2} - D_{5/2}$ manifold for spin initialization or the carrier transition in the case of sideband cooling. In the pulsed scheme, for large excitation strengths, i.e. short π-pulses, off-resonant excitations are mainly caused by the respective Fourier components, which can in turn be suppressed by utilizing transform-limited pulses. In the continuous scheme, the off-resonant transitions are driven because of the increased effective linewidth, see Fig. 2.10. Another counterintuitive effect

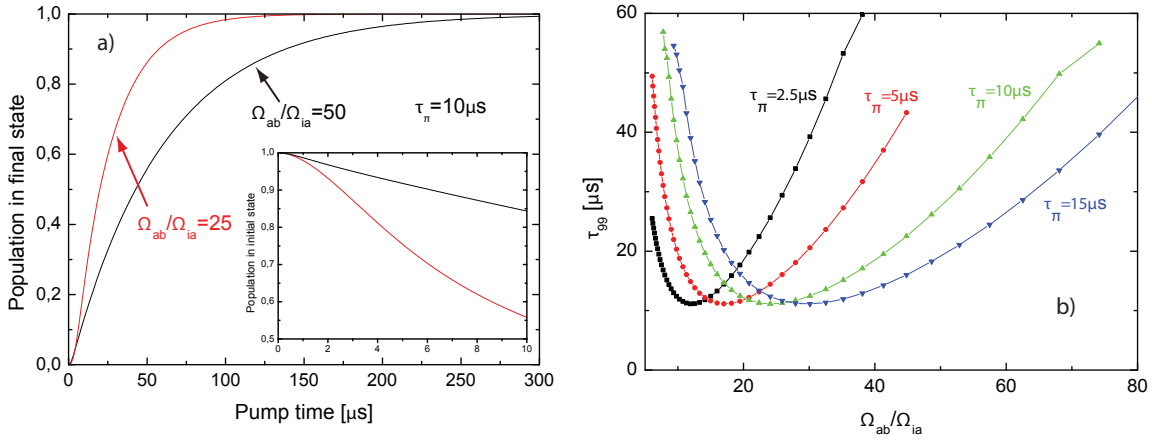

Figure 2.8.: Investigation of the continuous pump scheme: **a)** shows the population in the final state after pumping time t, where the initial population is assumed to be in the initial state $|i\rangle$, for a coherent excitation Rabi frequency corresponding to a π-time of 10μs. The curves show the pump dynamics for two different quench intensities, corresponding to $\Omega_{ab}/\Omega_{ia} = 25$ and $\Omega_{ab}/\Omega_{ia} = 50$. It can clearly be seen that the larger quench intensity leads to a reduced total pumping rate. The inset shows the initial depletion of $|i\rangle$. Note the stronger suppression of the quadratic onset for the larger quench strength. **b)** shows time required to accumulate 99% of the population in $|f\rangle$ as a measure of the pump efficiency, versus the ratio of quench to excitation Rabi frequency for different excitation strengths. Note the nonintuitive fact that the minimum time is independent of the excitation strength.

occurring here is that in the case of population cycling in a three-level system, the quench laser does *not* directly increase the linewidth of the $|i\rangle \rightarrow |a\rangle$ transition, but acts as to merely suppress the excitation. This can be understood by the fact that population cycled back to the initial state is not taken into account. By contrast, when the population transfer to $|f\rangle$ is considered, an effective broadening manifests itself in the final state population. An important conclusion to be drawn from this is that when a substructure of level $|a\rangle$ is present, e.g. when performing sideband cooling, adverse effects by off-resonant excitation of the carrier is not directly visible by performing a spectroscopy measurement on the sideband with the additional quench laser on.
Other techniques for population transfer employed for trapped ions are the STIRAP method [Sor06], where short pulses are used in a counterintuitive sequence to drive the system through a dark state, ending up in the desired final state [Ber98a]. Another possibility is the exploita-

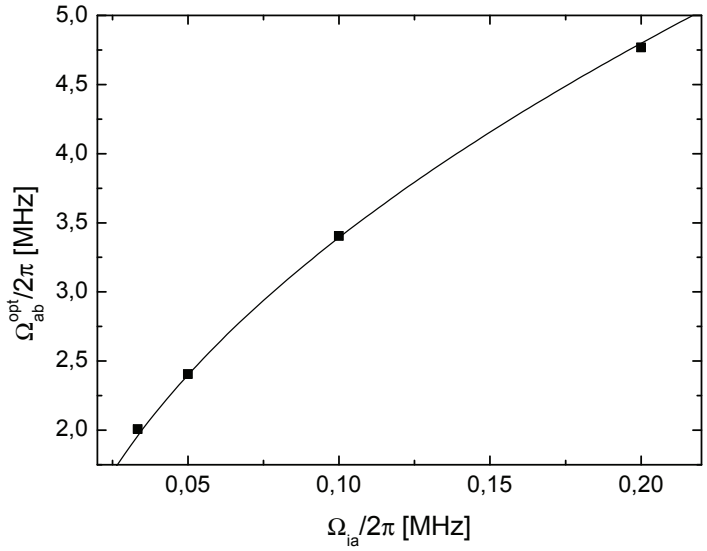

Figure 2.9.: Optimum quench Rabi frequency Ω_{ab} from Fig. 2.8 b) versus excitation Rabi frequency Ω_{ia}, which displays a square-root behavior.

tion of electromagnetically induced transparency for the selective inhibition of unwanted transitions [McD04].

2.1.6. Multilevel Systems Interacting with Off-Resonant Laser Fields: Stimulated Raman Transitions and Decoherence Effects

Here, we explain a powerful method for the treatment of time dependent coherent and incoherent effects in atomic multilevel systems, which is adapted from Ref. [Sto07]. We specify on alkaline-like ions without nuclear spin, i.e. without hyperfine structure. It is therefore directly applicable for popular ion species such as $^{24}Mg^+$, $^{40}Ca^+$, $^{88}Sr^+$, $^{138}Ba^+$, $^{172}Yb^+$ and $^{202}Hg^+$, and can be easily extended to species with nonzero nuclear spin.

$$\dot{\hat{\rho}} = -\frac{i}{\hbar}\left[\hat{H}, \hat{\rho}\right] + \sum_{J_e,\sigma} \hat{\mathcal{D}}(\Gamma_{J_e}, \hat{A}_{J_e,\sigma}), \tag{2.60}$$

where the dissipator $\hat{\mathcal{D}}$ is given by

$$\hat{\mathcal{D}}(\Gamma, \hat{A}) = \Gamma\left(\hat{A}\hat{\rho}\hat{A}^\dagger - (\hat{\rho}\hat{A}^\dagger\hat{A} + \hat{A}^\dagger\hat{A}\hat{\rho})/2\right). \tag{2.61}$$

J_e assumes the values 1/2 and 3/2 for the ions mentioned above, and Γ_{J_e} gives the decay rate, i.e. the Einstein A coefficient for the corresponding transitions to the ground state. The jump operators are given by

$$\hat{A}_{J_e,\sigma} = \sum_{m_{J_g}, m_{J_e}} \begin{pmatrix} J_g & 1 & J_e \\ -m_g & \sigma & m_e \end{pmatrix} |J_g\ m_{J_g}\rangle\langle J_e\ m_{J_e}|. \tag{2.62}$$

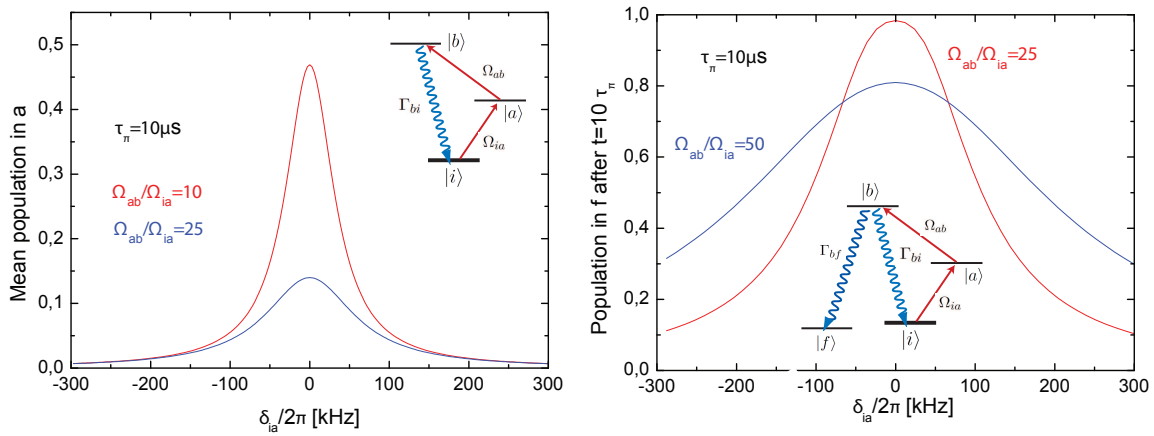

Figure 2.10.: Illustration of the effective line-broadening of the quench laser. **a)** shows the steady-state population in $|b\rangle$ in a three-level system with missing $|f\rangle$ versus detuning of the excitation laser frequency, for two different quench intensities. Note that for the three-level system, increased quench strength merely leads to a suppression of the excitation. **b)** shows the population of 10 μs pumping in the $|f\rangle$ state of the four-level system. Here, the quench indeed effectively increases the linewidth of the excitation transition.

The Hamiltonian consists of three parts:

$$\hat{H} = \hat{H}_B + \hat{H}_e + \hat{H}_i. \tag{2.63}$$

The Zeeman Hamiltonian $\hat{H}_B$ simply describes the energy splitting of the m_J sublevels in the presence of the quantizing magnetic field B:

$$\hat{H}_B = \mu_B g_J \sum_{m_J} m_J B |J\ m_J\rangle\langle J\ m_J|, \tag{2.64}$$

with the Bohr magneton μ_B and the Landé factors g_J. $\hat{H}_e$ simply sets the energies of the excited states:

$$\hat{H}_e = \sum_{J_e} \hbar\ \omega_{J_e} |J_e\rangle\langle J_e|. \tag{2.65}$$

Finally, the light-atom interaction Hamiltonian is given by

$$\hat{H}_i = \sum_l \frac{\hbar\Omega_l}{2\sqrt{2}} e^{i\omega_l t} \sum_{J_e,\sigma} \epsilon_{l,-\sigma} \hat{A}_{J_e,\sigma} + \text{h.c.}, \tag{2.66}$$

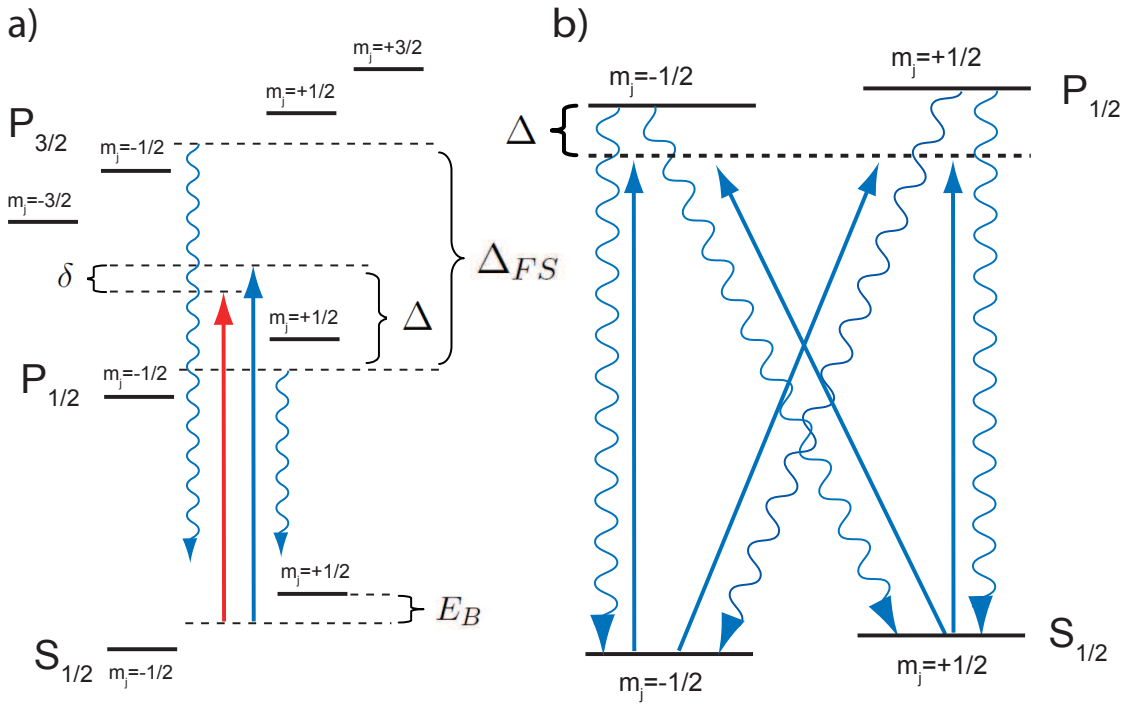

Figure 2.11.: Level scheme for off-resonant interactions: **a)** illustrates the general situation of a $^{40}Ca^{+}$ ion in two off-resonant laser fields, along with the relevant energy scales. **b)** shows in detail the various excitation and decay pathways for one laser beam with arbitrary polarization components within the $S_{1/2}$-$P_{1/2}$ manifold.

where l runs over the different laser beams, which each have 'bare' Rabi frequencies Ω_l, angular frequencies ω_l and are comprised of the polarization components $\epsilon_{l,\sigma}$. Due to short lifetime of the excited states, the detailed quantum dynamics is not really of interest, we are rather interested in the dynamics of the ground state levels only. In Schrödinger equation framework, one performs an adiabatic elimination of the exited state levels to obtain an effective Schrödinger equation for the ground state manifold. This does of course not include decoherence effects. An analogous adiabatic elimination procedure on the master equation is done as follows [Sto07]: Considering the projection on the ground state manifold,

$$\begin{aligned} \hat{P}_{gg} &= |S_{1/2}, m_J = +1/2\rangle\langle S_{1/2}, m_J = +1/2| + |S_{1/2}, m_J = -1/2\rangle\langle S_{1/2}, m_J = -1/2| \\ \hat{\rho}_{gg} &= \hat{P}_{gg}\hat{\rho}\hat{P}_{gg}, \end{aligned} \tag{2.67}$$

and under the assumption of a small saturation parameter (see above), one obtains the required equation of motion:

$$\begin{aligned}\dot{\hat{\rho}}_{gg} &= -i\left[\hat{H}_B, \hat{\rho}\right] \\ &+ i\hat{\rho}_{gg}\sum_{J_e}\frac{\hat{H}_i\hat{P}_{J_e}\hat{H}_i}{\Delta_{J_e} - i\Gamma_{J_e}/2} + \text{h.c.} \\ &+ \sum_{J_e,\sigma}\hat{A}_{J_e,\sigma}\frac{\hat{H}_i\hat{\rho}_{gg}\hat{H}_i}{i\Delta_{J_e} + \Gamma_{J_e}/2}\hat{A}^{\dagger}_{J_e,\sigma} + \text{h.c.}\end{aligned} \tag{2.68}$$

Upon feeding all required properties of the atomic system and the laser beams into this equation, the parameters characterizing the dynamics of the effective two-level system can be extracted. This is described in detail in Appendix A, where we restrict ourselves to the interaction via the $P_{1/2}$ state, which corresponds to the regime where all measurements within this thesis have been performed. The relevant dynamical parameters are the Raman Rabi frequency, ac Stark shifts, the scattering rates at which population is incoherently transferred between the spin levels and the dephasing rate at which the off-diagonal elements of the density matrix decay. In principle, all these quantities can be derived by hand from simpler arguments. The power of the method however lies in the fact that it provides a generalized framework by means of which these quantities can be obtained for general multilevel systems interacting with arbitrarily many laser fields. Furthermore, even for the relatively simple case presented in Appendix A, effects occur which are not predicted by standard treatments. It is unclear by now if these are mere mathematical artifacts or actual physical effects. Additionally, it could be shown that the dephasing rate does not correspond to the one expected from making an exact analogy to the simple two-level system. For more complicated level structures, e.g. if the detuning is large enough to lead to relevant contribution from the $P_{3/2}$ state, or if another isotope with hyperfine structure is used such that several electronic ground state levels are present, quantum interference effects occur in the dynamical quantities which can be beneficial for quantum information processing purposes [Oze05, Oze07]. The central result obtained in the appendix, Eq. A.16, is to be used at various places throughout this thesis.

2.2. Linear Segmented Paul Traps

2.2.1. Confinement Mechanism

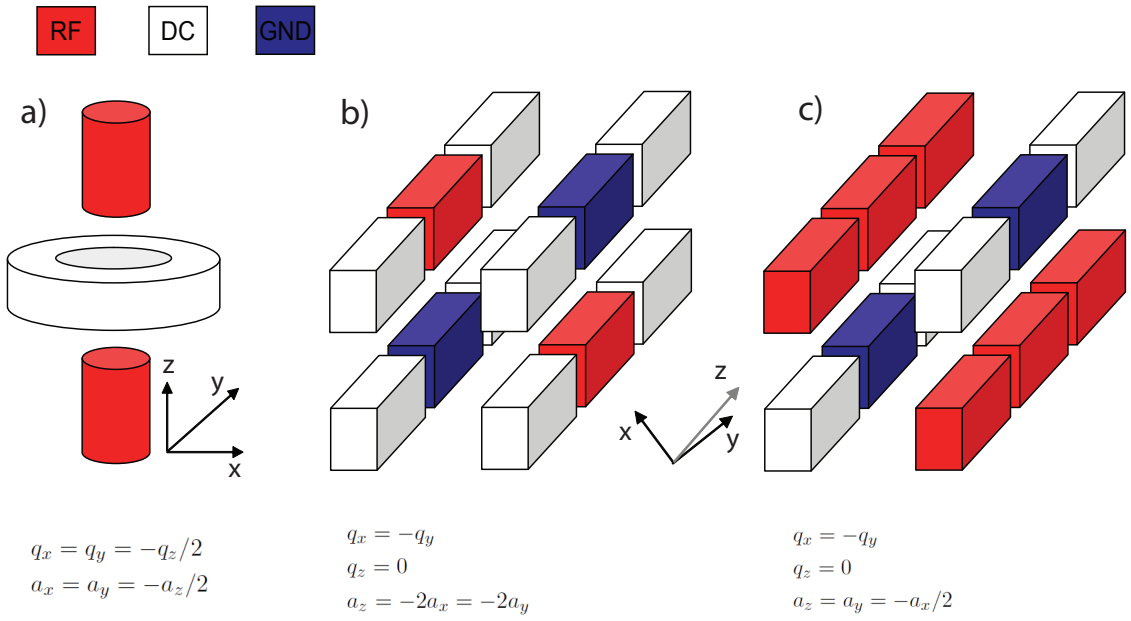

Figure 2.12.: Geometry for four basic types of Paul traps along with confinement parameters: **a)** Original ring trap. The trap is also working without additional dc-voltage, i.e. $a = 0$. **b)** Standard linear Paul trap. The dc-potential in the $x - y$ plane is anti-confining and half as strong as along the z-axis, which has to be counteracted by the rf potential. The rf-field is vanishing along $x, y = 0$, which makes it a very convenient geometry for ion strings. **c)** Segmented trap geometry. This geometry can be arrayed along the z-axis to obtain scalable trap. Note that the rotational symmetry in the $x-y$ plane is broken. One obtains a confining dc-potential in the y-direction, whereas the dc-potential in x-direction is anti-confining with twice the curvature as for the other directions.

According to the Earnshaw theorem, it is not possible to confine a particle in space only by means of static electric fields [Ear42]. The solution is therefore either to use a combination of magnetic and electric fields, which led to the invention of the *Penning trap*, or by employing oscillating inhomogeneous electric fields giving rise to a ponderomotive force, which is the underlying principle of the *Paul trap* [Pau58]. The origin of the ponderomotive force is that a charged particle exposed to a rapidly oscillating electric field, will undergo rapid oscillations at the same frequency. In a very pictorial view, this oscillation is an extra degree of freedom, which can exchange energy with the particle motion on a slower timescale.

The required frequency for the oscillating field lies in the radio frequency range for atomic ions, it is therefore termed rf-field from now on.If the rf-field is inhomogeneous, the particle will move towards regions with smaller field amplitudes, minimizing its oscillation energy. Thus, the rf-field gives rise to an effective potential, termed the ponderomotive potential or pseudopotential. The ponderomotive potential is generally given by

$$V_{\text{pond}} = \frac{Z^2 e^2 |\vec{E}|^2}{4m\Omega_{\text{rf}}^2} \tag{2.69}$$

where Ze is the charge of the ion to be trapped, m is its mass, Ω_{rf} is the angular oscillation frequency of the rf field and $|\vec{E}|$ is the field magnitude. A better understanding of the origin of the effective restoring force arises from the following viewpoint: Imagine a charged particle moving towards an electrode supplied with an rf-voltage. The oscillating electric field will cause an oscillatory motion of the ion which is by 180^o out of phase to the drive, i.e. the ion is always closer to the electrode when the polarity is such that it acts repulsive. As now the field magnitude is larger close to the electrode, the maximum repulsive force during one oscillation cycle is stronger than the maximum attractive one, leading to a net repulsive force when averaged of many oscillation periods. Therefore the ion is always driven to the trap center along the rf electric field lines. One might now wonder if there could be a possible leakage route out of the trap volume if the ion moves along the static equipotential lines $x = y$ of the potential from Eq. 2.13, as the field then has no components driving the ion back to the trap center. This is resolved by recognizing that the ion undergoes the same driven out-of-phase oscillations as in the other case, only in the direction orthogonal to the presumed escape route. It will thus always reside on a positive potential saddle lobe, where a small force towards the origin persists. Note that the ponderomotive effect explains the confinement mechanism in a Paul trap, but this *effective* potential cannot be simply superimposed to additional dc potentials which are also present in a Paul trap, therefore a dynamical treatment of the mechanical behavior of a trapped particle has to be performed for a qualitative quantitative understanding of the confinement stability and strength.

The basic structure of the rf-potential providing the confinement is a purely quadrupolar one for an ideal 2D Paul trap geometry with hyperbolic electrode surfaces:

$$V(x, y, t) \propto (x^2 - y^2) \cos(\Omega_{(\text{rf})} t), \tag{2.70}$$

which generates a harmonic ponderomotive potential. Multipolar geometries of higher order can be used as well, leading to different trapping properties. Fig. 2.13 shows the potential of Eq. 2.70 along with the basic confinement mechanism. 3D confinement in a linear trap however requires an additional dc field. We assume the particle to be near the symmetry center of a sum of two harmonic potentials at dc and rf. For three spatial dimensions, the total potential reads:

$$\begin{aligned} V(x, y, z) &= \alpha_x^{(\text{dc})} x^2 + \alpha_y^{(\text{dc})} y^2 + \alpha_z^{(\text{dc})} z^2 \\ &+ \left(\alpha_x^{(\text{rf})} x^2 + \alpha_y^{(\text{rf})} y^2 + \alpha_z^{(\text{rf})} z^2 \right) \cos(\Omega_{\text{rf}} t). \end{aligned} \tag{2.71}$$

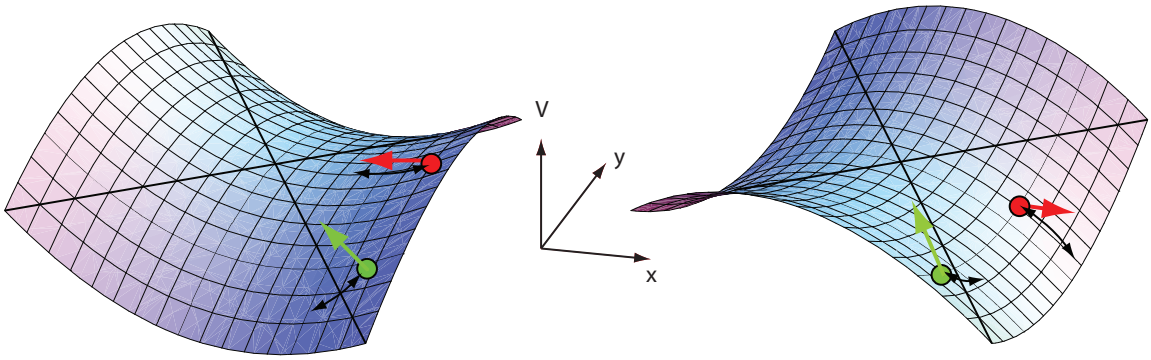

Figure 2.13.: Mechanism for confinement in a quadrupolar rf potential: The potential from Eq. 2.70 for two different oscillation phases. The red and green example particles serve to illustrate the confinement mechanism. The red ion moves along the x axis, experiencing a strongly oscillating field oscillating along the same axis. The field is stronger on the left side, when the ion is at a larger distance from the trap center, and points towards the origin. The green ion moves along a static equipotential line, undergoing transverse oscillations. It can be seen that it always experiences a force towards the trap center.

The potentials at dc and rf have to individually obey to the Laplace equation $\triangle V = 0$, such that

$$\begin{aligned} \alpha_x^{(\mathrm{dc})} + \alpha_y^{(\mathrm{dc})} + \alpha_z^{(\mathrm{dc})} &= 0 \\ \alpha_x^{(\mathrm{rf})} + \alpha_y^{(\mathrm{rf})} + \alpha_z^{(\mathrm{rf})} &= 0. \end{aligned} \tag{2.72}$$

where the potential curvatures α are given by

$$\begin{aligned} \alpha_u^{(\mathrm{dc})} &= \xi_u Z e V_{\mathrm{dc}} \\ \alpha_u^{(\mathrm{rf})} &= \zeta_u Z e V_{\mathrm{rf}}, \end{aligned} \tag{2.73}$$

V_{dc} and V_{rf} are the voltages applied to the respective electrode sets and ξ_u and ζ_u are geometry parameters. In the following, we deal only with the case $Z = 1$. We can now directly write down the equation of motion for an ion of mass m and coordinate u:

$$m\ddot{u} = -2\alpha_u^{(\mathrm{dc})} u - 2\cos(\Omega_{\mathrm{rf}} t)\alpha_u^{(\mathrm{rf})} u, \tag{2.74}$$

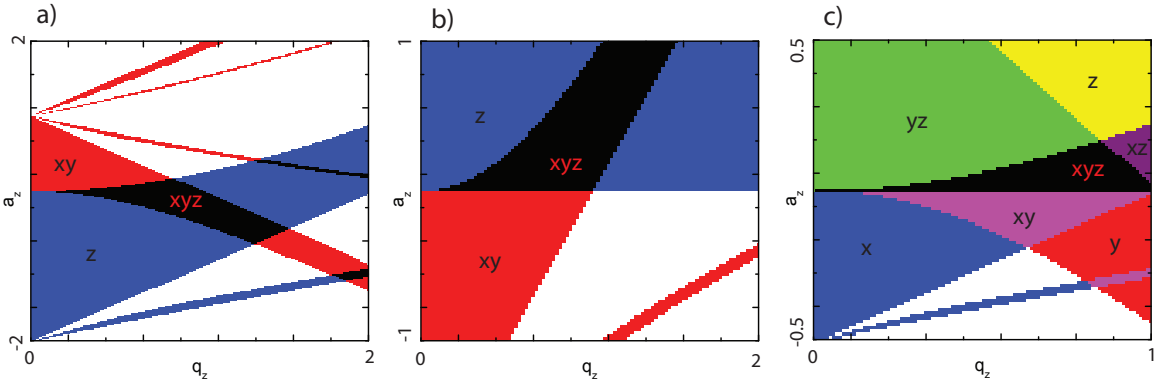

Figure 2.14.: Regions of stability for different trap geometries: The regions for which $|\beta_u| <= 1$, $u = x, y, z$, resulting from Eq. 2.78 are shown. The regions for the individual coordinate axes are shown for the three basic trap geometries, consistent with the axes labels and parameter relation from Fig. 2.12. **a)** shows the stability regions for the 3D trap, **b)** and **c)** show the regions for the linear and segmented trap design, where it was additionally taken into account that stable 3D-trapping requires $a_z > 0$.

with the radiofrequency $\Omega_{\mathrm{rf}}/2\pi$. Redefining

$$\begin{aligned} \tau &= \frac{1}{2}\Omega_{\mathrm{rf}} t \\ a_u &= \xi_u \frac{8eV_{\mathrm{dc}}}{m\Omega_{\mathrm{rf}}^2} \\ q_u &= \zeta_u \frac{4eV_{\mathrm{rf}}}{m\Omega_{\mathrm{rf}}^2}, \end{aligned} \tag{2.75}$$

we finally obtain

$$\ddot{u} = a_u u + \cos(2\tau) 2 q_u u \quad u = x, y, z \ , \tag{2.76}$$

which has the form of three uncoupled *Mathieu differential equations*. The coefficients a_u and q_u are interrelated due to the Laplace equation and possible symmetries of the electrode geometry, see Fig. 2.12. The general solution for Eq. 2.76 for arbitrary a, q along a single coordinate is found by means of the Floquet theorem and continued fractions [Gho95]:

$$y(t) = A \cos\left(\beta_y \frac{\Omega_{\mathrm{rf}}}{2} t\right) \left(1 - \frac{q_y}{2} \cos(\Omega_{\mathrm{rf}} t)\right). \tag{2.77}$$

This describes a simple oscillation at a frequency $\beta\Omega_{\mathrm{rf}}/2$, where β is function of a and q, which is called secular motion. On this secular motion, a rapid small-amplitude oscillation at

Ω_{rf} is superimposed, which is called micromotion. The stability of the motion is determined by the value of β:

$$\beta^2 \approx a - \frac{(a-1)q^2}{2(a-1)^2 - q^2} - \frac{(5a+7)q^4}{32(a-1)^3(a-4)} - \frac{(9a^2+58a+29)q^6}{64(a-1)^5(a-4)(a-9)} \tag{2.78}$$

Stable trajectories are only obtained if $|\beta| < 1$, which is intuitively clear as the secular motion must be slower than its ponderomotive drive. The regions of stability in the space of the parameters a and q are universal properties of the Mathieu equation, only the scaling of the axes depends on a given set of physical trapping parameters. Considering stable trapping in three dimensions, the global region of stability is the intersection of the stability regions for the individual spatial directions. This is illustrated in Fig. 2.14 for the three basic Paul trap geometries. Due to the dependence of the trap parameters on the ion mass m, the trap can be made very mass selective when the parameters are set to an outer tip in the region of stability. This is exactly what the geometry was initially conceived for, namely as a mass filter for mass spectrometry [Pau53].

2.2.2. Vibrational Modes of Ion Crystals

The linear and segmented traps now offer the possibility to store an entire string of ions along the node of the rf-field, which coincides with z-axis, such that none of the ions is exposed to the rf electric field under ideal conditions. This leads to the fact that an ion string in a linear Paul trap represents a physical realization of a quantum register whose controllability properties have so far not been beaten by any other experimental approach. The ion string is characterized by its static and dynamic properties, namely by its equilibrium ion positions, the frequencies and the structure of the vibrational modes. These are found by writing down the potential energies for a set of N ions aligned along the z-axis, where the x, y and z coordinates of the n-th ion are denoted as $\vec{r}_n = (u_{xn}, u_{yn}, u_{zn})^T$:

$$V = \frac{1}{2} m \sum_n^N \left(\omega_x^2 u_{xn}^2 + \omega_y^2 u_{yn}^2 \omega_z^2 + u_{zn}^2\right) + \frac{e^2}{4\pi\epsilon_0} \sum_{n,m,n\neq m}^N \frac{1}{\sqrt{(\vec{r}_n - \vec{r}_m)^2}}. \tag{2.79}$$

The trap frequency ω_z^2 along the trap axis has to be smaller than the transverse frequency ω_r, for simplicity we assume a cylindrical symmetry here. Setting the elongations along the x, y directions to zero, the equilibrium positions along the trap axis are found by balancing the external trap force with the repulsive Coulomb force:

$$\sum_n^N \frac{dV}{du_{zn}}\Big|_{u_{zn}^{(0)}} \equiv 0 = m\omega_z^2 \sum_n^N u_{zn}^{(0)} - \frac{e^2}{4\pi\epsilon_0} \sum_{m,n\neq m}^N \frac{u_{zn}^{(0)} - u_{zm}^{(0)}}{|u_{zn}^{(0)} - u_{zm}^{(0)}|^3}, \tag{2.80}$$

which can be solved analytically only for up tp $N = 3$. Now expand V around the equilibrium positions to the second order in the coordinates:

$$V \approx \sum_{a,b=x,y,z} \sum_{i,j}^N \frac{d^2V}{du_{ai}du_{bj}}\Big|_{u_{ai}^{(0)}, u_{bj}^{(0)}} \delta u_{ai}\delta u_{aj} \equiv \tilde{V}_{ij}^{(ab)} \delta u_{ai}\delta u_{bj}. \tag{2.81}$$

The δu_{ai} are small elongations from the equilibrium positions: $\delta u_{ai} = u_{ai} - u_{ai}^{(0)}$. As mixed derivatives vanish if the ions are aligned in a linear string, e.g.

$$\frac{d^2V}{du_{ai}du_{bj}}\Big|_{u_{zi}^{(0)},u_{xj}^{(0)}} = 0 \quad \text{for} \quad a \neq b, \tag{2.82}$$

we can separately write down the matrix elements $\tilde{V}_{ij}^{(aa)}$:

$$\tilde{V}_{ij}^{(zz)} = \begin{cases} m\omega_z^2 + \frac{e^2}{4\pi\epsilon_0}\sum_{k\neq i}\frac{2}{|u_{zi}^{(0)}-u_{zk}^{(0)}|^3} & i = j \\ -\frac{e^2}{4\pi\epsilon_0}\frac{2}{|u_{zi}^{(0)}-u_{zj}^{(0)}|^3} & i \neq j \end{cases} \tag{2.83}$$

$$\tilde{V}_{ij}^{(xx)} = \begin{cases} m\omega_x^2 - \frac{e^2}{4\pi\epsilon_0}\sum_{k\neq i}\frac{1}{|u_{zi}^{(0)}-u_{zk}^{(0)}|^3} & i = j \\ +\frac{e^2}{4\pi\epsilon_0}\frac{1}{|u_{zi}^{(0)}-u_{zj}^{(0)}|^3} & i \neq j, \end{cases} \tag{2.84}$$

and correspondingly for $\tilde{V}_{ij}^{(yy)}$. These matrices can be diagonalized:

$$\tilde{V}^{(aa)} = M_a^T \Lambda_a M_a \tag{2.85}$$

with the diagonal matrix

$$\Lambda_a = \begin{pmatrix} \mu_1^{(a)} & 0 & \cdots \\ 0 & \mu_2^{(a)} & \cdots \\ \vdots & \vdots & \ddots \end{pmatrix}, \tag{2.86}$$

and the orthogonal matrices

$$M_a = \begin{pmatrix} M_{11}^{(a)} & M_{12}^{(a)} & \cdots \\ M_{21}^{(a)} & M_{22}^{(a)} & \cdots \\ \vdots & \vdots & \ddots \end{pmatrix}. \tag{2.87}$$

The oscillation frequency of the n-th vibrational mode in a direction is given by the diagonal entries of Λ_a:

$$\nu_n^{(a)} = \sqrt{\mu_n^{(a)}}. \tag{2.88}$$

The structure of the motional modes can be inferred from the orthogonal matrices M_a. The relative amplitude and phase of the i-ion of an ion string oscillating at the n-th mode in a direction is directly given by the matrix entry $M_{jn}^{(a)}$. We introduce a set of generalized coordinates $q_n^{(a)}$:

$$q_n^{(a)} = \sum_j M_{nj}^{(a)} \delta u_{aj} \quad \text{and} \quad \delta u_{aj} = \sum_j M_{jn}^{(a)T} q_n^{(a)} \tag{2.89}$$

Therefore the coupling strength of a motional mode to a given laser field, i.e. the corresponding Lamb-Dicke factor, can be calculated from the eigenvector components, which is of crucial

importance for entangling gates with single ion addressing [Jam98] or by means of a running standing wave [Iva09]. The eigenvalues of the radial modes of vibration from Eq. 2.84 yield information about the stability of ion crystals: negative eigenvalues indicate instabilities, i.e. it occurs that for a too weak radial confinement and too many ions, the string assumes a zig-zag configuration instead of a linear one. Results for the equilibrium ion positions and the radial stability are shown in Fig. 1.2. The eigenvectors and eigenvalues of the matrices $\tilde{V}^{(aa)}$ are used in appendix for a generalized framework for the coherent interaction of ion crystals with laser beams.

3. Experimental Setup

This chapter is devoted to a description of our experimental setup. Sec. 3.1 describes the installation of the trap in its UHV chamber, and Sec. 3.2 gives a detailed account on the setup of the laser systems. Sec. 3.3 shows how the imaging and fluorescence detection is performed, and sections 3.4 and 3.5 briefly explain how suitable electric and magnetic field are supplied to the trap site. Finally, Sec. 3.6 describes how simultaneous computer control of the lasers, rf-sources, trap voltages and readout is accomplished.

3.1. The Trap, Vacuum Vessel and the Ovens

The fabrication, assembly and mounting of the trap is described in detail in [Sch09, Sch06, Sch08] and shall be only briefly outlined here. The microchip Paul trap is basically a sandwich design of three alumina wafers, where the trap structure is created by a laser cutting procedure. The top and bottom layers making up the trap electrodes are gold coated. The three layers are glued and mounted in a commercial chip carrier. The rf and dc voltages are supplied to the electrodes via bond wires. The chip carrier in turn is mounted on a PCB board from which the voltage wires run to four 25 pin Sub-D connectors of the top flange of the ultra high vacuum (UHV) chamber. Additional electric feedthroughs are for the rf-supply and for the current for the two Ca ovens. The UHV is maintained by an ion pump [1] and an additional titanium sublimation pump [2], such that after bakeout at 120°C a pressure of typically $4{\cdot}10^{-10}$ mbar is achieved, which is monitored by a UHV gauge [3]. The effusive Ca ovens are built according to ref. [Rot03]. They consist of a stainless steel tube filled with Calcium granules, connected to a stainless steel rod by a sheet of Tantalum. The resistive heating is provided by a current of typically 3.4 Ampere flowing from the rod via the Tantalum sheet through the tube, where heat is generated due to the thin tube walls. According to [Rot03], a temperature of roughly 200°C is attained, corresponding to a vapor pressure of less than 10^{-12} mbar, such that the background pressure is not affected. The oven is operated continuously, because its heating takes place on a timescale of 10 minutes, as compared to a trap loss on a similar time scale. After three years of continuous operation during experiments, no adverse effects from possible coating of the trap electrodes have ever been observed. Neither did we observe any visible changes on the trap surface when the trap is monitored by an extra CCD camera with macro objective (which is used for beam alignment), nor did we observe any effects on the heating rate or trapping behavior, as is

[1] DN63CF StarCell, Varian Inc., Palo Alto, USA
[2] tectra GmbH, Frankfurt am Main, Germany
[3] Varian Inc., Palo Alto, USA

argued in many research articles. An adverse effect which *had* to be taken care of is current ripple from the Statron current supply, which is adversely affecting the qubit coherence time. The oven is situated close to the ion, and the low inductance leads to a low rejection of high frequency current ripple. Therefore, a low pass filter with 10 Hz cutoff was inserted [4], which lead to an increase of spin coherence time from 100 μs to about 400 μs (see Sec. 4.2.2).

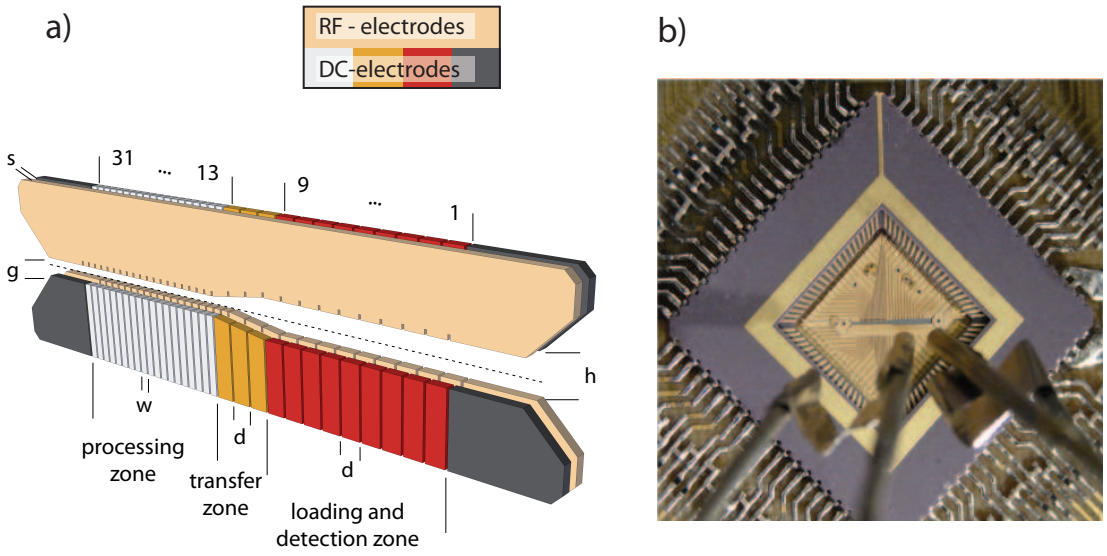

Figure 3.1.: Our microchip ion trap: **a)** shows a schematic layout of the trap, where dc and rf electrodes can be distinguished, furthermore the distinct loading and processor regions can be seen. **b)** shows a picture of the trap, with the effusive Ca ovens in front of it. The bond wires are too small to be seen, they run across the gap between the trap chip and the chip carrier.

3.2. Laser Systems

All laser systems are derived from commercial laser diode systems [5]. Except for the laser at 375nm, they are extended cavity diode laser systems (ECDLs), operating at a single longitudinal mode. All ECDL wavelengths are simultaneously monitored on a wavemeter [6] with a relative accuracy of 10 MHz, to which the respective probe beams are supplied via an

[4]The filter is comprised of 4x1 Ω power resistors and 8x500 μF capacitors
[5]TOPTICA AG, Gräfelfing
[6]WSU, High Finesse, Tübingen

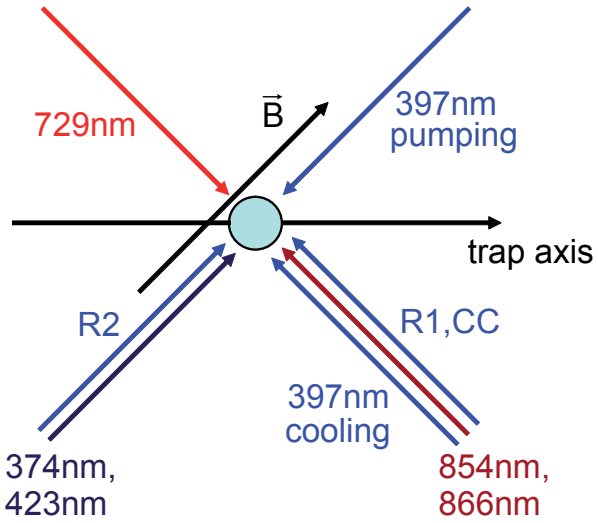

Figure 3.2.: General beam geometry of our setup: The picture illustrates how all laser propagation directions are aligned with respect to the trap axis and the quantizing magnetic field, which determines how the lasers couple the internal and motional state of the ions.

eight-port optical switching box [7]. A general overview how the various lasers are irradiated on the trap site is shown in Fig. 3.2.

3.2.1. 423 nm and 375 nm for Photoionization

The technique of resonantly enhanced two-photon photoionization is used to ionize ^{40}Ca isotope-selectively from the effusive Ca beam. Here, a beam at 423 nm excites the strong 4^1S_0 to 4^1P_1 dipole transition, and a laser at about 375 nm excites from the 4^1P_1 state to the continuum. The laser at 423 nm is a frequency doubled ECDL [8], where the doubling takes place in a bowtie cavity with a BIBO doubling crystal at the focal point, generating up to 10 mW (typically only 1 mW) of blue laser power out of 150 mW of seed power. The laser diode itself is free running, and optimum ionization is taking place at fundamental wavelengths from 845.58260 nm to 845.58290 nm, the optical grating of the ECDL has to be adjusted from time to time via the piezo controller to compensate for drift effects. The SHG cavity is locked to the seed laser to maintain high fundamental power at the doubling crystal. Typically, about 200 μW up to 500 μW of laser power is delivered to the trapping site, with a focusing lens of 250 mm and an estimated beam FWHM of 3 mm this leads to saturation of the transition over a broad range of atomic velocities. It is empirically found that the trapping rate is decreased below laser powers of about 100 μW. The laser at 375 nm

[7] High Finesse, Tübingen
[8] DL-SHG

is merely a free running diode, as the transition to the continuum is independent of this wavelength to a large extent. Superposition of the two ionization beams is done by matching the position of the respective beam spots at low power on the trap chip surface near the trapping site, viewed by a CCD camera with a macro objective.

3.2.2. 397 nm for Doppler Cooling, Ion Detection and Optical Pumping

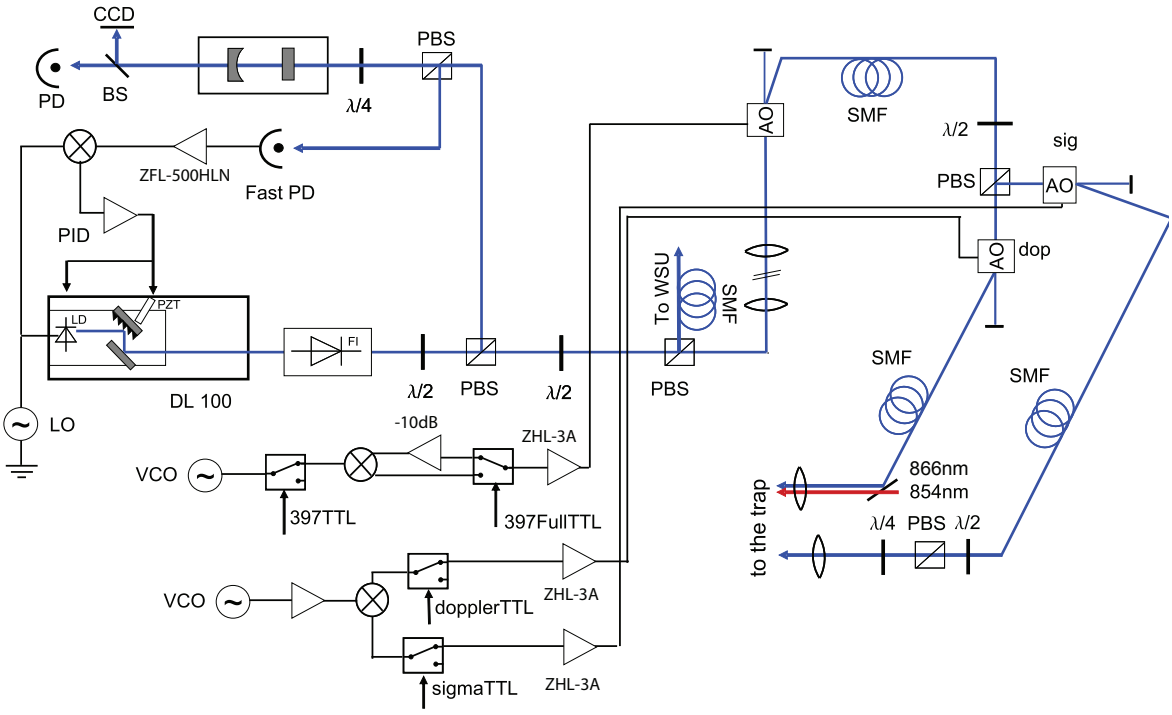

Figure 3.3.: Optical setup for the laser at 397 nm for Doppler cooling, fluorescence detection and optical pumping.

The light at 397 nm, resonantly driving the $^2S_{1/2}$ to $^2P_{1/2}$ dipole transition of $^{40}Ca^+$, is derived from a UV ECDL [9] [Lan03]. The beam layout is shown in Fig. 3.3. This laser is frequency stabilized onto an external reference cavity by means of a Pound-Drever-Hall (PDH) locking scheme. The power in the lock branch is about 1 mW which is needed because of the poor quality of the spatial mode profile of the UV ECDL. The FSR of the reference

[9] DL 100

cavity is 1.5 GHz, and its Finesse ranges at about 100. The transition is located at about 397.95920 nm. The cavity is mounted on an ultralow thermal extension ceramic block [10], its drift is slow enough to be ignored. One of the cavity mirrors is mounted on a ring piezo, such that one electrode can be supplied with a static high voltage [11] in order to obtain a resonance for a Gaussian transversal mode within the wavelength range of interest, whereas the other electrode is supplied by an HV amplifier [12] in order to perform controlled spectroscopy on the corresponding transition. The largest portion of the laser output (about 12 mW, 10 mW remaining after an external Faraday isolator) is supplied to the experiment via a polarization maintaining single mode fiber [13]. The low fiber output of only up to 1.4 mW is due to the bad quality of the transversal mode profile of the UV diode. The input into the fiber is controlled by an acousto-optical modulator (AOM) running at 80 MHz and up to 2 W input power [14]. The AOM supply can be switched between no power, full power or attenuated power, such that the laser power at the ion can either be a multiple saturation of slightly below saturation, see Figs. 4.4 and 3.3. The beam is then supplied near the vacuum chamber, where it is split into two branches serving different purposes: one branch with typically about 130 μW is used for Doppler cooling and fluorescence detection, and the remaining power is used for initializing the spin state by optical pumping. The respective beams are switched by individual AOMs, where the first orders are coupled into short single optical fibers for spatial filtering. This was found to be of crucial importance for the fidelity of the optical pumping process, especially in connection with Raman sideband cooling, see Sec. 4.6. The reason for this is that a substantial amount of stray light is still irradiated onto the ion if the AOM in the corresponding branch is switched off. This stray light is due to solarization in the UV fiber and diffraction at the AOM apertures and in the AOM crystal. Only with SM fibers in both beams, good results for optical pumping and Raman sideband cooling could be obtained. The Doppler cooling beam is π-polarized, such that mainly vertical (m_J conserving) transitions are driven. The advantage is then that the Zeeman splitting between these two transitions is smaller than it is the case for the $\Delta m_J = \pm 1$ transitions driven by $\sigma_\pm$ polarized light, yielding higher fluorescence rates and better Doppler cooling. The NIR beams at 866 nm and 854 nm are superimposed onto the Doppler cooling beam on a UV reflective/NIR transmissive dielectric mirror. The optical pumping beam is directed along the quantizing magnetic field. A $\lambda/2$ and PBS are used to control the power, and a $\lambda/4$ is used to control the polarization. It was initially tried to use additional compensation coils to align the magnetic field better along the beam propagation axis, such that the observed fluorescence is minimized upon irradiation with a circularly polarized beam with the Doppler cooling light switched off. However, fluorescence rates already close to the detection threshold can be observed, and as the trap lifetime is substantially shortened without Doppler cooling, this method was found to be not useful for further improvements of the pumping fidelity.

[10] Hellma Optics GmbH, Jena
[11] EHQ-8010p, iseg Spezialelektronik GmbH, Radeberg
[12] miniPiA 103, TEM Messtechnik GmbH, Hannover
[13] PMC-400Si-2,9-NA011-3-APC-50-P, SUK Hamburg
[14] QZF-80-20, Brimrose Corporation of America, USA

3.2.3. 854 nm and 866 nm for Repumping and Quenching

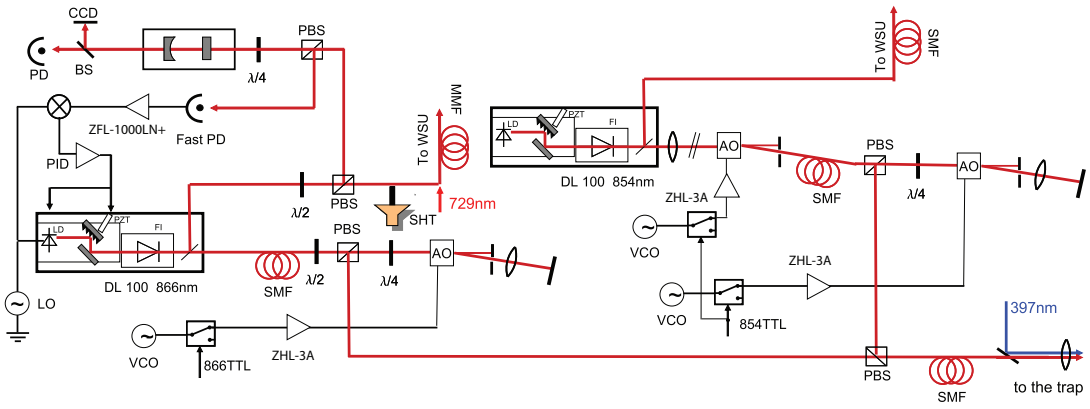

Figure 3.4.: Optical setup of the laser at 866 nm and 854 nm for repumping and quenching. The 866 nm laser is PDH locked onto a cavity, whereas the 854 nm laser is free-running, but it is switched with a second single-pass AOM in addition to the double-pass one.

The laser at 854 nm and 866 nm are used to remove population from the $^2D_{5/2}$ and $^2D_{3/2}$ electronic states respectively. The beam layouts for both laser systems are shown in Fig. 3.4. The context in which this happens is however different for the two transitions: The $^2D_{3/2}$ state is frequently populated due to decay from the $^2P_{1/2}$ state during cycling of the 397 nm transition, where the corresponding branching factor is about 1/12. Therefore, illumination of the ion without the 866 nm laser on leads to rapid pumping into the dark metastable $^2D_{3/2}$ state. In contrast, decay from the $^2P_{1/2}$ to the $^2D_{5/2}$ is dipole forbidden, therefore continuous observation of resonance fluorescence is possible without the 854 nm laser for repumping. However, $^2D_{5/2}$ plays a crucial role for spectroscopy and spin readout (see Sec. 4.2.2), such that this laser is needed for the *reset* of the qubit and is therefore referred to as the *quenching* laser in the following. Both lasers are infrared ECDLs [15]. The 866 nm laser is PDH locked in entirely the same way as the 397 nm laser (see Sec. 3.2.2), the resonance is typically located at 866.45218 nm. The wavelength is adjusted via the HV-amplifier of the reference cavity piezo such that the resulting fluorescence level is maximized. The 854 nm laser is free running, the quenching process is sufficiently robust in the wavelength range between 854.44380 nm and 854.44420 nm. Both lasers are supplied to individual double pass

[15] DL 100

AOMs [16] for switching via single mode fibers. The AOM outputs are superimposed on a PBS and coupled into another single mode fiber. Finally, 500 μW up to 1 mW of 866 nm light and about 130 μW of 854 nm light is supplied to the experiment. The beam is superimposed to the 397 nm beam by means of a dichroitic mirror. Both beams have a FWHM of roughly 2 mm at the f=250 mm focusing lens, leading to high saturation parameters. The power at 866 nm is high enough to make the experiment insensitive against wavelength drifts of the corresponding PDH cavity, and small enough that the light is almost not seen during fluorescence detection. For the 854 nm laser it was found that imperfect switch-off of the beam, with only a few nW of power in the off-state, already has a deterioration effect on the spin readout (see Sec. 4.4). Therefore, a second AOM [17] was inserted between the laser output and the first fiber coupling, leading to an off-power level below the detection threshold [18], which made a spin readout fidelity of 99.6% possible.

3.2.4. 729 nm for Electron Shelving

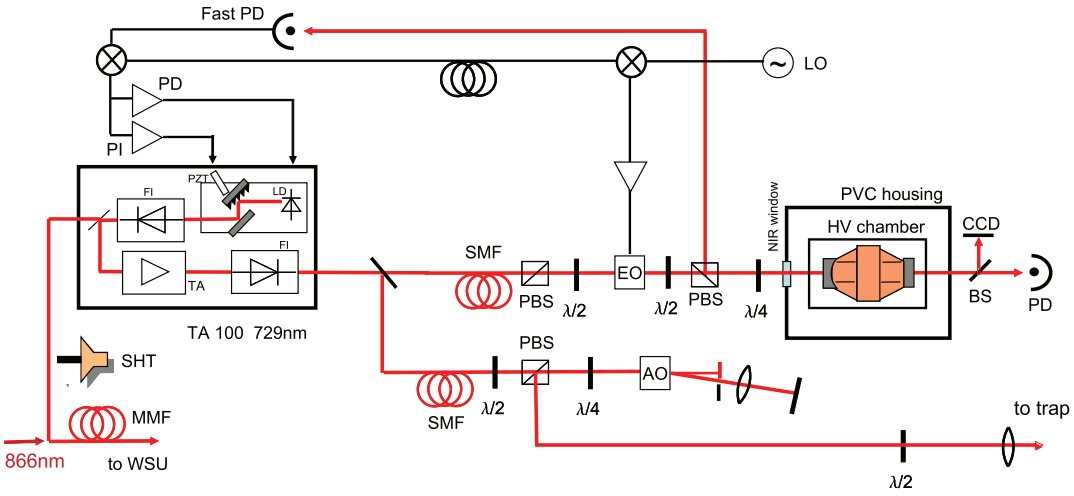

Figure 3.5.: Optical setup of the 729 nm laser for spectroscopy and qubit readout. Note that the beam supplied to the lock branch is derived from the amplified main beam despite its worse noise background, because it was found that larger powers are essential for the lock stability.

[16] TEF-270-100, Brimrose Corporation of America, USA
[17] GEF-80-20, Brimrose Corporation of America, USA
[18] as measured with an OPHIR NOVA II power meter

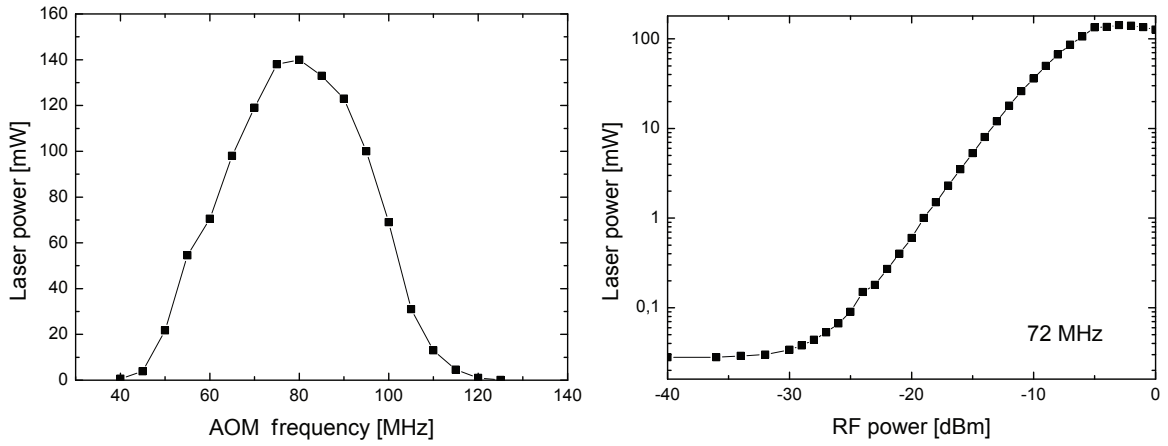

Figure 3.6.: Characterization of the double pass AOM for the 729 nm laser: **a)** shows the frequency response, which essentially determines the accessible internal state transitions. **b)** shows the laser power in the diffracted output beam versus rf drive power, which determines the maximum attainable Rabi frequencies.

The diode laser running at 729 nm is driving the dipole forbidden $^2S_{1/2}$ to $^2D_{5/2}$ transition, which has a linewidth of about 1 Hz. The optical layout is depicted in Fig. 3.5. Due to the weak quadrupolar coupling, a lot of power is needed in order to reach Rabi frequencies on the order of 1 MHz, such that the output power of an ordinary ECDL is not sufficient. In contrast to the Innsbruck experiment, this transition is only used for auxiliary tasks like spectroscopy, spin read-out, pumping and cooling, there the requirement of a narrow laser linewidth is not as strict as in the case that fully coherent dynamics are to be driven on this transition. Therefore a low-cost, easy to operate amplified diode system is the system of choice. The master laser is amplified by a taper amplifier supplied with a current of 1400 mA, yielding 800 mW of single mode output power after the final Faraday isolator, with an ASE background given by the gain bandwidth of the semiconductor laser medium of the amplifier, suppressed by more than 40 dB. A probe beam of the master laser is supplied to the wavemeter by a multi mode optical fiber. A portion of the main output beam is used for the PDH lock to a high finesse, ultra-low expansion cavity [19], with a mirror transmittance of 10 ppm at the required wavelength. The cavity is vertically mounted in a HV chamber in order to minimize gravitational distortion effects. In contrast to all other laser systems, the sidebands are not modulated onto the master laser by means of the Bias-T in the diode current supply because they would be visible in the corresponding atomic spectra due to the narrow width

[19] Advanced Thin Films, Boulder, USA

of the transition. Instead, frequency modulation is achieved by means of an electro-optical modulator (EOM), which is supplied by 33 dBm of power at a frequency of 18 MHz. No extra rf resonator is used on the EOM. A $\lambda/2$ plate in front of the EOM is used to align the polarization along the optical axis of the EOM crystal, otherwise this would lead to spurious amplitude modulation, which causes an offset in the resulting PDH signal adversely affecting the lock stability. Mode-matching to the optical cavity is achieved by using the movable collimator lens of the fiber output, such that the optimum beam waist is created at the cavity input. The cavity vacuum vessel is enclosed in a PVC housing with a wall strength of 1 cm to reduce heat exchange with the environment and the influence of sound waves. The power in the PDH branch is limited by the transmission of the NIR reflective mirror directly after the laser output, see Fig. 3.5, which is about 800 μW. At maximum 400 μW is then available after the cleaning PBS after the fiber. It is empirically found that the lock stability becomes better with increasing power, however the heating of the cavity is mainly due to this power source, such that a better lock stability is bought at the price of an increased frequency drift rate. Due to the fact that the linewidth of the cavity is much smaller than the linewidth of the free-running laser, no error signal can be observed while scanning the laser frequency. Therefore, a cavity with low finesse simply consisting of two NIR reflective coated curved mirror in free-space configuration was established close to the high-finesse cavity such that the geometrical dimensions with respect to fiber output and PDH photodiode were about the same distance. An appropriate error signal was then established by inserting an extra length of coaxial cable between local oscillator and PDH mixer. By mere luck, a resonance of a transverse Gaussian mode was found at 729.34775(5) nm, which allowed for reaching all relevant atomic transitions with a 80 MHz double-pass AOM. Therefore, no extra AOM in the PDH branch is necessary, but due to the lack of the fast switching capability, the linewidth of the cavity could not be obtained by means of a transmission ring-down measurement. The on-resonance dip in the power reflected from the cavity is only 5%, which could not be improved by any effort to improve the mode matching. It is therefore attributed to bad impedance matching, i.e. mismatch of the mirror reflectivities and losses, which is presumably due to dust grains on the lower cavity mirror. For future high-finesse cavity setup, assembly in a clean room is therefore strongly recommended. The PDH error signal suffers from a bad signal-to-noise ratio, which (together with the ASE background from the TA) ultimately limits the achievable laser linewidth. The error signal is produced by mixing the cavity reflection signal, detected by a New Focus 1801 FS 125 MHz photoreceiver with the LO signal on a minicircuits ZRPD-1+ phase detector. It is then supplied to two servo controllers: A slow PI controller is used to control the ECDL grating via the piezo element, the design is similar to the one in Ref. [Tha99]. A fast PD controller, also similar to the one in Ref. [Tha99] except for replacement of the CLC425 opamp by an AD817. The resulting laser linewidth is determined by Ramsey spectroscopy on the quadrupole transition, see Sec. 4.2.2. The longest coherence time observed was 400 μs, corresponding to a linewidth of 2.5 kHz. The fact that the linewidth is not limited by other decoherence sources is justified by the observation of much longer coherence times for Ramsey experiments on the Raman transition between the ground state spin levels, see Sec. 4.7. Together with the free spectral range of 2 GHz, under the rough assumption that the laser is frequency-stabilized to about

1% of the cavity linewidth, this is giving a finesse of only 8000, compared to the finesse of 300000 inferred from the mirror manufacturer data.
The main laser output is delivered to the experiment via a single mode fiber, where round about 300 mW of power is available. The light is switched and modulated by a double-pass AOM [20], which allows better switch-off and scanning of the frequency for spectroscopy purposes without changing the beam alignment. The characterization of the diffraction performance of this AOM with respect to input frequency and amplitude is crucial for exerting control over the atomic system, the corresponding measurement results are shown in Fig. 3.6. For details of the rf supply of this AOM, see Fig. 3.9. The beam is directed orthogonally to the magnetic field, and a $\lambda/2$ plate is used to align the polarization at roughly 45°with respect to the magnetic field, such that all quadrupole allowed transition between the various sublevels can in principle be addressed, see Sec. 4.2.2. In front of the vacuum window, 150 mW of laser power at a beam FWHM of roughly 8 mm is focused onto the ion with a f=250 mm lens, such that high enough Rabi frequencies of up to $2\pi\cdot500$ kHz are readily obtained.

3.2.5. 397 nm for Stimulated Raman Transitions

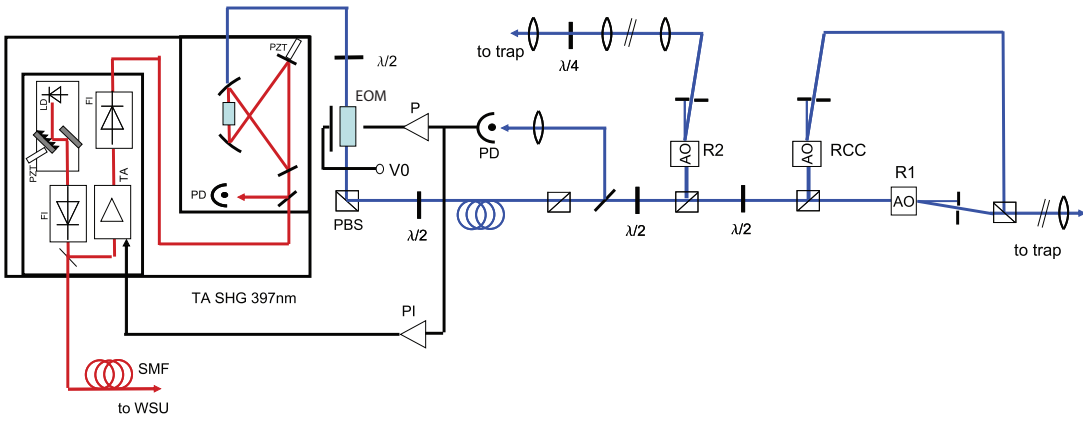

Figure 3.7.: Optical setup for the laser at 397 nm for off-resonant coherent manipulations. The EOM is superior to an AOM for the task of lossless fast switching.

A single mode laser close to the $^2S_{1/2}$ to $^2P_{1/2}$ dipole transition is used for driving stimulated Raman transitions between the ground state spin levels, which is supposed to be the

[20] GEF-80-20, Brimrose Corporation of America, USA

workhorse for quantum logic experiments in our setup. As explained in Sec. 4.5, a large amount of laser power is necessary for suitably fast quantum logic under sufficient suppression of decoherence effects. Therefore, an amplified NIR laser diode with subsequent second harmonic generation (SHG) with a LBO crystal in a bowtie cavity is used [21]. The generated SHG output laser power of up to 120 mW at a TA current of 1400 mA is sufficient for basic quantum information experiments. The laser is typically used with wavelengths of the fundamental beam in a range from 793.813 nm to 794.020 nm, corresponding to detunings of ±100 GHz from the atomic resonance. The SHG beam is passed through a commercial EOM [22] used for switching and intensity stabilization. A $\lambda/2$ plate is inserted to match the polarization angle to the optical axis of the EOM, such that the on- to off- power ratio is maximized, see Fig. 3.8. The EOM voltage leading to a 90°rotation of the polarization was

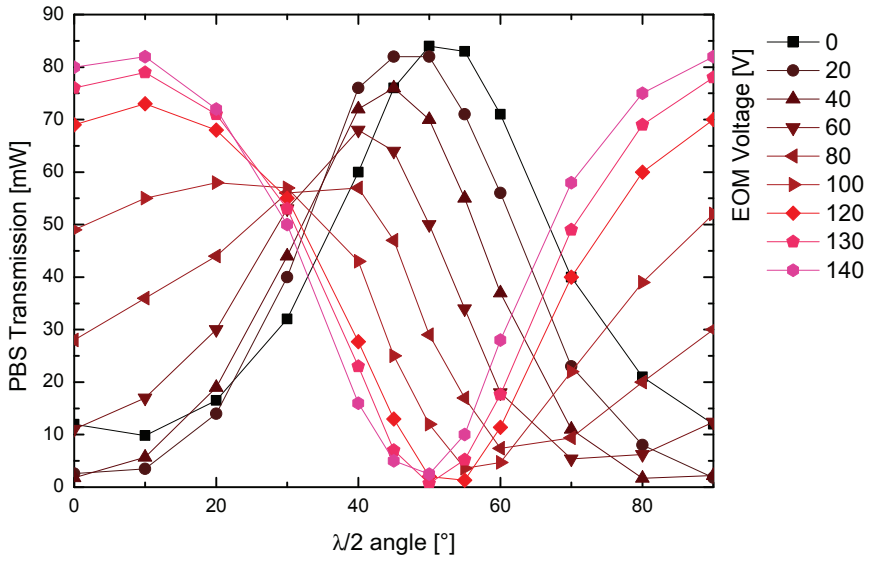

Figure 3.8.: Characterization of the switching EOM: If the EOM is to be used for intensity stabilization, one faces a tradeoff between maximum power and sensitivity to the feedback.

found to be 130 V, where is one of the EOM electrodes is supplied by standard laboratory voltage supplies in series connection. The voltage actually supplied is typically 90 V to give a steep transfer function for the fast branch of the intensity stabilization, however at the expense of about 20% of the laser power. The reflected part of the power after a PBS behind the EOM is coupled into a polarization maintaining (PM) single mode fiber with low solarization loss. An additional $\lambda/2$ plate in front of the fiber coupler is used to match the

[21] TA-SHG pro, Toptica AG, Gräfelfing
[22] LM 0202, Linos Photonics GmbH, Göttingen

polarization to the PM axis. After a polarization cleaning PBS behind the fiber output collimator, typically 20 mW of UV laser power is available. A beam sample is taken by means of single side UV AR coated microscope object carrier, which is attenuated and monitored on a fast photoreceiver. The signal is used as the feedback signal for the intensity stabilization servo. A fast servo acts onto the free EOM electrode, whereas an integrator servo is used to maintain long term stability via feedback onto the TA current. This way, the fast servo output can be dc-coupled in order to keep the mean output level at 0 V, allowing for large output voltage swings without cutoff.

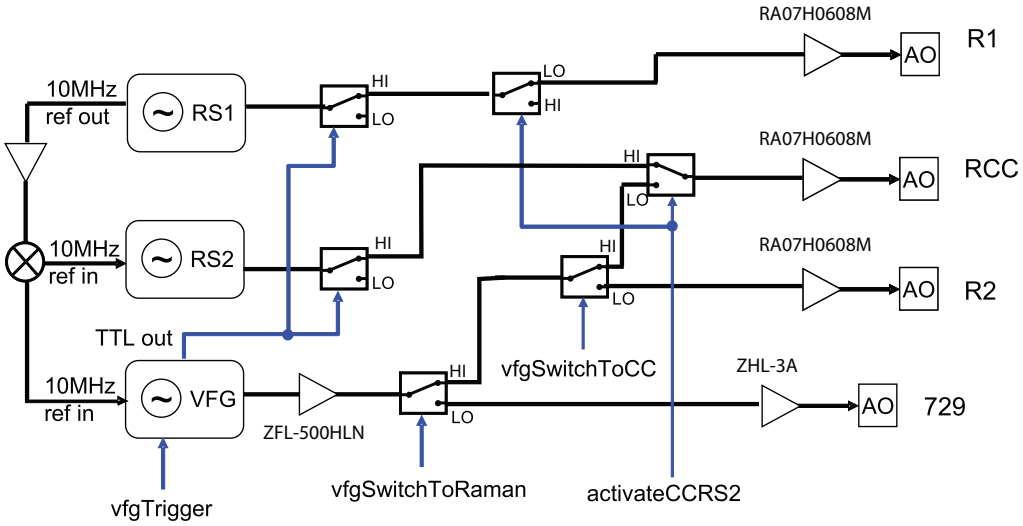

Figure 3.9.: rf network for the supply of the AOMs in the Raman beamline from Fig. 3.7. Several switches determine which rf source is fed to which AOM, the corresponding truth table is given in Table 3.1.

The main laser power is split into three parts by a series of $\lambda/2$ plates and PBSs, where the splitting ratios are dependent on the actual experiments which is to be performed. The beamlines after splitting are kept as short as possible, as optical path length fluctuations due to air currents and mechanical vibrations of mirrors can cause fluctuations of the relative phase, leading to additional decoherence rates mainly depending on the effective interferometer areas. A beam propagation along the magnetic field axis, denoted *R2* in the following, is passed through an AOM for switching and modulation. The +1st diffraction order is separated with an iris diaphragm after a 2:1 magnification telescope comprised of a f=50 mm and a f=100 mm lens for tighter focusing. A $\lambda/4$ plate is used to manipulate the polarization, which is of crucial importance for this beam. The beam is then focused onto the ion with a f=250 mm lens. Of the other two beams, the one subsequently referred to as *R1* is polarized

1	2	3	R1	R2	CC	Purpose
0	0	X	-	VFG	-	Scattering and Stark shift measurements
0	1	X	-	-	VFG	Stark shift measurements
1	0	0	RS1	VFG	-	Raman transitions with $\eta \neq 0$
1	0	1	-	VFG	RS2	Spin dependent forces
1	1	1	-	-	RS2	CC beam alignment
1	1	0	RS1	-	VFG	Raman transitions with $\eta = 0$

Table 3.1.: Truth table for the required TTL settings of the Raman beams. The first three columns show the logic states of the relevant TTL channels of the experiment control system and the next three columns indicate which rf source is connected to the AOMs R1, R2 and CC, see Fig. 3.7. The last columns describes the purpose of each configuration. The TTL channels are referred to Fig. 3.9 as follows: TTL **1** $\rightarrow$ VFG TTL channel 1, **2** $\rightarrow$ vfgSwitchToCC, **3** $\rightarrow$ activateCCRS2. An X in the TTL setting columns means that the logical state of the corresponding line is irrelevant for this setting.

horizontally with respect to the optical table, whereas the other one, called *RCC* is vertically polarized. Both beams are passed through individual AOMs and are re-superimposed on a PBS. The beam pair is directed orthogonally to the magnetic field, such that R1 is π polarized, driving $\Delta m_J = 0$ transitions, and RCC has balanced σ_+ and σ_- components, driving the $\Delta m_J = \pm 1$ transitions equally strong. The respective +1st diffraction orders are selected by means of an iris diaphragm and focused onto the ion with a f=250 mm lens. In contrast to the R2 beamline, no additional telescope is necessary because of the shorter propagation distance. All AOMs are QZF-80-20. The rf supply network is shown in Fig. 3.9, its sophistication arises from the fact that the beams are to be used in different combinations. All AOMs are oriented such that the propagation direction of the sound wave in the crystal is perpendicular to the beam polarization, which drastically affects the diffraction performance of the QZF-80-20, in contrast to AOMs working in the IR. All three AOMs are situated at approximately the same distance from the delivery fiber output, such that the beam diameter inside the crystals can be adjusted to be the same value for all modulators by means of the fiber collimator focusing screw. This way, high diffraction efficiencies of up of 65% to 75% are achieved for all the AOMs.
In principle, much tighter focusing of the Raman beams is feasible, with illumination of the complete 1" diameter of the focusing lenses spot sizes in the μm range are achieved. This would provide much stronger Raman couplings, such that reduced decoherence can be achieved by choosing larger Raman detunings. However, for small spot sizes strong decoherence effects set in that are not fully understood but that can only be caused by an unstable illumination strength of the ion, see Sec. 4.7. Possible physical effects are therefore pointing instabilities of the beams or radial position drifts of the ion on the second scale.

3.3. Imaging and Detection

The imaging system allows for simultaneous detection of ion fluorescence near 397 nm on an electron multiplier CCD (EMCCD) camera system [23] or on a photomultiplier (PMT) [24]. While the camera mainly serves for asserting that the right number of ions is loaded and that the ions are properly cooled and localized, the fluorescence data from which the experimental results are obtained is collected with the PMT. This is because the PMT readout is more easily accomplished than the readout of the EMCCD camera images. Simultaneous readout of several ions however can only be accomplished with the spatially resolving camera, which is already demonstrated in chapter 9 and will serve as the standard readout method in the future. The spatial resolution also enables an improved filtering of the stray light background as the image of the ion is directly at hand, in the PMT case this can be only accomplished by adjusting a 2D aperture consisting of 4 independently movable blades [25].
The fluorescence is collected by a specially designed objective [26] with a focal length of 48 mm. The inverted viewport allows for placing the objective at an approximate distance of 50 mm from the ion, resulting in a covered solid angle of $d\Omega/4\pi \approx 6\%$ and a magnification factor of 28 at an image distance of about 1400 mm, which allows for the distinction of ions aligned in a string at a typical ion distance of 3 μm and a pixel size of 24 μm. As the PMT photon count rate sets the minimum time in which the bright and dark states of an ion can be reliably distinguished, see Sec. 4.2.1, most of the fluorescence light is directed in the PMT branch of the detection optics using a 80:20 beam splitter [27]. Both in the PMT and EMCCD branches, the light is spectrally filtered with a 397 nm band-pass filter [28]. Considering the photon collection solid angle, 96% transmission through the objective, 88% filter transmission and the PMT quantum efficiency of 20% at 397 nm, a photon count rate in the range of 500 s^{-1} is expected. By contrast, only count rates of 30 s^{-1} are actually attained, the huge discrepancy between these rates is still unclear.

3.4. Trap Voltage Supplies

As the trap confinement mechanism relies on the application of suitable electric fields both at dc and rf, individual supply systems for each of these components are needed. As the dc supply electronics is of crucial importance especially in conjunction with the scalability scheme based on the segmented trap, Appendix B is entirely devoted to this issue. Important experimental findings for the characterization of the voltage supply are found in Secs. 2.1.3,4.2.3 and 4.3. It shall be briefly mentioned here that two main types of dc supplies were used throughout this thesis: Most experiments were carried out with a purely static voltage supply providing only voltages for a single segment pair, and all the other segments were

[23] iXon DV860DCS-BV, Andor, Belfast, Northern Ireland, 128x128 pixels
[24] P25PC, ET Enterprises, Uxbridge, United Kingdom
[25] SP60, OWIS GmbH, Staufen
[26] Sill Optics GmbH, Wendelstein
[27] CVI Melles Griot, Bensheim
[28] FF01-377/50-23.7-D, Semrock, Rochester, USA

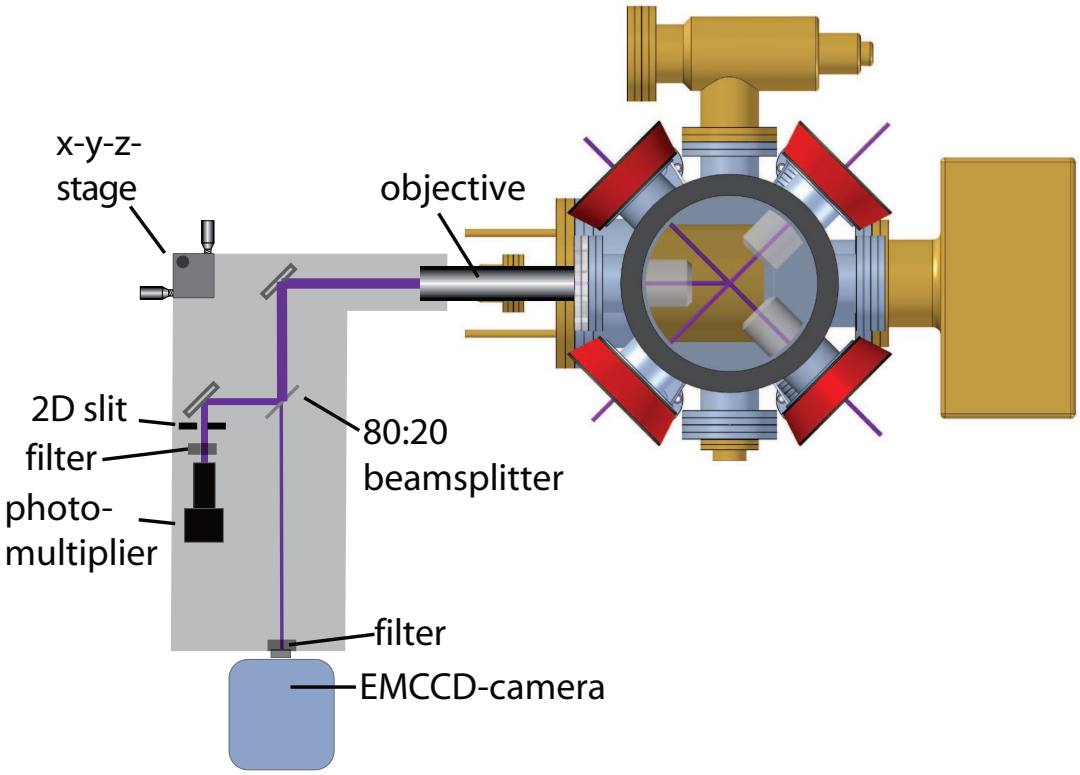

Figure 3.10.: Setup for imaging and fluorescence detection: The gray shaded area indicates a solid box which provides shielding against ambient light. It is suspended on a 3D translation stage, and the camera rests on two rails such that free movement of the whole imaging system along the direction of the trap axis is possible.

grounded. This is because for the establishment of the qubit manipulation techniques that constitute the main part of this thesis, the segmentation of the trap is not needed. A scalable version of the voltage supply for controlling 60 channels independently with computer generated voltages has also been used and further developed, technical details are also given in the Appendix B.
The rf supply electronics is mostly determined by the need for relatively large peak-to-peak voltages of up to 600 V at a frequency of about 24 MHz. To achieve this, a seed signal generated by a Marconi synthesizer with output levels typically ranging between -15 and -9 dBm is fed to a Minicircuits ZHL-5W-1 amplifier providing about 40 dB of amplification. From there it is passed to a helical resonator as it is typically used in Paul trap experiments, which possesses a Q-factor of about 30. The resulting voltage fed to the trap segments is divided

on a capacitive 1:100 divider as described in Appendix A of Ref. [Deu00], measured with a 1:10 voltage probe and monitored on an oscilloscope.

3.5. Quantizing Magnetic Field

The magnetic field defines the quantization direction. It is therefore absolutely necessary to apply a magnetic field at a magnitude much larger than any ambient magnetic field fluctuation in order to prepare a well defined atomic system. Furthermore, the field magnitude defines the Zeeman splittings in the system and therefore sets all transition frequencies, such that it is important to keep the magnetic field stable at short and long timescales to suppress undesired decoherence effects, see Sec. 4.7. The field is generated by a pair of coils mounted at adjacent diagonal viewports on the vacuum vessel. The coils each have a diameter of about 28 cm and 280 windings each. They are supplied in series with a current of 2 A, which is derived from a Statron power supply and stabilized with a feedback circuit designed by the Innsbruck group. This relies on the measurement of the current via the voltage drop at a temperature insensitive precision resistor (Vishay) and PID feedback regulation via a power transistor. Additional monitoring of the current on a HP digital multimeter shows that a static stability of better than 50 ppm is attained. From the measured Zeeman splitting between the ground state spin levels $|\downarrow\rangle$ and $|\uparrow\rangle$ of about 18 MHz implies a magnetic field of roughly 6.5 Gauss at the trap position.

3.6. Experimental Control System

In complex quantum control experiment, a considerable amount of data is to be exchanged between various devices and experiment control computers at a fast rate. Laser powers, frequencies and phases have to be controlled via AOMs for the quantum state manipulation pulse sequences, all laser sources have to be switched on and off via TTL switches, voltages waveforms have to be supplied to the trap segments and fluorescence data has to be collected and evaluated. The experiment control hard- and software therefore plays a crucial role and was subject to constant change and improvement. Therefore, we describe here the configuration which served for most of the measurements presented in the chapters 7,6, 9 and 8.
Three personal computers serve to control the experiment. The main control computer exerts all control tasks that are related to the conduction of the experimental sequences, i.e. it controls the laser frequencies and on/off states. The devices attached to this computer are depicted in Fig. 3.11. In earlier versions of the setup, this computer controlled the laser frequencies and amplitudes mostly via GPIB control of RS SML synthesizers, in the present version these synthesizers are operated at fixed frequencies and dynamic control is performed only via fast USB data transfer to the VFG synthesizer. Moreover, the main control computer serves for data acquisition by using the onboard counter electronics of the NI PCI-6733 to read out the PMT.

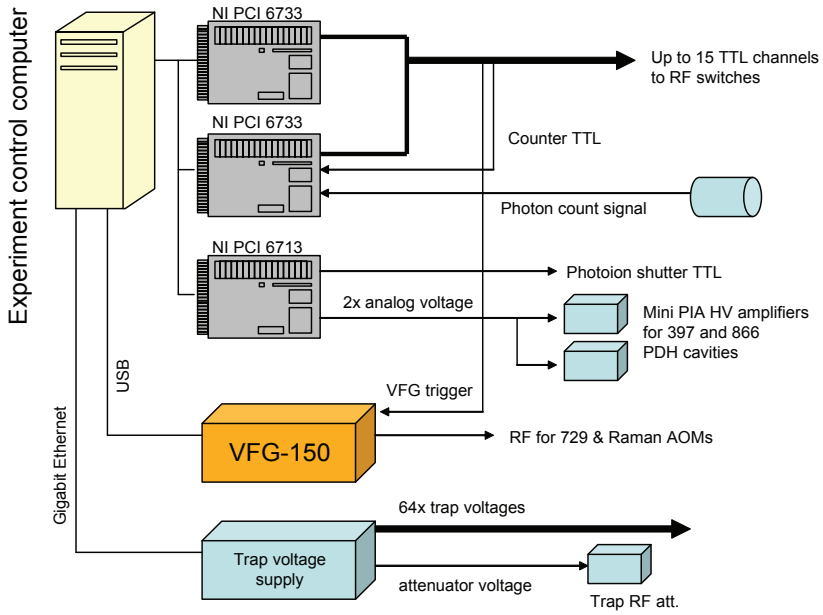

Figure 3.11.: Experimental control system: The main control computer controls the experiment mainly via digital output channels of NI PCI-6733 cards and the USB-driven VFG synthesizer. The 64 channel voltage control box has actually been used on another computer for historical reasons, but will be attached to the main control computer in the future setup.

Another computer involved in the experiment control is the camera computer which exclusively serves for the readout of the EMCCD camera, see Sec. 3.3. The remaining computer mainly serves for the readout of the wavemeter and is also assigned to some less critical control tasks. As the wavemeter provides laser frequency measurements with an accuracy of below 10 MHz, it can be used to regulate laser frequencies by feedback if the frequency stability is not crucial, which is exactly the case for the laser at 397 nm driving the Raman transitions. The feedback signal obtained from a discrete software PI controller is fed back to the master grating by means of a digital to analog converter circuit to which the digital information is supplied via a standard serial interface. To assure proper laser operation, a galvanic separation between the systems was found to be necessary, which was achieved by utilizing an IL300 analog optocoupler. Furthermore, the computer is connected via a CAN-bus interface to the iseg high voltage generator that coarse-controls the PDH cavity piezo voltage for the 866 nm and 397 nm lasers.

4. Implementation of the Spin Qubit

The foundation for all experiments with trapped ion aiming in the direction of quantum computation and simulation rely on the possibility to encode quantum bits and to provide initialization and read-out of this quantum bit. Furthermore, the ability to perform single qubit manipulations is required. Of course all of these steps need to be performed as efficiently as possible, i.e. with a high *speed* and high *fidelity*. In order to keep the experimental effort reasonable, *robustness* against experimental parameter drifts is advantageous. Furthermore, the qubits represent a *quantum memory*, therefore one has to take care to suppress environment-included decoherence. To fulfill these requirements, A lot of knowledge from the fields of atomic physics and coherent control is needed, along with high degree of experimental try-and-error. In this chapter, it is shown how this is done in our particular experiment. The chapter is organized as follows: First, in Sec. 4.1 we give a short survey on the different possibilities to encode qubits in trapped atomic ions. In the following section, Sec. 4.2, we describe how very basic steps such as internal state discrimination, spectroscopy on the quadrupole transition, qubit initialization and qubit reset are implemented. In Sec. 4.3, we present results from a simple fluorescence-based heating rate measurement. In the next section Sec. 4.4, we show in detail how the spin qubit is read out via electron shelving. Then we show in Sec. 4.5 how coherent manipulations can be performed by means of stimulated Raman transitions and in Sec. 4.6 how sideband cooling is achieved, along with detailed results of a heating rate measurement. The last section Sec 4.7 is devoted to an extensive characterization of relevant decoherence processes.

4.1. A Brief Survey of Trapped Ion Qubit Types

In order to store any information in an atomic system, one need at least two internal states which possess lifetimes which are longer than the time at which one intends to store, process and retrieve this information. Three basic types of internal state are suitable: metastable electronic states, hyperfine sub-levels of the electronic ground state and Zeeman sub-levels of the electronic ground state. We have chosen to implement the latter approach, which is especially well-suited in conjunction with our microtrap, for several reasons that will become clear throughout this chapter. Fig. 4.1 shows the level scheme of a $^{40}Ca^{+}$ ion, along with the transitions used for our particular qubit realization. All of these qubit types have been successfully implemented within the last two decades, each with unique advantages and disadvantages. Two main issues are of key relevance for the experimental approach:
Qubit handling: The type of qubit used defines the challenges occurring in the experimental realization of basic experimental steps such as qubit readout and coherent manipulation.

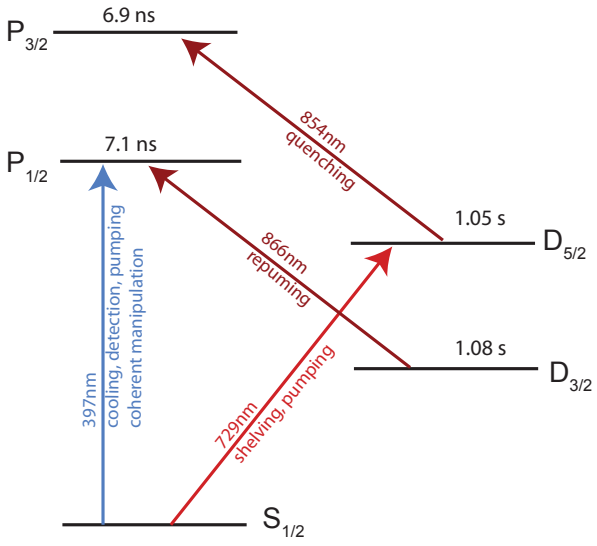

Figure 4.1.: Level scheme of the relevant electronic states of the $^{40}Ca^{+}$ utilized in our experiment. The Zeeman substructure is omitted here. The laser-driven transitions between the states are shown along with their purpose and the wavelength.

In the case of the metastable qubit, coherent manipulations are driven directly on dipole-forbidden transition, typically of electric quadrupolar type, which possess lifetime of some hundreds of milliseconds up to about one second for common species. The timescales for these manipulations are set by the frequency spacings present in the system, which typical range in the MHz regime, such that typical operations have durations in the microsecond range. Thus, a large number of operations is possible within the metastable state lifetime, however the bottleneck in this case is given by the coherence time of the driving laser. Working with this type of qubit, one therefore has to face the technological challenge of stabilizing the driving laser in the 1 Hz regime, which is nowadays routinely achieved in quantum optics laboratories. One particular advantage for this qubit type is that the readout process is relatively simple, as fluorescence on the fundamental dipole transition will only be detected if the qubit is projected into the ground state. The other two qubit types allow for coherent manipulations to be performed by utilizing stimulated Raman transitions, as the frequency splitting lies in the range of some MHz up to several GHz, which can be coherently bridged. If the two beams driving the Raman transitions are derived from the same laser source or two phase-locked lasers, the problem of phase stability is mostly circumvented, even free-running lasers can be used. This is because now the relative phase of the two beams plays the role of the absolute optical phase in the metastable qubit case. However, the qubit readout for these types is more difficult: Generally, both qubit levels will yield fluorescence upon reso-

nant irradiation on a dipole transition. There are basically three ways to circumvent this: First, a particular subtransition can be singled out (closed) by appropriate choice of the laser polarization and sufficiently large frequency splittings, which provides a large enough number of fluorescence photons before branching to other states takes place. Second, one can make use of coherent effects to turn one of the qubit levels into a dark state by means of auxiliary lasers, which requires careful control of the lasers intensities, polarization and detunings. The last approach is the one we make use of for our spin qubit implementation, namely to use a quadrupole transition to 'hide' the population in one of the qubit levels in a metastable state.

Qubit coherence: For the actual implementation of large-scale quantum algorithms, a decisive key bottleneck defining the error rate is given by the qubit decoherence by te coupling to fluctuating external fields. The predominant decoherence source is given by fluctuating magnetic fields generated mostly by electrical power supplies. If qubits with hyperfine structure are used, so-called clock states can be chosen for encoding the qubit. These do not possess a first-order Zeeman splitting, such that this decoherence process is strongly suppressed. Clockstate encoding is possible for both the hyperfine and the metastable qubit. However, a strong suppression of magnetic-field induced decoherence is also possible for the other qubit types by shielding the experimental setup and performing the experiments at a defined timing with respect to the AC power line. Furthermore, advanced rephasing techniques can be used for coherence protection [Bie09]. Moreover, it is possible to use two physical qubits (ions) to make up one logical qubit, and then encode the qubit information in a decoherence free subspace DFS. Therefore, the coherence time for the metastable qubit is ultimately limited by the metastable states lifetime, whereas for the other types decoherence is mainly caused by off-resonant scattering during coherent manipulations, see Sec. 2.1.6.

This section is concluded by an incomplete collection of references on the various experimental realizations of the different qubit types: The metastable qubit based on $^{40}Ca^{+}$ has been realized in Innsbruck [SK03a], where also basic one- and two qubit operations with DFS qubits have been performed [Mon09] and the clock state variant has been demonstrated with $^{43}Ca^{+}$ [Kir10]. The hyperfine qubit based on $^{9}Be^{+}$ has seen a long history of success in the Boulder group [Win98], where the same isotope has also been used for clock state qubits [Lan09] and DFS qubits [Kie01]. For hyperfine qubits, the isotope $^{117}Yb^{+}$ recently became very popular [Olm07]. The spin qubit has been realized based on $^{40}Ca^{+}$ in Oxford [Hom06c] and within this thesis [Pos09].

4.2. Basic Qubit Operations

4.2.1. State Discrimination by Fluorescence Counting

Any qubit readout scheme realized up to date is based on interrogating whether a given ion irradiates fluorescence photons under exposure to resonant radiation or not. The discrimination procedure is always to count photons for a given time δt and compare the photon number to a predetermined threshold σ. According to whether the measured photon number is below this threshold or not, the ion is attributed to have been projected to the corresponding qubit

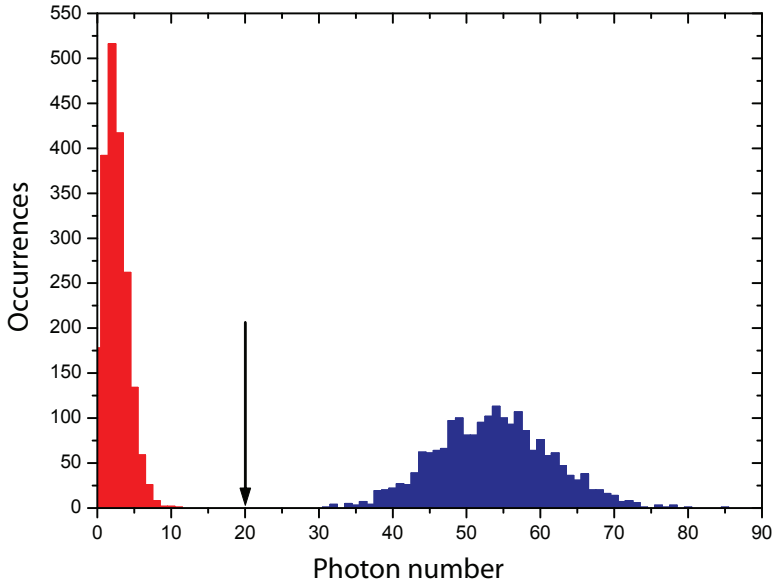

Figure 4.2.: Fluorescence histogram: The number of occurrences is plotted versus the counted phonon number for a count time of 10 ms. The arrow indicates the discrimination threshold according to Eq. 4.1.

state upon readout. This basic information is used statistically to build up all high-level measurement results. The decisive questions on this step are in what minimum exposure time this can be answered at a given fidelity. This figure of merit is mostly given by the rates at which fluorescence can be produced and detected and the corresponding background count rate. The fluorescence rate is ultimately limited by the lifetime of the excited state on the fluorescence transition, the other limits are of technical nature, i.e. the solid angle of photon collection, light absorbance in the imaging system, the quantum efficiency of the detector and the suppression of background light, both from the laser beam giving rise to the fluorescence and background light at other wavelengths which is to be filtered out. The technical details for our particular setup are described in Sec. 3.3, a histogram of photomultiplier counts is shown in Fig. 4.2. For this measurement, PMT events were counted within a fixed count time interval for the situation with repump laser at 866 nm off, such that mostly photons from scattering of the 397 nm laser at the trap structure are seen, and with the repump laser on, such that also resonance fluorescence photons from the ion are seen on the PMT. The advantage of this approach is that due to the known switching state of the 866 nm laser, one knows a priori if the ion is to be expected in the bright or dark state. The disadvantage is on the one hand that imperfect off-switching of the 866 nm light leads to additional background photons as the ion might be eventually pumped out of the dark state in the measurement process. Furthermore, as the 866 nm laser is switched off for the background rate measure-

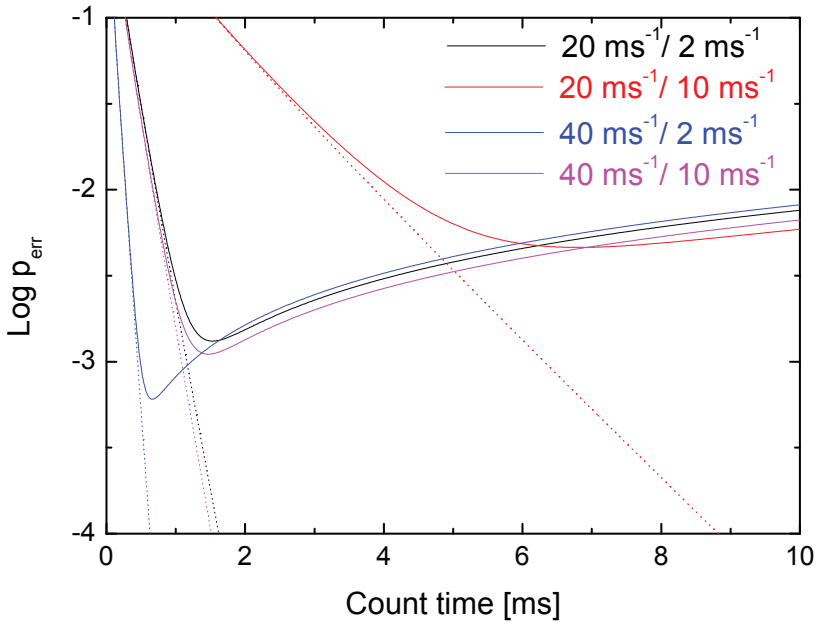

Figure 4.3.: Fluorescence discrimination errors for different count rates: The solid lines indicate the logarithmic total error probability for the fluorescence discrimination process versus the readout time Δt. The dashed lines indicate the hypothetical error under assumption of an infinite lifetime of the metastable state. The different photon count rates r_{on} and r_{off} indicated in the legend correspond to the extremal rates observed in our experiment. Note that for a high r_{on} rate, the sensitivity of the error on the background rate r_{off} is strongly reduced. The key message here is that it is relatively easy to achieve error rates below 10^{-2}, while it is hard to push the error below 10^{-3}.

ment, one obtains underestimated background rates if the 866 nm laser is imperfectly filtered. However, an alternative measurement procedure providing better results for later-on usage is explained below. The two peaks in Fig. 4.2 corresponding to ion fluorescence (average on-number $\bar{s}$) and background light (average off-number $\bar{n}$) are assumed to obey to Poissonian distributions, which is justified by the quantum statistics of the single-atom photon source and the random nature of the count process. We briefly summarize the key results from Ref. [Roo00], Sec. A.2 for the error estimation of the discrimination process: If the Poissonian count number distributions are replaced by Gaussian distributions, which is justified for large enough count rates and detection times, a simple choice for the discrimination threshold σ is found by demanding that the two possible discrimination errors, namely mistaking the ion to be bright while it is actually dark and vice versa, are equalized. Upon integrating the parts of the Gaussian distribution pertaining to these erroneous events, we obtain the threshold

$$\sigma = \sqrt{\bar{n}\bar{s}}. \tag{4.1}$$

Most of the results presented in this thesis have been obtained by using this threshold type, however it was found that it leads to problems if the background count rate is very low and the Gaussian approximation breaks down, i.e. the threshold is chosen to small. An advanced scheme for measuring $\bar{n}$ and $\bar{s}$ is to make use of the quadrupole transition at 729 nm to turn the ion bright or dark, which is more adapted to actual experiments where it is to be measured if the ion is in $|\uparrow\rangle$ or $|\downarrow\rangle$. Another advantage of this scheme is that the finite lifetime of the metastable state is included in the measurement. If the lifetime of this state was infinitely long, one could press the error probability below any given threshold by simply increasing the count interval in order to separate the Poissonians further from each other. For example, with a $D_{5/2}$ lifetime $\tau_{5/2}$ of about 1s, one would face an error probability in the 1% range for a count interval of 10ms. Thus, an optimal count time Δt along with and optimal threshold σ can be found by correcting the probability for wrong bright counts by probability for detecting above-threshold fluorescence from a spontaneous decay event. Δt is found by minimizing this probability, while σ can still be determined by the requirement that the other error type, which is not affected by the finite metastable state lifetime, is to occur equally often. The dependence of the discrimination fidelity on the count rates is visualize in Fig. 4.3. However, as the fidelity bottleneck for the spin readout is given by the optical pumping and shelving steps, see Sec. 4.2.4 and 4.4, we do not elaborate further on this. It shall be mentioned that the fidelity of the fluorescence discrimination can even be increased by time-resolved measurements, which was demonstrated in Ref. [Mye08]. In such a time-resolved measurement, spontaneous decay events are likely to be discerned because of the abrupt onset of fluorescence, furthermore error from cosmic ray events can be detected.
In general, fluorescence readout with a PMT is limited by the fact that for several ions, only the total number of bright ions can be determined. For simultaneous readout of increasingly large numbers of qubits, this represents a drastic information loss. It was shown in Ref. [Hom06b] that an almost-complete internal state tomography of two ions is still possible if this limited information is available. Other ways to circumvent this are single-ion laser addressing, which has so far only been realized by the Innsbruck group [Näg99], or to use a segmented trap and conduct a procedure of splitting and individual fluorescence measurement. Another approach which was realized in Ref. [Bur10] and in this thesis, see Sec. 9.1, is to make use of the EMCCD camera as an imaging device which provides spatial resolution in contrast to the PMT.
The fluorescence state readout provides only binary information: the ion is always found either bright or dark. In order to infer a dark state occupation probability as a measurement result, each measurement has to be performed repeatedly under exactly the same conditions such that the dark state probability can be inferred from the relative number of dark count events. Even if perfect fluorescence discrimination was possible, this inferred probability will statistically deviate from the physical occupation probability because of the finite number of experimental runs. The process leading to the final outcome can be seen as the realization of an unbalanced Galton board, where the decision probability at each stage is given by the physical occupation probability. After N stages, the probability distribution to find N_D dark

events is given by a Binomial distribution

$$P_D(N_D) = \binom{N}{N_D} p_D^{N_D} (1-p_D)^{N-N_D} \tag{4.2}$$

such that the stand error of the resulting probability $p_D^{meas} = N_D/N$ is

$$\sigma(p_D^{meas}) = \sqrt{\frac{p_D(1-p_D)}{N}}. \tag{4.3}$$

The key result is the $N^{-1/2}$ scaling of the error with the number of experimental interrogations. For example, 250000 interrogations would be needed to push the error reliably below 0.1%, whereas for the 200 interrogations typically used for the results of the thesis, one faces a maximum error of about 3.5%. This represents the major drawback when working with qubits based on single atoms, in contrast to ensemble based qubit realizations.

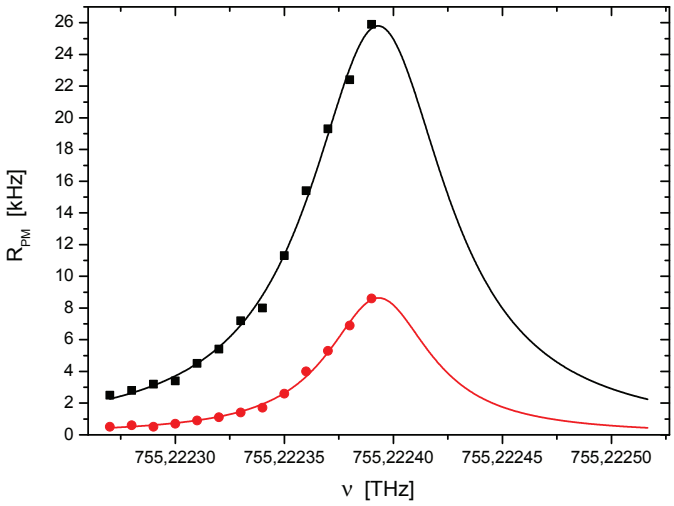

Figure 4.4.: Spectroscopy on the $S_{1/2}$ to $P_{1/2}$ Doppler cooling transition. Shown are spectra on the red side of the Doppler cooling transition near 397 nm for the typical saturated beam power of 120 μW (black) and the typical desaturated power of 20 μW (red). The linewidths resulting from the Lorentzian fit are about 2.5 times the natural linewidth of about 22 MHz for the low power case and 3.8 times this value for the high power case. If the broadening would be explained by mere power broadening, the corresponding saturation parameters would be S_{sat} ≈13.4 and S_{desat} ≈5.3, which would lead to a ratio of the peak fluorescence rates of roughly 1.1, drastically mismatching the actual ratio of about 2.7. The origin of the extra broadening can be attributed to residual micromotion, see Sec. 5.2, or a rather large thermal excitation of the radial oscillation modes, see Sec. 4.3.

Fig. 4.4 shows results of spectroscopy measurements on the $S_{1/2}$ to $P_{1/2}$ transition, revealing the basic characteristic features such as linewidth, saturation parameters and maximum

fluorescence rate. All following experimental results in the remainder of this thesis, unless noted otherwise, have been obtained using the same essential experimental sequence: The ion is first Doppler cooled for typically 2 ms and then prepared in either $|\uparrow\rangle$ or $|\downarrow\rangle$ by optical pumping, see Sec. 4.2.4. If required, it is sideband cooled to the ground state of the axial mode of vibration, see Sec. 4.6. Then, the coherent manipulations constituting the particular measurement take place, see Sec. 4.5.1. If the spin is to be read out, one of the spin populations is shelved to the metastable state as explained in Sec. 4.4, before finally the fluorescence is counted (Sec. 4.2.1) for 1..10 ms and the qubit is reset, see Sec. 4.2.5. The bottleneck steps taking most of the time are the Doppler and sideband cooling steps and the fluorescence readout, each taking up to several milliseconds. These durations can be reduced to the 100 μs range upon technological improvements.

4.2.2. Spectroscopy on the Quadrupole Transition

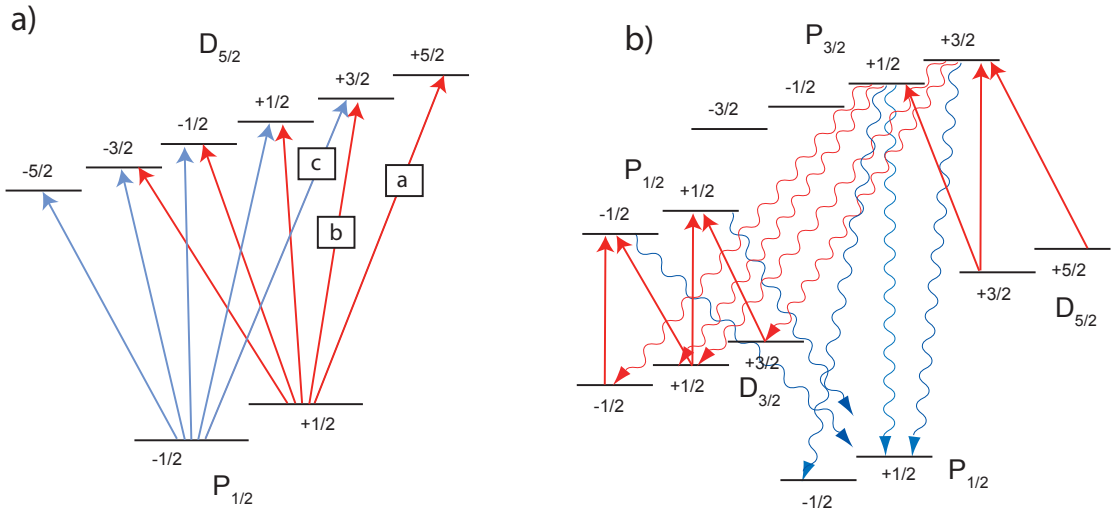

Figure 4.5.: **a)** Complete level scheme of the quadrupole transition between the $S_{1/2}$ and the $D_{5/2}$ state with the full Zeeman substructure. The transitions marked as **a**,**b** and **c** are actually used in the experiment.**b)** shows the decay channels for quenching the $D_{5/2}$ state on the dipole transition to the $P_{3/2}$ on 854 nm. One can see that the 854 nm needs to have circular polarization components for reliable quenching, furthermore the 866 nm repump beam has to be switched on to deplete the $D_{3/2}$ state.

With the fluorescence state discrimination explained in the previous section at hand, we are in the position to make use of the quadrupole transition $S_{1/2} \rightarrow D_{5/2}$ to perform resolved-sideband spectroscopy for a precise determination of the motional frequencies and a characterization of the trapped ion's motional state by investigating its coherent dynamics. A level

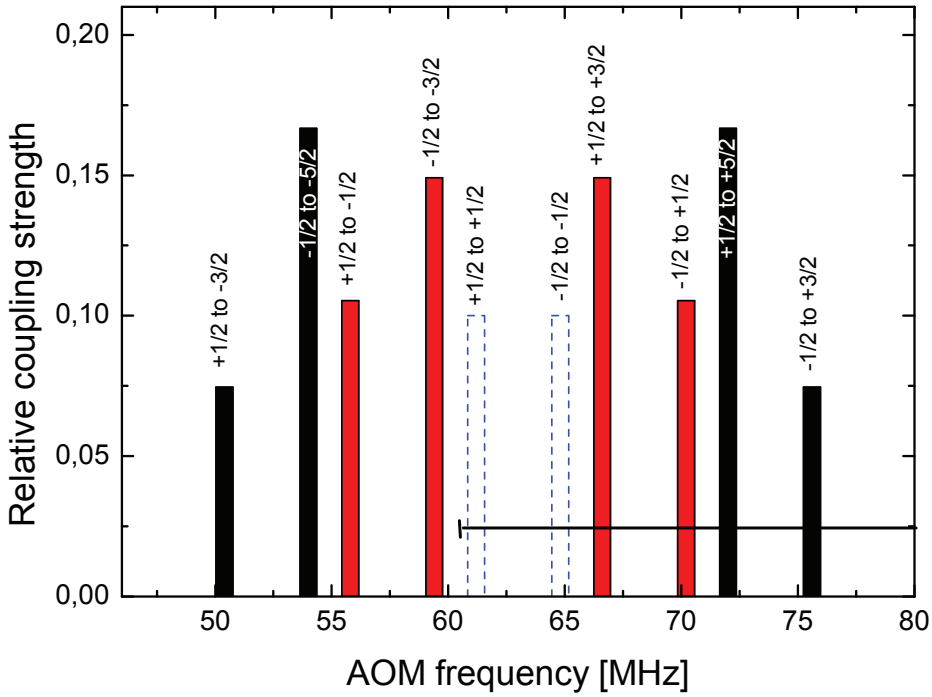

Figure 4.6.: Relative strengths and frequencies of the various transitions between the Zeeman level of the $S_{1/2}$ and $D_{5/2}$ states at a magnetic field of 6.5 G. The strengths are inferred from Eq. 2.24, and it is assumed that the 729 nm beam propagates perpendicular to the magnetic field with its polarization at 45°to the field direction, see Sec. 2.1.2. The black bars indicate the $|\Delta m| = 2$ transitions which are driven by the light field component with polarization orthogonal to the $\vec{k}, \vec{B}$ plane, and the red bars indicate $|\Delta m| = 1$ transitions driven by the in-plane polarization component. The dashed bars indicate $|\Delta m| = 0$ transition inaccessible with the laser propagating at 90°to the magnetic field. The horizontal bar indicates the accessible frequency range of the double pass AOM modulating the 729 nm beam, see Sec. 3.2.4.

scheme including the Zeeman substructure is shown in Fig. 4.5, the measurement presented in this section have been carried out on the particular $|\uparrow\rangle \rightarrow |D_{5/2}, m_J = +5/2\rangle$ transition. Fig. 4.6 gives an overview on how the different subtransitions can be accessed experimentally, which is of key relevance later on when we describe how the quadrupole transition can be used for optical pumping, see Sec. 4.6.

The spectroscopy measurement is performed by inserting a pulse of fixed duration (typically 100 μs) and fixed frequency after the preparation step. The measurement results after e.g. 100 runs then provides the probability that the ion has been excited to the metastable state. If this measurement is now repeated while the frequency of the 729 nm laser is scanned in

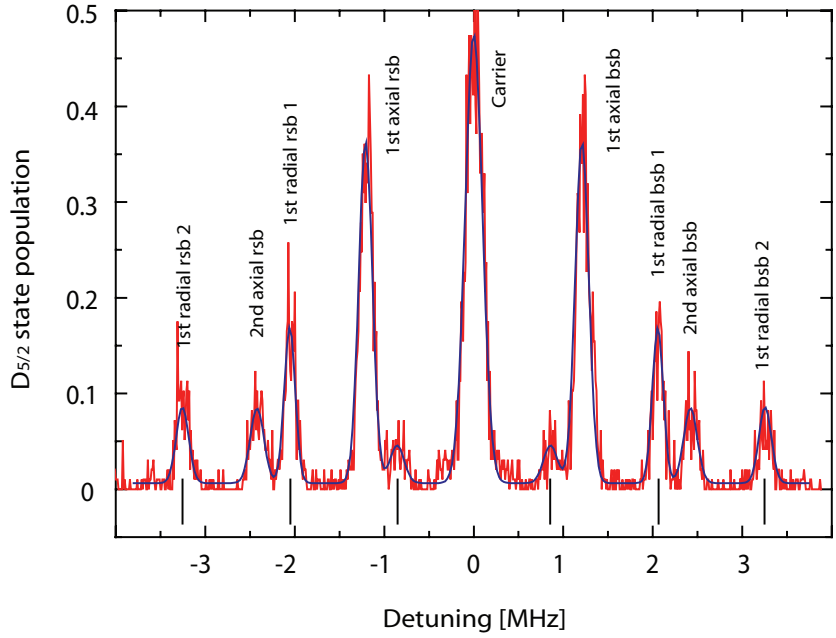

Figure 4.7.: Spectroscopy on the quadrupole transition: Data for a spectroscopy measurement on the $S_{1/2}$,m_J=+1/2 to $D_{5/2}$,m_J=+5/2 is shown. The axial and radial sidebands are well-resolved. The data was taken with the 729 nm locked to a on ordinary cavity with a resulting linewidth of about 100 kHz limiting the spectroscopic resolution.

discrete steps, a spectrum such as shown in Fig. 4.7 is obtained. This spectroscopy method is the most simple way for accurate measurements of the motional frequencies in our trap. On the other hand, it is the prerequisite for using the 729 nm transition as a tool for qubit preparation (Sec. 4.2.4), sideband cooling (Sec. 4.6) and readout (Sec. 4.4).

4.2.3. Coherent Dynamics on the Quadrupole Transition

We now turn to the coherent evolution of an the internal state of a single trapped ion under exposure to a laser beam driving the quadrupole transition. This is important for mainly two reasons: First, it reveals information about the motional state of the ion and second, it is a decisive foundation for the spin readout procedure explained in Sec. 4.4. As the beam is impinging horizontally at an angle of 45 with respect to the trap axis, it couples to the motion along all three oscillation directions of the vibrational modes. Fig. 4.8 shows the oscillatory behavior of he population in the metastable state upon exposure to a resonant 729 nm pulse of variable duration and fixed frequency. Information about the motional state after Doppler cooling can be inferred from the decay of the envelope.

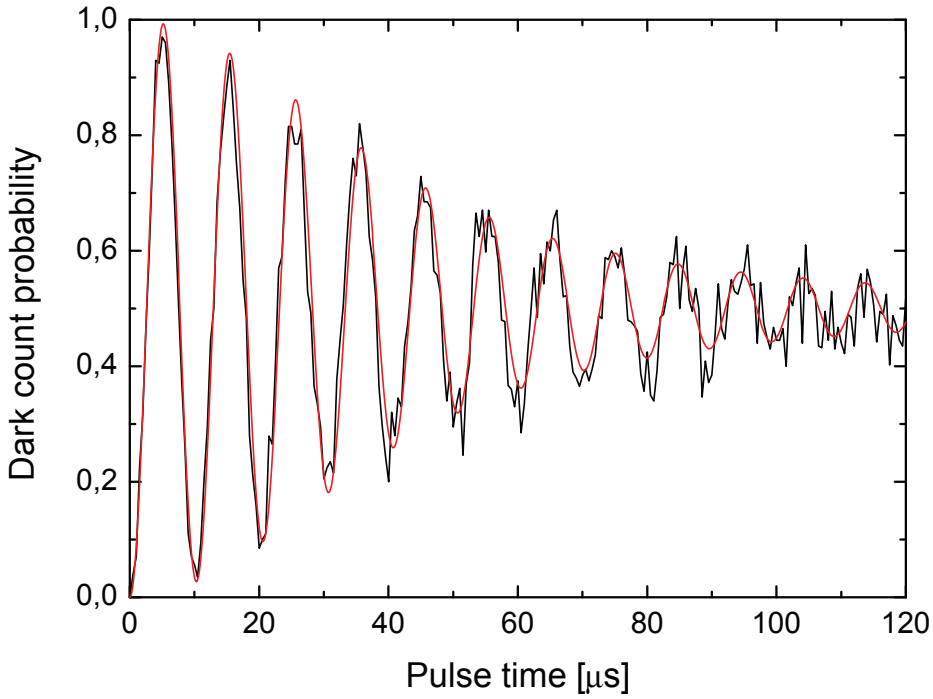

Figure 4.8.: Coherent dynamics on the quadrupole transition: The fraction of population in the metastable state is plotted against the duration of a square excitation pulse tuned to the $m_{1/2} = +1/2 \rightarrow m_{5/2} = +5/2$ transition. One can clearly see a very rapid dephasing due to the interaction with three thermally population vibrational modes.

Taking the coupling to all these modes into account, the signal for excitation with a square pulse of duration t is given by a multimode extension of Eq. 2.56:

$$P_D(t) = \sum_{\{n_i\}} \prod_i p_{th}(n_i, \bar{n}_i)) \frac{1}{2} \left(1 - \cos\left(\Omega_{\{n_i\}} t\right)\right), \tag{4.4}$$

where

$$\Omega_{\{n_i\}} = \Omega_0 \prod_i M_{n_i}^{car}(\eta_i^2). \tag{4.5}$$

The η_i and $\bar{n}_i$ are the Lamb-Dicke parameters and mean phonon numbers for mode i, and $p_{th}(n_i, \bar{n}_i))$ is the corresponding thermal phonon distribution Eq. 2.33. The probability for finding a specific Rabi frequency is given by

$$p(\Omega = \Omega_{\{n_i\}}) = \prod_i p_{th}(n_i, \bar{n}_i). \tag{4.6}$$

If we now assume that the Rabi frequency differences are smaller than the inverse observation time and the individual probabilities are small due to the many contributing frequencies, the

contributions of each of the frequencies can not be individually discerned and a description by a smooth continuous Rabi frequency probability distribution is justified. The probability for attaining a Rabi frequency of Ω during one individual measurement is then given by convolution of the discrete probability distribution with a Gaussian smoothing function:

$$\tilde{p}(\Omega) \approx \sum_{\{n_i\}} \prod_i p_{th}(n_i, \bar{n}_i)) e^{-\frac{(\Omega - \Omega_{\{n_i\}})^2}{2\sigma^2}}, \tag{4.7}$$

which is normalized to

$$p_b(\Omega) = \frac{\tilde{p}_b(\Omega)}{\int_0^{\Omega_0} \tilde{p}_b(\Omega) d\Omega} \tag{4.8}$$

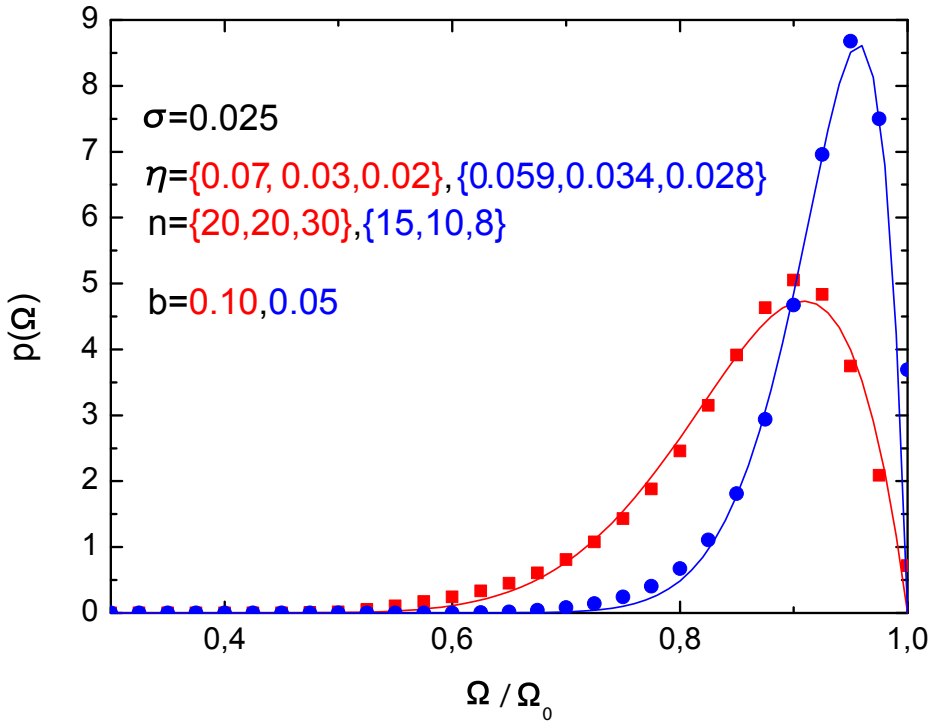

Figure 4.9.: Effective Rabi frequency distribution: The symbols show sample probability densities obtained from Eq. 4.8, and the solid lines result from a fit of this data to Eq. 4.10. Data for two different parameter sets is shown, where the blue data (circles) set assumes realistic experimental parameters which accurately reproduces the measurement results in Fig. 4.8.

This smoothed probability distribution is empirically found to be well described by

$$\tilde{p}_b(\Omega) = \frac{\Omega_0 - \Omega}{\Omega} e^{-\frac{\Omega_0 - \Omega}{b\Omega}}, \tag{4.9}$$

which is normalized to

$$p_b(\Omega) = \frac{\tilde{p}_b(\Omega)}{\int_0^{\Omega_0} \tilde{p}_b(\Omega) d\Omega}. \tag{4.10}$$

This distribution function is depending only on parameter b which can be fitted from a set numerically obtained probability values. A comparison of $p_b(\Omega)$ and calculated values from Eq. 4.7 for different parameter sets are shown in Fig. 4.7. The great simplification is the instead of six parameters $\eta_i, \bar{n}_i$, the thermal motion is characterized by only one parameter, and the three-fold summation in Eq. 4.6 is replaced by a single integral:

$$P_D(t) = \int_0^{\Omega_0} p_b(\Omega) \frac{1}{2} \left(1 - \cos(\Omega t)\right) d\Omega. \tag{4.11}$$

The relation between the bare Rabi frequency and the experimentally determined π-time is given by:

$$\Omega_0 = \frac{\pi}{\tau_\pi}(1 + b) \tag{4.12}$$

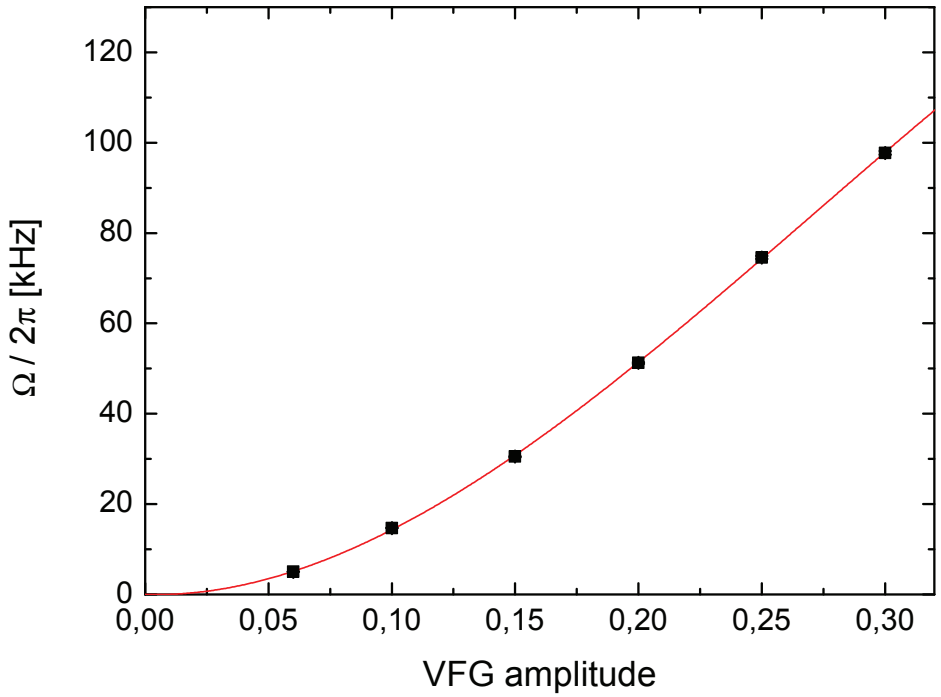

Figure 4.10.: Gauge of the Rabi frequency on the quadrupole transition: The Rabi frequency has been measured for several different output amplitudes of the VFG synthesizer (see Sec. 3.6). Only one oscillation period has been recorded per amplitude, such that thermal effects can be simply accounted for by an exponential decay factor. The result from the fit is then the bare Rabi frequency Ω_0 with a sub-percent inaccuracy.

It should be mentioned that the coherent evolution measured in Fig. 4.8 in the presence of thermal excitation can be equally well reproduced with the more simple approach from Ref. [Roo00], Sec. A.1, where an analytic approximation is performed directly on Eq. 4.4, where basically a Taylor expansion of the matrix elements $M_{n_i}^{car}$ with respect to η_i^2 is carried out. This yields the result

$$P_D(t) \approx \frac{1}{2}\left(1 - \mathrm{Re}\prod_k \frac{e^{2i\Omega_0 t}}{1 + 2i\Omega_0 t\eta_k^2\bar{n}_k}\right), \tag{4.13}$$

which reproduces the data shown in Fig. 4.8 for assumed parameters of $\{\bar{n}\} = \{b\}$ and $\{\eta\} = \{b\}$. However, this approach is not viable for calculating the time evolution for arbitrary time-dependent pulse shapes as it is performed in Sec. 4.4 for the spin readout. Finally, the ability to associate the experimentally determined π-time to a bare Rabi frequency offers the possibility to provide an accurate gauging of the Rabi frequency with respect to the amplitude values fed to the VFG synthesizer. The results are shown in Fig. 4.10. A relation of

$$\Omega_0 \approx -8.5 \cdot 10^4 x + 1.0 \cdot 10^7 x^2 - 1.3 \cdot 10^7 x^3 \tag{4.14}$$

with the VFG amplitude x is empirically determined, which of course only yields valid results over a limited amplitude range. The ability to perform such an accurate calibration of the coupling strength is a cornerstone for the experimental realization of coherent control techniques. Finally, it shall be mentioned that the additional dephasing due to a magnetic field fluctuations and the finite linewidth of the 729 nm laser was omitted here, which is justified by the finding of Sec. 4.7 that the T_2^*-time on that transition is longer than the observation time for the measurements presented here.

4.2.4. Qubit Preparation

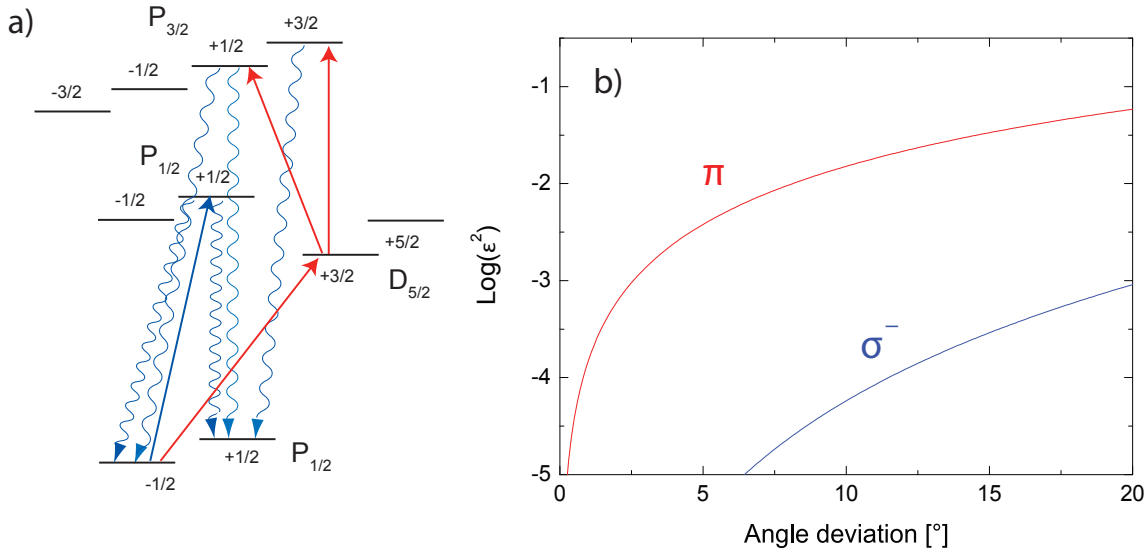

Figure 4.11.: Two different schemes for optical pumping: **a)** illustrates the optical pumping via the $P_{1/2}$ state or the alternative scheme via the quadrupole transition. **b)** shows the erroneous polarization components in the 397 nm pumping beam occurring due to either azimuthal or inclination tilt angles. One can see that preparation errors on the order of 1 % can occur if the beam is not carefully adjusted.

A decisive step for most experiments with trapped ions the initialization in a defined electronic state. In a quantum information context, this would amount to the DiVincenzo criterion of qubit initialization. Especially when working with more and more qubits, the quality of the initialization becomes very crucial as the total error probability scales exponentially with the number qubits. In order to devise robust high-fidelity initialization schemes, a detailed understanding of the underlying atomic physics is necessary. As ^{40}Ca has only the two stable ground states $|\uparrow\rangle$ and $|\downarrow\rangle$, the task is simply to selectively deplete one of these two levels. The most simple optical pumping scheme is to simply to deplete e.g. $|\downarrow\rangle$ by irradiation with a σ^+ polarized beam at the resonance at 397 nm, with the 866 nm beam also switched on to avoid population trapping in the $D_{3/2}$ state. If the irradiation is performed long enough, the $|\downarrow\rangle$ level will be depleted even if the detuning and power of the beams are not exactly controlled. However, the scheme is not robust with respect to angular tilts of the pumping beam with respect to the magnetic field direction, as the spurious π and σ^- components which are occurring then also couple the $|\uparrow\rangle$ level to the laser field. One can simply find the stationary solution of the pumping rate equations which take into account the powers pertaining to the different polarization components $\epsilon_-\epsilon_0, \epsilon_+$ and the branching ratios

given by the Clebsch-Gordan factors, which leads to the stationary remaining population

$$\frac{P_\downarrow}{P_\uparrow} \approx P_\downarrow = \frac{\epsilon_-^2 + \epsilon_0^2}{\epsilon_+^2 + \epsilon_0^2} \tag{4.15}$$

The Zeeman splitting leading to different pump rates on the sub-transitions and the branching to the $D_{3/2}$ state have been neglected here for the sake of simplicity. In order to obtain an estimation of the experimental accuracy requirements, the magnitude of the spurious polarization components has been plotted versus the tilt angle in Fig. 4.11 b), where the data was obtained by invoking Eqs. 2.28.

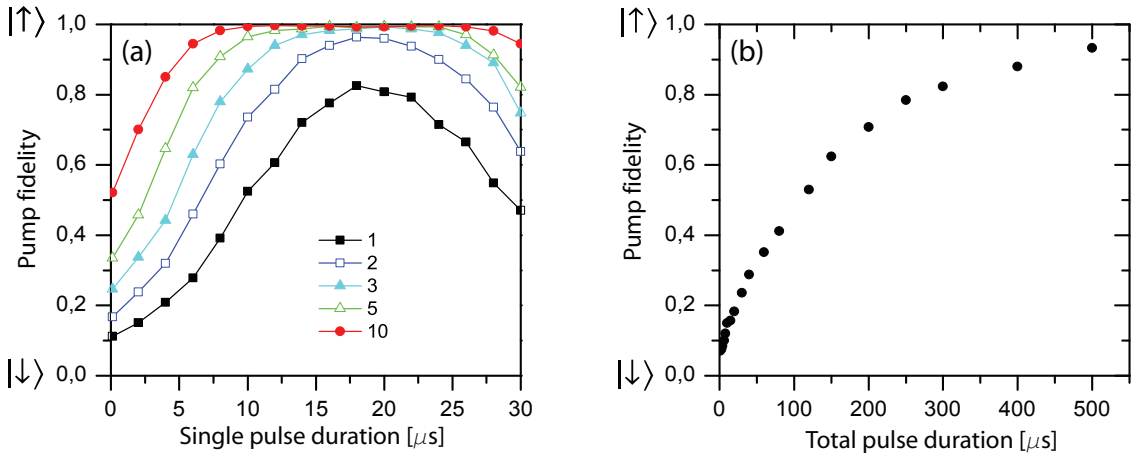

Figure 4.12.: Optical pumping on the quadrupole transition: **a)** shows results for the robust pulsed pumping scheme. The shelving probability is plotted against the duration of the individual square pulses on the quadrupole transition. Results are shown for various numbers of pulses in the pumping sequence. For increasing pulse numbers, one obtains a broad plateau, such that the scheme is robustified against drifts in the Rabi frequency, the detuning and the quench rate. **b)** shows results for continuous pumping with the 854 nm and the 729 nm beams switched on simultaneously, for the same beam powers as in a). One can see that the convergence behavior is very poor. Better results could however be obtained if the 854 nm power is optimized.

A more robust pumping scheme which can be realized for ^{40}Ca relies on the frequency selectivity on the narrow quadrupole transition instead of polarization selectivity. The laser at 729 nm is used to transfer population only from the level which is to be depleted to the metastable $D_{5/2}$ state, from which it transferred back to both ground state levels by quenching at 854 nm. After a large enough number of cycles, the unwanted initial level is sufficiently depleted. As can be seen from Fig. 4.11 a), the efficiency can be optimized if a purely π polarized quench laser is used, however this would require an additional quenching beam for

depletion of the m_J=+5/2 level for qubit reset. The results for the quadrupole pumping scheme can be seen in Fig. 4.12, where both a continuous and a pulsed scheme are shown. The pulsed scheme turned out to be more favorable for the experimental implementation as it does not require a precise setting of the quench power, see Sec. 2.1.5 for the theoretical treatment. One simply has to measure the π time on the pump transition, which would be the $|\downarrow\rangle$ to $D_{5/2}$,m_J=+3/2 transition in our case, which requires conventional optical pumping at 397 nm with σ_- polarized light. One also has to determine the time it takes the quench laser to deplete the metastable state, which can be simply done by measuring the remaining dark population after shelving with a subsequent 854 nm pulse of fixed duration. Typically, in takes about 1..2 μs to deplete the metastable state. The pumping is then performed by a series of alternating pump and quench pulses, where 5..10 are typically sufficient for achieve high pumping fidelities. The fidelity could be in principle improved by employing transform limited pump pulses to avoid off-resonant excitation from the desired final state $|\uparrow\rangle$. If the quadrupole pumping scheme is employed, the drawbacks are that one additionally has to keep track of the 854 nm laser wavelength and pumping transition frequency. The highest combined pumping, shelving and readout fidelity achieved was 99.6%, where it is hard to discern the effects from the various imperfections. It is assumed that the bottleneck in this case was given by the shelving efficiency. With the conventional 397 nm pumping, typical dark count probabilities after shelving of 97.5..98.5% are routinely achieved, which is still sufficient for the experiments on one and two ion described in the remainder of this thesis.

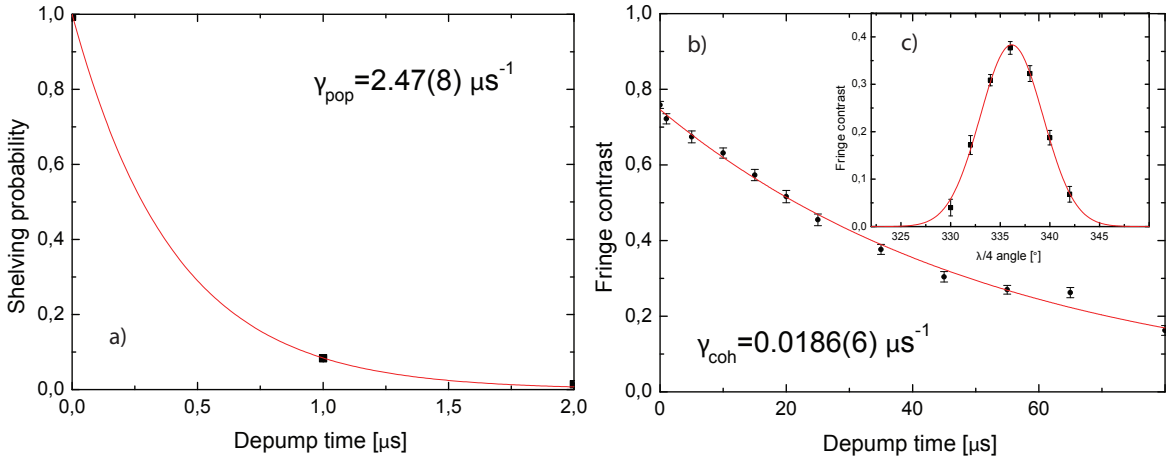

Figure 4.13.: Measurement of spurious polarization components: **a)** shows results for the depump rate measurement, which directly gives the pump rate. **b)** shows results for the coherence decay measurement on a superposition of $|\uparrow\rangle$ and $|D_{5/2}, m_J = +5/2\rangle$, which roughly determines the π component of the pump beam. **c)** shows the results for coherence measurements at fixed pump pulse time of 35 μs for different angles of the quarter wave plate.

It is difficult to measure the wrong polarization components because it is difficult to discern imperfect pumping from other experimental imperfections, however we show here how quantum coherence can be utilized as a measurement tool to achieve this. The idea is to compare the rate which the pump beam can transfer population to the rate at which it destroys a coherence between its 'dark' state and the metastable $D_{5/2}$ state, see Sec. 4.7 for a detailed explanation of coherence measurements. For the population measurement, the ion is pumped to $|\uparrow\rangle$ with the quadrupole pumping technique described above, and before the shelving a depump pulse of σ^- polarized light at 397 nm is applied. The remaining population in $|\uparrow\rangle$ vesus the depump pulse duration is shown in Fig. 4.13, and a depump rate of γ_{pop}=2.47(8) μs^{-1} is obtained. For the coherence measurement a coherent superposition is prepared on the $|\uparrow\rangle$ to $|D_{5/2}, m_J = +5/2\rangle$ transition by a $\pi/2$ pulse at 729 nm. Before probing, the superposition is decohered by pulses of σ^+ polarized light at 397 nm. If no σ^- or π components were present in the beam, it would not couple to the levels present in the superposition state such that it would remain unaffected. The coherence loss rate, which is found to be 0.0186(6) μs^{-1}, is therefore a direct measure of the spurious polarization components. Two assumptions are made to find the amount of wrong polarization: First, we assume that the driving strengths for σ^+ and σ^- light are the same, i.e. the Zeeman splitting is neglected. Second we assume that the π component is much stronger, which is justified when looking at Fig. 4.11 b). Taking the Clebsch-Gordan factors into account, we find

$$\begin{aligned} \gamma_{pop} &= \frac{1}{9}\epsilon_+^2\gamma_0 \approx \frac{1}{9}\gamma_0 \\ \gamma_{coh} &= \frac{1}{9}\frac{1}{2}\epsilon_0^2\gamma_0, \end{aligned} \tag{4.16}$$

where the appearance of ϵ_+^2 instead of the ϵ_-^2 actually used in the measurement is due to the first assumption above and the additional factor 1/2 in the second line is due to the fact that only half the population resides in $|\uparrow\rangle$ in the decoherence measurement. γ_0 is the raw pump rate defined by the Rabi frequency in the 397 nm, the detuning and the lifetime of the $P_{1/2}$ state. We then find

$$\epsilon_0^2 = 2\frac{\gamma_{coh}}{\gamma_{pop}} \approx 1.5\%, \tag{4.17}$$

which is completely consistent with the comparison of the efficiencies for the 397 nm and quadrupole pumping schemes. Fig. 4.13 shows measurement results revealing the required precision of the setting of the quarter wave plate for the pump beam: The coherence measurement was performed for a fixed decoherence pulse time of 25 μs at varying angle of the waveplate, such that a σ_- component is added to the beam, along with a fit to

$$C(\alpha) = C_0 e^{-A\sin(\alpha+\alpha_0)^2}. \tag{4.18}$$

It can be inferred that at the needed adjustment precision of the waveplate is about 1°, which should be independent of the power in the pump beam as only the ratio of the σ_+ and σ_- components determine the pumping fidelity. The power of the pump beam throughout all the measurements shown in Fig. 4.13 has been 52 μW.

4.2.5. Qubit Reset

For various applications, e.g. optical pumping for spin initialization, qubit reset and sideband cooling or more involved experiments like experiments on electromagnetically induced transparency or deterministic single photon generation [Alm10] which are not within the scope of this thesis, it is advantageous to be able to provide calibration of Rabi frequency and detuning also on dipole transitions which do not not allow for coherent driving. Here, we employ the shelving technique to demonstrate that precise Rabi frequency calibration is possible on the $D_{5/2}$ to $P_{3/2}$ transition at 854 nm as well as the $D_{3/2}$ to $P_{1/2}$ transition at 866 nm. The experimental procedure for the two transitions is essentially the same: The ion is initialized in the corresponding D-state, then a depump pulse of fixed duration is applied and the remaining population in the D-sate is measured. As this is repeated for a range of different depump pulse times, an exponential decay of the D-population is found such that a decay rate can be inferred. If the decay rate is measured for varying power, one can determine a relation between the dipole Rabi frequency and power. In our treatment we assume that we are on resonance of the corresponding dipole transitions, which is justified as the 866 nm laser can be tuned sufficiently precise to resonance by optimizing the 397nm fluorescence rate, ad the 854 nm resonance we determined by means of the same experimental technique as is used for the Rabi frequency measurement, except that the 854 nm frequency is scanned for a fixed depump pulse duration. On resonance, the optical Bloch equations with the loss channel included can easily be written down:

$$\begin{aligned}
\dot{\rho}_{11} &= \gamma\rho_{22} + \frac{i}{2}\Omega\left(\rho_{21} - \rho_{12}\right) \\
\dot{\rho}_{22} &= -(\gamma+\Gamma)\rho_{22} + \frac{i}{2}\Omega\left(\rho_{12} - \rho_{21}\right) \\
\dot{\rho}_{12} &= -\frac{1}{2}(\gamma+\Gamma)\rho_{12} + \frac{i}{2}\Omega\left(\rho_{22} - \rho_{11}\right) \\
\dot{\rho}_{21} &= -\frac{1}{2}(\gamma+\Gamma)\rho_{21} + \frac{i}{2}\Omega\left(\rho_{11} - \rho_{22}\right),
\end{aligned} \tag{4.19}$$

where Ω is the depump beam Rabi frequency, γ is the decay rate from the excited back to the metastable state and Γ is the decay rate from the excited to the electronic ground state. For not too small Rabi frequencies, one finds upon numerical solution of Eqs. 4.19 that the depump process can be sufficiently well described by simple exponential decay of the population the metastable state, where the decay constant Γ_{dep} is a function of Ω,γ and Γ. However, no analytical relation could be found, such that a number of decay constants was obtained for values of the Rabi frequency between $2\pi\cdot0.1$ MHz and $2\pi\cdot10$ MHz, where the values for γ and Γ were chosen to be the ones for the corresponding transition [Jam98]. It was found that

$$\Gamma_{dep} = C_{dep}\Omega^2 \tag{4.20}$$

matches the behavior very well over the entire range of Rabi frequencies, such that the proportionality constants

$$\begin{aligned} C_{dep}^{D_{3/2}\rightarrow P_{1/2}} &= 0.00332\text{MHz}^{-1} \\ C_{dep}^{D_{5/2}\rightarrow P_{3/2}} &= 0.00315\text{MHz}^{-1} \end{aligned} \tag{4.21}$$

could be determined.
For the first transition, the ion is initialized in $|\uparrow\rangle$ by optical pumping and shelved to the $D_{5/2}$, m_J=+5/2 state. Quenching pulses at 854 nm at variable duration are used to remove population from the metastable state, finally the remaining population measured. The results are shown in Fig. 4.14. For each specific depump power, a depump rate Γ_{dep} can be inferred, such that Eq. 4.21 can be invoked to yield the desired relation between power and Rabi frequency:

$$\Omega^2 = 1.0(1)\text{MHz}^2\mu\text{W}^{-1} \tag{4.22}$$

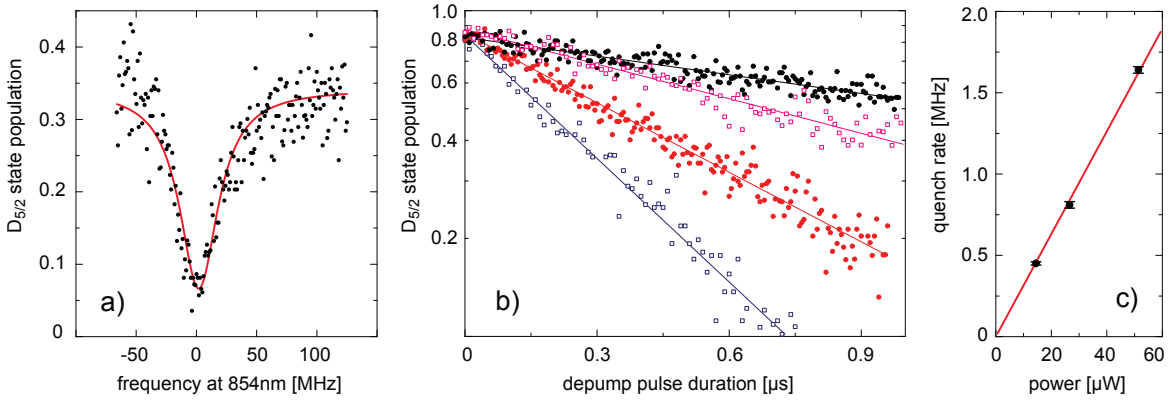

Figure 4.14.: Quenching of the $D_{5/2}$ state: **a)** illustrates spectroscopy on the 854 nm transition by depumping the $D_{5/2}$ state with a pulse of fixed duration and variable laser frequency. **b)** shows the dynamics of the depopulation of the $D_{5/2}$ state on resonance for varying pulse duration and different power levels. **c)** shows the quench rates versus power inferred from these measurements.

The measurement on the $D_{3/2}$ to $P_{1/2}$ transition at 866 nm had to be performed in a slightly different way, as no laser at 710 nm for coherent population transfer to the $D_{3/2}$ state was at hand. Here, population is simply pumped to the $D_{3/2}$ state with the 397 nm laser and the 866 nm switched off. The shelving from $|\uparrow\rangle$ is then performed after the 866 nm depump pulse, such that the remaining population in $D_{3/2}$ *and* in the $|\downarrow\rangle$ level is measured as bright.

Thus, only a limited fraction is counted dark after complete depump of the $D_{3/2}$, however the desired decay constant can still be measured with sufficient precision. The results are shown in Fig. 4.15, and the relation between power and Rabi frequency reads

$$\Omega^2 = 5.0(1)\mathrm{MHz}^2\mu\mathrm{W}^{-1} \tag{4.23}$$

The striking dissimilarity between the constants in Eqs. 4.22 and 4.23 is explained by the fact the data for the 854 nm depumping was taken at a much earlier time when the 854 nm and 866 nm beams were freely propagating over a large distance and the focus was much larger than necessary. One should expect to see very similar values for the present situation with the fiber output collimator for the 854 nm and 866 nm beams close the ion trap, see Fig. 3.4.

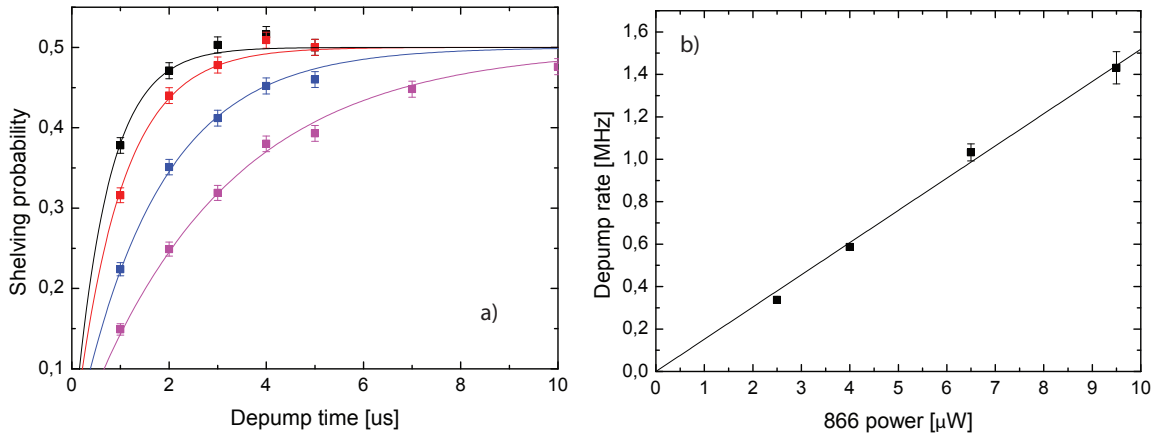

Figure 4.15.: Quenching of the $D_{3/2}$ state: **a)** shows the population transferred to the $D_{5/2}$ state after depumping the $D_{3/2}$ state with the resonant 866 nm laser with variable pulse duration for different depump powers, see text. **b)** shows the depump rates inferred from these curves.

4.3. 3D Heating Rate Measurement by Fluorescence Observation

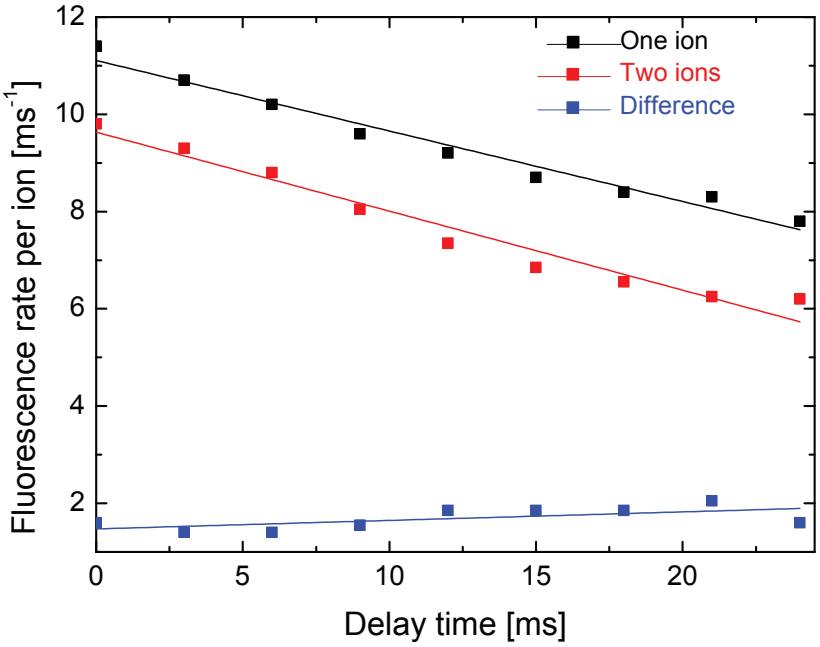

Figure 4.16.: Fluorescence heating rate measurement: The detected fluorescence is plotted versus waiting time between Doppler cooling and the start of the fluorescence detection. The precision is not good enough to claim a significant difference between the one and two ion case.

The most simple technique for measuring the heating rate of trapped ions is to measure the resonance fluorescence level after a variable waiting time. A more precise information can be inferred from time resolved fluorescence measurements, where the dynamics of the Doppler recooling process can directly be seen [Wes07, Eps07]. Here, we restrict ourselves to the simple static level measurement techniques providing information about all motional modes. In contrast to the approach in Refs. [Wes07, Eps07], the back-action of the near-resonant laser radiation on the motional state is ignored here. Fig. 4.16 shows fluorescence level measurement taken on one- and two ions with a delay between Doppler cooling and the start of the fluorescence counting interval. We can invoke Eq. 2.42 for the fluorescence rate, where we additionally consider a factor $\sigma \ll 1$ describing the collection efficiency of the imaging optics, an effective number of contributing modes d and a total kinetic energy described by linear heating: $E_{\mathrm{tot}}(t) = E_0 + \Theta t$. The time-dependent count rates per ion for one and two ions are then given by

$$R^{(1,2)}(t) = \sigma \left(R_0 - \left(R'_H(E_0^{(1,2)} + \Theta t) \right) \right) \tag{4.24}$$

The measurement results are fitted to a linear behavior $R^{(1,2)}(t) = a^{(1,2)} - b^{(1,2)}t$, yielding the results $a^{(1)}$=11.1(1)ms^{-1}, $a^{(2)}$=9.6(2)ms^{-1}, $b^{(1)}$=0.145(9)ms^{-2} and $b^{(2)}$=0.16(1)ms^{-2}. Due to the (expected) non-significant difference between $b^{(1)}$ and $b^{(2)}$, we used their mean value b in the following. If we neglect $E_0^{(1)}$, which is justified for about 20 initial phonons per mode after Doppler cooling of a single ion, we can solve for σ, Θ and $E_0^{(2)}$:

$$\sigma = \frac{a^{(1)}}{R_0} \approx \tag{4.25}$$

$$\Theta = \frac{bR_0}{a^{(1)}R'_H}$$

$$E_0^{(2)} = \frac{(a^{(1)} - a^{(2)})R_0}{a^{(1)}R'_H}. \tag{4.26}$$

All assumed parameters and resulting quantities are compiled in Table 4.1.

Parameter	Symbol	Value	Estimated uncertainty
Saturation parameter	S	5.1	±1.1
Mean oscillation frequency [MHz]	$\bar{\omega}$	2π·2.0	±0.5
Mean oscillation angle factor	$\cos^2\bar{\alpha}$	0.5	±0.05
Initial energy for single ion [phonons]	$E_0^{(1)}$	0.0	+20.0
Photon collection efficiency [%]	σ	0.02	±0.001
Heating rate [phonons/ms]	Θ	$2.1{\cdot}10^5$	$\pm\ 3{\cdot}10^{-4}$
Two-ion initial energy [phonons]	$E_0^{(2)}$	2100.0	± 300.0

Table 4.1.: Final results fluorescence heating rate measurement.

The validity of the results is justified as follows: The most critical approximation for deriving Eq. 2.42 is the Taylor expansion made in Eq. 2.40, which clearly holds as a linear decrease of the fluorescence is observed. As a conclusion, we find a 3D heating rate which is fully consistent with the more precise finding to be presented below. However, the astonishingly large number of initial quanta in the two-ion case could not be explained yet.

4.4. Qubit Readout via Electron Shelving

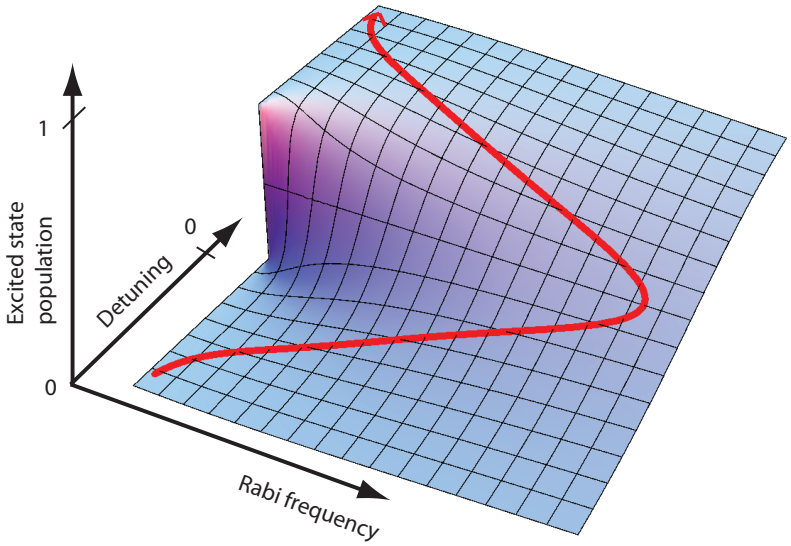

Figure 4.17.: Scheme of the RAP process: The portion of the excited (target) state in the eigenstate Eq. 4.27 is plotted versus laser detuning and coupling strength. Adiabatic switching of the coupling strength together with sweeping of the detuning across resonance guarantees a smooth transition into the target state.

As mentioned in the introduction of this chapter, an additional complication for the spin qubit is the requirement of an additional step for the discrimination of the qubit levels $|\uparrow\rangle$ and $|\downarrow\rangle$. Upon irradiation at 397 nm or 393 nm, both levels will give rise to fluorescence. Frequency selectivity at these dipole transitions would require Zeeman splittings much larger than the linewidth of about 24 MHz, which would lead to other experimental complications. Therefore, the only feasible solution is the mapping of the spin qubit to the metastable one. As only information about the occupation probabilities can be obtained anyway when the metastable qubit is read out by means of the fluorescence discrimination method, the mapping procedure does not have to be coherent, i.e. the phase information can be discarded. A phase coherent mapping would be realized by performing π-pulses on the quadrupole transition, which brings up the necessity of a careful experimental calibration and stabilization of the coupling strength and optical frequency for that transition. Even if this is realized, the Rabi frequency is subject to intrinsic statistics of the ions are not ground-state cooled on all modes to which the laser beam driving the quadrupole transition couples, see Sec. 4.2.2. Thus, a technique for fast, efficient and robust transfer of population is needed. One possibility is to perform optical pumping to the metastable state via the $S_{1/2} \rightarrow P_{3/2}$ transition at 393 nm, where the spin selectivity can be achieved by using another laser beam driving the $D_{3/2} \rightarrow P_{3/2}$

at 850 nm for suppressing excitation from e.g. $|\downarrow\rangle$ by means of an EIT resonance [McD04]. Out approach however is to make use of the optical quadrupole transition for realizing robust readout by application of the *rapid adiabatic passage* (RAP) technique. The basic idea is that the coupling laser gives rise to new eigenstates, in one of which the system stays if the coupling is switched on and off adiabatically, however it is driven from one the initial bare atomic level to the target one by simultaneously sweeping the laser across the corresponding resonance frequency. This basic process has first been demonstrated with metastable Helium atoms crossing an excitation beam at the Rayleigh length [Eks96]. The underlying quantum dynamics is illustrated in Fig. 4.17.

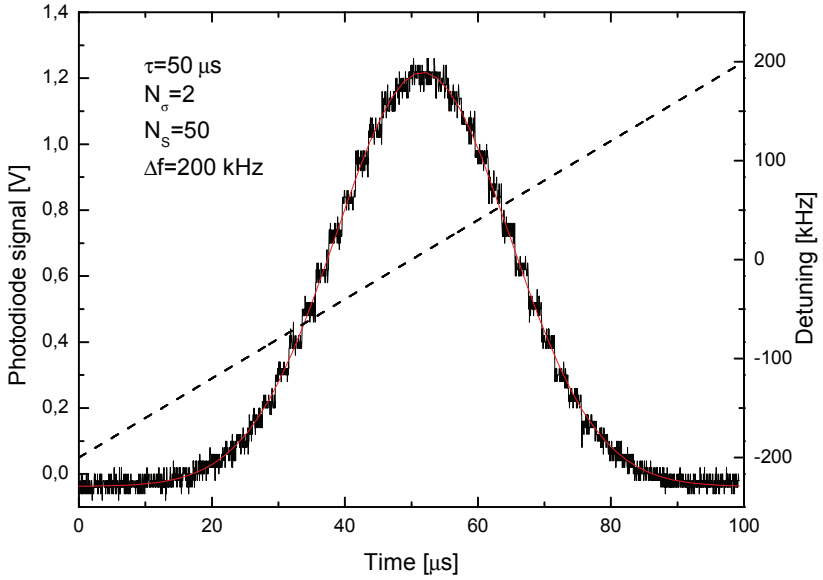

Figure 4.18.: Photodiode signal from a 729 nm pulse for rapid adiabatic passage. Note the discrete steps due to the sampling interval of the waveform generator. The dashed line indicates how the frequency is chirped across the resonance.

Consider a two level system with a laser induced coupling as described by the Hamiltonian from Eq. 2.10. Diagonalization of this Hamiltonian yields the new eigenstates

$$\begin{aligned} |\psi_-\rangle &= -\frac{\Delta+\sqrt{\Delta^2+\Omega^2}}{\Omega}\mathcal{N}_-^{-1/2}|g\rangle + \mathcal{N}_-^{-1/2}|e\rangle \\ |\psi_+\rangle &= -\frac{\Delta-\sqrt{\Delta^2+\Omega^2}}{\Omega}\mathcal{N}_+^{-1/2}|g\rangle + \mathcal{N}_+^{-1/2}|e\rangle, \end{aligned} \tag{4.27}$$

with

$$\mathcal{N}_\pm = \frac{\left(\Delta \mp \sqrt{\Delta^2+\Omega^2}\right)^2}{\Omega^2} + 1. \tag{4.28}$$

We obtain the populations

$$\begin{aligned} P_g^{(-)} &= P_e^{(+)} = \frac{1}{2}\left(1 + \frac{\Delta}{\sqrt{\Delta^2+\Omega^2}}\right) \\ P_e^{(-)} &= P_g^{(+)} = \frac{1}{2}\left(1 - \frac{\Delta}{\sqrt{\Delta^2+\Omega^2}}\right). \end{aligned} \tag{4.29}$$

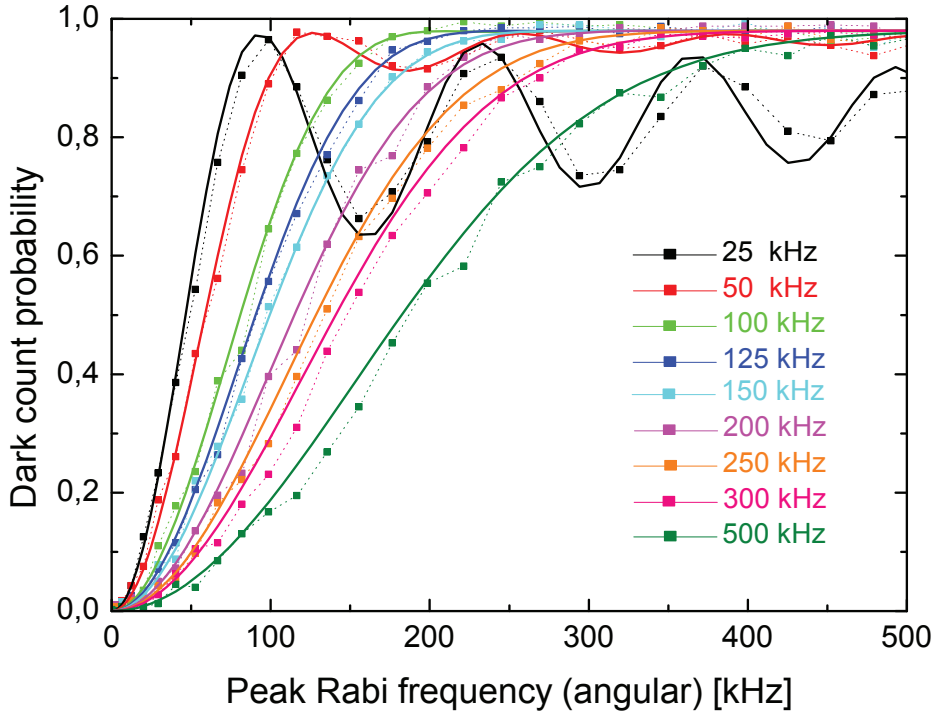

Figure 4.19.: RAP efficiency versus peak Rabi frequency for different chirp ranges: The plot shows resulting transfer efficiencies while the peak amplitude is scanned. The solid lines are obtained from a numerical solution of the time-dependent Schödinger equation for the two-level system, including thermal effects by averaging over a distribution Rabi frequencies, see text. For small chirp ranges, one observes a Rabi oscillation-like behavior, while adiabaticity is fulfilled for chirp ranges of 100 kHz or larger. For larger even chirp ranges, the increase in robustness is bought at the expense of a higher power requirement. Note that no free parameters were used for the simulation, all parameters were inferred from the puls width scan measurement of Fig. 4.8 and the power gauge measurement Fig. 4.10.

Starting in the ground state, with the laser switched of and far red detuned, $\Omega = 0, \Delta \ll 0$, the ground state is identical to $|\psi_+\rangle$. If the parameters are now changed adiabatically and the detuning is ramped to the blue side, the systems always stays in $|\psi_+\rangle$, and the final state is $|e\rangle$. The eigenenergies pertaining to $|\psi_-\rangle$ and $|\psi_+\rangle$ are given by $E_\pm = \pm(\hbar/2)\sqrt{\Delta^2+\Omega^2}$.

Adiabaticity is now guaranteed if the process is conducted such that

$$\hbar|\langle\psi_-|\dot{\psi}_+\rangle| \ll E_+ - E_- \tag{4.30}$$

is always fulfilled. The derivative of the ket is to be understood as the total derivative with respect to the time dependent parameters Ω and Δ.

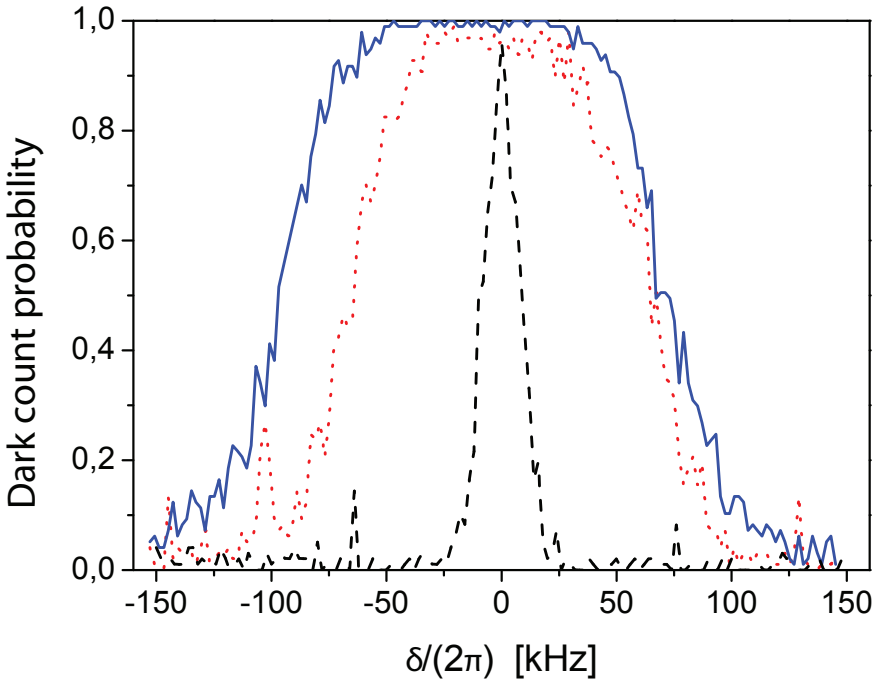

Figure 4.20.: Robustness of the shelving process with respect to frequency errors: The dark count probability is plotted versus the central frequency for different transfer pulses. The black dashed curve shows the results for a Gaussian pulse with fixed frequency with its amplitude chosen such that it yields a π-rotation at resonance, whereas the dotted red line and the solid blue line show the transfer efficiency for a single and a double RAP pulse, respectively. One can clearly see that the RAP pulses are indeed robust over a large frequency range, and the total efficiency of the double RAP is much better than for the single RAP.

In order to fulfill the adiabaticity criterion, the detailed pulse shape does not matter. Our choice is a linear ramp of the detuning along with Gaussian-like shape of the Rabi frequency:

$$\begin{aligned} \Delta(t) &= 2\pi\frac{R_\Delta t}{N_\sigma T_\sigma} \\ \Omega(t) &= \tilde{\Omega}\left(A_0 e^{-\frac{2t^2}{T_\sigma}}\right) \\ -N_\sigma T_\sigma/2 &< t < +N_\sigma T_\sigma/2, \end{aligned} \tag{4.31}$$

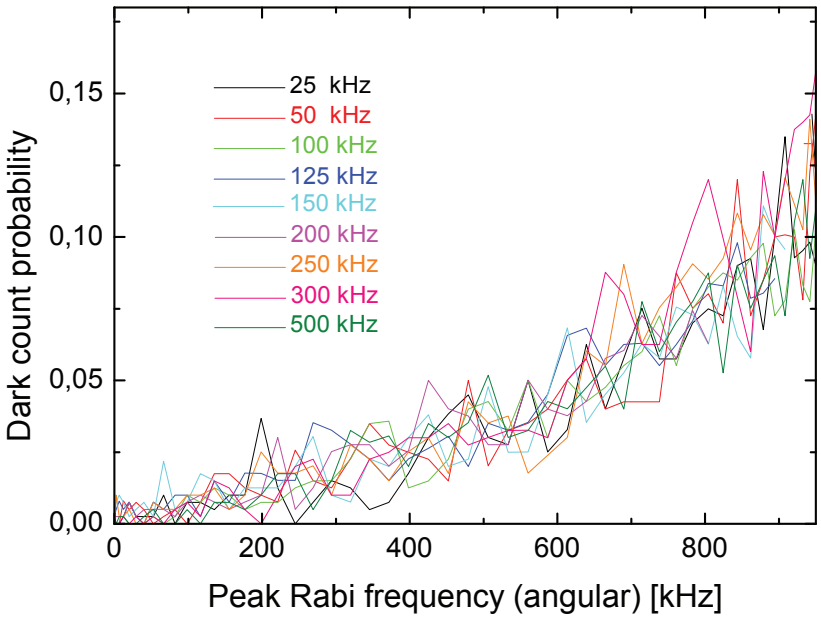

Figure 4.21.: Parasitic shelving: The figure shows the shelved population versus peak Rabi frequency for the same parameters as in Fig. 4.19. The central frequency is resonant with the $|\uparrow\rangle \rightarrow |D_{5/2}, m_j = +5/2\rangle$ transition, the ion was initialized in $|\downarrow\rangle$ such that no population should be transferred under ideal condition. Data for the same chirp range as in Fig. 4.19 is shown, where the coloring is identical. The population transfer is insensitive to the chirp range, which suggests a completely incoherent transfer mechanism.

with the chirp range R_Δ, the time scale T_σ, the peak amplitude A_0 and N_σ defining how many $1/e$ widths of the are taken into account. The function $\tilde{\Omega}(x)$ is the actual Rabi frequency pertaining to the VFG amplitude A, see Sec. 4.2.2. Such a pulse monitored on a photodetector is shown in Fig. 4.18. The crucial question is now how the parameters for the pulses, i.e. the peak Rabi frequency, the duration, the sample number and the chirp range are to be chosen. Plugging the pulses functions Eqs. 4.31 into the adiabaticity criterion Eq. 4.30 yields a complicated expression, furthermore it does not directly give information about the robustness. Suitable parameters were therefore found by an experimental investigation of the efficiency and robustness. First, a total pulse duration of 100 μs was chosen as this clearly lies within the T_2^* time on the quadrupole transition, see Sec. 4.7. To guarantee smooth on- and off-switching, we set the Gaussian envelope to be cut at $1/e^2$. The remaining free parameters are now the amplitude, the chirp range and the sample number. The latter parameter is set to 40 to keep the amount of transferred data to the VFG reasonable. Now the peak amplitude is scanned for various chirp ranges while the population transferred to the metastable state is measured, the results are shown in Fig. 4.19. One can see that adiabatic following is attained at a chirp range of 100 kHz. The amplitude is now chosen to be slightly above the kink to be robust against power drifts but also to keep the total pulse area small. The robustness

is now assessed by performing the transfer efficiency measurement at these parameters, but with varying center frequency. The results are shown in Fig. 4.20, where one can see that a broad plateau of a width roughly corresponding to the chirp range is given, indicating stability of the shelving rate despite the drift of the 729 nm laser frequency. The stability is even enhanced if the shelving on an additional backup transition is performed, which is the $|\uparrow\rangle \rightarrow |D_{5/2}, m_J = +3/2\rangle$ transition in this case. By contrast, population transfer with a transform limited Gaussian pulse leads to a strong dependence on the center frequency, such that no robustness is given and the transition frequencies would have to be recalibrated frequently.
A second important criterion for the fidelity of the shelving process is the amount of population transferred on the *wrong* transition, i.e. the excitation from $|\downarrow\rangle$ to the $D_{5/2}$ state. Fig. 4.21 shows the population transferred from $|\downarrow\rangle$ versus RAP amplitude under the same conditions as in Fig. 4.19. Four possible mechanisms could be responsible for this unwanted behavior: i) direct off-resonant excitation, ii) off-resonant excitation from the discrete amplitude and frequency steps in the pulse and iii) resonant background light from the laser and iv) (near-)resonant excitation on higher order motional sidebands. Simulation results indicate that the first two mechanisms lead to negligibly small population transfer for reasonable RAP parameters. The fact that the population transfer is does not depend on the chirp range excludes a resonant excitation mechanism such as iv). Therefore we conclude that the unwanted excitation is caused by incoherent background light. For optimum shelving fidelity, it is therefore necessary to chose the lowest RAP amplitude at which the shelving probability from $|\uparrow\rangle$ saturates, and one has to trade the robustness increase from larger chirp ranges against infidelity as larger saturation amplitudes are required for larger chirp ranges. A possible technological solution to this is to employ a filtering cavity with a linewidth in the MHz range for the amplified 729 nm beam.

4.5. Stimulated Raman Transitions

The possibilities to perform coherent manipulations by means of the 729 nm laser driving the quadrupole transition are quite limited. This is on the one hand due to the linewidth of the 729 nm, where a stabilization to the 1 Hz range is technologically possible but rather tedious. Furthermore, as will be worked out in Sec. 4.3, the radial motion of ions in our microtrap represents an even more limiting constraint. As a second possibility for laser-driven coherent manipulations, we utilize stimulated Raman transitions driven by a pair of laser beams detuned by some tens of GHz from the $S_{1/2}$ to $P_{1/2}$ state, which can be seen as a resonantly enhanced two-photon transition. Stimulated Raman transitions can be used for separate or joint manipulation of the internal and external degrees of freedom of trapped ions, such that they provide a versatile tool for quantum optics and quantum information experiments. The characterization of the various types of interactions along with the associated decoherence effects is the main focus of this thesis.

4.5.1. Raman Spectroscopy and Single Qubit Rotations

In order to perform single qubit rotations, one needs to provide a controllable coherent coupling between the qubit levels $|\uparrow\rangle$ and $|\downarrow\rangle$. This can be realized by simultaneous irradiation of two laser beams split by a frequency difference which is given by the Zeeman splitting of the qubit levels. It is intuitively clear that one of the beams has to include a π polarization component and the other one has to include a circular polarization component, such that one of the Zeeman levels of the excited $P_{1/2}$ state can serve as the intermediate level for the resonant population transfer. If we assume the blue beam to be completely π polarized and the red beam to consist only of circular components, we can invoke Eq. A.12 to obtain the Raman Rabi frequency upon neglecting off-resonant terms and usage of Eq. A.10:

$$\Omega = \frac{1}{2\Delta}\frac{1}{3\sqrt{2}}\epsilon_{b0}\epsilon^*_{r-}e^{i(\Delta k-\delta' t)}, \tag{4.32}$$

where $\delta' = \delta - \omega_L$ is the detuning of the frequency difference from the ground state Larmor frequency. Irradiating both beams simultaneously for a constant duration at fixed intensities therefore realizes the unitary transform Eq. 2.12. Two main advantages arise from the usage of stimulated Raman transitions: First, the optical frequency and phase of the driving laser does not occur in the expression for the Rabi frequency, only the *relative* frequency and phase play a role. The frequency difference can be controlled to arbitrary accuracy by usage of phase-locked rf sources driving the switching acousto-optical frequency shifters, and the relative phase is limited by the mechanical interferometer stability of the optical setup. Second, the coupling to the ionic motion can be controlled via the difference wavevector Δk.

As already mentioned in the description of the experimental setup in Sec. 3.2.5, we utilize two different beam geometries for driving Raman transitions: a *collinear* geometry without any coupling to the ionic motion (beam pair R1/CC) and an *orthogonal* geometry with a coupling only to the axial motion (beam pair R1/R2) described by a Lamb-Dicke factor in the range between 0.25 and 0.3, depending on the axial trap frequency. Fig. 4.22 shows a

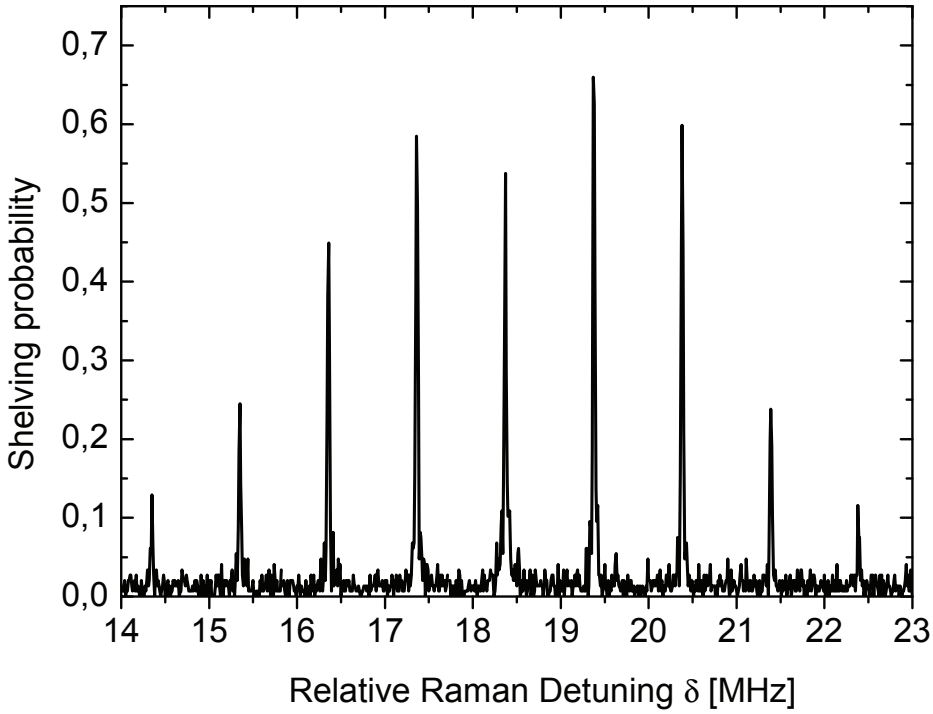

Figure 4.22.: Spectroscopy on the orthogonal Raman transition: This spectrum taken over a large frequency range nicely illustrates that the beam pair couples only to the axial mode of vibration.

Raman spectrum taken with the R1/R2 beam pair: in the experimental sequence, a Raman pulse of fixed duration is irradiated after the preparation step, then the spin is read out by the electron shelving technique presented in Sec. 4.4 along with the fluorescence discrimination technique from Sec. 4.2.1. This is the basic experimental sequence used whenever the qubit is manipulated and read out, which is used in the remainder of this thesis unless noted otherwise. The spectrum on the orthogonal Raman transition clearly displays a peak corresponding to the carrier spin-flip transition and symmetrically spaced sidebands pertaining to the harmonic axial motion. In contrast to the quadrupole transition, no radial sidebands appear in the spectrum.

Fig. 4.23 shows a Raman spectrum taken with the R1/CC beam pair. No axial sidebands are present. Due to the absence of inhomogeneous broadening of the coupling strength from thermal excitation of vibrational motion, the transition is driven fully coherent and strong oscillatory features are seen. The linewidth for this spectroscopy method is set by the inverse pulse duration and the power, such that long spectroscopy pulses at low power are needed for an accurate determination of the transition frequency. This method is however not particularly useful as various decoherence effects will set in for pulses of durations beyond the 100 μs range. Furthermore, the transition frequency is affected by ac Stark shifts from the

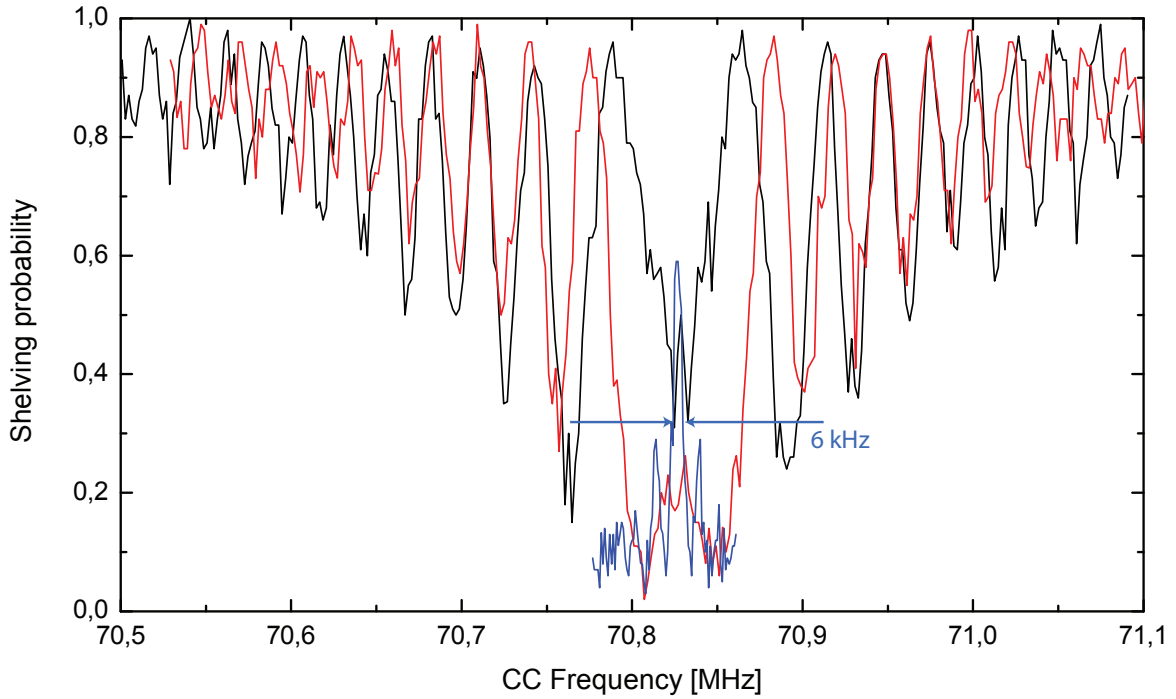

Figure 4.23.: Spectroscopy on the collinear Raman transition: Due to the absence of coupling to the motion, only one line is visible and the transition is driven fully coherent even for Doppler cooled ions. Spectra for high (black), intermediate (red) and low (blue) power are shown, where the low power spectrum has been flipped for the sake of visibility. A minimum linewidth of about 6 kHz is achieved this way, for a more accurate measurement of the transition frequency a Ramsey spectroscopy method has to be used.

off-resonant light, such that measurements at high power may lead to wrong results. With a typical Zeeman splitting of 19 MHz and a minimum linewidth of 6 kHz, a spectroscopic accuracy in the 10^{-5} range is achieved. On the orthogonal Raman transition, the accuracy is lower due to the thermal broadening of the Rabi frequency.

Due to the possibility to exclude the coupling to the ionic motion, the collinear Raman transition is the tool of choice for realizing the single-qubit rotations that are an essential building block of any quantum information protocol. Fig. 4.24 shows a pulse width scan on this transition, similar to the one performed for the 729 nm transition in Fig. 4.8. The striking difference between the two is clearly the absence of thermally induced dephasing for the Raman transition.

In contrast to direct driving of the qubit transition by the corresponding Radio frequency, the dynamics is driven by focused laser beams and therefore allows for addressing of individual ions or small ion groups in the segmented trap. The remaining decoherence effects one has to deal with are a) magnetic field fluctuations, b) intensity fluctuations along with nonzero

AC Stark shifts, c) off-resonant scattering and d) intensity fluctuations leading to pulse area fluctuations. The first three decoherence mechanisms are discussed extensively in Sec. 4.7. The mechanisms b) and d) stem from the same technical origin, but the mechanisms are sill fundamentally different, especially in that effect b) can be avoided in most cases. The off-resonant scattering can be suppressed by detuning the lasers further from resonance, one therefore faces a tradeoff between Rabi frequency and coherence time. Considering the results from Sec. 2.1.6, one recognizes that the Rabi frequency divided by the geometric mean is proportional to the detuning:

$$\frac{\Omega_{\mathrm{Rabi}}}{\sqrt{R_b R_r}} = \frac{3\sqrt{2}\Delta}{\Gamma}. \tag{4.33}$$

where R_b and R_r denote the scattering rates from the blue and red Raman beams respectively. This is confirmed for the collinear transition as can be seen in Fig. 4.25. The figure of merit on the left-hand side of Eq. 4.33 which is plotted on the ordinate of Fig. 4.25 is essentially the number of π-rotations that could be driven within the timescale at which decoherence by scattering occurs, if other decoherence sources are neglected. Similar data was taken on the orthogonal Raman transition, where it can be seen that the data is not described by Eq. 4.33. The Rabi frequency was measured for Doppler cooled ion, such that it is decreased by thermal effects. This decrease however is much smaller than the measured one, which can only be explained by a strong effective frequency modulation due to a residual RF component along the trap axis. This strong component has indeed been confirmed by a long range spectroscopy measurement in a much older version of the setup where 270 MHz long-range AOMs have been used. RF-echoes at the one- and twofold trap drive frequency have been found in the spectrum which were not significantly weaker than than the carrier peak. This indicates a large modulation index, consistent with the data in Fig. 4.25. The RF field expected to occur at the ions position due to the taper electrodes is by far too small to account for that effect, see Sec. 5.7. It is therefore concluded that unbalanced RF-pickup on the DC-electrodes is responsible for the strong modulation. However, it will be shown that the basic suitability of the trap for quantum logic is still given, see especially the measurement results in chapter 8.

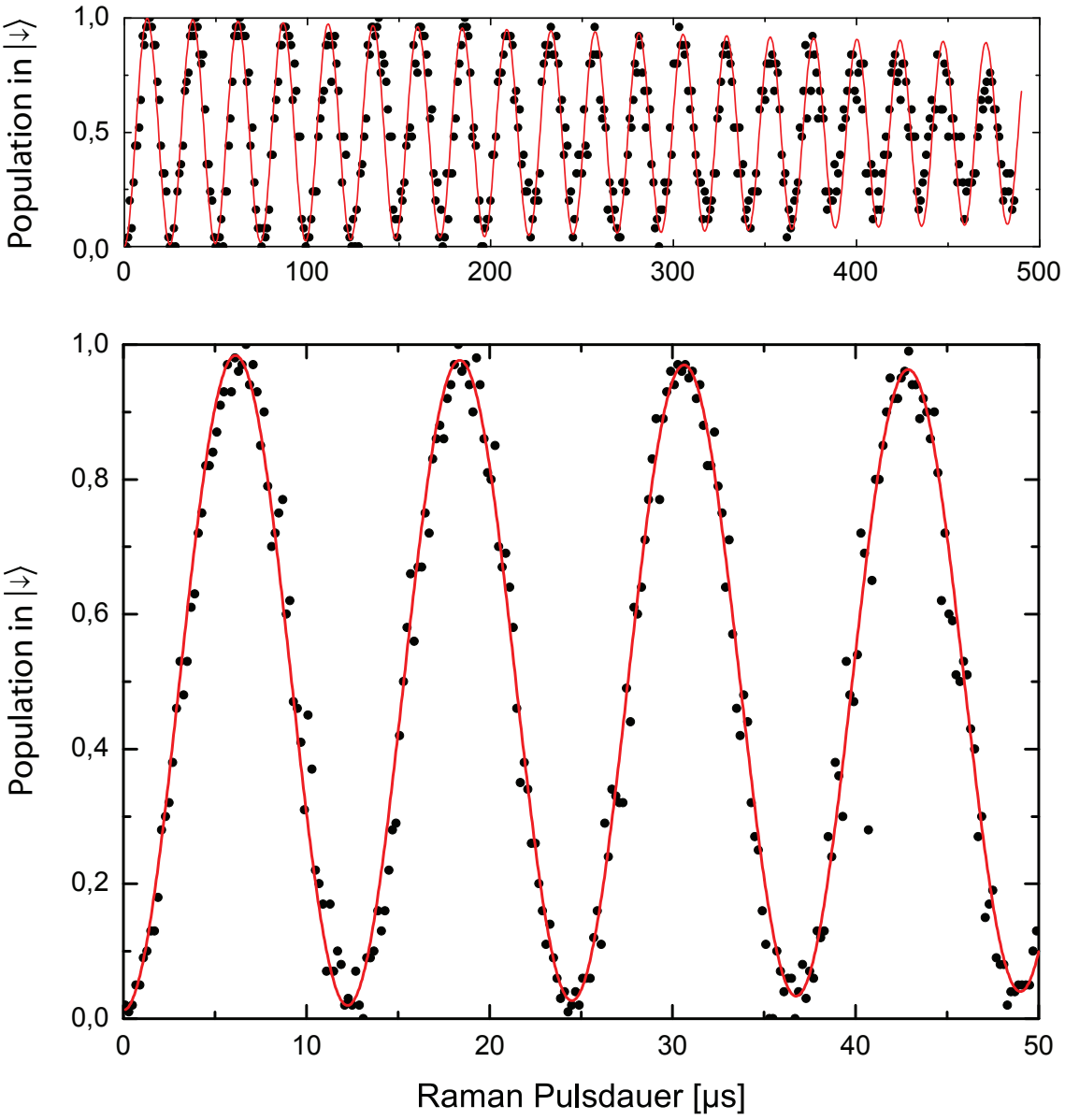

Figure 4.24.: Coherent dynamics on the collinear Raman transition: Single qubit rotations driven by the collinear R1/CC beam pair. The upper trace shows that 20 consecutive 2π rotations can be driven while the contrast stays at a considerable level. The lower trace shows four oscillation periods taken with 200 shots per data point, it is found the noise is within the projection noise limit and the fidelity of the single qubit rotations is 99.6%, mostly limited by the preparation and readout(shelving) steps.

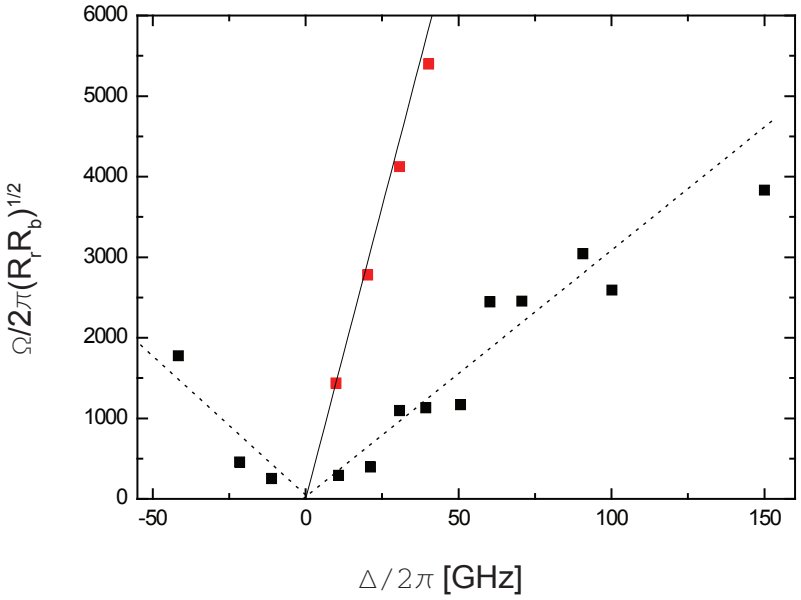

Figure 4.25.: Coherent versus incoherent effects on the Raman transition: The Raman Rabi frequency divided by the geometric mean of the scattering rates for the two driving beams is plotted versus the Raman detuning. The red squares are values for the collinear transition, whereas the black squares are values for the orthogonal transition. The solid black line is the theoretically expected behavior determined by the excited state lifetime. The dashed line is introduced to guide the eye, one clearly recognizes that the Rabi frequency for the orthogonal transition is strongly reduced with respect to the expected one.

4.6. Sideband Cooling and Phonon Distribution Measurements

This section describes diagnostics and manipulation of the ion temperature. We give a detailed account on how the axial mode of vibration can be cooled close to the ground state and on how temperature diagnostics on the few-phonon level is possible.

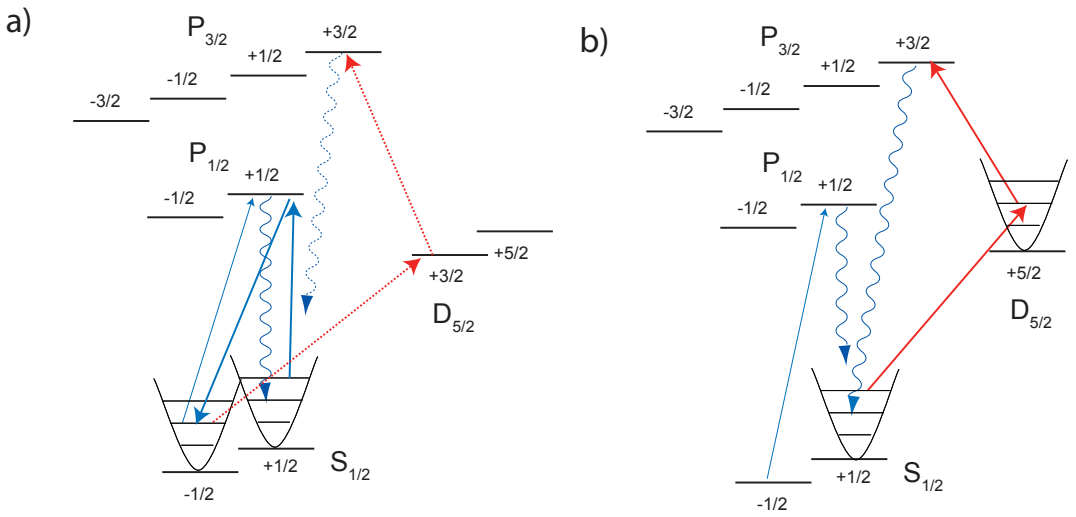

Figure 4.26.: Two different schemes for sideband cooling: **a)** shows the excitation and decay pathways for a Raman cooling cycles, whereas the cycle for the quadrupole cooling scheme is depicted in **b)**. The dashed arrows in a) indicate the alternative quadrupole repumping pathway. Both schemes have their advantages and drawbacks, see text.

Cooling close to the ground state of at least one vibrational mode is an essential prerequisite for two-ions gates, as even gate schemes for 'hot' ions require operation in the Lamb-Dicke regime $\eta\sqrt{n} \ll 1$ [Lei03b]. For cooling close to the ground state one has to resort to a narrow transition with resolved motional sidebands [Mar94], such that transitions to states with one less phonon (red sideband, RSB) can be driven preferentially and the $n = 0$ state acts as a dark state in which the population is finally trapped. In our system, we have two options to spectroscopically resolve sidebands, either the R1/R2 Raman transition or the quadrupole transition. We have successfully carried out sideband cooling on both of these transitions, the cycling pathways are depicted in Fig. 4.26. For the Raman sideband cooling, the red sideband of the Raman transition from $|\uparrow, n\rangle$ to $|\downarrow, n-1\rangle$ is driven, and the dissipative repumping step is carried out by employing the circularly polarized laser beam at 397 nm. By contrast, in the quadrupole pumping scheme, the red sideband of the $|\uparrow\rangle$ to $|D_{5/2}, m_J = +5/2\rangle$ transition is driven and the repumping is done by simply quenching the metastable state by irradiation

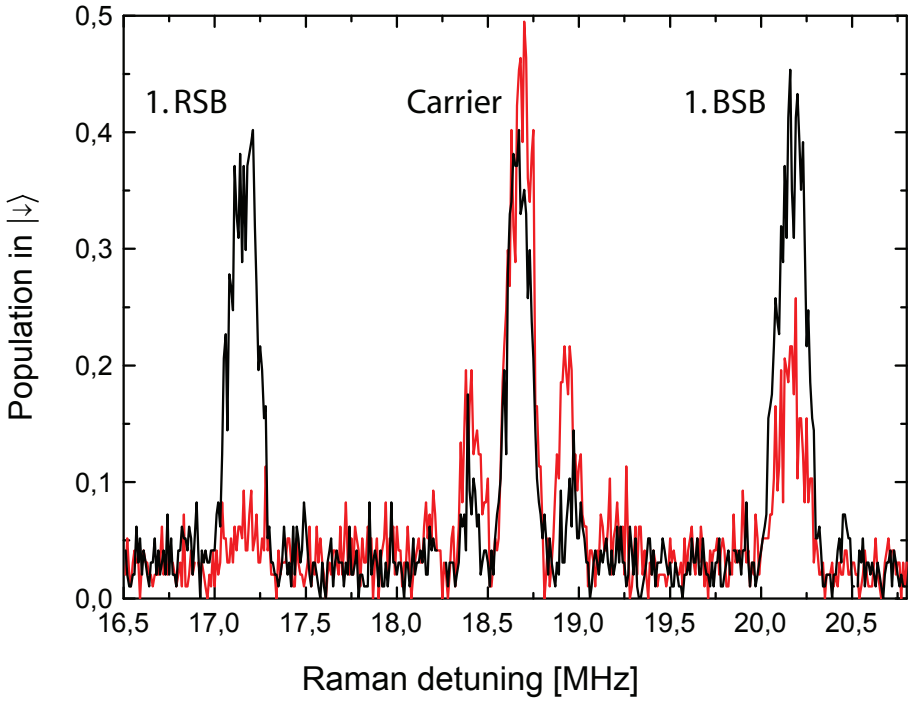

Figure 4.27.: Raman spectra with and without Raman sideband cooling: The plot shows spectra on the orthogonal Raman transition driven by the R1/R2 beam pair. A spectrum with (red) and without (black) applied sideband cooling is shown, note the almost vanishing red sideband and the enhanced coherent satellite peaks around the carrier for the cooled case.

at 854 nm.
As the cooling always competes with the heating rate from trap induced electric field noise, a high cooling rate is essential for a good cooling result. A priori, the Raman transition seems to be better suited for cooling because of the higher ratio of RSB to carrier Rabi frequency, which is essentially given by η on the decisive 'bottleneck' step from $n = 1$ to $n = 0$. However, the main problem arises in the dissipative step of cooling where the ion is repumped to the initial state to restart the red sideband excitation. In the case of the Raman cooling scheme, the repumping is accomplished by the circular 397 nm beam which suffers from the spurious polarization error discussed extensively in Sect. 4.2.4. Therefore the dark state $n = 0$ is not completely dark anymore, leading to a competing Doppler re-heating process which limits the attainable ground state purity.
In contrast, the sideband cooling on the $|\uparrow\rangle$ to $|D_{5/2}, m_J = +5/2\rangle$ quadrupole transition does not suffer from this because the repumping is achieved by the quench laser near 854 nm, which does not interact with the ion anymore once one photon has been spontaneously scattered. The cooling cycle is almost closed, because the decay from the $P_{3/2}$ state during the

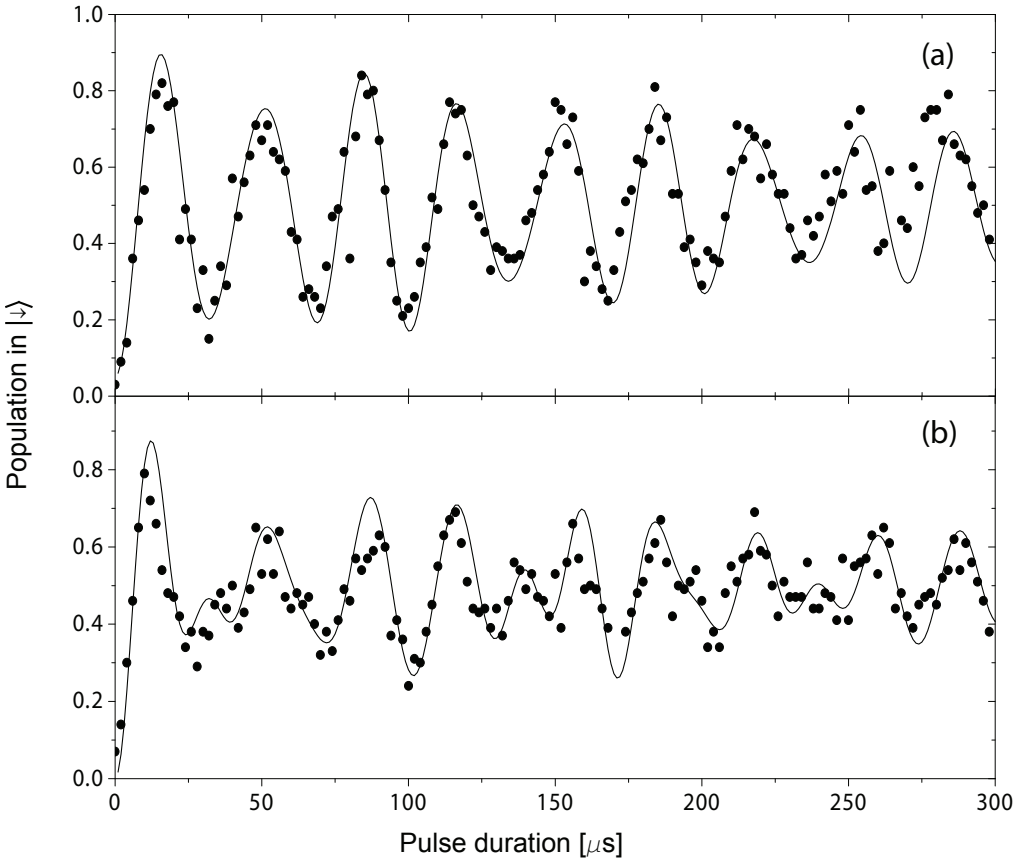

Figure 4.28.: Coherent dynamics on the R1/R2 BSB after sideband cooling. The graphs show the population in the $|\downarrow\rangle$ level versus pulse duration of a square Raman excitation pulse **a)** directly after sideband cooling and **b)** after a delay of 3 ms. The data were obtained with a Raman detuning of $\Delta \approx 40$ GHz. The solid lines are reconstructed from the extracted phonon distribution data with inclusion of a coherence decay time of 280 mus. We extract a mean phonon number of 0.24 for the data set without waiting time.

quench leads preferentially to the $|\uparrow\rangle$ level due to the selection rules. Only unlikely decay events into one of the D-states can lead to population of the $|\Downarrow\rangle$ level. We utilize a pulsed sideband cooling scheme, since as for the qubit initialization, the power and frequency of the quench laser are no longer critical parameters then. The cooling pulse time is set such that an excitation maximum is reached on the RSB. This time ranges typically between 10 μs and 20 μs, and increases as lower phonon numbers are reached because the RSB Rabi frequency scales as $\eta_{\mathrm{ax}}\sqrt{n}$ with the phonon number n. After the RSB pulse, a quench pulse of typically 2 μs completes the cooling cycle. After ten cooling cycles, about 10% of the population is accumulated in the wrong ground state spin level, such that a 397 nm repump pulse has to

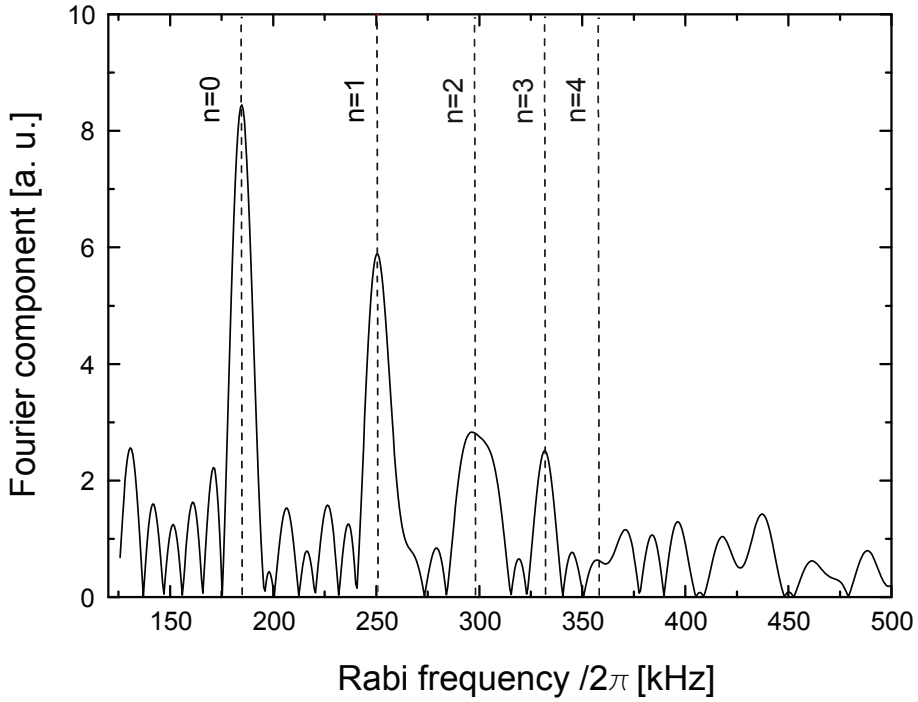

Figure 4.29.: Cosine transform of a R1/R2 pulse width scan on the BSB after a 3 ms delay between cooling and probing. The dashed lines indicate the different flopping frequencies given by the matrix element for the given transition.

be employed. After eight such sequences, we employ a second cooling stage where the RSB pulse duration is increased and the 729 nm optical pumping procedure is used instead of the circular 397 nm pulses. The longer time for repumping has no adverse effect on the cooling rate because it is used only every ten cycles.
We confirm the sideband cooling result by employing either the quadrupole transition or the R1/R2 Raman transition. The optimization of the cooling is performed by minimizing the peak excitation of the RSB of the quadrupole transition, which is essentially given by the probability of not finding the ion in the ground state. For more accurate determination of the phonon number distribution we employ Raman Rabi oscillations on the R1/R2 BSB, with the advantage that no contributions from the radial vibrational modes can influence the result, and on the other hand the larger Lamb-Dicke factor of the Raman transition leads to a better separation of the Rabi frequencies for the various $n \rightarrow n+1$ transitions. Excitation data are acquired until the oscillation contrast of the excitation signal has decreased beyond the projection noise limit for long pulse widths, see Fig. 4.28. The recorded traces are analyzed by cosine transform to obtain the frequency components for the different contributing transitions, in full analogy to experiments on the cavity QED realization of the Jaynes-Cummings

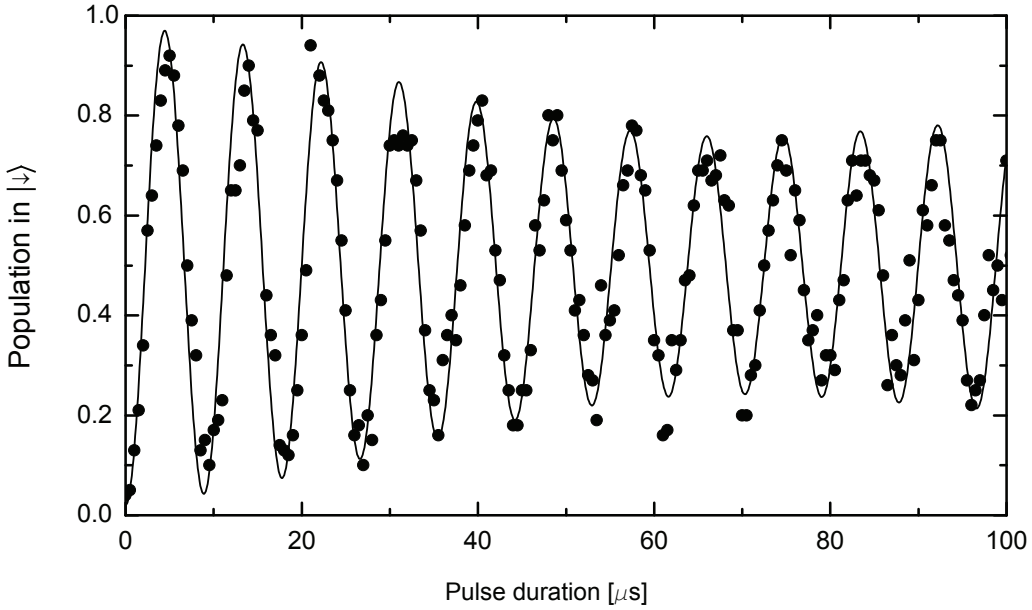

Figure 4.30.: Coherent dynamics on the R1/R2 carrier transition after sideband cooling. The graph shows the population in the $|\downarrow\rangle$ level versus pulse duration of a square Raman excitation pulse directly after sideband cooling. The mean phonon number of 0.24 inferred from the BSB Rabi oscillations is used for fitting the data.

model [Bru96] [1].
A resulting spectrum is shown in Fig. 4.29. Upon proper normalization, the peak heights directly correspond to the occupation probabilities for the different phonon numbers. This data can then be used to reconstruct the coherent dynamics, allowing for the empirical inclusion of a coherence decay time [Mee96]. This is done according to

$$P_{\downarrow}(t) = \sum_n \frac{P_n}{2}(A\ \cos(\Omega_{n,n+1}\ t)\ e^{-\gamma\ t} + 1), \tag{4.34}$$

where $P_{\downarrow}(t)$ is the probability for finding the ion in $|\downarrow\rangle$, P_n is the phonon number distribution, $\Omega_{n,n+1}$ is the Rabi frequency pertaining the specific BSB transition, A is the read-out contrast of 96% and γ is the coherence decay rate. The coherence time $1/\gamma$ is found to be 280(20) μs. As Ramsey contrast measurements on the R1/CC transition yielded a much

[1] Due to the finite data acquisition time, the peaks in the cosine transform pertaining to a given transition frequency are accompanied by aliases at other frequencies which lead to systematic errors when the phonon number occupation probability is inferred directly from the peak heights. A deconvolution procedure was used to remove this effect. The correctness of the method is proven by the fact that the method yields the correct input phonon number distribution when Monte-Carlo generated data with realistic parameters is used. The resulting accuracy is then limited by the read-out projection noise of the pulse width scan data.

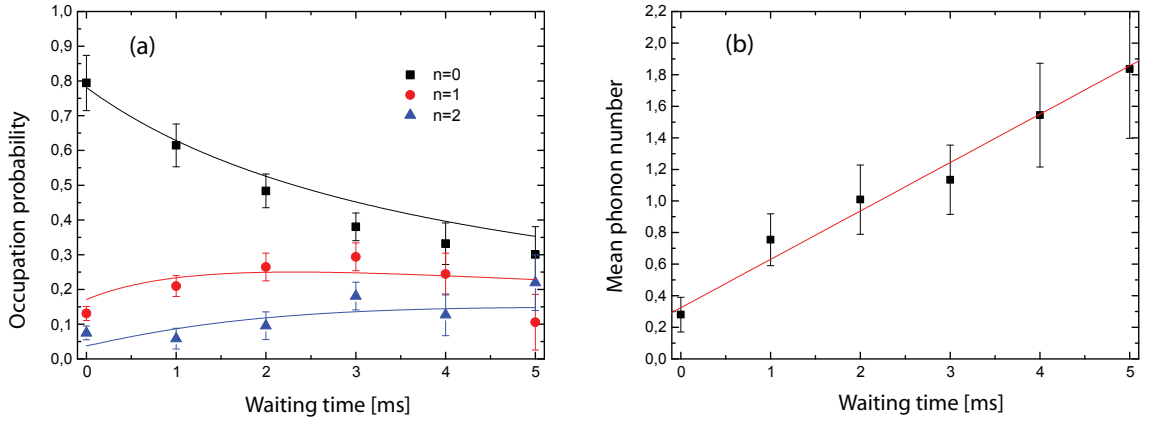

Figure 4.31.: Results of the heating rate measurement: **a)** Occupation probabilities P_n for the lowest vibrational levels $n \leq 2$, extracted from frequency spectra of the BSB pulse width scans (see Fig. 4.29) after different waiting times. For comparison, the solid lines show the occupation probabilities given by a thermal distribution $p(n) = \bar{n}^n/(\bar{n}+1)^{n+1}$, where $\bar{n}(t)$ is given by a linear fit through the mean phonon numbers calculated from the data. **b)** Mean occupation number $\bar{n}$ calculated from P_n at different times after cooling. The linear fit indicates a constant heating rate of $\dot{n} = (0.3 \pm 0.1)/\text{ms}$.

longer coherence time, the additional decoherence either stems from pulse area fluctuations or a reduced interferometric stability in the R1/R2 beam setup with respect to the R1/CC geometry. The phonon distribution is reconstructed for various waiting times after sideband cooling in order to reveal the trap induced heating dynamics. The time dependent phonon number distribution is shown in Fig. 4.31, along with the resulting mean phonon number. This directly gives the heating rate to be 0.3(1) phonons/ms[2].
The corresponding Rabi oscillations on the carrier of the R1/R2 Raman transition are shown in Fig. 4.30. Taking the phonon numbers after sideband cooling inferred from the BSB Rabi oscillations, we find excellent agreement with the measurements made on the carrier transition.

The cooling results presented in this chapter were obtained with the quadrupole cooling scheme, however at a later evolution state of the setup we have also successfully implemented Raman cooling with comparable and even better final temperatures. The results presented in chapter 8 were obtained based on Raman sideband cooling. The final temperature could be reduced such that the ground state purity does not deviate from 100% within the measurement accuracy, any effect of remaining population in e.g. n=1 would be overshadowed by decoherence effects in the interaction with the lasers driving the blue sideband Rabi oscillations when the motional state is read out. The improvement was mainly achieved by

[2]This is about one order of magnitude better than earlier findings of 2.13 phonons/ms [Sch08], which is attributed to an improved trap voltage supply.

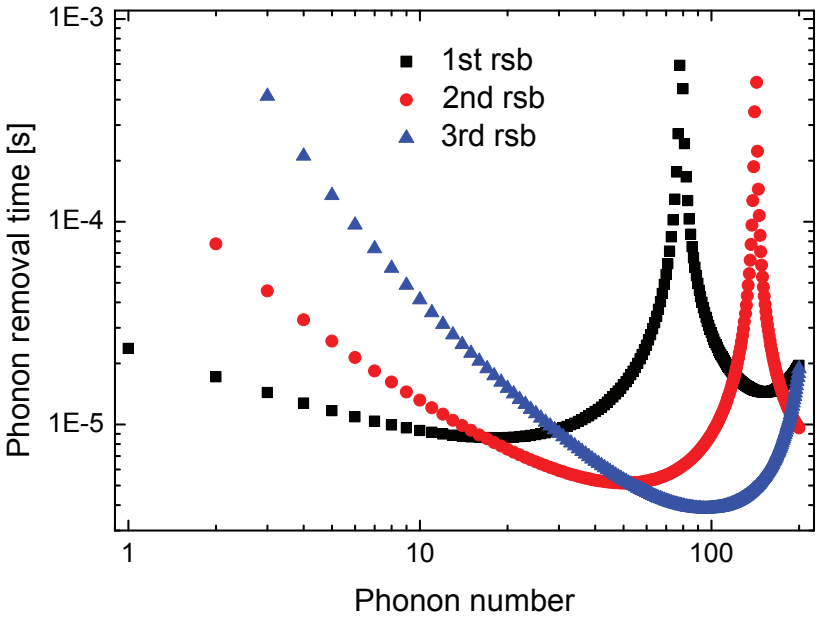

Figure 4.32.: Calculated phonon removal times for different red sideband transitions: The efficiency of the higher order cooling method is illustrated by visualizing the π-times on the red sidebands ($\eta \approx 0.21$ was assumed here) up to third order, divided by the sideband number. This gives an estimation of the time it takes on average to remove one phonon, not even including the time for the repump step which would render the higher order sidebands even more efficient as one single repump step can remove more than one phonon. Note that the plot is double-logarithmic. One recognizes that the second-order sideband becomes by far more efficient for more than 20 phonons, whereas beyond 60 phonon the third sideband takes over.

careful alignment and power adjustment of the repump beam at 397 nm. According to the results of Sec. 4.2.4 for the pumping fidelity, a ground state purity of 98.5% is to be expected if the repump step is the most pronounced bottleneck. To achieve even higher ground state purities, one could resort to employing the pumping at the quadrupole transition in an additional final stage of the cooling, as it is indicated in Fig. 4.26 a). In order to implement this scheme , one has to take care that the quench laser at 854 nm is π-polarized such that only the $\Delta m_J = 0$-transition from $|D_{5/2}, m_J = +3/2\rangle$ to $|P_{3/2}, m_J = +3/2\rangle$ are driven and only decay back to $|\uparrow\rangle$ can take place. If ideal repumping was realized, two processes limit the attainable ground state purity: a) off-resonant excitation of the carrier transition when the red sideband is driven with subsequent decay on the blue sideband, and b) off-resonant excitation of the blue sideband while the red sideband is driven with subsequent decay on the carrier. These processes both are of higher order and the expected impurities are so small that they can on the one hand not be measured in our setting, on the other hand our

experiment does not require complete ground state purity as we do not want to work with gate schemes as the Cirac-Zoller gate [Cir95],[SK03b]. Furthermore, with the heating rate of 0.3 phonons/ms, the ion would stay in the ground for only about 300 μs anyway. An extensive discussion of these limiting effects can be found in Ref. [Sta04].
The main advantage of the Raman cooling scheme is given by the much larger Lamb-Dicke factor, which is about 3..4 times larger than for the quadrupole transition and allows for driving the red sideband 2..3 times as fast, depending of course on the available powers and the used Raman detuning. If one resorts to higher m-th order sideband, the advantage becomes even more clear: Fig. 4.32 shows the average removal time for a single phonon on the first three sidebands, i.e.

$$\frac{\tau_\pi^{\mathrm{rsb}}}{m} = \frac{\pi}{m\ M_{n,n-m}\Omega_0}, \tag{4.35}$$

versus the phonon number n for an assumed bare Rabi frequency of Ω_0=2π·100 kHz. Division of the π-time by m is done because on the m-th sideband, of course m phonons will be removed in a single excitation step. In a sequential cooling scheme, one performs cooling on e.g. the third motional sideband, which becomes ineffective for the assumed parameters if no population beyond n≈60 is left. One then switches over to the second sideband, which is more efficient than the first sideband above n≈20. The remaining phonons can then be removed on the first red sideband. This is especially effective if hot tail from thermal phonon distributions with large $\bar{n}$ are to be cooled away, which turned out to be the case for two-ion crystals, see Sec. 9.3.

4.7. Coherence and Decoherence of the Spin Qubit

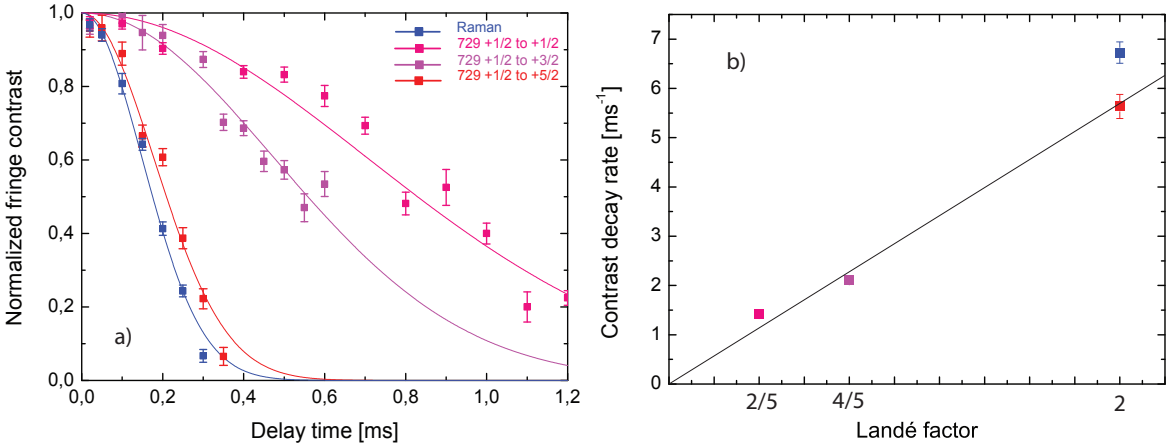

Figure 4.33.: T_2^* measurement on various transitions: **a)** Contrast measurement results from a Ramsey sequence for various transitions. As no unity initial contrast can be achieved in the quadrupole transitions due to the inability to drive perfect Rabi oscillations, the contrasts are normalized to the initial one. **b)** Inverse T_2^* time versus Landé factor of the respective transition. One can clearly infer a linear scaling, only the decoherence rate for the Raman transition is slightly increased.

In this section, we investigate the coherence time of the $^{40}Ca^+$ qubit in our experiment, i.e. the timescale on which the phase information stored if the qubit is in a superposition state between $|\downarrow\rangle$ and $|\uparrow\rangle$ is destroyed by uncontrolled interactions with the environment. We specify first on the investigation of 'bare' decoherence, i.e. the loss of phase information when no additional manipulations on the qubit are performed. The appropriate tool to do this is a Ramsey-type measurement [Ram86], where a superposition state is created by means of a resonant $\pi/2$-pulse before the qubit is exposed to a fixed waiting time. A second $\pi/2$-pulse then maps the phase ϕ of the qubit onto the final populations $P_\downarrow$ and $P_\uparrow$. This phase is comprised of the phase $\phi_0 = \delta t$ that was picked up during the free evolution if one is slight off-resonant by δ and the relative optical phase of the second pulse with respect to the first on $\Delta\phi$: $\phi = \phi_0 + \Delta\phi$. Upon repetition of the measurement while $\Delta\phi$ is scanned, one thus obtains information about δ, which offers an ultimately precise coherent spectroscopy method used for atomic clocks, and via the resulting contrast also the magnitude of the diagonal elements of the density matrix indicating the amount of coherence is revealed. It is straightforward to determine the resulting populations if we assume the ion was initialized in $|\uparrow\rangle$ the density matrix of the two-level system immediately before the concluding $\pi/2$-pulse is given by $\hat{\rho}$:

$$P_\uparrow = \frac{1}{2}\left(1 + 2|\rho_{12}|\cos(\phi)\right), \tag{4.36}$$

with $|\rho_{12}| \leq 1/2$, the resulting contrast of the measurement directly yields the coherence loss. If now the coherence loss is measured versus the free evolution time, the decoherence process is made visible. A compilation of such measurement results is shown in Fig. 4.33, where the measurement was performed on the orthogonal Raman transition and three subtransitions of the quadrupole transition. The coherence decays with a Gaussian behavior, where the timescale is called T_2^* time in contrast to the T_1 time at which population decay would occur. As the decoherence rate scales linearly with the Landé factor describing the linear coefficient of the Zeeman shift for the corresponding transition, it can be concluded that ambient magnetic field fluctuations are the main decoherence source in this regime.

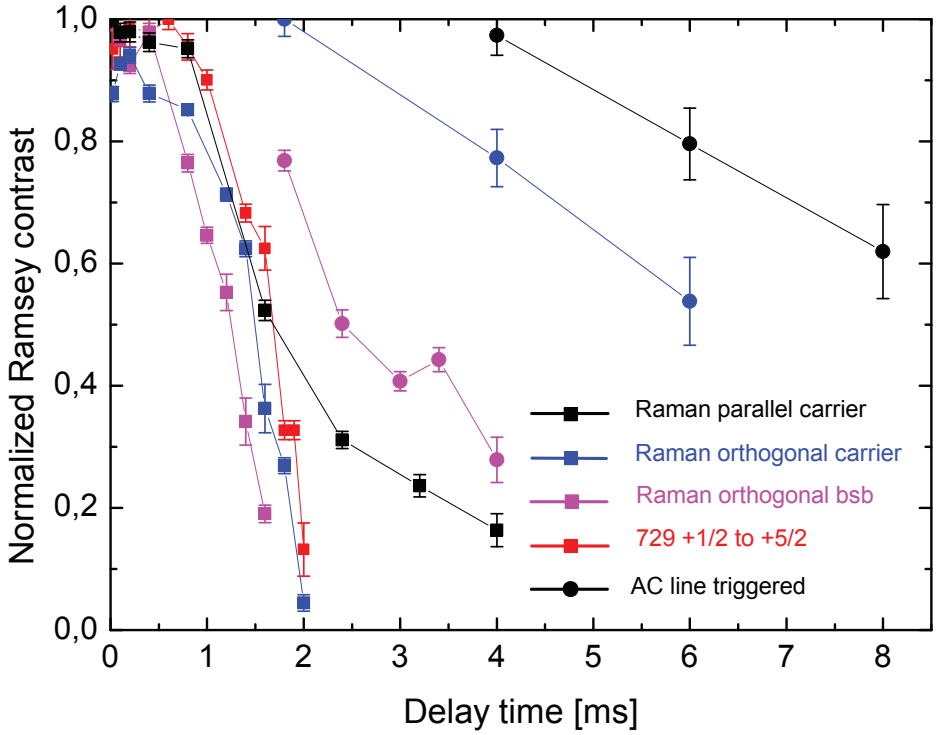

Figure 4.34.: T_2 measurement on various transitions: Results for spin-echo contrast measurement on various transitions. Note the strong increase of the coherence times if triggering on the AC-line is used.

The most tremendous source of the coherence loss is given by the low-frequency components of the magnetic field fluctuations. This can be understood by the fact that if we consider an additional magnetic field fluctuating at a period much shorter than the delay time of the Ramsey experiment, its effect will mostly average out, analogous to phase modulation where the modulation index scales with the inverse modulation frequency. By contrast, if the oscillation period is longer than the delay time, the effect can be reverted by means of the famous spin-echo technique originally conceived for NMR experiments. One simply

utilizes a π-pulse to swap the spin components in the middle of the delay time, such that any phase offset due to a static energy shift is simply reverted. This leads to much longer effective coherence times, corresponding measurement results are shown in Fig. 4.34. The timescale $T_2 \geq T_2^*$ obtained this way is of the key parameter describing the quality of a quantum memory, of course it is only meaningful in relation to the timescale at which coherent manipulations can be carried out. We performed this measurement also on different Raman transitions, namely the collinear, the orthogonal carrier and the orthogonal blue sideband transitions. The contrast decay on the orthogonal Raman transitions is additionally increased by the heating rate. Furthermore, data sets were taken where AC-line triggering was used in addition the spin-echo technique, which leads to an even more pronounced increase in coherence time. This is due to the fact that upon carrying out the experiment at a definite phase to the AC mains, the most part of the offset magnetic field behaves in the same way for each experimental run, leading to a more defined phase pick-up.
Now that the timescales and mechanisms for the bare decoherence have been investigated in detail, we shall focus our attention to laser induced decoherence processes. If we restrict the treatment to the interaction with a single off-resonant laser beam, the two processes occurring are dephasing due to intensity fluctuations in the presence of an unbalanced Stark shift and off-resonant scattering. The relevant physical parameters thus are the detuning of the laser from resonance, its polarization and its intensity noise spectrum.

We briefly derive how the spin decoherence due to intensity fluctuations is related to the power spectrum of the fluctuations. The Hamiltonian for the dispersive interaction of the effective two-level system with the off-resonant beam is simply given by $\hat{H}_{AC}(t) = \hbar\Delta_{AC}(t)\hat{\sigma}_z$. The corresponding unitary evolution operator is

$$\hat{U}_{AC}(t,0) = e^{i\Phi_{AC}(t)\hat{\sigma}_z/2} \tag{4.37}$$

with the accumulated Stark phase

$$\Phi_{AC}(t) = \int_0^t dt' \Delta_{AC}(t'). \tag{4.38}$$

The noisy character of $\Delta_{ACS}(t)$ is modeled by expanding it in a Fourier series:

$$\Delta_{AC}(t) = \sum_{n=-\infty}^{+\infty} \Delta_{AC}^n(t) = \sum_{n=-\infty}^{+\infty} p_n \ \cos(2\pi nt/T + \phi_n) \tag{4.39}$$

where T is much larger than the experimental time scale considered and every measurement result is to be averaged over all randomly distributed phases ϕ_n. The quantity of interest is the spin coherence

$$\begin{aligned} C(t) &= \langle e^{i\Phi_{AC}(t)} \rangle_{av} \\ &= \prod_{n=-\infty}^{+\infty} \left(\frac{1}{2\pi} \int_0^{2\pi} d\phi_n \right) \exp\left(i \sum_{m=-\infty}^{+\infty} \Phi_{AC}^{(m)}(t) \right) \\ &= \prod_{n=-\infty}^{+\infty} \left(\frac{1}{2\pi} \int_0^{2\pi} d\phi_n \right) \prod_{m=-\infty}^{+\infty} \exp\left(i\Phi_{AC}^{(m)}(t) \right) \end{aligned} \tag{4.40}$$

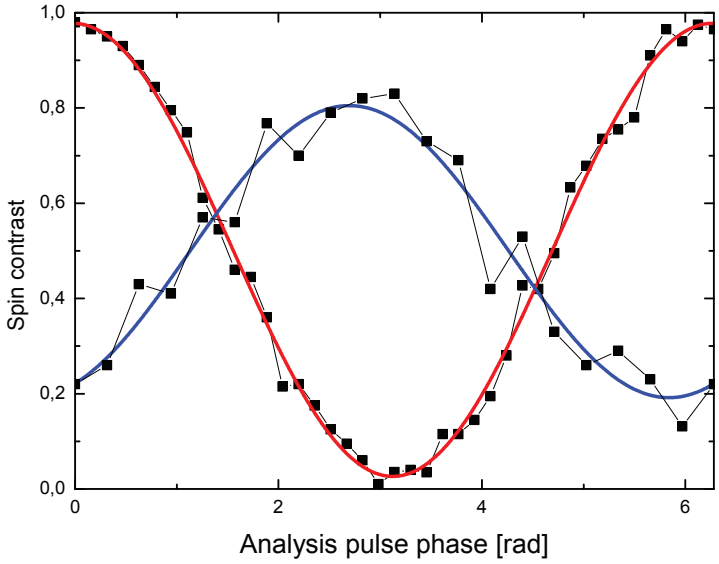

Figure 4.35.: Sample results from the spin echo contrast measurement: Resulting Ramsey fringes from scanning the duration of the shift pulse for the maximum Stark shift of $\Delta_0 \approx 2\pi \cdot 620$ kHz. The red curve pertains to a measurement without decohering pulse, and the blue curve pertains to a decohering pulse of 7 μs. The solid curves show the fit result to the model $p_\uparrow(t) = ae^{-\gamma\ t}\sin(\Delta_0 t + \phi) + b$.

where the solution of the integral from Eq. 4.38 for a single expansion term

$$\Phi_{AC}^{(m)}(t) = \frac{p_m T}{2\pi m}\cos\left(\frac{m\pi t}{T} + \phi_m\right)\sin\left(\frac{m\pi t}{T}\right) \tag{4.41}$$

is used. With

$$\frac{1}{2\pi}\int_0^{2\pi} d\phi_n \exp(i\Phi_{AC}^{(n)}(t)) = J_0\left(\frac{p_n \pi T}{n\pi}\sin\left(\frac{m\pi t}{T}\right)\right) \tag{4.42}$$

where

$$x_n = \frac{p_n}{2\pi n}, \tag{4.43}$$

we finally obtain for that the spin contrast is given by a product integral:

$$C(t) = \lim_{\substack{T\to\infty \\ N\to\infty}} \prod_{n=1}^{N} J_0\left(\frac{p_n \pi T}{n\pi}\sin\left(\frac{m\pi t}{T}\right)\right)^2 \tag{4.44}$$

The product is evaluated numerically for finite N, T and convergence for sufficiently large values is assured. It is found that the behavior of $C(t)$ now depends on the scaling of p_n.

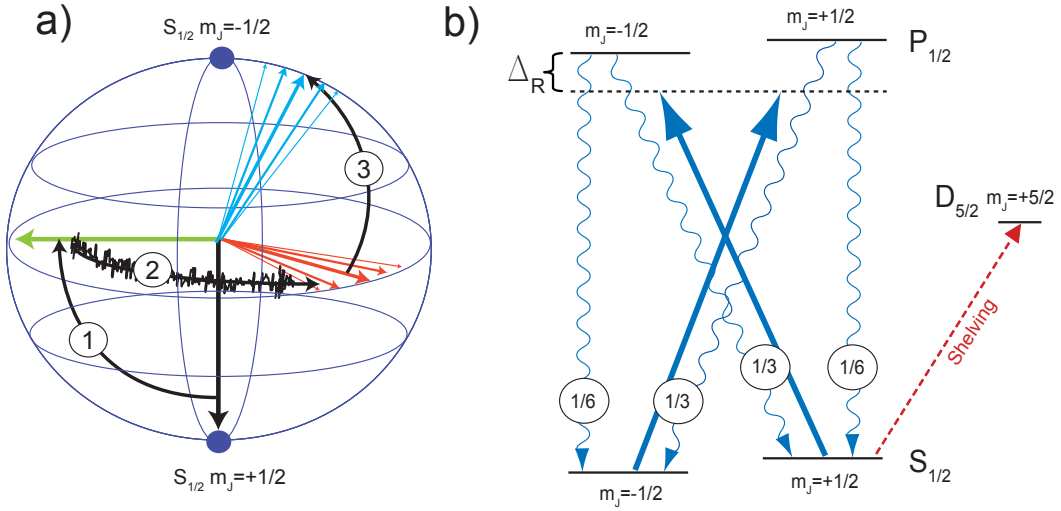

Figure 4.36.: **a)** Illustration of spin diffusion on the equator of the two-level system's Bloch sphere. Note that one is not dealing with shot-to-shot fluctuations on slow timescales which could be undone by employing spin echo techniques. **b)**Relevant energy levels and transitions of $^{40}Ca^{+}$. All relevant excitation and spontaneous decay pathways are shown for the $S_{1/2}$ - $P_{1/2}$ transition. The squared Clebsch-Gordan coefficients are indicated on the different transitions. The shelving to the metastable $D_{5/2}$ state is indicated to the right.

Under the assumption of white noise, $p_n = const.$, the noise correlation time vanishes and $C(t)$ displays an exponential coherence decay. Under the more realistic assumption of 1/f noise, $p_n = \Delta_0 \; p_0/n^{1/2}$, the nonvanishing autocorrelation can by modeled by a Gaussian decay:

$$C(t) = \exp\left(-\frac{t^2}{2\tau^2}\right) \tag{4.45}$$

with

$$\tau \propto \frac{1}{\Delta_0} \tag{4.46}$$

This scaling relationship is empirically tested to be invariant against the detailed structure of the noise spectrum, the only necessary condition for it to hold is that the noise is band limited.
Additionally to the Gaussian decay caused by the intensity fluctuations, spontaneous photon scattering from the off-resonant beam also leads to exponential decoherence, see Eq. A.16. The total coherence decay can then be modeled by

$$C(t) = \exp\left(-\frac{t}{\tau_1(\Delta_0)} - \frac{t^2}{2\tau_2^2(\Delta_0)}\right) \tag{4.47}$$

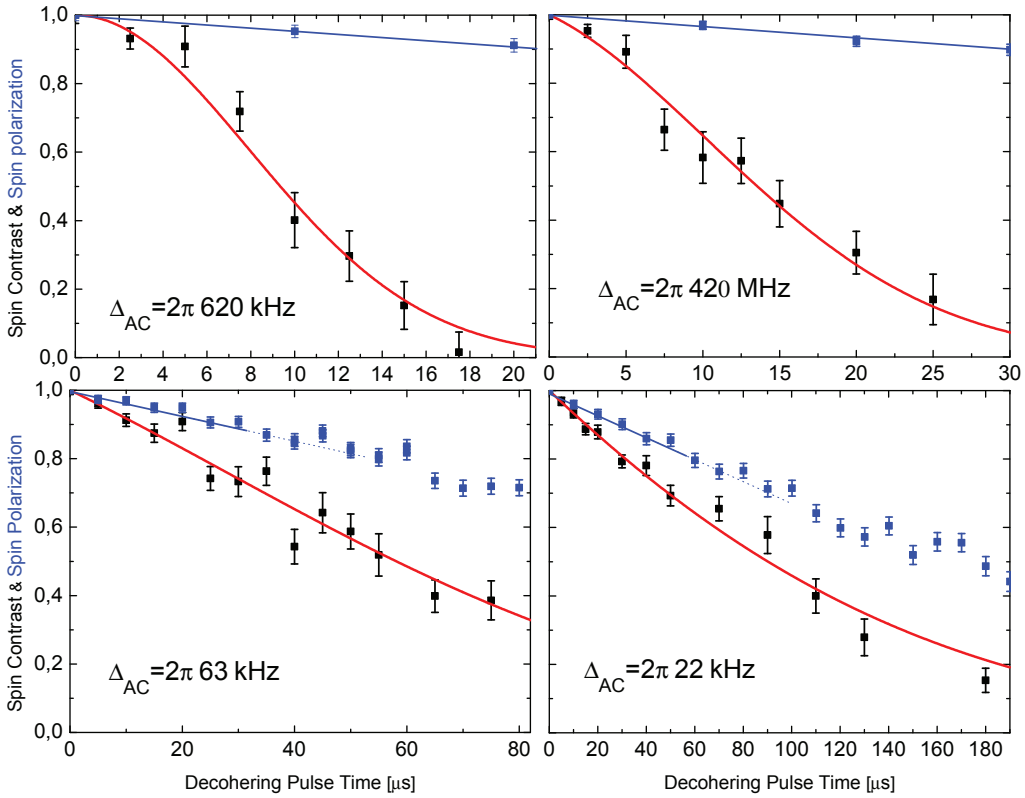

Figure 4.37.: Spin-echo contrast versus decohering pulse time for the various data sets pertaining to different Stark shifts (black squares). Both spin polarization and contrast are normalized to the values for zero decohering pulse time. The solid curves are fits to the model Eq. 4.47. The blue squares are the results of the scattering rate measurements. Note the different timescales.

Datasets charactering the decoherence process were taken for various differential Stark shifts. The Stark shift is tuned by adjusting a quarter waveplate in the decohering beam, which is the R2 beam propagating in parallel to the quantizing field. For each setting of the waveplate, we measured the magnitude of the Stark shift caused by the imbalance of the circular polarization components, the Raman spin-flip rate and the coherence decay for various decohering pulse times. The Stark shift Δ_S is measured by employing a spin-echo sequence, where a phase shift pulse with varying duration is inserted between the first $\pi/2$ pulse and the π pulse. The induced phase shift leads to an oscillating spin polarization upon read-out after the concluding $\pi/2$ pulse, where the oscillation frequency directly gives the differential shift with an accuracy of better than 2%. The spin-flip rate caused by Raman scattering is then characterized by simply imposing the ion to a scattering pulse of varying

duration. The fraction of population remaining in the initial $|\uparrow\rangle$ state versus the scatter pulse time then yields the scattering rate by simply considering the slope at $t = 0$. The spin-flip behavior is indicated in Figs. 4.37.

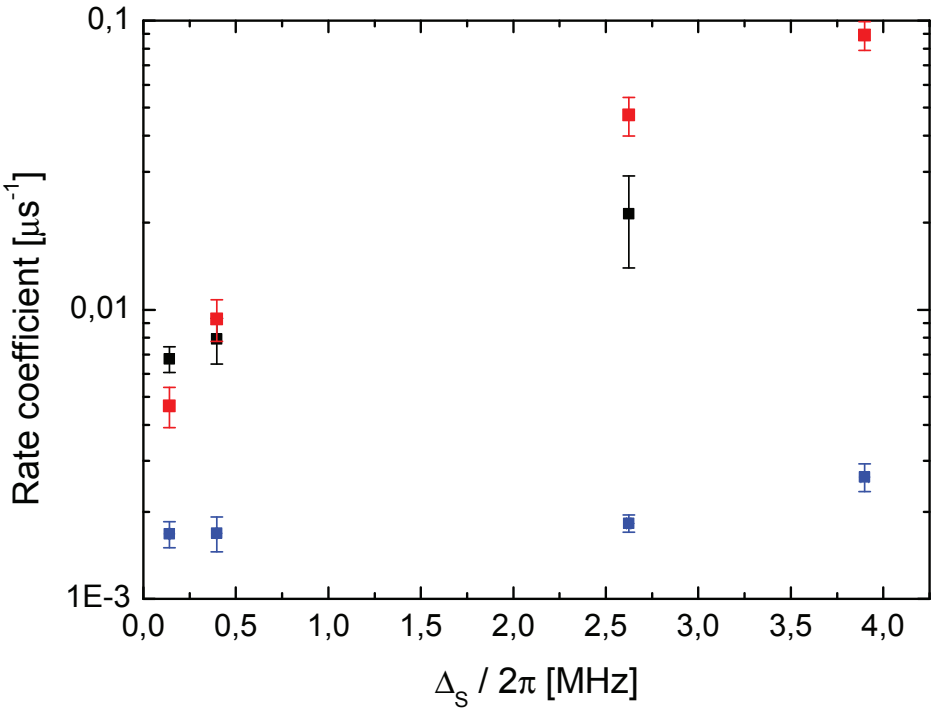

Figure 4.38.: Resulting decoherence rate coefficients for exponential (black squares) and Gaussian (red diamonds) decoherence from Eq. 4.47 and spin depolarization timescale (blue dots) versus the measured Stark shift.

The coherence decay is measured by means of the following procedure: For various fixed decohering pulse times, the spin echo sequence for the measurement of the Stark shift is applied where the phase of the concluding analysis pulse is scanned from 0 to 2π radians. Without perturbations and assuming ideal preparation and read-out, this resulting spin population signal is given by the cosine of the analysis phase. As the decohering pulses shift the mean superposition phase by $\Delta\phi = \Delta_S t$ and the contrast is reduced, the signal is fitted to a cosine with floating contrast and phase. Due to a possible slightly asymmetric read-out and preparation fidelity, a floating baseline is taken into account as well. The fringe amplitude directly corresponds to the magnitude of the spin density matrix off-diagonal elements. Example spin-echo measurements are shown in Fig. 4.35. The resulting contrast versus decohering pulse time is shown in Fig. 4.37. The crossover from exponential to Gaussian decoherence behavior can be clearly seen from these curves. In order to quantify this, the model from Eq. 4.47 is fitted to these curves and the coefficients τ_1, τ_2 are extracted. In Fig. 4.38, these are plotted versus the corresponding Stark shift. For the data point pertaining to

the maximum Stark shift, the Gaussian coherence decay is completely dominating such that no valid linear coefficient could be fitted from the data. As the exponential decoherence is caused by Raman scattering, it does not vanish at zero Stark shift, as can be seen clearly from the data. Note the different scaling behavior of the spin depolarization rate and the exponential decay coefficient. Upon increasing the Raman detuning Δ_R and cranking up the laser power to leave Δ_S unaffected, the crossover point between exponential and Gaussian decoherence would be shifted towards smaller Stark shifts, rendering the spin diffusion mechanism more dominant. It is interesting to compare the exponential decoherence rate at vanishing Stark shift to the scattering rate: From the data at the lowest Stark shift, the figure $R_{deph}/R_{1\to 2} = 4.0 \pm 0.58$ is obtained. Comparing this to Eqs. A.14 and A.16, under the consideration that $|\epsilon_+|^2 = |\epsilon_-|^2 = 1/2$, the scattering rate

$$R_{1\to 2} = \frac{1}{2\cdot 3}\frac{\Gamma\Omega^2}{4\Delta^2} \tag{4.48}$$

and the decoherence rate

$$R_{deph} = \frac{1}{2\cdot 3}\frac{\Gamma\Omega^2}{4\Delta^2} \tag{4.49}$$

are obtained, such that the decoherence rate should the threefold scattering rate. If the additional term $\mathcal{L}_{23}$ from Eq. A.19 is additionally considered and the phase shift between the circular components is such that $\epsilon_+\epsilon_-^* = +1/2$, the decoherence rate would be exactly the fourfold scattering rate, which is clearly supported by the experimental data. This would represent an additional, yet unknown decoherence mechanism which is dependent on the phase relation between the + and - circular polarization components. For a linearly polarized beam propagating along the magnetic field axis, this corresponds to a breaking of the cylindrical symmetry of the physical system. Furthermore, the source of the increase of the exponential decoherence rate coefficient with the Stark shift is yet unknown: R_{deph} from Eq. A.16 is independent of the balance of the circular components, and the extra term $\mathcal{L}_{23}$ should be of maximum magnitude for balanced components. A possible explanation is a white noise floor in the power spectrum of the intensity fluctuations, but as the effect is only manifested in a single data point, no thorough claim on this can be supported.

Attempts were made to reduce the decoherence due to intensity fluctuations in the presence of a nonzero Stark shift. This was done by establishing an intensity stabilization by means of the fast switching EOM, which allows for regulation bandwidths of up to 1 MHz and larger. However, no effect on the coherence time could be seen between measurements where the intensity stabilization was switched on or off. Furthermore, a common observation while measuring either Stark shifts or Rabi oscillations (even with nulled Stark shift) is that for longer pulse times the oscillatory patterns become distorted and even spiky. This raised the suspect that not direct laser intensity noise is responsible for the observed strong decoherence, but rather the localization of the ion in the Raman beams is subject to drifts at a second timescale. It was therefore checked if the readout values indeed obey to the statistical error given by Eq. 4.3. This was done by means of a repeated ac stark shift measurement with only the R2 beam involved to exclude other error sources. The results are shown in Fig. 4.39, where the measurement was performed for two different ac stark shifts, and each curve was

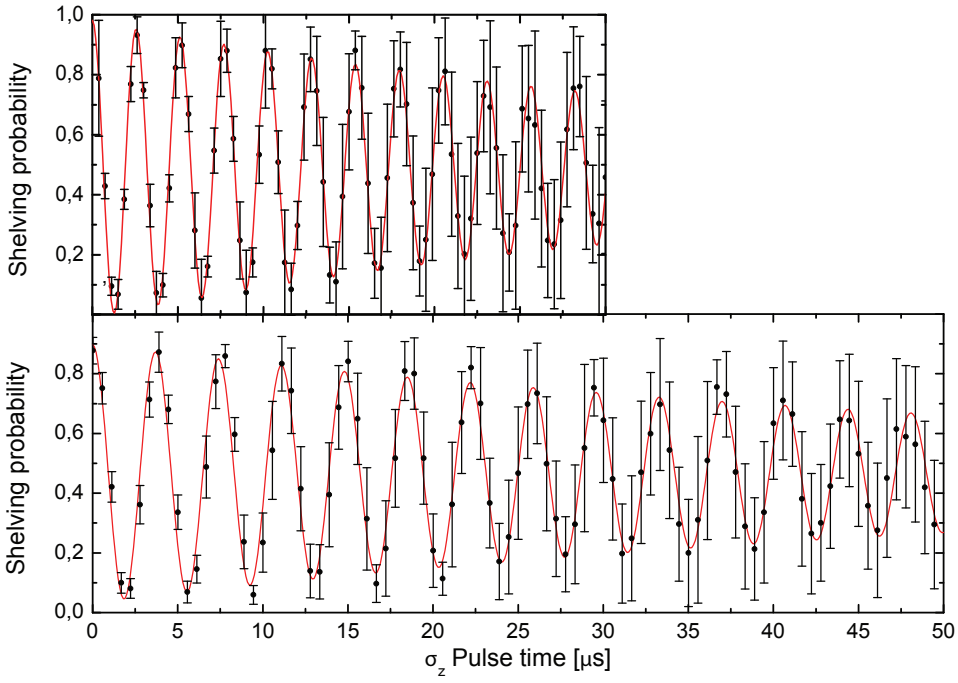

Figure 4.39.: Investigation of the intensity-fluctuation induced decoherence process: The fact that the error bars increase for longer pulse times clearly indicates that the error is due to pulse area fluctuations. As the error results from the statistics over several runs of the same measurement, it can be concluded that these fluctuations take place on slow timescales, i.e. beyond the time for the acquisition of a single data point, which is about 1 s.

measured ten times repeatedly. The error bars from the statistics over these measurements clearly reveal that the error increases in time, and that it becomes indeed much larger than the expected projection noise error. The conclusion is that the error arises due to effective pulse area fluctuations, which occur on longer time scales than the acquisition of a single data point, otherwise the exponential envelope would be seen in a single measurement run and the error bars would obey to the statistical limit. If the ac stark shift is divided by the decay time scale for each setting, similar figures of 60.6(2.5) and 64.0(2.4) result, proving that the decoherence is indeed given by pulse area fluctuations. The underlying reasoning is that the ideal signal for the ac stark measurement is given by

$$P_{\uparrow}(t) = \cos^2(\Delta_S t/2), \tag{4.50}$$

the signal deviation due to a small Stark shift offset δ_S is given by

$$\begin{aligned}\langle P_\uparrow(t)\rangle &= \int d\delta_S \frac{1}{\sqrt{2\pi\sigma_S^2}} e^{-\frac{\delta_S^2}{2\sigma_S^2}} \cos^2((\Delta_S(1+\delta_S)t/2) \\ &= \frac{1}{2}\left(1 + e^{-\frac{1}{2}\sigma_S^2\Delta_S^2 t^2}\cos(\Delta_S t/2)\right) \end{aligned} \tag{4.51}$$

In conclusion, there are only two possible mechanisms giving rise to these observations: Either the ion moves in the beam on a second timescale, or the beam has pointing instabilities. The latter possibility could be excluded by focusing the beam on a remotely placed CCD chip, where no drift could be observed. The first possibility in the strict sense is also unlikely as a movement in the μm range over longer timescales should be visible on the EMCCD camera. Therefore, a likely mechanism is the delocalization of the ion in the radial plane on the trap due to the strong radial heating measured in Sec. 4.3. If the heating was mediated by micromotion, the delocalization would be influenced by random charging of the trap electrodes. The suggested mechanism is further supported by the fact that strongly enhanced decoherence was observed for tightly focused Raman beams.

5. Trap Characteristics

This chapter presents a characterization of the confinement properties of our microstructured segmented ion trap. Sec. 5.1 describes how electrostatic simulations are performed and linked to measurement results and Sec. 5.2 gives a detailed account on the measurement and compensation of micromotion. For further details on the characterization of our trap, the reader is referred to Refs. [Sch09] and [Hub10a].

5.1. Electrostatic Potentials

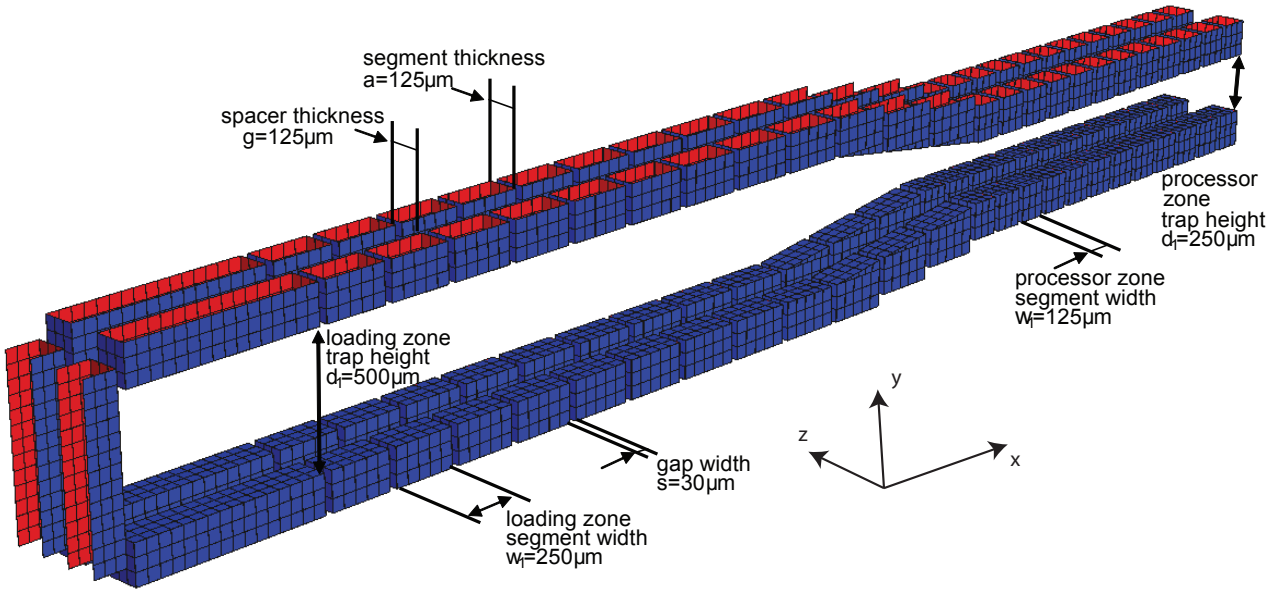

Figure 5.1.: Trap layout for electrostatic field simulation. The relevant trap dimensions are indicated. Several simplifications are made: The rf electrodes are assumed to be segmented in the same way as the dc ones, and only a limited amount of segments in the processor region is taken into account. For the calculation of the axial rf components, the full number of processor region segments is used, resulting in a geometry containing about 25000 nodes. The x-axis origin is located 1160μm to the left of the inner edge of the endcap electrode of the loading region by convention, the y and z origins are located at the symmetry center.

The key feature of our experimental approach towards scalable quantum logic is the fact that our trap possesses multiple segments in order to store and control a quite large number of qubits. Furthermore, the electrode structures are small compared to macroscopic standard-type Paul traps. This has the consequence that the structure of the confining potentials is more complicated than in a macroscopic setting, where the basic properties of electrostatic theory guarantee very harmonic potentials. For microstructured ion traps in general, it is very advantageous to know the electrostatic potentials with a high degree of precision, be it in the design process to obtain structures that provide the desired confinement properties, be it for the determination of possible operating voltages at the first attempts to trap with a new device or be it for the optimization of transport operations in segmented traps. This chapter is structured as follows: In Sec. 5.1, we briefly explain how we calculate the potentials for complicated trap structures and then analyze the properties of our trap based on the results of these simulations. Sec. 5.2 gives a detailed account on residual micromotion, its adverse effects on our experiments and how it is compensated in our setup.

The calculation of the electrostatic fields and potentials in an arbitrary electrode geometry, i.e. the solution of the Laplace equation for complicated boundary conditions is an interesting but rather complicated matter on its own, and it was found that a homebuilt customized software was needed to calculate the potentials with sufficient accuracy and efficiency. Conventional tools employ the finite-element method (FEM), which was found to produce resulting potential with additional spurious irregularities, furthermore commercial tools were found to be difficult to adapt to our custom geometries and calculation requirements, e.g. the feature to calculate trajectories can not easily be implemented. We therefore use a program written by Kilian Singer which employs the boundary element method (BEM) instead of FEM, which does not not require a 3D collocation of the volume of interest but rather a 2D one of the electrode surfaces. The basic idea is that each surface in the geometry is subdivided into small basic elements. The surface charge on each element is then given by the voltages applied to the electrodes and analytic relations for the mutual capacitance between each two segments. The surface charges are obtained from the inversion of a inverse capacitance matrix which has the dimension of the number of surface elements, which can range in the 10^5 regime. As the computational effort for matrix inversion scales to the third power of the number of surface elements N, a simplification which renders the calculation more effective is needed. The *fast multipole method* was found to be extremely useful for this, as it reduces the scaling law to $N \log N$. The underlying idea is that surface elements far away from the element of interest are bundled in a group, for which a multipolar expansion of the potential is performed. If the surface charges are known, the potential at a given point $\vec{r}$ is obtained by summing the potential arising from each surface element, which are in turn calculated by employing Greens functions. A more extensive discussion of all these methods is found in Ref. [Sin10]. Fig. 5.1 shows the geometry model of our trap used for the calculation of the electrostatic potentials. For this model, the inverse capacitance matrix inversion takes only about 20 minutes on a conventional personal computer. Potentials can be directly computed by application of the appropriate Greens functions, electric fields are obtained by finite differencing. The resulting potentials and fields are free of numerical artifacts, which

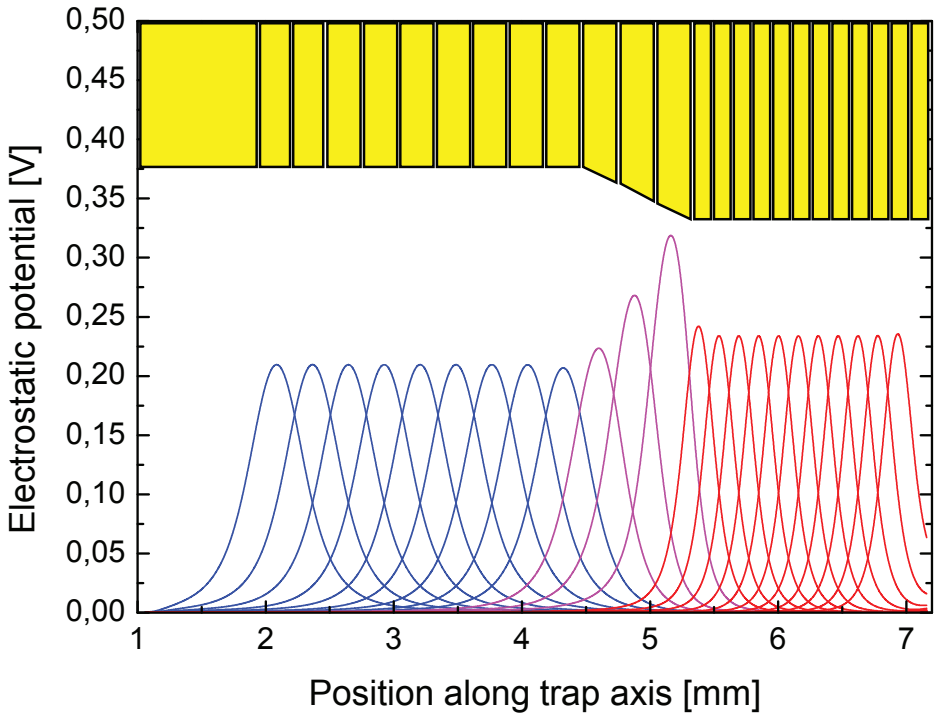

Figure 5.2.: Electrostatic axial confinement potentials: The potentials along the trap axis $(y, z = 0)$ arising if dc electrode n is set to +1 V and the other ones are grounded. The potentials for the loading region electrodes are shown in blue, the taper region ones in magenta and the processor region ones in red. It can be seen that the potential wells overlap each other such that a strong linear potential, i.e. a force, can be generated at a given trapping state by setting a neighboring electrode to nonzero voltage, which enables fast and efficient ion transport in the throughout the trap structure. Furthermore, considerable potential depths in the 2 V range are readily attained.

allows for a very precise calculation of the potential curvatures which are needed to predict secular frequencies of trapped ions.

Resulting axial confinement potentials for the individual segments are shown in Fig. 5.2. A quantitative characterization of the confinement strengths is given in table 5.1, from which the axial secular frequency and the a and q parameters can be directly inferred by multiplication with the respective voltages. In contrast to the axial confinement, the radial confinement is influenced by both dc and rf potentials and is therefore more complicated to analyze quantitatively. Calculated radial cuts at the trapping site of segment 5 for the rf and dc potentials are shown in Fig. 5.3. An important result is that the potential ellipsoids around the origin are aligned differently for the dc and rf fields. The deviation of the dc axes from the rf ones originates from the fact the rf voltage is applied along the whole trap length, whereas the neighboring segments of segment 5 are set to ground, which breaks the symmetry between

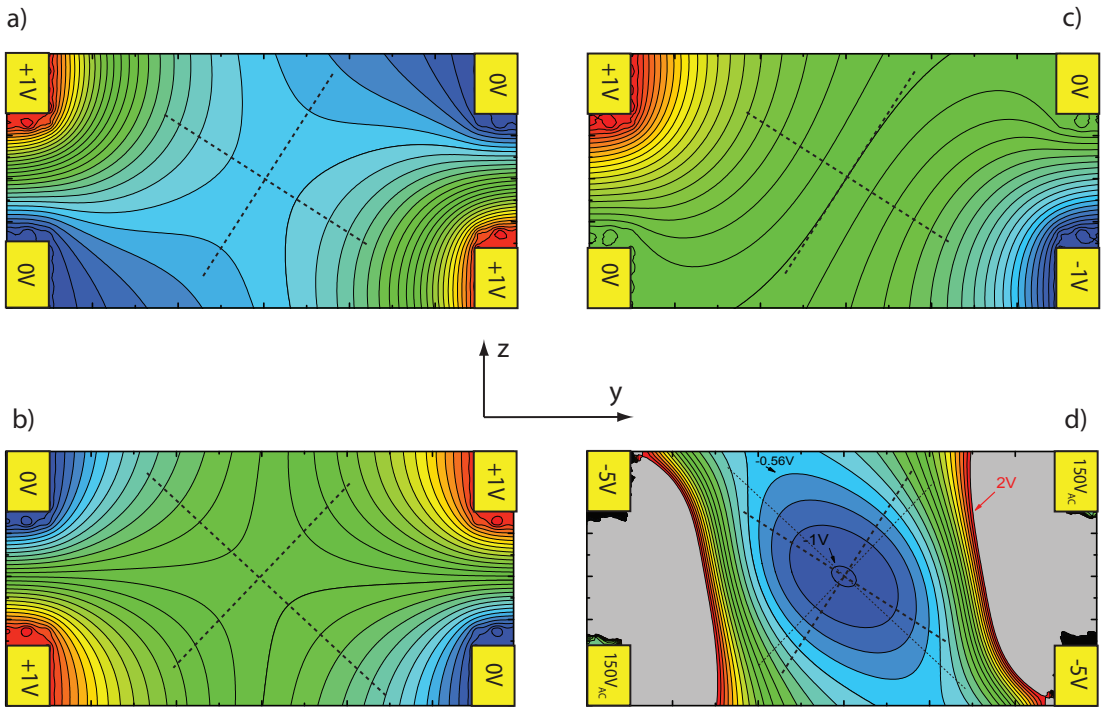

Figure 5.3.: Radial potential cuts: **a)** shows a radial plane cut of the potential arising from application of +1 V to the dc electrodes of segment 5 while all other segments are grounded. The asymmetry results from the field penetration of the neighboring grounded dc electrodes. **b)** shows the same but with the rf segments set to +1 V and all dc ones to ground. The potential is more symmetric in this case, the quadrupole symmetry axes are almost aligned along the yz and the orthogonal $\bar{y}z$ directions. **c)** shows the potential arising from the application of a differential voltage of ±1 V to the dc electrodes, one can see that the compensation field is quite homogeneous in the trapping region and it points along the direction with the largest curvature of the potential in a). **d)** shows the sum of the ponderomotive potential at an rf amplitude of 150 V and a dc level of -5 V. Note that this sum is not a physical potential, but it still gives an estimation of the minimum trap depth, which is about 500 mV in this case. For all plots, the x coordinate is always chosen to be the center of electrode 5. See Fig. 5.1 for the dimensions. The main axes of the potential ellipsoids are indicated as dashed lines. Note that the orientation of the total potential ellipsoid if d) coincides with the dc potential orientation. The irregularities near the electrodes are merely plotting artifacts. Note that the color coding is different for the subimages.

dc and rf electrodes which is not directly apparent when one is looking at the yz cuts of Fig. 5.3. The tilt angle between dc and rf axes is about 11°. This raises the question how the

Parameter	Loading zone value	Processor zone value
$\nu_{\mathrm{ax}}/\mathrm{V}_{\mathrm{dc}}^{1/2}$ [MHz $\mathrm{V}^{-1/2}$]	0.388(3)	0.744(9)
$a_{zy}/\mathrm{V}_{\mathrm{dc}}$ [$\mathrm{V}_{\mathrm{dc}}^{-1}$]	-0.00194(2)	-0.0077(2)
$a_{z\bar{y}}/\mathrm{V}_{\mathrm{dc}}$ [$\mathrm{V}_{\mathrm{dc}}^{-1}$]	0.003909(7)	0.01496(5)
$q/\mathrm{V}_{\mathrm{dc}}^{1}$ [$\mathrm{V}_{\mathrm{rf}}^{-1}$]	0.00201(6)	0.0075(4)

Table 5.1.: Operating parameters of the trap: The parameters determining the motional frequencies for applied unit voltages are given for the loading and processor regions. The uncertainties indicate the spread of these values over the segment ranges comprising these zones.

particle dynamics is different from the results of the standard Mathieu equation treatment where decoupled radial coordinates are assumed. If we consider a general tilt angle of the dc potential with respect to the rf one, the Mathieu equation Eq. 2.76 reads as:

$$\begin{aligned} \ddot{x} &= a_1 \cos^2\phi\ x - a_1 \cos\phi \sin\phi\ y + a_2 \sin^2\phi\ x + a_2 \cos\phi \sin\phi\ y + \cos(2\tau)\ q_x x \\ \ddot{y} &= a_1 \sin^2\phi\ y - a_1 \cos\phi \sin\phi\ x + a_2 \cos^2\phi\ y + a_2 \cos\phi \sin\phi\ x - \cos(2\tau)\ q_y y. \quad (5.1) \end{aligned}$$

A detailed mathematical analysis of these coupled Mathieu equations is beyond the scope of this thesis, however numerical simulations were performed which indicate that the radial secular frequencies are the same as for the untilted case, i.e. one can simply employ Eq. 2.78 for $a = a_{1,2}$. The corresponding main axes are aligned along the dc axes. It is interesting to note that this holds only for q values below the maximum stability value, for larger q values the secular frequencies deviate from the untilted ones, which also changes the stability diagram: due to the coupling of the coordinates, instability in one direction can be compensated by the stability in the other one, thus the stability at large q and a values even increases with the tilt angle. For example for $q = 0.8$, $a_1 = -0.08$ and $a_2 = 0.04$, the untilted trap is unstable in the direction of the positive (anticonfining) a parameter, whereas a trap with a tilt angle of 45°is still stable.

It is the essential feature of microstructured multisegmented Paul traps that ions can be shuttled between different trapping sites. This is accomplished by supplying suitable voltage waveforms to the dc electrodes, see appendix B for technological details. The set of n voltages supplied to n different electrodes determines the number and position of the trapping sites as well as their associated trap frequencies. One way to determine appropriate voltages for a required operation is a bottom-up approach, where shuttling operations are considered as *local* operations for which only a small number of nearby electrodes is used. It is then even possible to utilize tailored waveforms which are designed such that a minimum amount of energy is transferred to the ion(s) during shuttling operations, an example is illustrated in [Sch06]. An alternative approach is a top-down approach, where the full set of electrode voltages for generation of a specific trapping potential is calculated via a regularization approach for the solution of the underdetermined linear problem, see Ref. [Sin10] for a full mathematical account. Here, we present a set of measurement results which represents the first exploitation

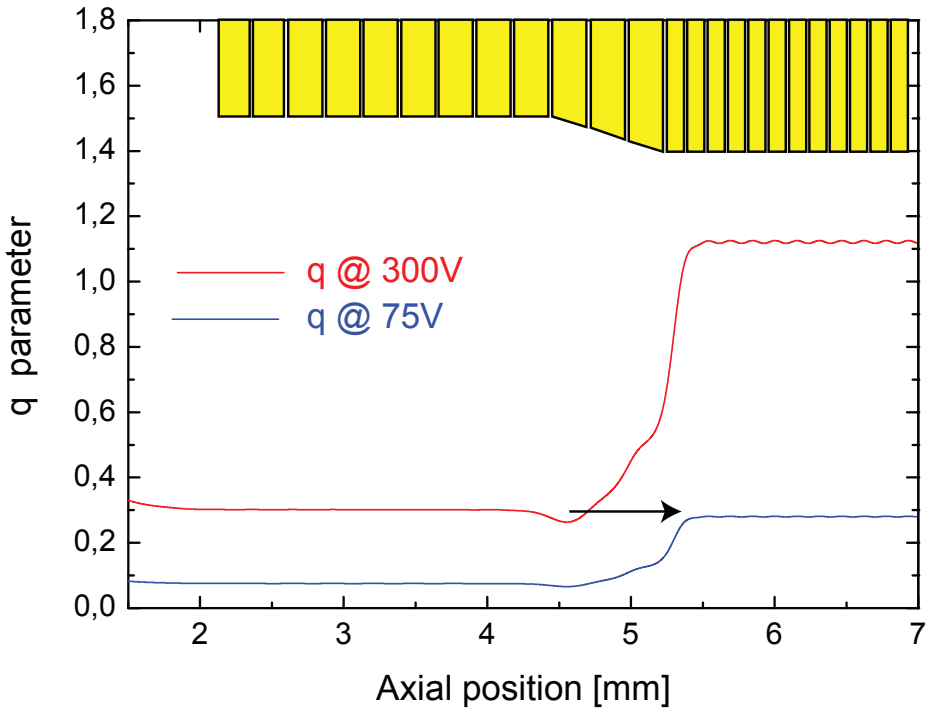

Figure 5.4.: Radial confinement strength along the trap axis. The curves show the q parameters calculated from the radial rf potential curvature, showing that a drive amplitude of 300 V (red) leading to stable trapping the loading region leads to instability in the processor region. On the other hand, an amplitude of 75 V, yielding a similar q parameter in the processor region as lower amplitude yields in the loading region, the secular frequency in the loading region in turn becomes smaller than the axial secular frequency, also leading to instability. The arrow indicates that the rf drive amplitude has to be ramped when transferring ions from the loading to the trapping region and back. Experimentally, no rf amplitude was found which provided simultaneous trapping in both trap regions, which is clearly a design flaw of our trap.

of the features of our multisegmented trap: via off-site spectroscopy measurements on the quadrupole transition (see Sec. 4.2.2), we measure the axial trap frequencies for various trapping sites along the trap axis. The sequence is as follows: after the qubit preparation, the ion is shuttled to the destination site within a transport time in the millisecond range. A spectroscopy pulse at 729 nm with the laser beam readjusted on the destination site transfers population to the metastable state, then the ion is transported back to the original trap site before the state is read out. The voltage waveforms for this experiment were calculated with the regularization approach described above, see [Hub10b] for details. The voltages are chosen such that the trap frequency is kept mostly constant at about 1.35 MHz, however residual variations occur which arise from the utilization of other constraints such as limited

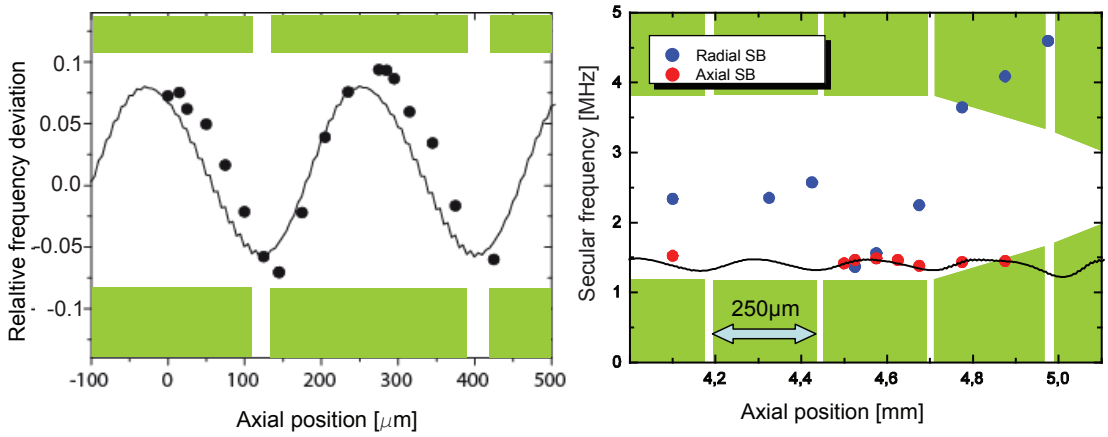

Figure 5.5.: Off-site spectroscopy: **a)** Shows the deviation of measured axial secular frequencies with respect to the desired one for different positions along the trap axis, see text. **b)** Shows the absolute values of the axial frequencies (red) along with measured radial sidebands (blue), note that the radial confinement changes drastically as the ion approaches the taper region.

voltage magnitudes, fixed potential offset and of course the trap site position. The expected trap frequencies for the applied waveforms are shown as the solid line in Fig. 5.5 a), it can be seen that the measured data fits with sub-percent accuracy besides a small offset from the oscillatory pattern, which is presumably due to a residual dc electric field along the trap axis caused by stray charges. This proves on the one hand that the potentials obtained from our solver are accurate, on the other hand we have shown that transport through the whole trap structure is possible and that the trap is not impaired by the presence of stray charges or deviations of the actual structure from the ideal geometry.

5.2. Micromotion Compensation

Driven motion of trapped ions at the trap rf is termed *micromotion*. It occurs if the ion is shifted out of the rf node, where it is assumed to reside in all idealized considerations on Paul trap operation. It has several adverse effects on most conceivable experiments in such traps: The most prominent one is that any driving laser pointing along an axis with nonzero micromotion amplitude will be frequency modulated. This impairs Doppler cooling on dipole transitions and also precision spectroscopy and coherent manipulations on narrow higher order or Raman transitions. Normally, one will only observe reduced effective intensities of the beams, i.e. the fluorescence level on a cycling transition will drop and the Rabi frequencies

for coherently driving a quadrupole or stimulated Raman transition will be reduced. More severe effects might also be present: the Doppler cooling will be less efficient if the cooling transition line is effectively broadened by the micromotion echoes, and if these are on the blue side of the transition they will even counteract the cooling. Furthermore, the power in the FM sidebands acts as to increase laser-driven decoherence mechanisms when driving Raman transition, see Sec. 4.7. In the worst case, echo components might even hit other resonance, e.g. higher order motional sideband or different Zeeman transitions in the case of a quadrupole transition. It should be also noted that for precision spectroscopy, especially for designing optical atomic clocks based on trapped ions, the ac Stark shift from uncompensated micromotion will be the predominant error source. Micromotion can be compensated by applying dc voltages to a set of compensation electrodes to shift the ion into the node of the rf field. The difficulty lies in precise measurement of the micromotion amplitude. Throughout the last decades, several methods for this have been conceived:

- **Ion position shift:** This technique does not directly measure effects of the micromotion, it rather monitors the change of the ion position upon change of the rf level which can only occur of dc and ac potential minima are offset with respect to each other, such that a residual dc field drives the ion out of the rf node. The accuracy of the method is very limited by the spatial resolution of the imaging optics.

- **Coherent echo strength measurement:** If a narrow transition is at hand which can be coherently driven, the strength of micromotion echoes can be directly measured and minimized.

- **Phonon correlations:** The fluorescence counting electronics can be set up such that time resolved measurements of the photon arrival times can be correlated with the trap rf. Nonvanishing correlation will be found in the presence of micromotion. The advantage of this method is that its implementation is possible without coherently driven optical transitions or even without imaging, however it requires a considerable amount of data acquisition.

- **Fluorescence heterodyning:** The fluorescence can be heterodyned with a phase-locked laser offset by about the drive rf. The signal then directly provides information about the oscillation amplitude [Raa00].

- **Coherent Raman effects:** Phase coherent modulation of a repump laser with the trap rf can be used to obtain a modulation of the fluorescence level [All10]. The advantage of this technique is essentially that the vertical direction, which is inaccessible for the cooling laser due to stray light issues in surface traps, can be accessed.

- **rf modulation:** If the rf voltage is fed onto the different electrodes via distinct pathways, it is possible to modulate one of these by a secular frequency. It the ion senses the rf field, its secular motion will be driven by the resulting beat, which strongly affects the fluorescence level. This method is also especially suited for planar traps [Dan09].

- **Fluorescence measurement:** The primary effect of micromotion is the alteration of the line shape on a cooling transition. Due to the broadening, the fluorescence level will increase due to micromotion for sufficient detunings and appropriate range of rf frequencies and modulation amplitudes. As this is the technique of our choice due to its simplicity, it will be discussed in detail below.

The first three techniques are discussed in detail in Ref. [Ber98b]. We have realized both the echo strength measurement and the correlation measurement, however the first technique yields high accuracy but accounts only spatial direction, while the latter was found to be rather impractical. We have found that for the every-day lab routine, it is most useful to red-detune the Doppler cooling laser at 397 nm by more than one linewidth and to minimize the fluorescence level at that detuning. The compensation is performed by applying a voltage difference between the adjacent dc trapping electrodes. The accuracy of this method is to be assessed in the following. If we assume the ion to be a free particle, which is justified by the timescale separation $\omega_{\mathrm{rad}} \ll \Omega_{\mathrm{rf}}$, its motion in a homogeneous rf field is given by

$$\begin{aligned} x(t) &= \frac{qE_x^{(\mathrm{rf})}}{m\Omega_{\mathrm{rf}}^2}\cos(\Omega_{\mathrm{rf}}t) \\ v(t) &= \frac{qE_x^{(\mathrm{rf})}}{m\Omega_{\mathrm{rf}}}\sin(\Omega_{\mathrm{rf}}t), \end{aligned} \tag{5.2}$$

where we consider the motion along a laser beam direction x with wavenumber k and the corresponding component of the rf electric field $E_x^{(\mathrm{rf})}$. The maximum first-order Doppler shift during one motional cycle is then

$$\delta_{\max} = k\ v_{\max} = k\frac{qE_x^{(\mathrm{rf})}}{m\Omega_{\mathrm{rf}}}. \tag{5.3}$$

The oscillatory motion then leads to frequency modulation of the laser with a modulation index of

$$\beta = \frac{\delta_{\max}}{\Omega_{\mathrm{rf}}} = k\frac{qE_x^{(\mathrm{rf})}}{m\Omega_{\mathrm{rf}}^2} = 2\pi\frac{x_{\max}}{\lambda} \tag{5.4}$$

If the beam is detuned from the atomic resonance by δ_0, one obtains effective saturation S_n parameters for the frequency components $\delta_n = \delta_0 + n\Omega_{\mathrm{rf}}$ with $n = -\infty..+\infty$:

$$S_n = S_0 J_n^2(\beta). \tag{5.5}$$

The total fluorescence level upon neglecting the motional effects due to a changed Doppler cooling efficiency then is

$$R = \sum_{n=-\infty}^{+\infty} \frac{\Gamma}{2}\frac{S_n}{1 + S_0 + 4\left(\delta + n\Omega_{\mathrm{rf}}\right)^2/\Gamma^2}, \tag{5.6}$$

where a reasonable parameter regime is of course only given for small enough modulation indices, such that the summation will include only a few nonvanishing terms around $n = 0$.

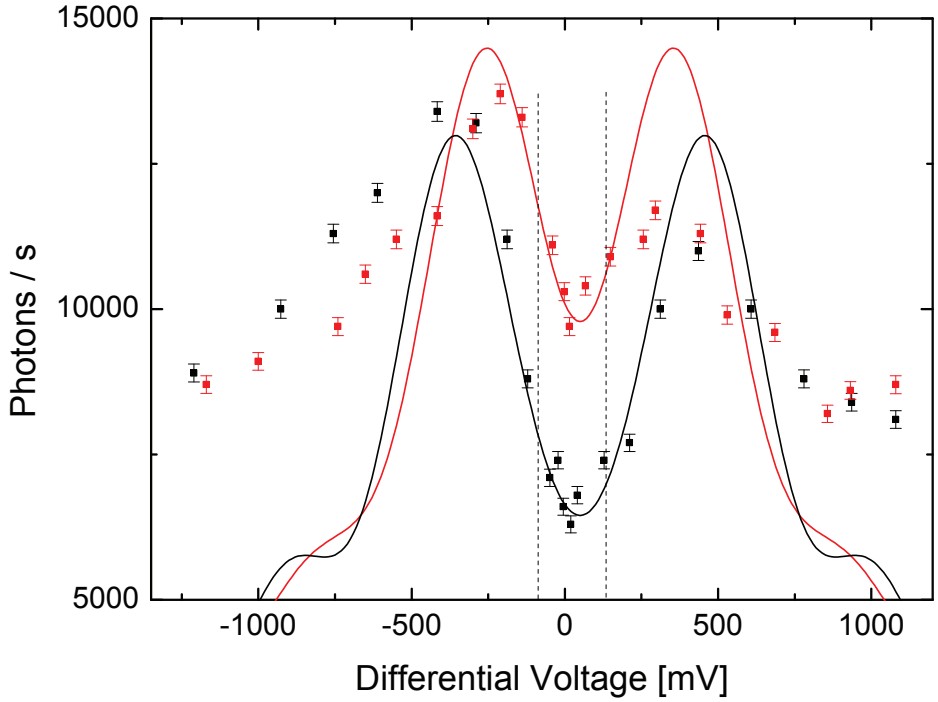

Figure 5.6.: Micromotion compensation by fluorescence measurement: The plot shows the fluorescence rate from a single ion versus the differential voltage between the adjacent electrodes of segment 5. Two different data sets are shown for detunings of $\delta/\Gamma \approx$-2.5 (black) and $\delta/\Gamma \approx$-1.9 (red), clearly demonstrating that the compensation voltage and accuracy is robust against the detuning. The solid curves are fits to a simple theoretical model Eq. 5.6(see text), which reproduces the essential features but fails to quantitatively describe the complete behavior.

Our setup allows for the compensation of micromotion along one direction aligned perpendicular to the trap axis and along one direction given by the propagation direction of a laser, which is chosen to be the Doppler cooling beam in our case. The compensation is accomplished by application of a voltage difference across the two electrodes comprising a segment pair, the corresponding potential is plotted in Fig. 5.3 c), the corresponding electric field at the ion position is rather homogeneous and the field lines run in the radial trap plane. The magnitude of the electric field for $\pm$1 V applied at the adjacent electrodes of segment 5 is calculated to be $E^{(5)}_{\mathrm{comp}} \approx$1.45 kV/m, and the displacement Δr is given by

$$\Delta r = \frac{qE^{(5)}_{\mathrm{comp}}}{m\omega^2_{\mathrm{rad}}}. \tag{5.7}$$

The dependence of the rf-field magnitude for 1 V applied rf voltage on the displacement along the compensation field lines is in turn given by $dE^{(\mathrm{rf})}_{\mathrm{comp}}/\Delta r \approx 8.9{\cdot}10^6 \mathrm{Vm}^{-2}$, such that

we obtain $dE^{(rf)}_{\mathrm{comp}}/dV^{(5)}_{\mathrm{comp}}$. Inserting this into Eq. 5.4 yields

$$\beta \approx k_{\mathrm{eff}} \frac{q}{m\Omega_{\mathrm{rf}}} \frac{dE^{(rf)}_{\mathrm{comp}}}{dV^{(5)}_{\mathrm{comp}}} V^{(5)}_{\mathrm{comp}} V_{\mathrm{rf}}, \tag{5.8}$$

which can be inserted into Eq. 5.6 to predict the behavior of the fluorescence on the compensation voltage. A comparison between the model and measured data is shown in Fig. 5.6. The detunings are inferred from a measurement of the fluorescence rate versus 397 nm wavelength, and a saturation parameter of S_0=5 is assumed. The applied rf voltage amplitude is V_{rf}=200 V at $\Omega_{\mathrm{rf}} \approx 2\pi\cdot$24.8 MHz, resulting in $\omega_{\mathrm{rad}} \approx 2\pi\cdot$3.5 MHz. A compensation offset voltage of 50 mV is inferred and a factor for scaling the absolute photon collection rate is introduced. As can be seen, the width and depth of the fluorescence dip is correctly reproduced by the model for both detunings, however the decrease for large compensation voltage magnitudes is much less pronounced for the measured data. Furthermore, the asymmetry of the dip is not at all explained by the model. The reason for the first discrepancy might be that the Zeeman splitting of the two driven transitions $|S_{1/2}, m_J = \pm 1/2\rangle \rightarrow |P_{1/2}, m_J = \pm 1/2\rangle$ of about 12 MHz is not included, as is the effect of the photon scattering on the motional state of the ion. The asymmetry might arise from a displacement giving rise to additional micromotion in the y-direction, which is not directly visible in the 397 nm fluorescence but might be responsible for an inhomogeneous compensation field. The precision attained by this compensation method is indicated by the dashed lines in Fig. 5.6, from the voltage window of about 80 mV, a maximum residual modulation index of $|\beta_{\mathrm{res}}| \lesssim 0.56$, equivalent to 85% of the laser power acting on the carrier transition. As can be seen from simulations for various parameter sets, the width of the dip is rather independent of the laser and trap parameters, however the attainable micromotion suppression is quite poor. However, all methods used for qubit preparation, manipulation and readout are designed to be resilient against the presence of a tolerable amount of micromotion, as is explained in detail in chapter 4.

Micromotion aligned along the trap axis can not be directly compensated by means of a differential voltage. The origin of axial micromotion is on the one hand given by the translational asymmetry along the trap axis. To make this more clear, we consider an ion placed at any given site in the loading region. It has a direct line of sight on the rf-electrode surfaces in the taper region, which is not present in the other direction along the trap axis. The modulation index inferred from the simulation axial rf field strength by the same reasoning as above is plotted for standard operating parameters in Fig. 5.7. It can be seen that the expected modulation might be sufficiently small in the processor region. An additional increase of the modulation will occur if rf pickup is present on the confining dc electrode and the ion is shifted into a nonzero electric field arising from this electrode by stray charges acting in the axial direction. An estimation along the same lines of thought as above is readily obtained by considering the axial potential from the confining electrode can be written as

$$V(x) = \frac{1}{2} m\omega^2_{\mathrm{ax}} x^2 = q\ V_{\mathrm{dc}} c_{\mathrm{dc}} x^2, \tag{5.9}$$

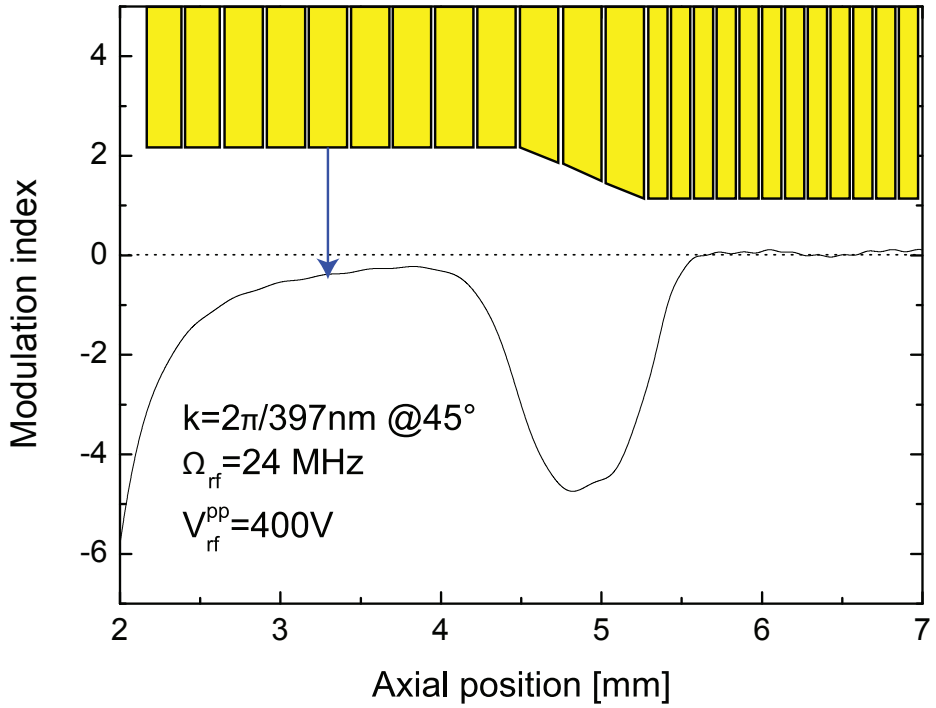

Figure 5.7.: Modulation index along the trap axis: The modulation index for the Doppler cooling beam is shown versus the ion position along the trap axis. The ion is assumed to be at the radial rf-node, such that modulation is only due to the residual rf field along the trap axis arising from the translational asymmetry of the trap. Standard operating parameters are assumed, note the strong modulation arising from the taper electrodes and the additional ripple which is due to the segment periodicity.

resulting in the additional modulation index

$$\beta(\Delta x) = k_{\text{eff}} \frac{\omega_{\text{ax}}^2 V_{\text{rf}}}{\Omega_{\text{rf}}^2 V_{\text{dc}}} \Delta x, \tag{5.10}$$

where V_{rf} is the rf pickup amplitude and Δx is the displacement due to the axial offset field. Plugging in the operating parameters $\omega_{\text{ax}} = 2\pi{\cdot}1.35$ MHz and a typical measured value of V_{rf} =500 mV, we would obtain a modulation index of only $3{\cdot}10^{-2}$, therefore this mechanism can be neglected.

The difficulties to obtain a stable ion trapping at tight radial confinement mentioned in chapter 9 can be explained by considering a recent publication [Vah10] where it was shown experimentally that in a situation with competing Doppler cooling and heating processes, stable oscillatory motion of ions at the secular frequency can occur. The oscillation amplitude is fixed such that cooling and heating are balanced throughout one secular motion cycle. This is a critical phenomenon, i.e. oscillations at finite amplitude set in beyond a threshold of

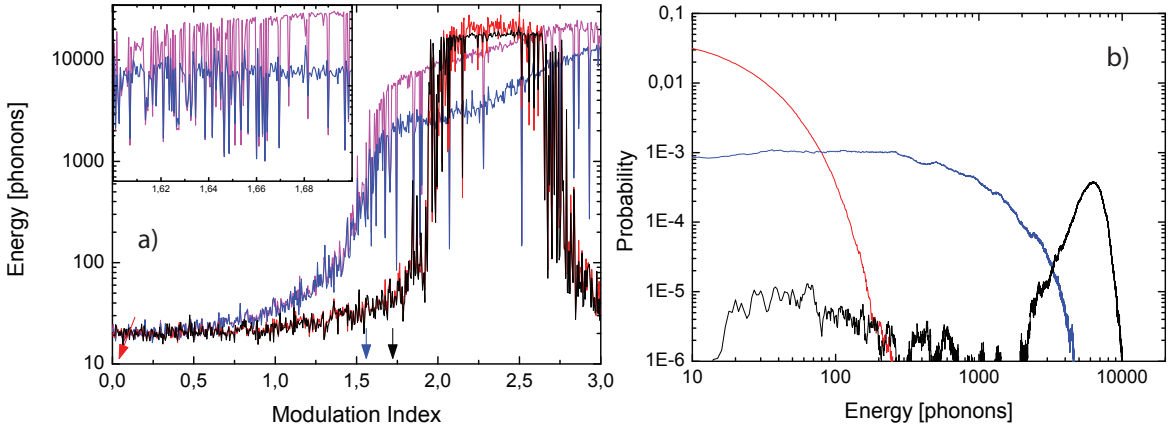

Figure 5.8.: Micromotion induced phonon lasing effect: **a)** The plot shows the average energy (purple/red) and energy standard deviation (blue/black) versus micromotion induced modulation index Eq. 5.4 for $\Omega_{\mathrm{rf}} = 2\pi{\cdot}24.77$ MHz (purple/blue) and $\Omega_{\mathrm{rf}} = 2\pi{\cdot}59.54$ MHz (red/black) resulting from semiclassical simulations, see text. One clearly observes the onset of stable oscillations with a nonthermal phonon distribution beyond a threshold modulation index. Plotting the curves for different trap drive frequencies within the same plot is justified by the fact that both $\beta \propto \Omega_{\mathrm{rf}}^{-1}$ and roughly $\omega_{\mathrm{rad}} \propto \Omega_{\mathrm{rf}}^{-1}$, i.e. in order to attain comparable radial confinement at a higher trap drive frequency, one would have to increase the rf voltage such that about the same modulation index as for the lower drive frequency is obtained. The inset demonstrates the bistability of the system, i.e. that the onset of the oscillations is noise driven and does therefore not occur in every simulation run. **b)** shows energy probability distribution function on a double-logarithmic scale for the $\Omega_{\mathrm{rf}} = 2\pi{\cdot}24.77$ MHz case, at modulation indices given by the accordingly colored arrows in Fig. a). While the two curves below the onset threshold pertain the thermal phonon distributions with $\bar{n} \approx 20$ (red) and $\bar{n} \approx 500$ (blue), the distribution beyond the threshold is clearly nonthermal but pertains to a state with stable oscillations.

heating power, which led the authors to coin the term *phonon lasing* to describe this effect. In this work, a second heating laser was employed additionally to the Doppler cooling beam, and both beams are aligned along the trap axis of a Paul trap such that only the axial mode is to be taken into account. Furthermore, the trap was operated at very small axial trap frequencies of about 50 kHz, in order to be able to stroboscopically observe the motion. We show here that the same effect can be induced by the presence of micromotion, furthermore we show that the onset of the oscillations can be driven by a Langevin force which describes

the random recoil kicks from emitted photons during Doppler cooling. Finally, we comment on the impact of these effects on micro ion trap based quantum information experiments and point out possible technological improvements.
In the presence of a Doppler cooling laser, the position coordinate x_i in direction i with harmonic confinement ω_i obeys to the equation of motion

$$\ddot{x}_i + \frac{\hbar k_i}{m} R(\dot{\vec{x}}) + \omega_i^2 x_i = \chi_i(t, R(\dot{\vec{x}})), \tag{5.11}$$

where the second (cooling) term is comprised of the photon recoil $\hbar k_i$ and the photon scattering rate $R(v)$ given by Eq. 2.30. The term on the right-hand side is a Langevin force arising from photon emission in random direction. In contrast to Ref. [Vah10], this is a more general approach which does not require small saturation parameters and allows for the consideration of three spatial dimensions. For the solution of this differential equation by numerical integration with time step dt, $N_{ph} = R(\dot{\vec{x}}) \cdot dt$ photons are scattered within dt (which is assumed to be smaller than the trap periods). This results in a momentum kick in direction i which is a random variable with Gaussian distribution with zero mean and a standard deviation of $\sigma = \sqrt{N_{ph}/3}$. Micromotion is included by employing Eq. 5.6 for the scattering rate, where the modulation index β is given by the projection of the micromotion amplitude vector on the normalized laser wavevector: $\beta = \vec{\beta} \cdot \vec{k}_0$. The effect of the micromotion thus is to add 'extra laser beams' at frequencies $\pm n\Omega_{\mathrm{rf}}$ with integer n. Frequencies on the blue side of the atomic resonance contribute to heating instead of cooling. The net effect depends on the total saturation, the carrier detuning and the secular and rf frequencies as well as the beam and micromotion alignment. Due to this rather complex parameter space, the situation is not easily accessed. To start with, we illustrate the effect by calculating an atomic trajectory over a long time interval (several ms) for typical trap operating parameters (S_0=2, $\Delta = -\Gamma/2$, $\Omega_{\mathrm{rf}} = 2\pi{\cdot}24.77$ MHz, $\omega_{z,y,x} = 2\pi{\cdot}1.4$,3.1,3.6 MHz), but varying micromotion amplitude β. The beam is assumed to be at 45° with the z direction and at 60° with the y and x directions. The resulting energy statistics are shown in Fig. 5.8. One can clearly observe how the Doppler cooling is adversely affected at increasing micromotion amplitudes, however the energy distribution is still thermal until at the critical micromotion amplitude the mean energy exceeds the energy variance and classical oscillations set in.

6. Determination of Atomic Matrix Elements with Off-Resonant Radiation

This chapter describes a new measurement method for atomic matrix elements for dipole transitions, i.e. Einstein A coefficients or lifetimes developed as a side-product during the establishment of the methods for the spin qubit. The basic measurement idea is to compare absorptive and dispersive effects occurring in the interaction of a trapped ion with an off-resonant laser beam. The chapter is organized as follows: Sec. 6.1 gives a scientific motivation, while Sec. 6.2 introduces the particular measurement scheme. Sec. 6.3 explains in detail how the absorptive effect is measured, whereas Sec. 6.5 explains the measurement procedure for the dispersive effects and 6.4 describes how a calibration of the laser detuning is carried out. Sec. 6.6 treats the robustness of the method against dominant experimental imperfections, while Sec. 6.7 describes in detail how the error estimates are obtained. Sec. 6.8 then presents the final results. Sec. 6.9 discusses the relevance of additional error sources, and Sec. 6.10 concludes with the presentation of an alternative measurement scheme for the dispersive effects.

6.1. Motivation

6.2. Basic Idea of the Measurement Procedure

Exposure to an off-resonant light beam can cause two different effects in an atomic system: Spontaneous Raman transitions between atomic levels by off-resonant inelastic scattering and AC Stark energy shifts of the levels, i.e. absorptive and dispersive effects. Both effects can be quantitatively measured, and both depend on the intensity and detuning of the off-resonant beam, whereas only the Raman transition rates depend on the lifetime of the intermediate excited state. The idea is therefore to measure the AC Stark shift as a calibration of laser intensity, such that the lifetime can then be inferred from the Raman transition rates.

The *inelastic* spontaneous Raman transition rates, from now on referred to as spin-flip scattering rates between the ground state Zeeman sublevels upon exposure to the off-resonant beam are inferred from Eq. A.14 and Eq. A.15

$$\begin{aligned} R_{\uparrow} &= \Gamma_{PS}\frac{\Omega^2}{4\Delta_R^2}\frac{1}{9}\left(\epsilon_-^2+\epsilon_0^2\right) \\ R_{\downarrow} &= \Gamma_{PS}\frac{\Omega^2}{4\Delta_R^2}\frac{1}{9}\left(\epsilon_+^2+\epsilon_0^2\right), \end{aligned} \tag{6.1}$$

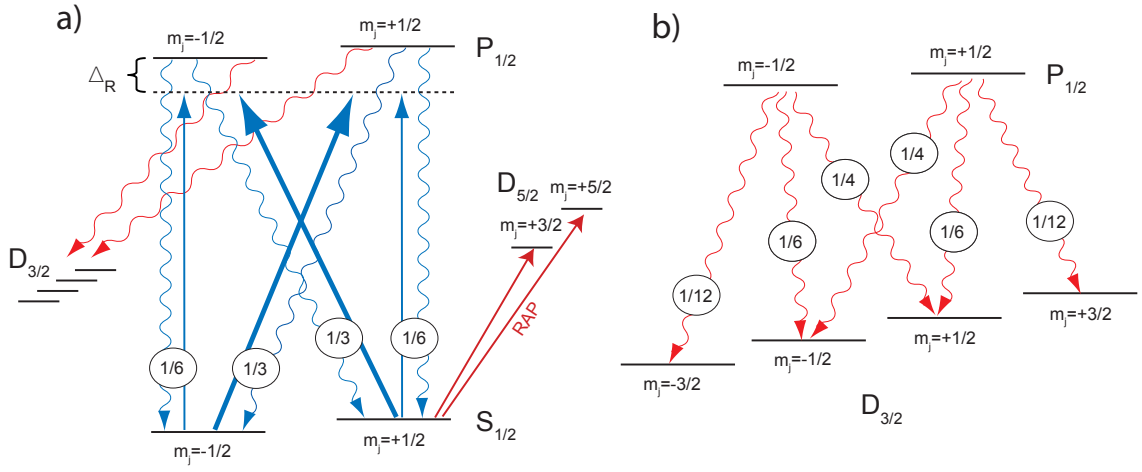

Figure 6.1.: Relevant levels and transitions for the measurement scheme. **a)** shows the scattering pathways within the $S_{1/2}$,$P_{1/2}$, and **b)** shows the pathways for the $P_{1/2}$,$D_{3/2}$ manifold. The squared coupling coefficients Eq. 6.3 are indicated on the transitions.

when exposure to a single beam with arbitrary polarization is assumed. Ω^2 indicates the dipolar coupling strength given by the laser intensity, Δ_R is the detuning from the $S_{1/2}$ to $P_{1/2}$ transition, the ϵ_i^2 give the relative strength of the polarization components of the laser beam and Γ_{PS} is the spontaneous transition rate of interest, i.e. the Einstein coefficient of the transition. Necessary conditions for Eqs. 6.1 to hold are

$$\begin{aligned} \Delta_R^2 &\gg \Gamma_{PS}^2 \\ \Delta_R^2 &\gg \Omega^2. \end{aligned} \tag{6.2}$$

Here, there transition rates between the specific Zeeman levels are given by the Wigner 3j symbols:

$$c_{m_S m_P} = \begin{pmatrix} J_S & 1 & J_P \\ -m_S & q & m_P \end{pmatrix}, \tag{6.3}$$

where the $J_S = 1/2$ and $J_P = 1/2$ indicate the initial and final total angular momentum and the $m_{S,P} = \pm 1/2$ indicate the initial and final Zeeman sublevels. For the derivation of Eqs. 6.1, the off-resonant laser excitation rate $\Omega^2/4\Delta_R^2$ is multiplied with $\epsilon_{if}^2 c_{m_S m_P}^2$ to yield the excitation rate for a specific transition between sublevels. For the subsequent decay, the excitation rate is multiplied by the *normalized* coefficient $c_{m_S m_P}^2 / \sum_{m_S'} c_{m_S' m_P}^2 = 2\, c_{m_S m_P}^2$.

The AC Stark shifts of the spin levels are given by Eq. A.13:

$$\Delta_S^{\uparrow} = \frac{\Omega^2}{4\Delta_R}\left(\frac{1}{3}\epsilon_-^2 + \frac{1}{6}\epsilon_0^2\right)$$
$$\Delta_S^{\downarrow} = \frac{\Omega^2}{4\Delta_R}\left(\frac{1}{3}\epsilon_+^2 + \frac{1}{6}\epsilon_0^2\right). \tag{6.4}$$

Together with the condition

$$\epsilon_-^2 + \epsilon_+^2 + \epsilon_0^2 = 1, \tag{6.5}$$

this yields an expression for the transition rate between $P_{1/2}$ and $S_{1/2}$ state,

$$\Gamma_{PS} = 3\ \Delta_R \frac{R_{\uparrow} - R_{\downarrow}}{\Delta_S^{\uparrow} - \Delta_S^{\downarrow}}, \tag{6.6}$$

which is entirely independent of the beam intensity and polarization components. Furthermore, only the *differential* Stark shift is occurring in the denominator, which is easier to access experimentally.
A complication occurring in our atomic system is the presence of a loss channel to the metastable $D_{3/2}$ state. The leakage rates into the $D_{3/2}$ manifold read

$$R_{\uparrow D} = \Gamma_{PD}\frac{\Omega^2}{4\Delta_R^2}\left(\frac{1}{3}\epsilon_-^2 + \frac{1}{6}\epsilon_0^2\right)$$
$$R_{\downarrow D} = \Gamma_{PD}\frac{\Omega^2}{4\Delta_R^2}\left(\frac{1}{3}\epsilon_+^2 + \frac{1}{6}\epsilon_0^2\right). \tag{6.7}$$

The total depletion rate of $|\uparrow\rangle$ is now given by

$$R_{\uparrow} + R_{\uparrow D} \equiv R_{\uparrow}(1+b), \tag{6.8}$$

such that $b = R_{\uparrow D}/R_{\uparrow\downarrow}$. The leakage factor b can be directly extracted from the measurement data. Assuming $\epsilon_0^2 = 0$, we find

$$\Gamma_{PD} = b\ \Gamma_{PS}/3. \tag{6.9}$$

The justification of this assumption is given in the error analysis below. For symmetry reasons, the same result is obtained when the depletion rate of $|\downarrow\rangle$ is considered. With the spin-flip scattering rate Eqs. 6.1 , the dynamics of the populations are given by the following rate equations:

$$\dot{c}_{\uparrow}(t) = -R_{\uparrow}(1+b)c_{\uparrow}(t) + R_{\downarrow}c_{\downarrow}(t) \tag{6.10}$$
$$\dot{c}_{\downarrow}(t) = -R_{\downarrow}(1+b)c_{\downarrow}(t) + R_{\uparrow}c_{\uparrow}(t) \tag{6.11}$$

The analytical solution for Eq. 6.10 reads

$$\begin{aligned} c_{\uparrow}^{\uparrow}(t) &\equiv p_0^{\uparrow}(t) \\ &= \frac{1}{2\,f}\, e^{-\frac{1}{2}((1+b)(R_{\uparrow}+R_{\downarrow})+f)t} \left((1+b)(R_{\uparrow}-R_{\downarrow})(1-e^{ft}) + f\left(1+e^{ft}\right)\right) \\ c_{\uparrow}^{\downarrow}(t) &\equiv p_0^{\downarrow}(t) \\ &= \frac{R_{\downarrow}}{f}\, e^{-\frac{1}{2}((1+b)(R_{\uparrow}+R_{\downarrow})+f)t}(e^{ft}-1), \end{aligned} \tag{6.12}$$

where the upper spin label accounts for initialization in spin $|\uparrow\rangle/|\downarrow\rangle$ respectively, with

$$f \equiv \sqrt{-4b(2+b)R_{\uparrow}R_{\downarrow} + (1+b)^2(R_{\uparrow}+R_{\downarrow})^2} \tag{6.13}$$

6.3. Measurement of the Scattering Rates

The spin-flip scattering rate can be measured by utilizing the techniques for spin initialization and read-out developed for the spin qubit. The ion is simply prepared in either $|\uparrow\rangle$ or $|\downarrow\rangle$ by means of optical pumping on the $S_{1/2}$ to $P_{1/2}$ transition. It is then exposed to square pulse of off-resonant light, detuned from the $S_{1/2}$ to $P_{1/2}$ transition by several GHz. The population in $|\uparrow\rangle$ is the transferred to the metastable $D_{5/2}$ state by means of a double Rapid Adiabatic Passage (RAP) pulse. Then, fluorescence is counted upon irradiation of resonant light for 3 ms on the $S_{1/2}$ to $P_{1/2}$ transition, giving the fraction of population remaining in the $|\downarrow\rangle$ level upon several repetitions of the same sequence. We performed 100 measurement cycles each for a set of 50 non-uniformly spaced scatter pulse times which were chose to show the scatter dynamics well. This set is measured this way 8×20 times, yielding 16000 single interrogations for each scatter pulse time. The block of 20 repetitions for a scattering curve were interleaved for the two initialization levels. The raw data for one data set measured with a Raman detuning of $\Delta_R \approx$13 GHz is shown in Fig. 6.2.

For each scatter pulse time, the mean values and standard deviations for the dark count numbers are calculated from the 160 data points pertaining to 100 interrogations each. A post selection is then performed, where all of the 160 data points are removed from data which are off the mean value by more than three standard deviations. This way, measurements where the ion was heating up or the shelving laser was lock to the right wavelength are sorted out. It is important to mention that the error is not artificially reduced this way, as the total number of valid interrogations is decreased upon removal of a data point, see Sec. 6.7. The mean values and standard deviations are recalculated from the cleaned data, and the standard deviations are compared to the ones to be expected by simple statistics, the results are shown in Fig. 6.3 for all data set taken. The agreement between actual and theoretical standard deviations is a key result, as it demonstrates that the measurement is indeed limited by statistical noise and no drift effects have occurred. However, even data with a significant increase of the actual errors can be used to infer valid scattering rates, as long as the actual errors are used for the error estimation procedure, Sec. 6.7.

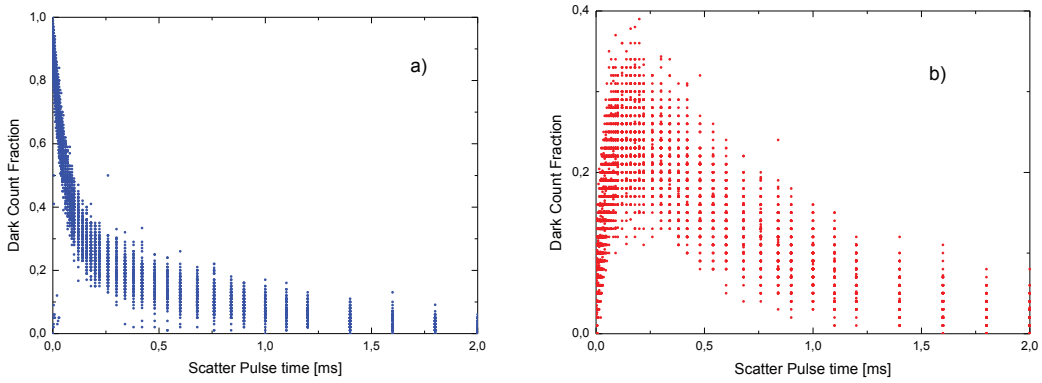

Figure 6.2.: Raw data from the scattering rate measurement. Each point corresponds to 100 interrogations. Curve **a)** results from initialization in $|\uparrow\rangle$, **b)** is for initialization in $|\downarrow\rangle$. Note the different vertical scales.

6.4. Measurement of the Raman Detuning

The remaining quantity to be measured is the Raman detuning Δ_R occurring in Eq. 6.6. The laser frequency is simply read off an High Finesse WSU wavemeter which has 10 MHz relative accuracy. As the detuning is relative to the atomic resonance, its position has to be measured as well. This can be done in two ways: First, the scattering laser can be simply tuned to resonance as the laser frequency for which the maximum fluorescence occurs is identified as the atomic resonance. The results are shown in Fig. 6.5.

The second method is to perform additional Stark shift measurements for different detunings. According to Eq. 6.4, $1/\Delta_S$ should depend linearly on the detuning, such that the zero of a line fitted through several measured Stark shifts also gives the resonance frequency. However, it is found that the deviation of the measured data from the fit exceeds the expected error. This is attributed to optical elements in the beam which might change the intensity and polarization of the laser at the location of the ion depending on the frequency. Furthermore, for small detunings the Stark shift deviates from Eq. 6.4, and for large detunings the Stark shift arising from the $P_{3/2}$ also plays a role.

6.5. Measurement of the AC Stark Shift

The differential Stark shift measurement is accomplished in entirely the same way as already described in Sec. 4.7: A pulse from the off-resonant laser beam at variable duration is inserted between two Ramsey pulses, the resulting oscillatory pattern with respect to the shift pulse duration reveals the Stark shift Δ_S according to

$$S(t) = a\ e^{-\gamma\ t} \sin(\Delta_S\ t + \phi) + b, \tag{6.14}$$

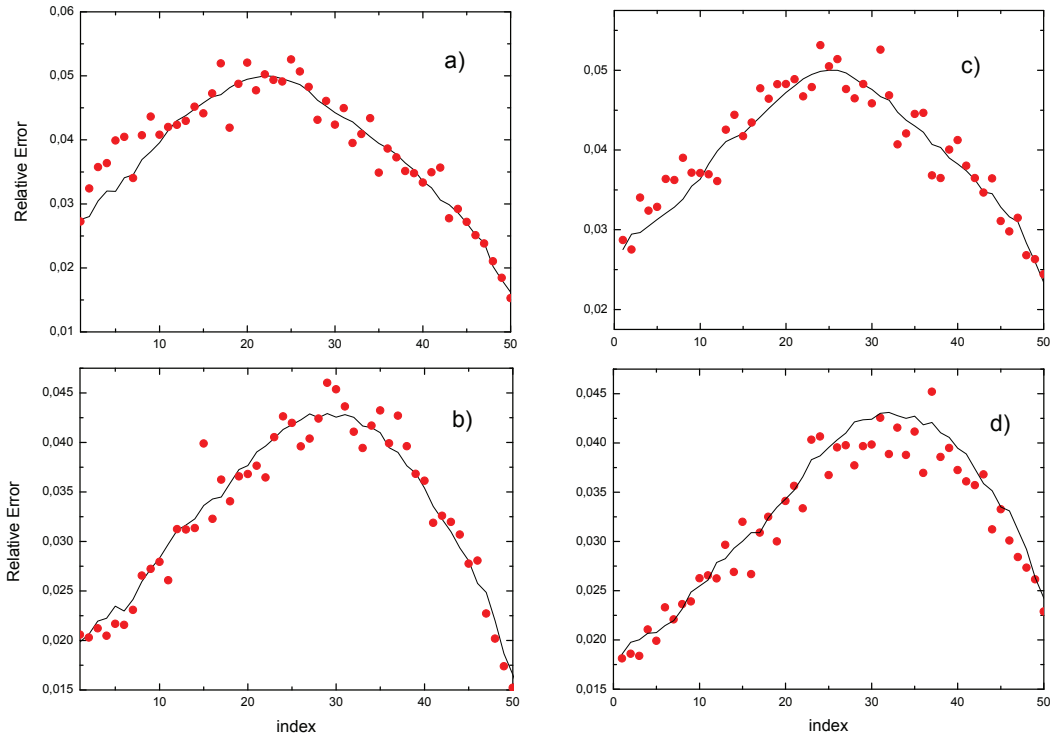

Figure 6.3.: Comparison between the actual spreads of the raw data point (red dots) and the statistical expectation (solid curve). Curves a) and b) pertain to the 15 GHz datasets, c) and d) to the 14 GHz ones. a) and c) are for initialization in $|\uparrow\rangle$, b) and d) for initialization in $|\downarrow\rangle$. The horizontal axis gives the data index instead of the scatter pulse time.

where amplitude a, baseline b, dephasing rate γ and offset phase ϕ are floating. Due to the fact that the oscillation frequency can be extracted from the data with high precision, this measurement takes much less effort in data acquisition and evaluation as the scattering rate measurement. Furthermore, as only the frequency of the oscillation pattern is relevant, the precision does not rely on stable readout and preparation, such that the stability of the laser intensity and polarization can also be evaluated. An example data set is shown in Fig. 6.6.

Measurements of the Stark shift were performed several times for each data set pertaining to a fixed Raman detuning. From the spread of the obtained values, the long-term stability limiting the total accuracy is calculated, which is used in the final evaluation to determine the total accuracy. The measured values for the shift are shown in Fig. 6.7, note that the total spread in the 0.25% range is much larger the uncertainty of a single measurement, which is in the sub-per mil range.

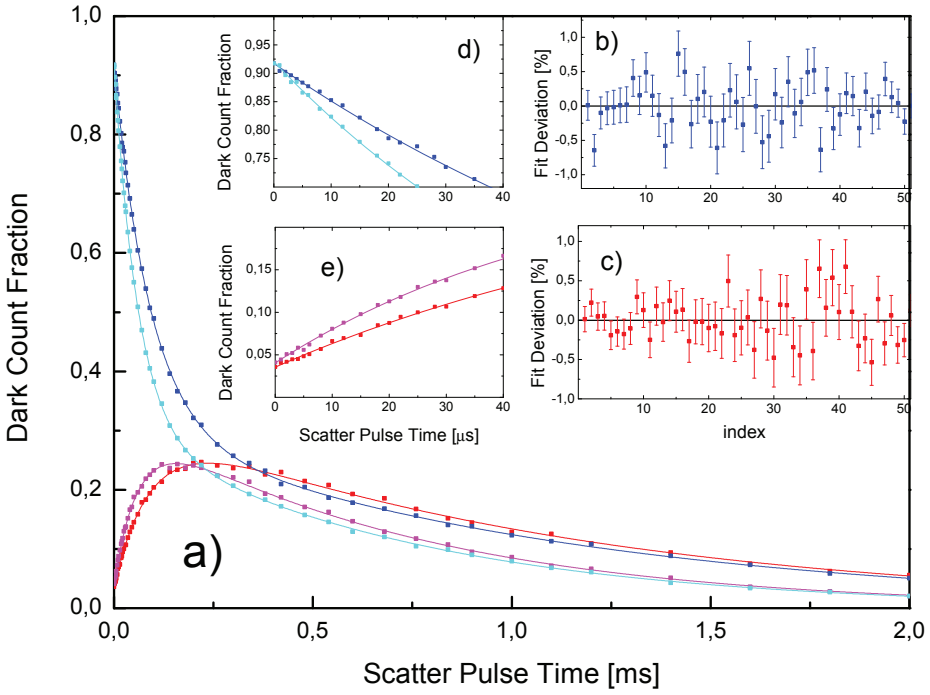

Figure 6.4.: Final result of the spin-flip measurement: **a)** Average over the scattering raw data after post processing and the corresponding fits to the model Eqs. 6.20. **b)** and **c)** show the deviation of the data points with respect to the fit model along with the error bars.

The quite high measurement precision in principle allows for a precise calibration of the Raman detuning Δ_R: By taking a set of Stark shift measurements for various Raman detunings, a fit to Eq. 6.4 will reveal which frequency read-off exactly corresponds to the atomic resonance. Upon inverting both sides, a linear function can be fit through the data whose zero crossing is located at the resonance frequency. Corresponding data is shown in Fig. 6.8, one can see that the deviation of the individual data point clearly exceeds the expected uncertainty and leads to a large inaccuracy of the Raman detuning in the range of several 100 MHz. The reason for the bad quality of this data is improper air current shielding and thermal insulation of the setup at the time when this data was taken, especially the $\lambda/4$ waveplate in the R2 beam was found to cause strong Stark shift deviations upon small temperature changes despite being of zero order type.

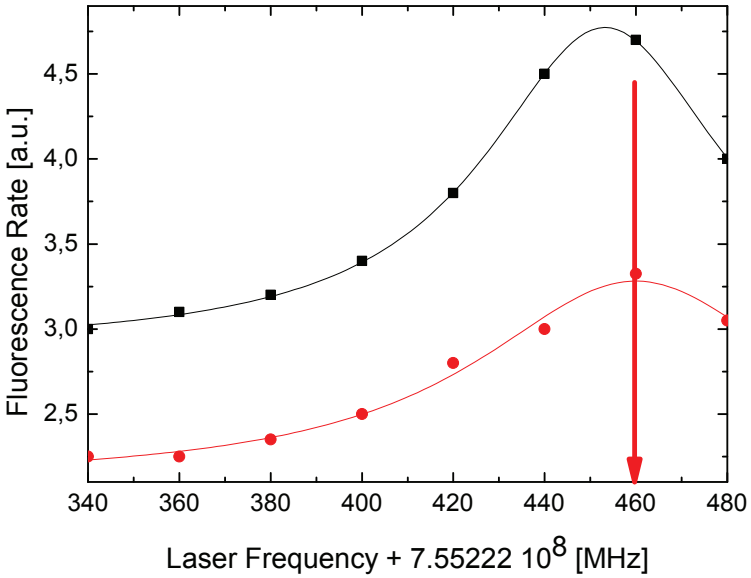

Figure 6.5.: Calibration of the wavemeter by means of fluorescence measurement. The Lorenzian fits give an accuracy of 20 MHz. The lower curve is recorded with very low beam intensity, therefore additional broadening due to bad Doppler cooling occurs, however the resonance is shifted more into the blue side as Doppler heating is suppressed as well.

6.6. Robustness against Experimental Imperfections

Assuming ideal spin initialization, ideal state transfer to the metastable $D_{5/2}$ state and ideal fluorescence state discrimination, the probabilities for finding the ion in the metastable state are

$$\begin{aligned} p^{\uparrow}_{\mathrm{dark}}(t) &= p^{\uparrow}_{0}(t) \\ p^{\downarrow}_{\mathrm{dark}}(t) &= p^{\downarrow}_{0}(t) \end{aligned} \tag{6.15}$$

Considering imperfect spin initialization, the probabilities for finding the ion in spin up after a scatter pulse of time t are

$$\begin{aligned} p^{\uparrow}(t) &= a^{\uparrow}_{\uparrow} p^{\uparrow}_{0}(t) + a^{\uparrow}_{\downarrow} p^{\downarrow}_{0}(t) \\ p^{\downarrow}(t) &= a^{\downarrow}_{\uparrow} p^{\uparrow}_{0}(t) + a^{\downarrow}_{\downarrow} p^{\downarrow}_{0}(t) \end{aligned} \tag{6.16}$$

where the upper index of the p's and a's account for the intended initialization spin level and the lower index of te a's accounts for the actual population remaining in the respective

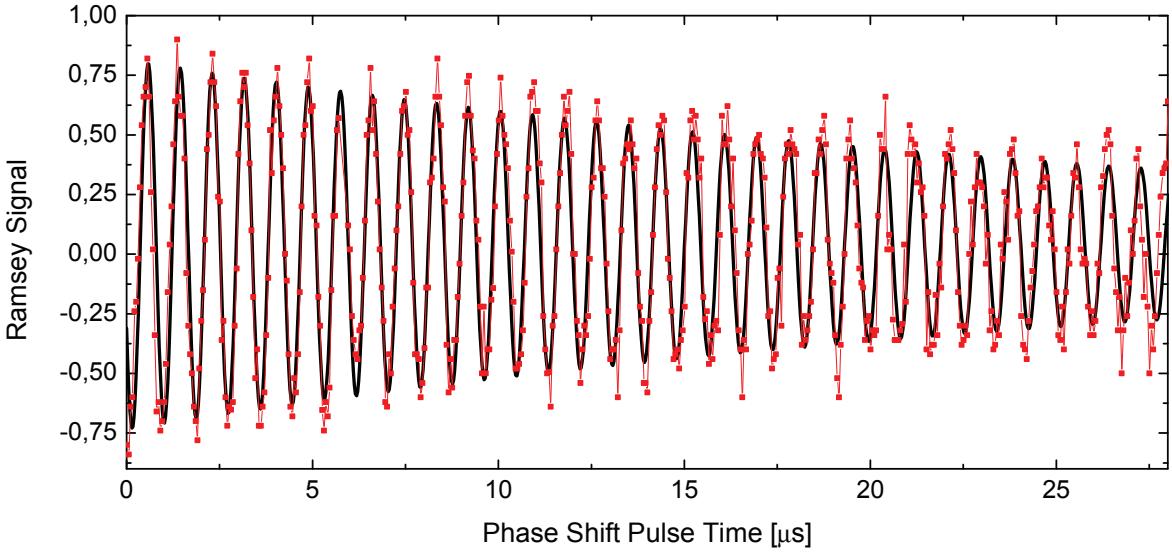

Figure 6.6.: Example Stark shift measurement. The dots show the dark count signal (symmetrized) for varying exposure time to the phase shift pulse within the Ramsey sequence. The dephasing is mainly due to intensity fluctuations of the laser. The fit to Eq. 6.14 is indicated by the solid curve.

levels after initialization. The a's fulfill $a_{\uparrow}^{\uparrow}, a_{\downarrow}^{\downarrow} \lesssim 1$ and $a_{\downarrow}^{\uparrow}, a_{\uparrow}^{\downarrow} \gtrsim 0$. Imperfect shelving to the metastable state is accounted for by the transfer probabilities $r_{\uparrow,\downarrow}$, where $r_{\uparrow} \lesssim 1$ and $r_{\downarrow} \gtrsim 0$:

$$\begin{aligned} p_D^{\uparrow}(t) &= r_{\uparrow} p^{\uparrow}(t) + r_{\downarrow}(1 - p^{\uparrow}(t)) \\ p_D^{\downarrow}(t) &= r_{\uparrow} p^{\downarrow}(t) + r_{\downarrow}(1 - p^{\downarrow}(t)). \end{aligned} \tag{6.17}$$

Errors in the fluorescence discrimination are incorporated by considering dark count probabilities $p_{\mathrm{dark}}^{S,D}$:

$$\begin{aligned} p_{\mathrm{dark}}^{\uparrow}(t) &= p_{\mathrm{dark}}^{D} p_D^{\uparrow}(t) + p_{\mathrm{dark}}^{S}(1 - p_D^{\uparrow}(t)) \\ p_{\mathrm{dark}}^{\downarrow}(t) &= p_{\mathrm{dark}}^{D} p_D^{\downarrow}(t) + p_{\mathrm{dark}}^{S}(1 - p_D^{\downarrow}(t)). \end{aligned} \tag{6.18}$$

In total, this leads to

$$\begin{aligned} p_d^{\uparrow}(t) &= \Delta p_d \; \Delta r \; (a_{\uparrow}^{\uparrow} p_0^{\uparrow}(t) + a_{\downarrow}^{\uparrow} p_0^{\downarrow}(t)) + \Delta p_d \; r_{\downarrow} + p_d^{S} \\ p_d^{\downarrow}(t) &= \Delta p_d \; \Delta r \; (a_{\uparrow}^{\downarrow} p_0^{\uparrow}(t) + a_{\downarrow}^{\downarrow} p_0^{\downarrow}(t)) + \Delta p_d \; r_{\downarrow} + p_d^{S}. \end{aligned} \tag{6.19}$$

Here, $\Delta p_d = p_{\mathrm{dark}}^{D} - p_{\mathrm{dark}}^{S}$ and $\Delta r = r_{\uparrow} - r_{\downarrow}$. Therefore, the model

$$\begin{aligned} p_d^{\uparrow}(t) &\equiv \vartheta_{\uparrow}(R_{\uparrow}, R_{\downarrow}, b, \alpha_{\uparrow}, \beta_{\uparrow}, \gamma, t) = \alpha_{\uparrow} \; p_0^{\uparrow}(t) + \beta_{\uparrow} \; p_0^{\downarrow}(t) + \gamma \\ p_d^{\downarrow}(t) &\equiv \vartheta_{\downarrow}(R_{\uparrow}, R_{\downarrow}, b, \alpha_{\downarrow}, \beta_{\downarrow}, \gamma, t) = \alpha_{\downarrow} \; p_0^{\downarrow}(t) + \beta_{\downarrow} \; p_0^{\uparrow}(t) + \gamma. \end{aligned} \tag{6.20}$$

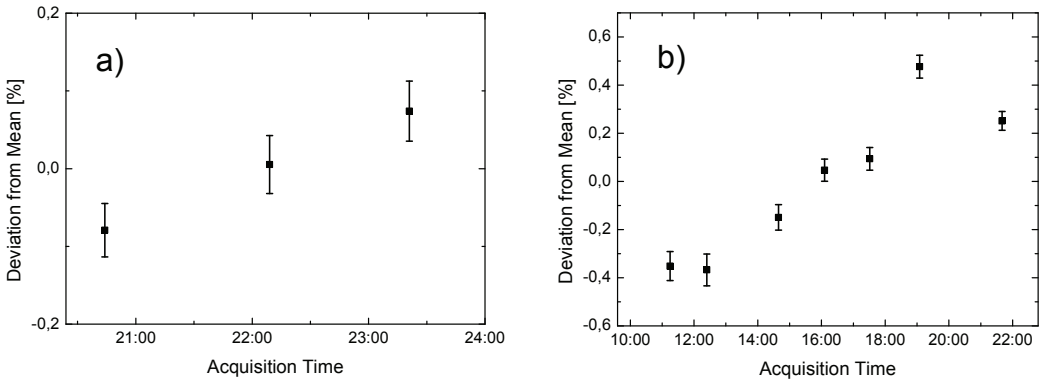

Figure 6.7.: Drift of the measured AC Stark shift throughout the measurement. **a)** shows the data for the 15 GHz measurement and **b)** the data for the 13 GHz one. The errors bars are the confidence intervals obtained from the fit. It can be seen that the accuracy of the AC Stark shift measurement is limited by long term drifts, see Sec. 4.7.

is reproducing the complete physics of the measurement. Hence, all *static* imperfections are included into the model and therefore do not spoil the accuracy of the figures of interest, which are the *dynamic* parameters of the curve. However, a necessary requirement is that the initialization, transfer and read-out have to be kept constant during the whole measurement.

6.7. Extraction of the Scattering Parameters and Error Analysis

For the sake of notation, the parameter sets describing the two measured curves are labeled

$$\begin{aligned} X_\uparrow &= \{R_\uparrow, R_\downarrow, b, \alpha_\uparrow, \beta_\uparrow, \gamma\} \\ X_\downarrow &= \{R_\uparrow, R_\downarrow, b, \alpha_\downarrow, \beta_\downarrow, \gamma\} \\ X &= X_\uparrow \cup X_\downarrow \end{aligned} \tag{6.21}$$

The parameter sets Eqs. 6.21 are extracted from the post processed data by means of a conventional least-squares minimization using the *NMinimize* function of *Mathematica*. The crucial point is to fit *both* scattering curves at once, as then the requirement of consistency leads to an enhancement of accuracy. The accuracy of the values obtained from the fit are then calculated by checking how likely the measurement data could be reproduced be deviating parameter sets. The probabilities $\hat{p}_i^\uparrow$,$\hat{p}_i^\downarrow$ that the test parameter sets $X_\uparrow$,$X_\downarrow$ could

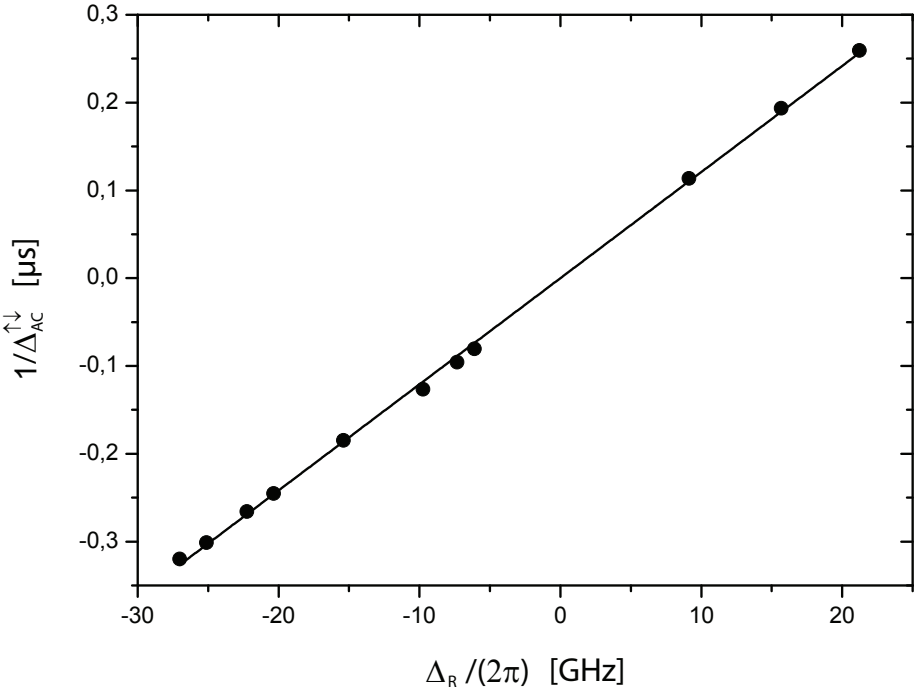

Figure 6.8.: Calibration by means of the Stark shift: The plot shows values of the inverse ac Stark shift measured at various detunings along along with a linear fit. One can clearly see that the linear behavior is well reproduced, the accuracy is however not good enough for a precise enough calibration of the Raman detuning. This insufficient precision is attributed to drifts of the laser polarization due to imperfect shielding of the setup from air currents when the data was taken.

yield the measurement dark count value $P_i^{\uparrow}$,$P_i^{\downarrow}$ for scatter times t_i are given by

$$\begin{aligned} \hat{p}_i^{\uparrow}(X_{\uparrow}) &= \tilde{p}(\vartheta_{\uparrow}(X_{\uparrow}, t_i), P_i^{\uparrow}, N_i^{\uparrow}) \\ \hat{p}_i^{\downarrow}(X_{\downarrow}) &= \tilde{p}(\vartheta_{\downarrow}(X_{\downarrow}, t_i), P_i^{\downarrow}, N_i^{\downarrow}), \end{aligned} \tag{6.22}$$

where $\tilde{p}(\vartheta(X,t), P, N)$ describes the statistical occurrence probability of P dark counts in N measurements given the physical dark count probability $\vartheta(X, t_i)$, which is given by a Binomial distribution:

$$\tilde{p}(\vartheta(X,t), P, N) = \binom{N}{P} \vartheta(X,t)^P \ (1 - \vartheta(X,t))^{N-P} \tag{6.23}$$

which is replaced by a Gaussian PDF with mean $\vartheta(X,t)\ N$ and standard deviation $\sqrt{\vartheta(X,t)\ (1-\vartheta(X,t))\ N}$ for the sake of easier computation. The total likelihood of a given unified parameter set to yield the two measured curves is then the product of the probabilities

for all measured values:

$$\hat{p}^{\mathrm{tot}}(X) \quad = \quad \left(\prod_{i=1}^{N} \hat{p}_i^{\uparrow}(X_{\uparrow})\right)\left(\prod_{i=1}^{N} \hat{p}_i^{\downarrow}(X_{\downarrow})\right) \tag{6.24}$$

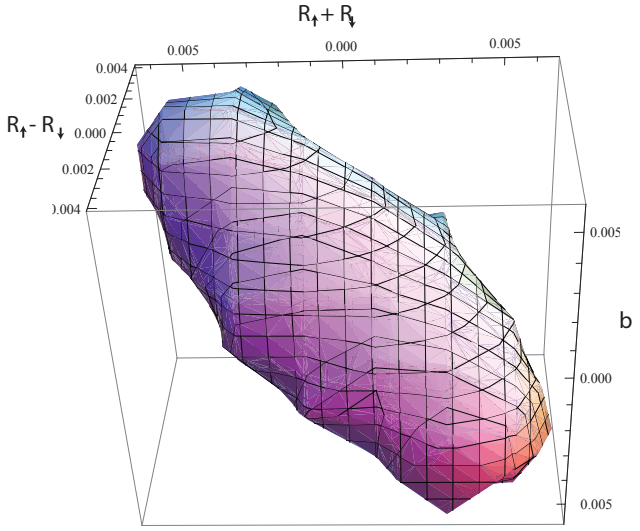

Figure 6.9.: Error ellipsoid resulting from the calculation of the parameter set probabilities Eq. 6.24 within a 3D parameter cube around the optimum values determined from the fit in Fig. 6.4, see text. The axes are normalized to the optimum values.

The parameter likelihood Eq. 6.24 is calculated on grid in $\{R_{\uparrow}, R_{\downarrow}, b\}$-space around the values found from the fit. The points where $\hat{p}^{\mathrm{tot}}$ has dropped to $1/\sqrt{e}$ of the maximum likelihood constitute the error ellipsoid. As the difference of the scattering rates Eqs. 6.1 is needed, the ellipsoid is transformed to the $\{R_{\uparrow} - R_{\downarrow}, R_{\uparrow} + R_{\downarrow}, b\}$ coordinate set. The extremal points along the $R_{\uparrow} - R_{\downarrow}$ then determine the accuracy of the scattering rate difference including all parameter correlations, the same holding for the branching parameter b.

6.8. Final Results

Table 6.1 shows the figures from the evaluation from the two datasets at different Raman detunings. It can be seen that the measurements of the Stark shifts and scattering rates are quite accurate with respect to their statistical errors and should therefore provide results for the lifetimes with an accuracy below 1%. The deviation of the two obtained values for the lifetimes however clearly lies outside the statisitcal confidence interval, such that an unknown error source must have been present. An error source which might be responsible for this was

Data Set	1	2
$\Delta_R/2\pi$ [GHz]	13.06±0.02	15.90±0.02
$\Delta_S/2\pi$ [MHz]	1.423±0.004	1.1623±0.0009
$R_\uparrow$ $[s^{-1}]$	10060	6601
$R_\downarrow$ $[s^{-1}]$	5054	3360
ΔR $[s^{-1}]$	5006±34	3242±24
b	0.209	0.201
$\alpha_\uparrow$	0.921	0.918
$\alpha_\downarrow$	0.940	0.914
$\beta_\uparrow$	0.035	0.013
$\beta_\downarrow$	0.040	0.035
γ	0	0
τ_S [ns]	7.26±0.05	7.52±0.06
τ_D [ns]	109±0.8	113±0.9

Table 6.1.: Fit results for the parameter sets Eqs. 6.21 for two individual measurements

found later on: The switching EOM for the off-resonant beam was always switched on for a duration given by the maximum pulse length. During that timespan, if the R2 AOM is not switched on, remaining light from the 0th order still impinges onto the ion where it causes scattering, which causes a systematic error in the scattering rate measurement. Further data will be taken where the EOM is directly switched off after the scattering pulse, such that this error source is avoided.

6.9. Additional Error Sources

Lorenzian lineshape and power broadening: The assumed dependence of the scattering rates on the Raman detuning $R \propto \Delta_R^{-2}$ is only valid for $\Delta_R \gg \Gamma'$, where $\Gamma' = \Gamma\sqrt{1-S}$ is the saturation broadened effective linewidth, see Sec. 2.1.1. Under consideration of saturation broadening, Eqs. 6.1 have to be replaced by:

$$\begin{aligned} R_\uparrow &= \Gamma_{PS}\frac{\Omega^2}{\Gamma_{PS}^2 + \frac{2}{3}\Omega^2 + 4\Delta_R^2}\frac{1}{9}\left(\epsilon_-^2 + \epsilon_0^2\right) \\ R_\downarrow &= \Gamma_{PS}\frac{\Omega^2}{\Gamma_{PS}^2 + \frac{2}{3}\Omega^2 + 4\Delta_R^2}\frac{1}{9}\left(\epsilon_+^2 + \epsilon_0^2\right). \end{aligned} \tag{6.25}$$

For the parameter set in the left column of Table 6.1, the error given by the relative difference of the scattering rates with and without consideration of saturation broadening is estimated to be about $5{\cdot}10^{-4}$, which is sufficiently small. A similar estimation still has to be carried out for the Stark shift. In a more sophisticated treatment, saturation broadening can be incorporated in the final result Eq. 6.6 to increase the accuracy.

Scattering curve offset: One might be surprised by the fact that the values for γ in the scattering parameters Eq. 6.21 are found to be zero, however an analysis of the underlying physics leads to a justification the γ is indeed negligible. According to Eq. 6.20, the defining quantities for γ are the false transfer probability from $|\downarrow\rangle$, $r_\downarrow$, and the probability the fluorescence below discrimination threshold is detected albeit the ion is in the bright $S_{1/2}$,$D_{3/2}$ manifold, p_d^S. The false transfer probability is below 1%, which is shown in Fig. 4.21. This translates into a much smaller error in the scattering parameters, because the offset is only a static parameter. p_d^S can be calculated from the fluorescence rates, which were 25 kHz bright counts and 4 kHz dark counts for 3 ms detection time. The result is $p_d^S \simeq 10^{-7}$,see Ref. [Roo00], pp. 119.
Resonant beam components: The laser source for the off-resonant beam is derived from an amplified system with an ASE background spanning several nm, such that sum frequency generation (SFG) with a laser photon and an ASE photon could in principle lead to near resonant components in the doubled beam which might strongly enhance the scattering rate. The conditions for this process would be that the Raman detuning is an integer multiple of two times the SHG cavity FSR of about 500 MHz, furthermore phase matching conditions for SFG have to be fulfilled. To assert that this effect plays no role, a measurement was performed where a scattering pulse of fixed power and duration such that roughly 20% of population of the initially populated $|\uparrow\rangle$ level is removed, while the laser wavelength is scanned sufficiently slow over four SHG cavity FSRs. No resonant features were observed, such we can claim that the SFG effect does not contribute to scattering.
Presence of the $P_{3/2}$ state: The $P_{3/2}$ state also contributes to the Stark shift and scattering rates, however the fine-structure splitting of about 6.8 THz is large compared to the typical Raman detuning, leading to errors in the per mil range for the Stark shift and in the 10^{-6} range for the scattering rates. However, the $P_{3/2}$ contributions can be included in the treatment leading to the result Eq. 6.6.
Zeeman splitting: The Zeeman splitting of roughly 18 MHz within the $S_{1/2}$ manifold and roughly 6 MHz in the $P_{1/2}$ manifold is small compared to the Raman detuning, the errors are of similar magnitudes as for the reasoning for the $P_{3/2}$ state above. Also in this case, the model can be extended to include the Zeeman splitting.

6.10. Complete Measurement by Measuring Absolute Stark Shifts

In this section we briefly present an extension of the measurement scheme which allows for a complete determination of the parameters characterizing the interaction between an atomic system and a classical laser beam. In the final result for the lifetime of the excited state, Eq. 6.6, the Rabi frequency Ω and the polarization components ϵ_i drop out. However, if the Stark shifts of the levels $|\uparrow\rangle$ and $|\downarrow\rangle$ can be measured individually, one obtains sufficient

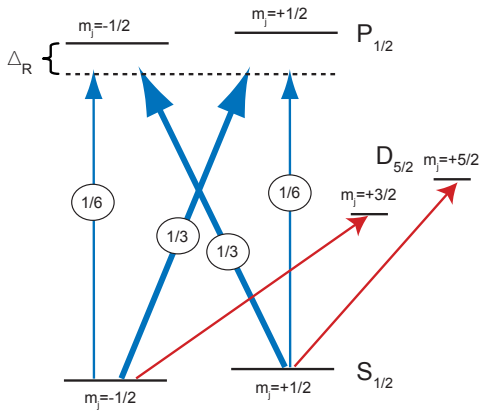

Figure 6.10.: Level scheme for absolute Stark shift measurement: The two red arrows indicate the transitions on which the absolute Stark shifts of the $|\uparrow\rangle$ and $|\downarrow\rangle$ are probed.

information to determine all unknown parameters. We obtain the Rabi frequency

$$\Omega^2 = 12\ \Delta_R\ \left(\Delta_S^{\uparrow} + \Delta_S^{\downarrow}\right), \tag{6.26}$$

and the polarization components:

$$\begin{aligned}
\epsilon_+^2 &= \frac{R_{\downarrow}\Delta_S^{\downarrow} + R_{\downarrow}\Delta_S^{\uparrow} - 2\ R_{\uparrow}\Delta_S^{\downarrow}}{\left(\Delta_S^{\uparrow} + \Delta_S^{\downarrow}\right)(R_{\uparrow} - R_{\downarrow})} \\
\epsilon_-^2 &= \frac{2\ R_{\downarrow}\Delta_S^{\uparrow} - R_{\uparrow}\Delta_S^{\downarrow} - R_{\uparrow}\Delta_S^{\uparrow}}{\left(\Delta_S^{\uparrow} + \Delta_S^{\downarrow}\right)(R_{\uparrow} - R_{\downarrow})} \\
\epsilon_0^2 &= -2\frac{R_{\downarrow}\Delta_S^{\uparrow} - R_{\uparrow}\Delta_S^{\downarrow}}{\left(\Delta_S^{\uparrow} + \Delta_S^{\downarrow}\right)(R_{\uparrow} - R_{\downarrow})}.
\end{aligned} \tag{6.27}$$

In the case of the $^{40}Ca^+$ ion, the quadrupole transition at 729 nm can be utilized to measure the absolute Stark shifts. Fig. 6.10 shows the relevant transitions: The Stark shift of the $|\uparrow\rangle$ levels is probed on the $|\uparrow\rangle \rightarrow |D_{5/2}, m_J = +5/2\rangle$ transition and the shift of the $|\downarrow\rangle$ levels is probed on the $|\downarrow\rangle \rightarrow |D_{5/2}, m_J = +3/2\rangle$ transition. The same basic Ramsey sequence as in Sec. 6.5 is used, only that the 729 nm laser is employed for the Ramsey pulses, the measurement sequences are depicted in Fig. 6.11 d). The precision of these measurements is mostly impaired by the drift of the PDH cavity of the 729 nm laser stabilization. For a Ramsey delay time of 20 μs and an absolute shift $2\pi{\cdot}2$ MHz, a resonance drift of 25 kHz would lead to an additional phase slip by π throughout the data acquisition, leading to a difference of one fringe compared 40 expected ones, which amounts to an error of 2.5%. At typical drift

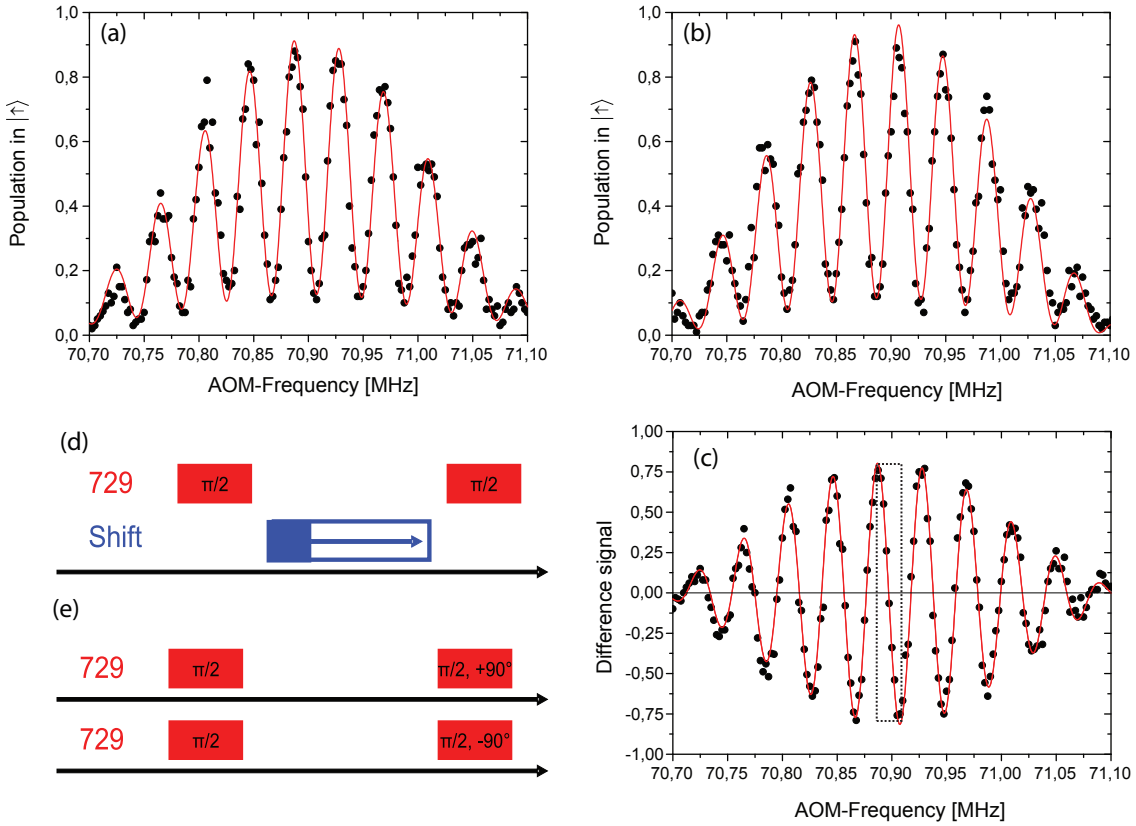

Figure 6.11.: Measurement scheme for the absolute Stark shift: **a)** and **b)** show resulting Ramsey fringes for the two measurement sequences indicated in **e)**. The difference signal is shown in **c)** along with the capture range of the resonance tracking (dashed box). **d)** shows the measurement sequence for the absolute Stark shift measurement.

rates of about 10 kHz per hour and data acquisition times of up to 20 minutes, this can lead to considerable measurement errors. The solution for this problem is an automatic tracking of the resonance performed during the actual measurement. To keep the measurement effort for this at a minimum, a single measurement providing a value (instead of a curve from which the resonance locations can be derived as a fit parameter) from which the location of the resonance can be inferred is required. Such a measurement scheme was demonstrated in Ref. [Let04]: Two Ramsey measurements (without shift pulse) are performed where in one case the concluding pulse has a $+\pi/4$ phase shift with respect to the first pulse, and the in the other case the phase shift is $-\pi/4$. The sequences are depicted in Fig. 6.11 e). Measurement results for the two sequences are shown in a) and b), and the difference between the two signals is shown in c). The signal within the dashed box has a zero crossing at resonance, this represents the capture range for which a correction frequency can be calculated to calculate the new resonance frequency. The extra phase shift from an off-resonance of δ for a Ramsey delay τ

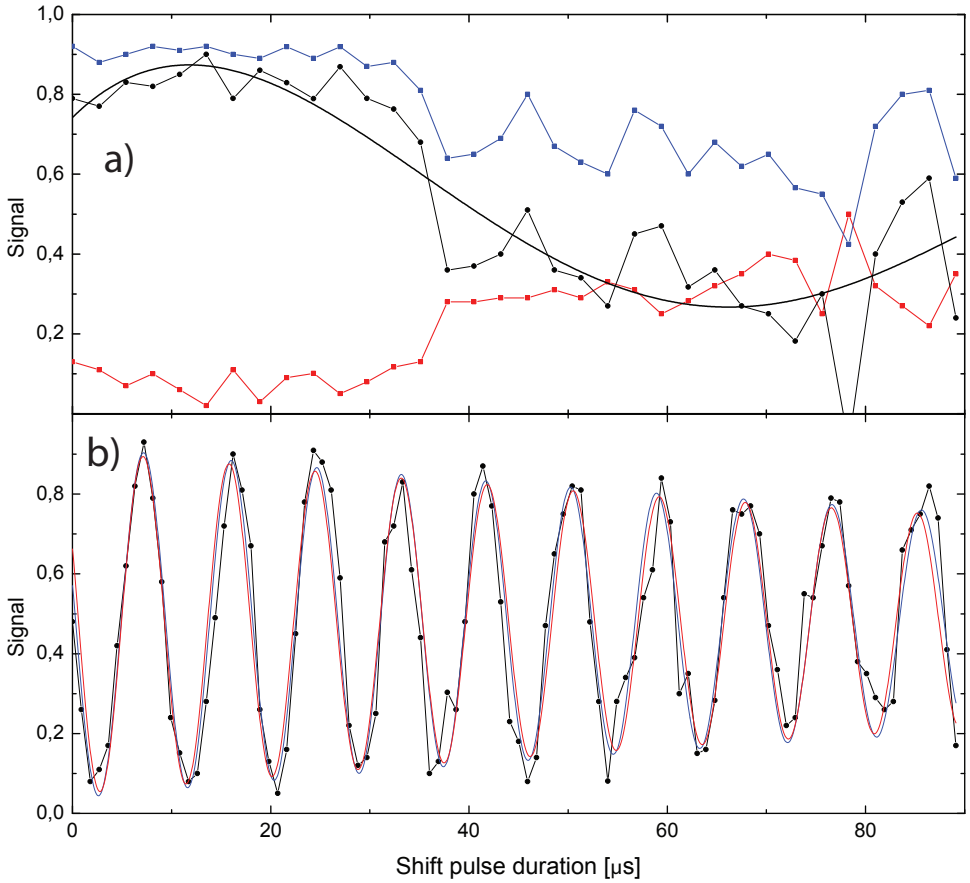

Figure 6.12.: Drift compensated Stark shift measurement: **a)** shows the signals from the measurement sequences from Fig. 6.11 e) (red and blue curves) performed during a Stark shift measurement run on the $|\uparrow\rangle \rightarrow |D_{5/2}, m_J = +5/2\rangle$ transition. The difference signal (black) along with a 5th order polynomial fit (black solid curve) is indicating the drift of the resonance. **b)** shows the corresponding Stark shift measurement data (black) along with a simple fit to Eq. 6.14 (blue) and a fit including the drift measurement data (red).

is given by $\phi_\delta = \delta\tau$, and the difference signal is calculated using Eq. 2.12 to be

$$\Delta X = -\frac{1}{\sqrt{2}}\sin(\delta\tau), \tag{6.28}$$

which leads to

$$\phi_\delta = \arcsin(-\sqrt{2}\Delta X) \tag{6.29}$$

Fig. 6.12 shows data from an absolute Stark shift measurement with resonance tracking. The tracking data was taken only at every second data point. A polynomial fit to the difference signal from the sequences with the two different analysis phases is of 5h order is performed,

giving a smooth approximate time-dependent extra phase shift $\Delta X(t)$, which is incorporated into Eq. 6.14:

$$S(t) = a\ e^{-\gamma\ t} \sin(\Delta_S\ t - \phi_\delta(t) + \phi) + b. \tag{6.30}$$

Fits to the simple model and the corrected model are shown in Fig. 6.12 b), where on can see a considerable difference between the results. In this specific case, the relative difference of the resulting shift is about 1.8%, which is clearly beyond the accuracy of the fit result of 0.18%. We therefore conclude that the accuracy of the measurement can be increased by about one order of magnitude by utilizing the resonance tracking method, which only doubles the data acquisition effort.

7. Motional State Tomography

This chapter deals with the experimental reconstruction of the density matrix describing the quantum state of the axial mode of vibration of a single trapped atom. The techniques established for coherent qubit manipulation are now extended by Raman sideband cooling, which represents a necessary ingredient for the investigation of the quantized harmonic motion of the ion. The measurement presented in this chapter is to be seen as a demonstration of quantum state tomography. The precise control and measurement of the ion's motional state which is accomplished serves as a basis for many experiments, some of which have been performed within the scope of this thesis such as the ones presented in Sec. 8.3, while envisaged experiments in the field of quantum thermodynamics heavily rely on the techniques demonstrated here, see [Hub08],[Hub10a]. Rabi oscillations on the blue motional sideband of the stimulated Raman transition between the qubit levels $|\uparrow\rangle$ and $|\downarrow\rangle$ provide information about the motional state, as it was demonstrated in Sec. 4.6. As can be seen from Eq. 2.56, only the phonon occupation probabilities, i.e. the diagonal elements of the density matrix can be extracted from a single scan, no information about the off-diagonal elements is obtained. Thus, one has to resort to a measurement protocol where phonon distributions are acquired for various conditions, and from this data the density matrix can be reconstructed. Because of the analogy to experiments utilizing photons, where integrals of phase space distribution functions are measured from which these distribution can be obtained by means of the inverse Radon transform, these measurement methods are summarized as *quantum state tomography*. A pioneering experiment on the generation and characterization of nonclassical states has been performed in [Mee96], which was extended to a tomographic reconstruction of the density matrix characterizing the quantum state of the system in [Lei96].

7.1. The Method

The tomography method of our choice consists in the acquisition of blue sideband Rabi oscillations after an arbitrary additional displacement of the motional mode. The general expression for the probability $Q_k(\alpha, \rho)$ the find k phonons after a displacement operation $U(\alpha)$ on the initial state described by the density matrix ρ is

$$Q_k(\alpha, \rho) = \langle k|U^\dagger(\alpha)\ \hat{\rho}\ U(\alpha)|k\rangle. \tag{7.1}$$

In order to find an expression which can be evaluated in terms of α, k and the matrix elements ρ_{nm}, this can be rewritten as

$$\begin{aligned} Q_k(\alpha,\rho) &= \sum_{nm} \rho_{nm}\langle k|U^\dagger(\alpha)|n\rangle\langle m|U(\alpha)|k\rangle \\ &= \sum_{nm} \rho_{nm}\langle n|U(\alpha)|k\rangle^*\langle m|U(\alpha)|k\rangle, \end{aligned} \tag{7.2}$$

with the matrix element

$$\langle k|U(\alpha)|n\rangle = \begin{cases} \sqrt{\frac{n!}{k!}}e^{-\frac{|\alpha|^2}{2}}\alpha^{k-n}L_n^{k-n}\left(|\alpha|^2\right) & \text{for } k > n, \\ \sqrt{\frac{k!}{n!}}e^{-\frac{|\alpha|^2}{2}}(-\alpha)^{n-k}L_k^{n-k}\left(|\alpha|^2\right) & \text{for } n \leq k, \end{cases} \tag{7.3}$$

from Ref. [El-99]. It was found that the matrix elements Eq. 7.3 do not correctly account for imaginary α's, which inevitably occur in the measurement scheme as the orientation of the frame of reference is fixed by possible initial displacement. An alternative derivation along the lines of Ref. [Lei96] is as follows:

$$\begin{aligned} Q_k(\alpha,\rho) &= \langle 0|a^k U^\dagger(\alpha)\ \hat{\rho}\ U(\alpha)a^{\dagger k}|0\rangle \\ &= \frac{1}{k!}\langle\alpha|U(\alpha)a^k U^\dagger(\alpha)\ \hat{\rho}\ U(\alpha)a^{\dagger k}U^\dagger(\alpha)|\alpha\rangle \\ &= \frac{1}{k!}\langle\alpha|(a-\alpha)^k\ \hat{\rho}\ a^\dagger - \alpha^*)^k|\alpha\rangle \\ &= \frac{1}{k!}\sum_{nm}\rho_{nm}\langle\alpha|(a-\alpha)^k|n\rangle\langle m|(a^\dagger-\alpha^*)^k|\alpha\rangle. \end{aligned} \tag{7.4}$$

The matrix elements herein are found to be

$$\begin{aligned} \langle\alpha|(a-\alpha)^k|n\rangle\top &= \sum_{j=0}^{k}\binom{k}{j}(-1)^j\alpha^j\langle\alpha|a^{k-j}|n\rangle \\ &= \sum_{j=0}^{k}\binom{k}{j}(-1)^j\alpha^j\sqrt{\frac{n!}{(n-k+j)!}}\langle\alpha|n-k+j\rangle \\ &= e^{-\frac{|\alpha|^2}{2}}\sum_{j=0}^{k}\binom{k}{j}(-1)^j\alpha^j\frac{\sqrt{n!}}{(n-k+j)!}\alpha^{*(n-k+j)}. \end{aligned} \tag{7.5}$$

Equivalently, one finds

$$\langle m|a^\dagger-\alpha^*)^k|\alpha\rangle = e^{-\frac{|\alpha|^2}{2}}\sum_{j=0}^{k}\binom{k}{j}(-1)^j\alpha^{*j}\frac{\sqrt{\angle m!}}{(m-k+j)!}\alpha^{(m-k+j)}. \tag{7.6}$$

This finally yields

$$\begin{aligned} Q_k(\alpha,\rho) &= \frac{e^{-|\alpha|^2}}{k!}\sum_{nm}\rho_{nm}\sum_{j_1,j_2=0}^{k}\binom{k}{j_1}\binom{k}{j_2}(-1)^{j_1+j_2}\alpha^{j_1}\alpha^{*j_2} \\ &\quad\times\frac{\sqrt{n!m!}}{(n-k+j_1)!(m-k+j_2)!}\alpha^{*(n-k+j_1)}\alpha^{(m-k+j_2)}. \end{aligned} \tag{7.7}$$

This is exactly the required implicit expression for the matrix elements ρ_{nm}, where quantities extracted from the measurement data are on the lhs of the equation. This allows for finding a density matrix leading to the measurement results by means of a maximum likelihood method.

In order find the density matrix pertaining to the phonon distributions found from the measured data, a parametrization in terms of a set real number has to be used that keeps the matrix in the space of matrices with the required properties, i.e. a) Hermiticity $\rho_{ij}=\rho_{ji}^*$ and b) trace normalization $\mathrm{Tr}\rho=1$ and c) ρ has to be positive definite $\langle\Psi|\rho|\Psi\rangle>0$ and real for any $|\Psi\rangle$. Such a representation is given by [Jam01]

$$\rho=\frac{T^\dagger T}{\mathrm{Tr}T^\dagger T} \tag{7.8}$$

with

$$T=\begin{pmatrix} t_0 & 0 & 0 & \cdots \\ t_{01} & t_1 & 0 & \cdots \\ t_{02} & t_{12} & t_2 & \cdots \\ \vdots & \vdots & \vdots & \ddots \end{pmatrix} \tag{7.9}$$

The quantity to be minimized is then sum of the squares of the measured phonon occupation probabilities and the ones predicted by a trial ρ_T:

$$F=\sum_{k=0}^{k_{max}}\sum_{p=0}^{N}\left(P_k(\alpha_p)-Q_k(\alpha_p,\rho_T)\right)^2, \tag{7.10}$$

where the minimization is carried out in the space of the $n_{\max}+1+n_{\max}(n_{\max}+1)/2$ real parameters from Eq. 7.9.

7.2. The Measurement Scheme

Displacement operations are carried out by connecting two phase-locked rf-synthesizers (termed in the following as the *preparation* and the *analysis* synthesizers) to the two different electrodes making up the endcap electrode of the loading region. These electrodes are located far enough from the ion that the arising electric fields at the ion position (segment 5) can be considered as homogeneous and pointing along the trap axis. If the synthesizer frequency corresponds to the axial vibrational frequency, a displacement operation of the axial mode is

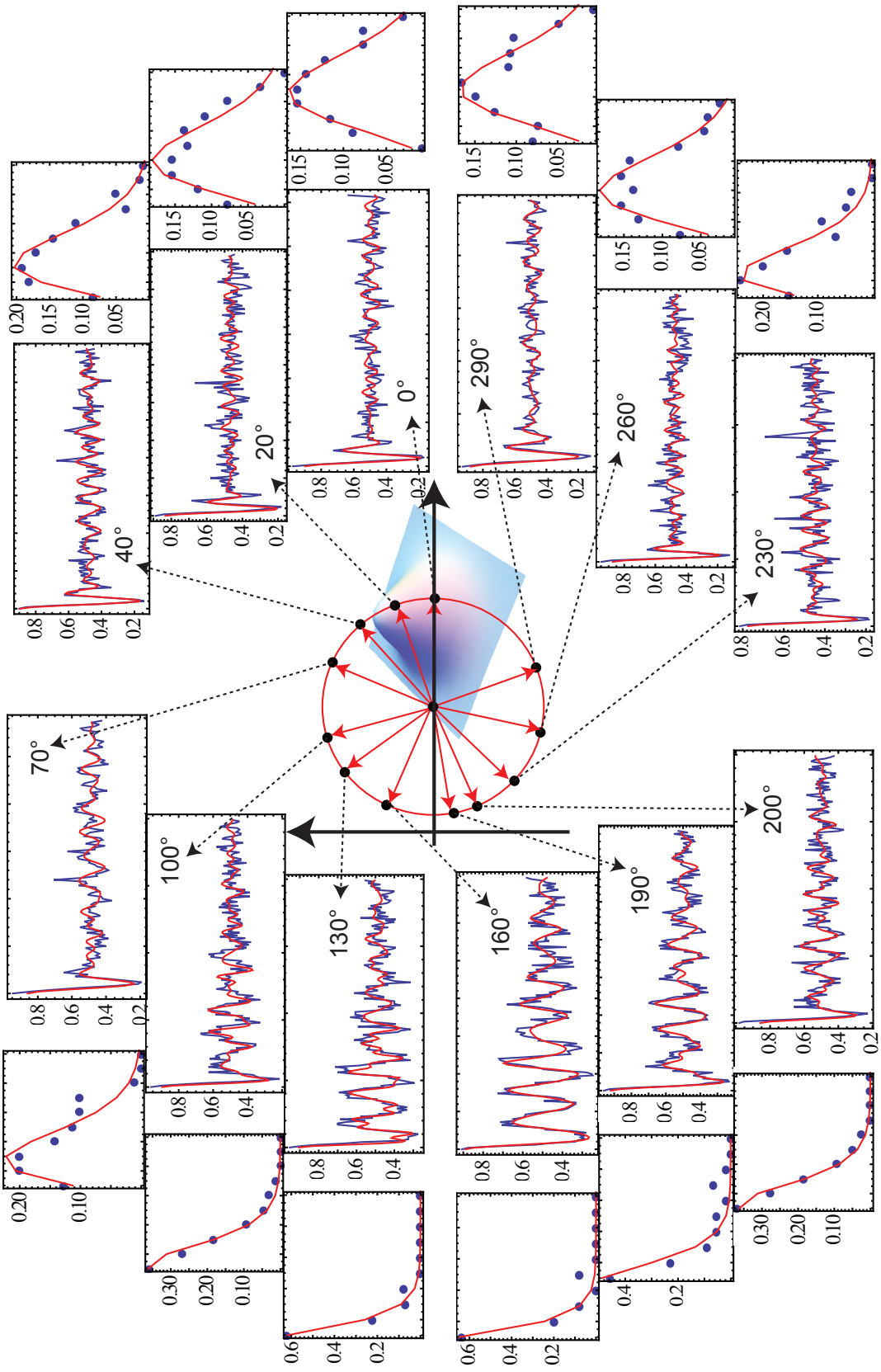

Figure 7.1.: The complete tomography measurement: For each analysis displacement, the resulting Rabi oscillations are shown along with the fitted phonon distributions.

achieved, where the resulting displacement is proportional to the pulse time if one is exactly at resonance. The displacements achieved this way are analyzed by performing a pulse width scan on the bsb of the stimulated Raman transition. The bsb Rabi oscillation data is fitted to a slightly modified version of Eq. 2.56:

$$\begin{aligned} p_e(t) &= \frac{1}{2}\left(b - a_0 \sum_n e^{\gamma_n t} p_n \cos(\Omega_{n,n+1} t)\right) \\ &\approx \frac{1}{2}\left(b - a_0 e^{\gamma_{eff} t} \sum_n p_n \cos(\Omega_0 M_{n,n+1} t)\right), \end{aligned} \tag{7.11}$$

which takes several experimental imperfections into account. Readout errors are accounted for by the contrast parameter a_0 and the baseline b. Decoherence effects manifest themselves through the motion dependent rate γ_n, which can hardly be individually resolved, thus an effective rate γ_{eff} depending on the overall motional state is used. The fitting method is explained in detail in Appendix C.

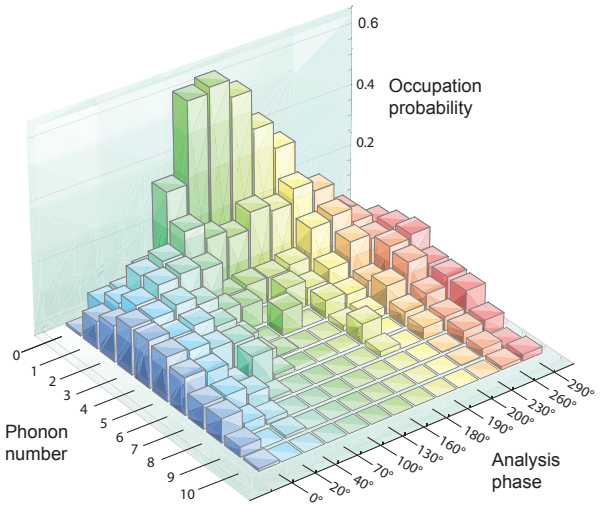

Figure 7.2.: Resulting phonon distributions: The diagram shows the measured phonon distributions as shown in the small insets in Fig. 7.1 versus the analysis phase. Not that the data point for 180° was not included in Fig. 7.1. One clearly recognizes the narrowing of the distributions as the analysis pulse drives the wavefunction back to the origin of phase space.

In order to make a reconstruction of the quantum state of the ion motion possible, the resulting displacements from the rf drive have to be gauged versus the synthesizer amplitude. This is done by taking bsb Rabi oscillation scans for four pulse amplitudes of the analysis synthesizer, which drives the ion for 10 μs prior to the bsb pulse. The resulting signal is fitted to Eq.7.11 by means of the method described in appendix C. The result is a linear relation between the analysis displacement and the analysis rf amplitude of $\alpha = 0.104(1)\ \text{mV}^{-1}$. The

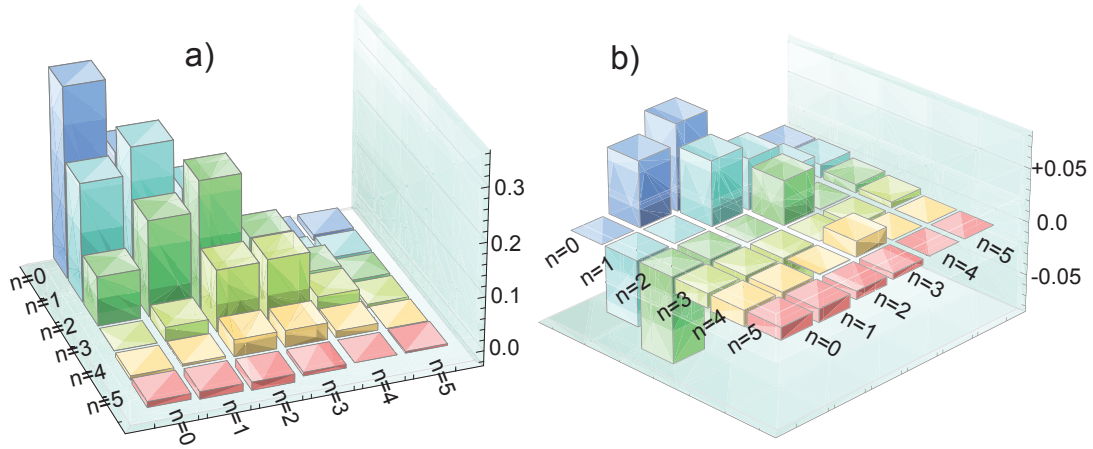

Figure 7.3.: Resulting density matrix: The density matrix obtained from the measurement data shown in Fig. 7.1 by means of a maximum-likelihood reconstruction is shown. The left diagram shows the real parts and the right diagram shows the imaginary parts. The density matrix pertains to a coherent state with a displacement of $\alpha \approx 0.295 + i\ 0.195$, where the imaginary part is presumably due to slight off-resonance of the displacement drive from the vibrational frequency.

tomography itself is then carried out by preparing a coherent state by displacing the motion by means of a pulse of fixed amplitude, duration and phase from the preparation synthesizer, and then exerting a second displacement pulse with fixed duration and amplitude but varying phase with the analysis synthesizer. The preparation amplitude is 70 mV, and the analysis amplitude is chosen to be 100 mV. The resulting signal then depends on the difference vector of the two displacement operations. Fig. 7.1 shows the resulting data for the different analysis displacement phases in detail. For the resulting phonon distributions establish the lhs of Eq. 7.7, while the calibration data determines the rhs. The data is then fed into a genetic algorithm which builds test density matrices out of initially random number according to the recipe given by Eq. 7.9. The *fitness* of each each test density matrix is then evaluated by comparing the expected phonon distributions from the test matrix to the measured data according to the fidelity function Eq. 7.10. After several iterations of the algorithm, a valid density matrix optimally reproducing the measurement data is found. The real and imaginary

parts of the retrieved matrix are shown in Fig. 7.3. This matrix pertains to a coherent state with a displacement of $\alpha \approx 0.295 + i\ 0.195$. The nonvanishing imaginary part is presumably due to a detuning of the drive rf from the motional mode. This is due to the fact that the spectroscopic determination of the motional frequency is always obscured by Stark shifts from the off-resonant light and from the off-resonant driving of carrier Rabi oscillations.

8. Preparation and Characterization of Schrödinger Cat States

This chapter gives a detailed account on the preparation and characterization of states with entanglement between spin and motion. The basic mechanism for the generation of these states is the usage of spin-dependent light forces, which is explained in detail in Sec. 8.1. In sec. 8.2, the influence of the preparation of the initial state on the evolution under these forces is investigated, and in Sec. 8.3, the dynamics of the phonon distribution during this kind of dynamics is presented. Finally, in Sec. 8.4, results from measurements where spin-dependent forces are used to establish a general, precise and efficient state tomography scheme are shown.

8.1. Preparation of a Schrödinger Cat State of a Single Ion

In order to express his objections against quantum theory, Erwin Schrödinger devised a famous Gedankenexperiment where a quantum superposition state of a microscopic object is mapped to a superposition state of a macroscopic object, which was exemplified by a cat being dead and alive at the same time. It is known today that quantum interference phenomena of macroscopic objects are not observed in every day life because unavoidable interaction of such objects with their surroundings leads to a loss of their quantum coherence on extremely fast timescales determined by the distinguishability. This process is termed *decoherence*, and it is the reason why most experiments demonstrating pure quantum behavior are carried out on either microscopic objects which are isolated from other objects with a tremendous experimental effort, or on particles that are interacting weakly with the environment, e.g. photons. It is however still an open question how far the transfer of quantum coherence from smaller to larger scale, which is termed the von-Neumann chain, can be principally pushed, i.e. if there is a yet unknown fundamental limit leading to the impossibility of observing quantum superpositions in the macroscopic world. This is one of the main motivations for creating large-scale entanglement of many qubits in devices like our segmented ion trap.

Schrödinger cat states could be successfully prepared in ion traps by utilizing state dependent light forces [Mon96]. Their decoherence behavior in engineered reservoirs was extensively studied in [Mya00]. In these experiments, the state of an internal (electronic) degree of freedom determines the motional behavior upon exposure to a tailored laser field. Therefore, an internal state superposition leads to a nonclassical superposition of motional states, which could in principle be made arbitrarily large under perfect conditions. The resulting joint quantum states exhibit entanglement between internal and external degrees of freedom, which suggests the usage of spin dependent forces for two-qubit entangling gates. How two-

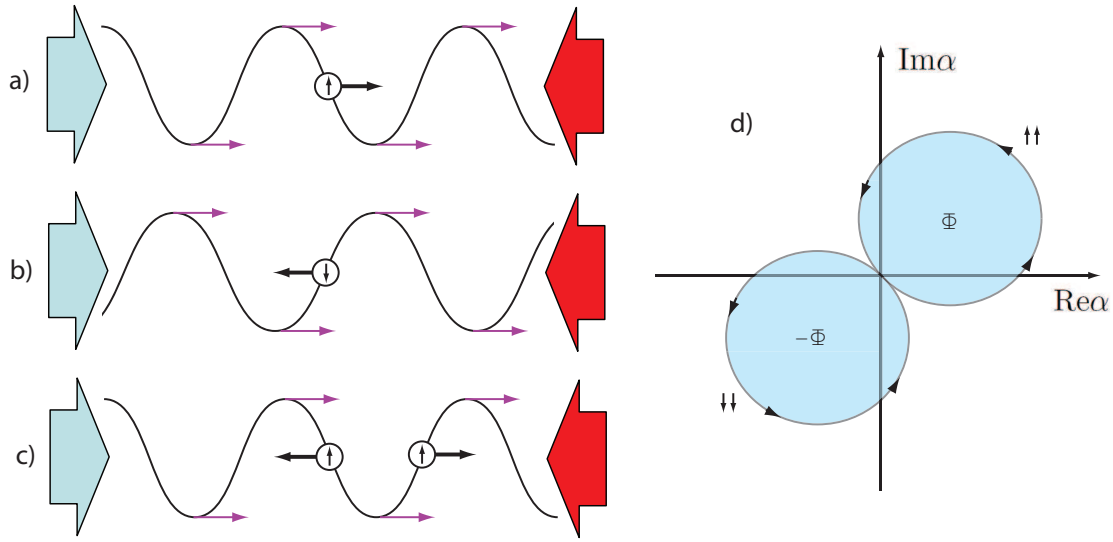

Figure 8.1.: Illustration of the spin-dependent light force: **a)** shows an ion in the internal state $|\uparrow\rangle$ in two counterpropagating laser fields with a relative detuning δ. The solid sinusoidal lines indicate the Stark shift arising from the beat pattern for the corresponding spin state. The purple arrows indicate the movement of the beat pattern due to the relative detuning, and the arrow on the ion shows the force arising due to the inhomogeneous Stark shift. **b)** shows the same situation with the ion being in the $|\downarrow\rangle$ state, experiencing the opposite force. **c)** shows a two-ion crystal with both ions in the $|\uparrow\rangle$ state, aligned along the standing wave such that their distance matches half the wavelength, such that the stretch mode of the crystal is excited by the moving beat pattern. **d)** shows the trajectories for different states in the phase space of a motional mode, where the relative laser detuning slightly mismatches the vibrational frequency by δ_ϵ. For the $|\uparrow\downarrow\rangle$ and $|\downarrow\uparrow\rangle$ states, the force cancels and the mode is not displaced throughout the exposure to the light field. The geometric phase Φ accumulated during one closed cycle in phase space is indicated in the circles.

ion gates can be realized via the creation Schrödinger cat state is explained in detail in Sec. 9.5.

We consider a situation where a single ion is placed into a beat pattern of the Raman beams R2 and CC, see Sec. 3.2.5, which is aligned along the trap axis. The effective k-vector thus reads

$$\Delta\vec{k} \approx \frac{2\pi}{\lambda} \sin\theta \vec{e}_x, \tag{8.1}$$

where $\theta \approx \pi/2$ is the relative angle of the two beams and the small frequency difference has been neglected. The CC beam is blue detuned by δ_R relative to the R2 one. It is assumed that the Raman detuning is much larger than the Zeeman splitting $|\Delta_R| \gg \mu_B g_{S_{1/2}}$ and

the atomic linewidth $|\Delta_R| \gg \Gamma$. As we do not want to drive stimulated Raman processes between $|\uparrow\rangle$ and $|\downarrow\rangle$ but rather to give rise to Stark shifts, we chose the beam geometry such that only circular components are present. We can now invoke Eq. A.16 to obtain the Stark shift exerted by the two beams:

$$\begin{aligned}\Delta_S &= \frac{1}{12\Delta_R}\left(\Omega_b^2\left(\epsilon_{b-}^2-\epsilon_{b+}^2\right)+\Omega_r^2\left(\epsilon_{r-}^2-\epsilon_{r+}^2\right)\right)\\ &+ \Omega_r\Omega_b\left(\epsilon_{r-}\epsilon_{b-}^* e^{i(\Delta kx-\delta_R t+\Delta\phi)}-\epsilon_{r+}\epsilon_{b+}^* e^{i(\Delta kx-\delta_R t+\Delta\phi)}+\text{c.c.}\right).\end{aligned} \tag{8.2}$$

Considering that the $-$ components act only on the $|\uparrow\rangle$ state and the $+$ components act only on the $|\downarrow\rangle$ state, we can write down a corresponding Hamiltonian operator

$$\begin{aligned}H_S &= \frac{\hbar}{12\Delta_R}\left(\Omega_b^2\epsilon_{b-}^2+\Omega_r^2\epsilon_{r-}^2+\Omega_r\Omega_b\epsilon_{r-}\epsilon_{b-}^* e^{i(\Delta kx-\delta_R t+\Delta\phi)}\right)|\uparrow\rangle\langle\uparrow|\\ &+ \frac{\hbar}{12\Delta_R}\left(\Omega_b^2\epsilon_{b+}^2+\Omega_r^2\epsilon_{r+}^2+\Omega_r\Omega_b\epsilon_{r+}\epsilon_{b+}^* e^{i(\Delta kx-\delta_R t+\Delta\phi)}\right)|\downarrow\rangle\langle\downarrow|.\end{aligned} \tag{8.3}$$

The CC beam is vertically polarized, such that Eqs. 2.26 yield $\epsilon_{b-}=\epsilon_{b+}=i/\sqrt{2}$. R2 is assumed to propagate exactly in parallel to the quantizing magnetic field, only the rotation angle ϕ_r can be freely adjusted, which leads to $\epsilon_{r\pm}=(i\sin\phi_r\pm\cos\phi_r)/\sqrt{2}$. Inserting these polarizations into Eq. 8.3 yields

$$\begin{aligned}H_S &= \frac{\hbar\Omega_r\Omega_b}{12\Delta_R}\left(\sin\phi_r\cos(\Delta k\hat{x}-\delta_R t+\Delta\phi)-\cos\phi_r\sin(\Delta k\hat{x}-\delta_R t+\Delta\phi)\right)|\uparrow\rangle\langle\uparrow|\\ &+ \frac{\hbar\Omega_r\Omega_b}{12\Delta_R}\left(\sin\phi_r\cos(\Delta k\hat{x}-\delta_R t+\Delta\phi)+\cos\phi_r\sin(\Delta k\hat{x}-\delta_R t+\Delta\phi)\right)|\downarrow\rangle\langle\downarrow|.\end{aligned} \tag{8.4}$$

From the $\cos\phi_r$ factor, it can be seen that a pure *differential* shift only arises for $\phi_r=0$, i.e. if the R2 beam polarization is horizontally aligned. We then obtain

$$H_S=\hbar\Delta_S\sin(\Delta k\hat{x}-\delta_R t+\Delta\phi)\hat{\sigma}_z. \tag{8.5}$$

with the *dynamical* Stark shift amplitude

$$\Delta_S=\frac{\Omega_r\Omega_b}{12\Delta_R}, \tag{8.6}$$

which is not to be confused with the *static* Stark shift

$$\hat{H}_S^{(0)}=\frac{1}{12\Delta_R}\left((\epsilon_{r+}^2-\epsilon_{r-}^2)\Omega_r^2+(\epsilon_{b+}^2-\epsilon_{b-}^2)\Omega_b^2\right)\hat{\sigma}_z, \tag{8.7}$$

which is set to zero by appropriate choice of the polarizations. The Hamiltonian contains products of the position and spin operators, it therefore becomes immediately clear that it can be used to entangle spin and motion. Eq. 8.5 can be rearranged to

$$\hat{H}_S=\hbar\Delta_S(\sin(\Delta k\hat{x})\cos(\delta_R t-\Delta\phi)-\cos(\Delta k\hat{x})\sin(\delta_R t-\Delta\phi))\hat{\sigma}_z. \tag{8.8}$$

Upon Taylor expansion of the spatial parts this yields

$$\hat{H}_S \approx \hbar\Delta_S(\Delta k\hat{x}\cos(\delta_R t - \Delta\phi) - \sin(\delta_R t - \Delta\phi))\hat{\sigma}_z + \mathcal{O}(\Delta k^2\hat{x}^2). \tag{8.9}$$

This holds in the Lamb-Dicke regime, where $\Delta kx \ll 1$. The $\sin(\delta t - \Delta\phi)$ term simply gives rise to an oscillating phase:

$$\phi_{\text{osc}} = \frac{\Delta_S}{\delta_R}(\cos(\delta_R t - \Delta\phi) - \cos(\Delta\phi))\hat{\sigma}_z, \tag{8.10}$$

which vanishes for $t = 2\pi n/\delta_R$. The Hamiltonian therefore reduces to

$$\hat{H}_S = \hbar\Delta_S\Delta k\hat{x}\cos(\delta_R t - \Delta\phi)\hat{\sigma}_z. \tag{8.11}$$

We can now write $\hat{x}$ in terms of ladder operators, $\hat{x} = x_0(\hat{a} + \hat{a}^\dagger)$, and replace these by their interaction picture versions $\hat{a}_I = e^{iH_0 t/\hbar}\hat{a}e^{-iH_0 t/\hbar} = e^{i\omega t}\hat{a}$, with $H_0 = \hbar\omega(\hat{a}^\dagger\hat{a} + 1/2)$ where ω is the motional frequency of the harmonic oscillator. We finally obtain the Hamiltonian in the interaction picture:

$$\begin{aligned}\hat{H}_S^{(I)} &= \hbar\Delta_S\Delta k\ x_0(\hat{a}e^{-i\omega t} + \hat{a}^\dagger e^{i\omega t})\cos(\delta_R t - \Delta\phi))\hat{\sigma}_z \\ &\approx \hbar\frac{\eta\ \Delta_S}{2}(\hat{a}e^{i(\delta t + \Delta\phi)} + \hat{a}^\dagger e^{-i(\delta t - \Delta\phi)})\hat{\sigma}_z,\end{aligned} \tag{8.12}$$

where $\eta = \Delta kx_0$ is the Lamb-Dicke factor and the detuning from the motional frequency, $\delta = \delta_R - \omega$ was introduced. The terms rotating at $\delta_R + \omega$ were dropped. The dynamics governed by this Hamiltonian can be easily understood by considering that according the Hellmann-Feynman theorem, the quantum mechanical analogue of a force is given by

$$\langle\mathcal{F}\rangle = \langle\Psi|\frac{d\hat{H}}{d\hat{x}}|\Psi\rangle, \tag{8.13}$$

such that the part proportional to $\hat{x}$ can be written as a spin-dependent oscillating force:

$$\langle\mathcal{F}\rangle_S = \hbar\Delta_S\Delta k\cos(\delta_R t - \Delta\phi)\hat{\sigma}_z. \tag{8.14}$$

Ignoring the dependence on the spin for the moment, this is the quantum version of the forced harmonic oscillator: If the initial state is a coherent state, the dynamics can be described semiclassically. The center-of-mass motion obeys the classical equation of motion with the force given by Eq. 8.14 and the wavefunction always retains its shape. Additionally, a non-classical geometric phase is picked up.
The propagator pertaining to the interaction picture Hamiltonian Eq. 8.12 is given by the following expression:

$$\hat{U}_{H_S^{(I)}}(t) = e^{i\phi_{osc}(t)\hat{\sigma}_z}e^{i\Phi(t)}\hat{D}(\alpha(t)), \tag{8.15}$$

with the displacement operator

$$\hat{D}(\alpha) = e^{\alpha\hat{a}^\dagger - \alpha^*\hat{a}}. \tag{8.16}$$

The parameters $\alpha(t)$ and $\Phi(t)$ can by analytically found by writing down the general solution of the time-dependent Schrödinger equation as a Magnus expansion up to second order:

$$\hat{U}_{H_S^{(I)}}(t) = \exp\left(-\frac{i}{\hbar}\left(\int_0^t \hat{H}_S^{(I)}(t')dt' - \frac{i}{2\hbar}\int_0^t\int_0^{t'}[\hat{H}_S^{(I)}(t'),\hat{H}_S^{(I)}(t'')]dt'dt'' + ...\right)\right). \quad (8.17)$$

Keeping only the first term of the Magnus expansion, inserting Eq. 8.12 and comparing with Eq. 8.16, we obtain the time-dependent displacement $\alpha(t)$

$$\begin{aligned}\alpha(t) &= -i\frac{\eta\Delta_S}{2}\int_0^t e^{-i(\delta t' - \Delta\phi)}dt' \\ &= \frac{\eta\Delta_S}{2\delta}e^{i\Delta\phi}(e^{-i\delta t}-1) \\ &= -i\frac{\eta\Delta_S}{\delta}e^{i\Delta\phi}e^{-i\frac{\delta t}{2}}\sin\frac{\delta t}{2}. \end{aligned} \quad (8.18)$$

The geometric phase results from the second order contribution from the Magnus expansion Eq. 8.17. With the commutator evaluated to be

$$[\hat{H}_S(t'),\hat{H}_S(t'')] = i\frac{\hbar^2\eta^2\Delta_S^2}{2}\sin(\delta(t'-t'')), \quad (8.19)$$

we can evaluate the double integral,

$$\int_0^t\int_0^{t'}[\hat{H}_S(t'),\hat{H}_S(t'')]dt'dt'' = -i\frac{\hbar^2\eta^2\Delta_S^2}{2}\frac{\sin\delta t - \delta t}{\delta^2} \quad (8.20)$$

such that we finally obtain for the geometric phase

$$\Phi(t) = \frac{\eta^2\Delta_S^2}{4}\frac{\sin\delta t - \delta t}{\delta^2}. \quad (8.21)$$

As can be directly seen in the derivation, the geometric phase is a consequence of the non-commutativity of the Hamiltonian at different intermediate times, i.e. the final state of the system depends on intermediate steps in the time evolution, such that different classical trajectories ending up at the same displacement can still yield different geometric phases. The geometric phase can also be expressed by the area encircled by the trajectory, which is given by

$$\begin{aligned}\Phi(t) &= \frac{1}{\hbar}\int_0^t \langle x(t')\rangle d\langle p(t')\rangle - \langle p(t')\rangle d\langle x(t')\rangle \\ &= \int_0^t \alpha(t')d\alpha^*(t') - \alpha^*(t')d\alpha(t') \\ &= \int_0^t (\alpha(t')\dot{\alpha}^*(t') - \alpha^*(t')\dot{\alpha}(t'))dt \\ &= -\frac{\eta^2\Delta_S^2}{4\delta}\int_0^t \sin^2\left(\frac{\delta t}{2}\right)dt \\ &= \frac{\eta^2\Delta_S^2}{4\delta^2}(\sin(\delta t) - \delta t) \end{aligned} \quad (8.22)$$

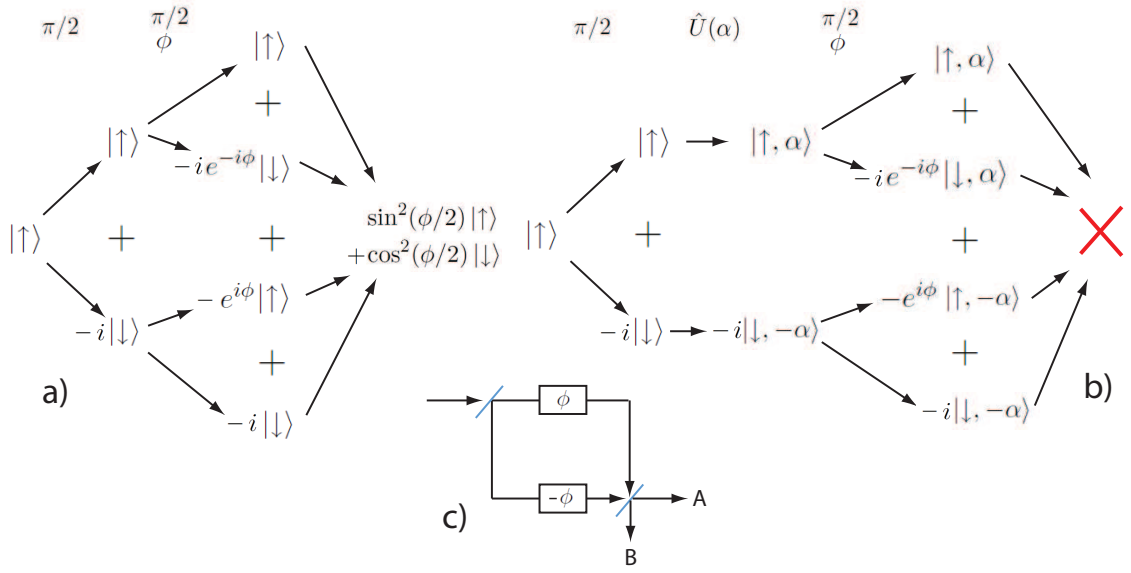

Figure 8.2.: Analogy between the Schrödinger cat experiment and a Mach-Zehnder interferometer: **a)** shows the state evolution during the Ramsey sequence as described in the text, superposition of the four possible paths clearly leads to interference fringes. In case **b)**, the additional displacement leads to cancellation of exactly this interference. **c)** illustrates the Mach-Zehnder interferometer, where a light beam is split into two separate branches which each have an adjustable phase delay. Resuperposition leads to interference fringes, which would be not the case if *which-path-information* can be additionally obtained. The displacement from case b) represents such an information, as the motional state can be read out independently of the spin.

which is identical to Eq. 8.21. Eq. 8.18 has been invoked in the second-last line. If $\delta = 0$, the oscillator is resonantly driven, which would continuously increase the displacement until higher order terms take effect. For a finite δ however, the drive counteracts the oscillation after time $t = \pi/\delta$, such that we end up at the origin at $t = 2\pi/\delta$. The circular trajectories occurring in this case are depicted in Fig. 8.1. The resulting geometric phase is then

$$\Phi(t_f) = 2\pi \frac{\eta^2 \Delta_S^2}{4\delta^2}. \tag{8.23}$$

This geometric phase cannot be observed in the described experimental situation, as both spin components pick up the same phase for balanced driving. However, it plays the crucial role for realizing a quantum gate with two ions, as is pointed out in detail in Chap. 9. How a single-ion Schrödinger cat state is measured by means of an interferometric scheme is illustrated in Fig. 8.2, where the geometric phase is omitted for the sake of simplicity. The interferometer in this case consists of a sequence of two $\pi/2$ pulses, between which

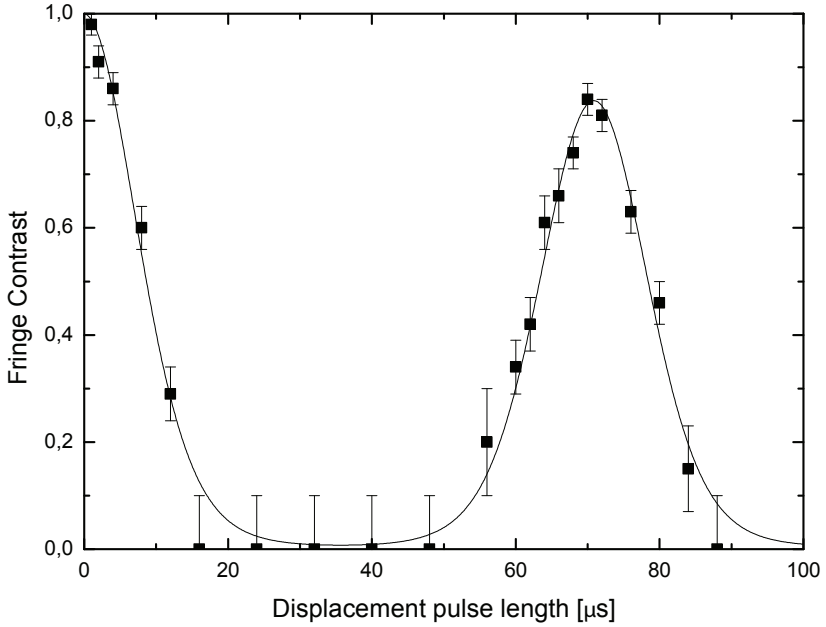

Figure 8.3.: Entanglement-induced contrast loss for the Schrödinger cat state: The curve shows the measured Ramsey contrast versus displacement pulse time, along with a fit to the model Eq. 8.26. After a rapid initial decay due to the displacement, the curve displays a contrast revival after $t = 2\pi/\delta$ when the trajectory goes back to the starting point, such that spin and motion are disentangled again. The maximum size of the cat is reached after half this time, and is found to be $2|\alpha|_{\max} \approx 1.55$.

the displacement force is applied. The final spin state depends on the phase of the second $\pi/2$ pulse, similar to the decoherence measurements of Sec. 4.7. In analogy to a Mach-Zehnder interferometer, the displacement caused by the light force, which is conditional on the spin state, gives a which-path information which leads to the collapse of the Ramsey fringe contrast. As the motional state after application of the force depends on the spin, which is in a coherent superposition of $|\uparrow\rangle$ and $|\downarrow\rangle$ after the first $\pi/2$ pulse, the force leads to entanglement between the spin and motional degree of freedom. This beautifully illustrates how entanglement between a small initial system under observation (the spin) and degrees of freedom of a larger Hilbert space (the motion) obscures the observation of coherence of the initial system.
For the displaced ion, the probabilities to find the ion in either $|\uparrow\rangle$ or $|\downarrow\rangle$ after the analysis

$\pi/2$-pulse are given by

$$\begin{aligned} P_\uparrow &= \frac{1}{2}(1 - \cos\phi\langle -\alpha|\alpha\rangle) = \frac{1}{2}(1 - \cos\phi\ e^{-2|\alpha|^2}) \\ P_\downarrow &= \frac{1}{2}(1 + \cos\phi\langle -\alpha|\alpha\rangle) = \frac{1}{2}(1 + \cos\phi\ e^{-2|\alpha|^2}). \end{aligned} \tag{8.24}$$

The fringe contrast obtained when measuring $P_\uparrow$ while scanning the phase ϕ, $\mathcal{C} = P_\uparrow^{\max} - P_\uparrow^{\min}$, is then given by

$$\mathcal{C} = e^{-2|\alpha|^2}. \tag{8.25}$$

If we now perform the contrast measurement for varying duration t of the displacement pulse, we can insert the time-dependent displacement from Eq. 8.18 into Eq. 8.25:

$$\mathcal{C}(t) = e^{-\frac{\eta^2\Delta_S^2}{\delta^2}\sin^2(\delta t/2)} \tag{8.26}$$

Measurement results are shown in Fig. 8.3, where a spin-echo sequence was used instead of the simple Ramsey sequence in order to reduce decoherence effects, which does not change the result Eq. 8.26. For each data point corresponding to a fixed displacement pulse duration, the phase of the analysis pulse was scanned from 0 to 2π in steps of $\pi/10$. The resulting signal is fitted to a single sine period with floating phase shift, offset and amplitude, and the amplitude gives the Ramsey contrast $\mathcal{C}(t)$. Eq. 8.26 is then fitted to the measured contrast curve, where the detuning from the vibrational frequency, δ, and the displacement amplitude $|\alpha|_{\max} = \eta\Delta_S/2\delta$ are floating and an additional decoherence induced contrast decay factor $e^{-\gamma t}$ with floating γ is included.

8.2. Temperature Dependence and Quantum Effects

For Schrödinger cat experiments under imperfect ground state cooling conditions, as they are discussed later on in Sec. 9.4, it is important to consider the influence of an initial thermal phonon distribution on the observed signal. This has been done in Refs. [Hom06a, Hal05], Sec. 7.4.1., with the result that one simply has to perform a thermal average in Eq. 8.24:

$$\langle -\alpha|\alpha\rangle \rightarrow \sum_n \frac{\bar{n}^n}{(\bar{n}+1)^{(n+1)}} \langle -\alpha, n|\alpha, n\rangle \tag{8.27}$$

with the matrix elements

$$\langle -\alpha, n|\alpha, n\rangle = \langle -\alpha|\alpha\rangle L_n^0(2\alpha^2). \tag{8.28}$$

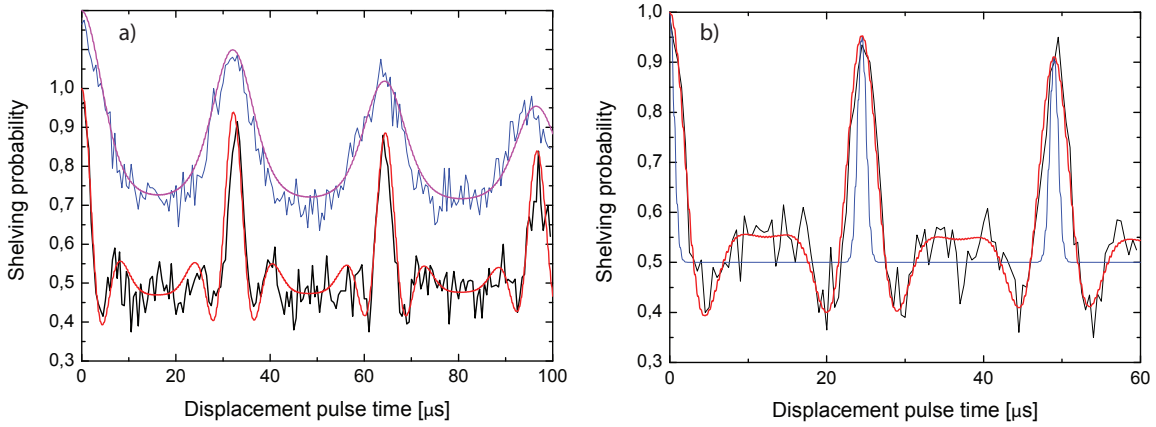

Figure 8.4.: Groundstate versus thermal signals: **a)** shows phase measurements performed under same conditions on a ground state cooled ion (blue line) and a Doppler cooled ion where $\bar{n} = 20$ is assumed (black line). The data for the thermal measurement is shifted upwards by 0.2 for clearness. The additional lines are data from the simulation, see text. **b)** shows similar measurement results for a thermal state (black) along with comparisons to the model Eq. 8.29 (blue) and simulation data according to Eq. 8.30 (red), clearly demonstrating that Eq. 8.29 does not reproduce the data.

The average can be performed analytically, such that the simple result

$$C(t) = e^{-(2\bar{n}+1)|\alpha(t)|^2} \tag{8.29}$$

is obtained. However, we performed phase contrast measurements for a thermal as well as for a ground state cooled ion and found a significant disagreement between the measurement

results and Eq. 8.29, where a mean phonon number of about 20 would produce revival peaks which are by far more narrow than the measured ones. The reason for this is that the strength of the driving light force itself is dependent on the initial state of the ion, such that α in Eq. 8.27 is dependent on n. Thus, Eq. 8.24 has to be replaced by the thermal average

$$P_{\uparrow}(t) = \frac{1}{2}\left(1 + \sum_n \frac{\bar{n}^n}{(\bar{n}+1)^{n+1}} L_n^0(2\ |\alpha(t)|^2) e^{-2\ |\alpha(t)|^2}\right). \tag{8.30}$$

Fig. 8.4 shows measurement results for Schrödinger cat experiments with a thermal ion. One can clearly see that Eq. 8.29 does not reproduce the experimental data, whereas Eq. 8.30 recovers the widths of the revival peaks and the dips originating from negative signs of the Laguerre polynomials. The input for the thermal averaging is data from a numerical solution of the underlying 1D time-dependent Schrödinger equation, where a Chebyshev propagator in conjunction with a Fourier grid has been used. The propagation was performed with 80000 steps and the initial states were taken to be the n-th eigenstates of the harmonic oscillator with n ranging between 0 and 40. The final results after averaging were corrected by a normalization factor $1/\sum_{n=0}^{40} p_n$. Moreover, a coherence decay factor of $\exp(-\gamma t)$ with γ=4 ms^{-1} was multiplied on all simulation curves to take decoherence effects into account. The fact that the revival features in the thermal case are more narrow despite the fact that the driving force is weaker for higher excited states has a simple intuitive explanation: Because the more highly excited states possess faster oscillatory structures, the mutual overlap of the spin components upon resuperposition is more sensitive to the displacement.

In the remainder of this section, we will shed light on the question how important genuine quantum effects are for the dynamics arising from the Hamiltonian Eq. 8.12. With 'genuine quantum' we refer to effects beyond the semiclassical evolution that can be intuitively understood in the framework given by the application of the Hellman-Feynman theorem, Eq. 8.14, and the resulting classical dynamics. The Hellman-Feynman theorem of course always holds, however, many physicists have fundamental misconception about its meaning: It is often thought that in a given time-dependent quantum system, the center-of-mass of a particle always follows its classical trajectory, and quantum effects will manifest in statistical measurements of higher order moments of distribution functions, e.g. asymmetric position and momentum variances for squeezed states. But if the shape of the wavefunction in the center-of-mass system is altered throughout the dynamics, the expectation value of the force will deviate from the classical value and the trajectory will fundamentally deviate from the classical one. We have carried out classical and quantum dynamical simulations for the same parameters, for varying driving strengths and two different Lamb-Dicke factors, i.e. axial vibrational frequencies. The resulting trajectories are shown in Fig. 8.5. The predominant effect seen for both classical and quantum mechanical trajectories is the distortion of the trajectory for strong driving and large displacements which is due to the spatial inhomogeneity of the force and an entirely classical effect. For extremely strong driving, the quantum mechanical trajectory is indeed seen to roll off of the classical one. Interestingly, the quantum mechanical effects seem to occur more strongly for larger Lamb-Dicke factors, where in

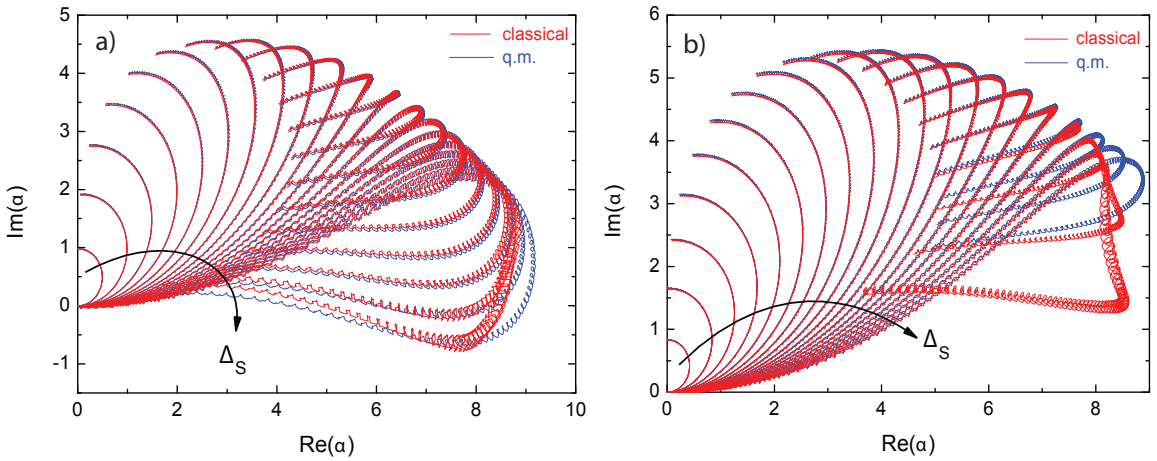

Figure 8.5.: Classical and quantum mechanical trajectories: **a)** Classical (red) and quantum mechanical (blue) trajectories resulting from the displacement drive at a motional frequency of $\omega_{ax}=2\pi\cdot 1$ MHz. **b)** the same for $\omega_{ax}=2\pi\cdot 1.4$ MHz. The black arrow indicates that the outer trajectories result from driving with larger Stark shift Δ_S, see Eq. 8.12. The maximum Stark shift for the outermost trajectories is $\Delta_S=2\pi\cdot 200$ kHz, changed in steps of $\pi\cdot 10$ kHz. The detuning from the motional mode is $\delta=2\pi\cdot 5$ kHz. Note the additional microoscillations resulting from the mismatch between drive and oscillation frequency.

turn the anharmonic distortion effect is less pronounced. It can be concluded that genuine quantum effects are not significant in the regime where quantum gates are usually driven, but one might have to take them into account. If a strong enough driving can be realized, it might be of interest to perform a proof-of-principle experiment where the occurrence of nonclassical trajectories of a single ion is unambiguously demonstrated.

8.3. Phonon Distribution Dynamics

A detailed analysis of the effect of the light force on the motional state is performed by reconstruction of the phonon distributions on the axial vibrational mode, with a method similar to the one presented in Chap. 7. Instead of a phase coherence measurement as it was performed in the Schrödinger cat experiment described above, we recorded Rabi oscillations on the blue motional sideband and used this information for a maximum-likelihood reconstruction of the phonon distribution function $p(n)$. For preceding displacement pulses of times of up to 64 μs, changed in steps of 4 μs, Rabi oscillations of a duration of 200 μs, including approximately 5.5 oscillation periods were recorded. The reconstruction of the phonon distribution is performed in entirely the same way as in Chap. 7, where the phonon distributions are obtained

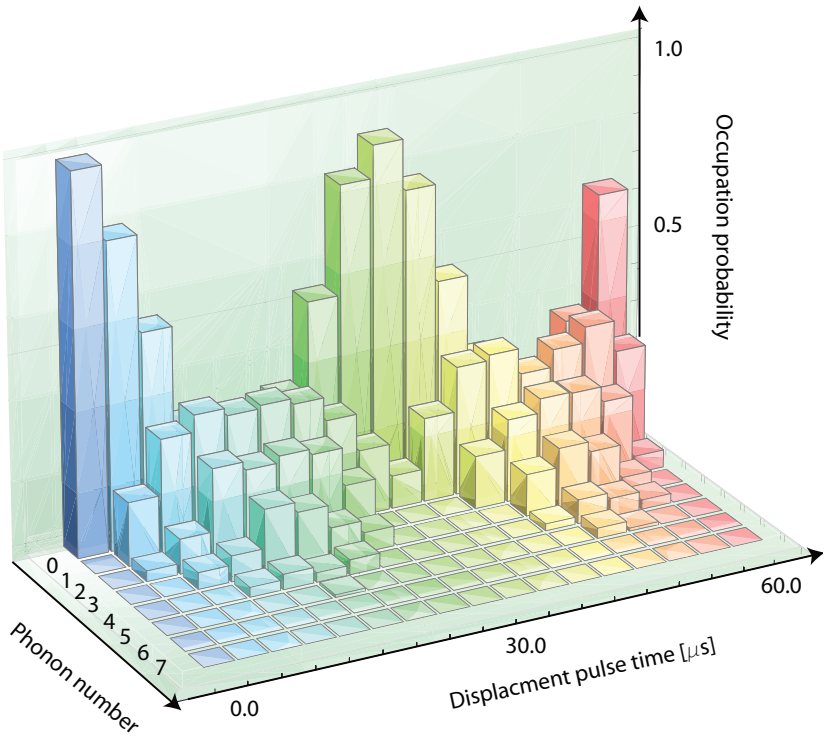

Figure 8.6.: Reconstructed phonon distributions. The plot shows the occupation probabilities of the phonon number states versus the displacement pulse duration.

from fitting of the Rabi oscillation data to Eq. 7.11. The resulting distributions are shown in Figs. 8.6 and 8.7. They are fitted to distributions pertaining to coherent states:

$$p(n) = e^{-\frac{|\alpha|^2}{2}} \frac{\alpha^2}{\sqrt{n!}}. \tag{8.31}$$

The displacement parameters inferred from the fits are shown in Fig. 8.8 a), along with a fit to Eq. 8.18, from which a detuning from the motional frequency of $\delta \approx 2\pi \cdot 28.4$ kHz is obtained. This data is used to reproduce the data from an independent phase contrast measurement similar to the type of Fig. 8.3, which is shown in Fig. 8.7 b). For this reconstruction, the fitted displacement curve is simply plugged into Eq. 8.25. Note that this is not a fit, only an empirical phase decoherence factor of $e^{-\gamma t}$ with $\gamma \approx 7$ ms^{-1} has been included.
The well-controlled displacement allows for a study on how the decoherence depends on the motional state, in extension of the decoherence studies presented in Sec. 4.7. In a similar study, Ref. [Mee96] empirically determined a relation between vibrational quantum number

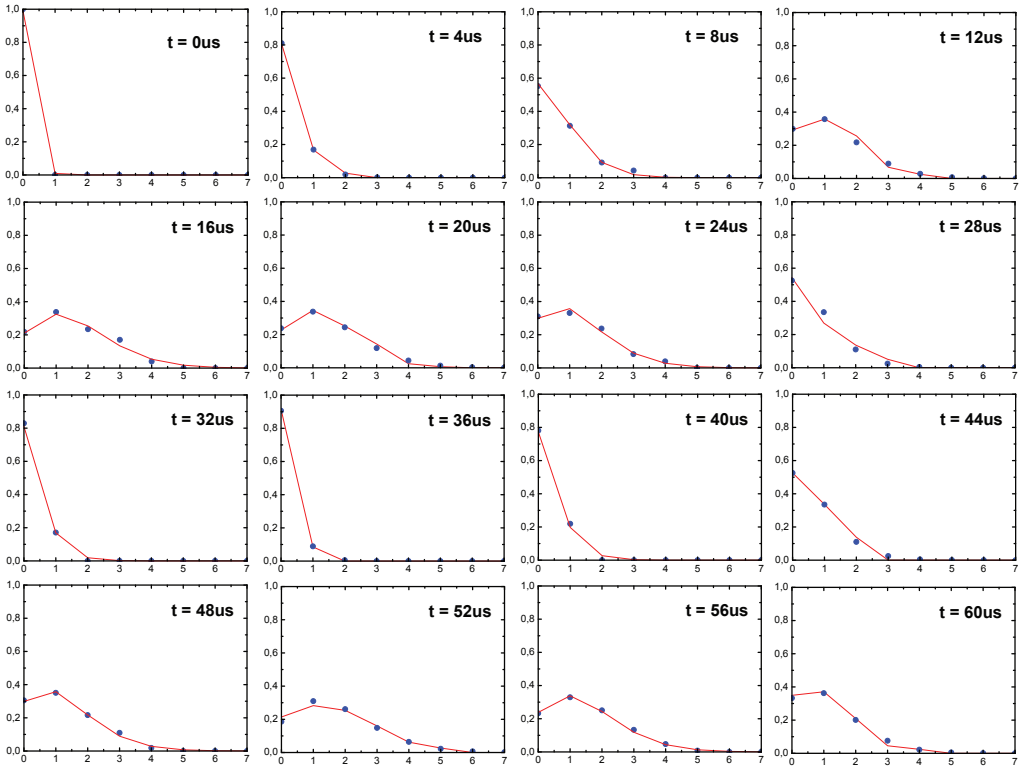

Figure 8.7.: Reconstructed phonon distributions with fits to coherent state distributions (red solid lines). Note the close to perfect agreement between the theoretical and the reconstructed probability distributions.

and decoherence rate of

$$\gamma_n \approx \gamma_0 (n+1)^{\chi}, \tag{8.32}$$

with $\chi \approx 0.7$. The motion-dependent decoherence was attributed to technical imperfections like fluctuating trap parameters. Theoretical investigations were performed in Ref. [Fid00] and [Bud02], where quantum jumps due to off-resonant light scattering were found to be responsible for the effect. However, in Ref. [Fid00], no dependence of the dephasing rate on the initial motional state was found. Ref. [Bud02] partially recovers this dependence by additionally considering the heating rate caused by fluctuating electric fields, but the heating rate required to cause a noticeable contribution to the dephasing would be way larger than the one found in our experiments, where it takes place on a slower timescale (about 3 ms per phonon in contrast to the 200 μs maximum BSB pulse time). Fig. 8.10 shows the different types of quantum jumps which contribute to the dephasing. The scattering *within* the $|\uparrow, n\rangle$ and $|\downarrow, n\rangle$ manifolds is not contained in Eqs. A.14 and A.15 as the scattering from and to the states is a balance of the last two terms in Eq. 2.68, where the motion is not taken

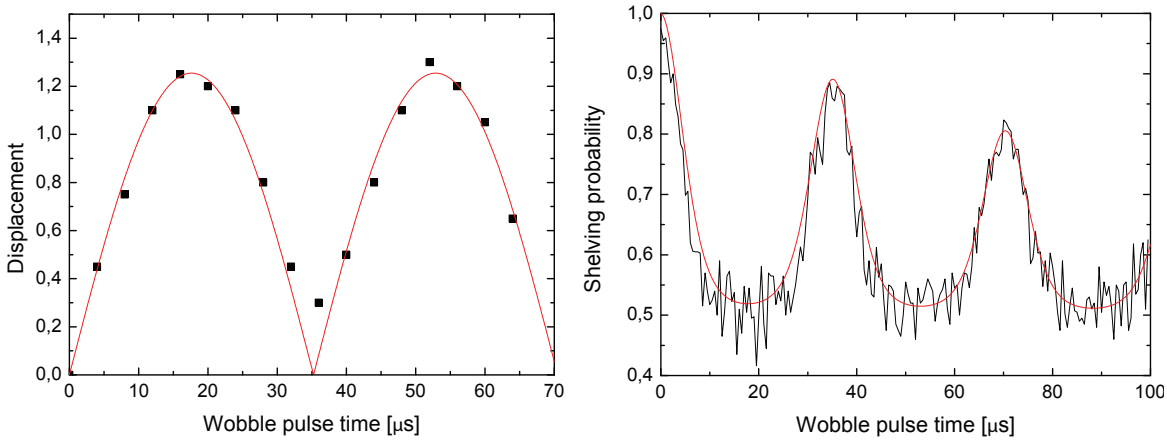

Figure 8.8.: Results from the phonon distribution measurements: **a)** Displacement parameter versus pulse time along with a fit to Eq. 8.18. **b)** Data of the phase coherence measurement (black curve) along with the reconstructed data from the phonon distribution analysis (red curve). This measurement is similar to the one of Fig. 8.3, except that for each data point, an analysis phase of zero degrees is used rather than recording an entire interference fringe. This relies on a properly balanced static AC Stark shift for both spin and motion manipulation laser pulses.

into account. The ratio of non-spin-flip to spin-flip jumps can be at least 1:1 in a situation with balanced Stark shifts. The dephasing from to the non-spin-flips jumps is caused by the fact that the Rabi frequency after the jump is changed if the motional quantum number is altered. For larger quantum numbers, the probability of jumps between different motional state increases due to the larger matrix elements. Furthermore, the dephasing rate will be larger due to the increased sideband Rabi frequencies. However, this reasoning leads to the result that the total dephasing rate can be increased by not more than a factor of about two. This extremal case would require large Rabi frequency changes upon non spin flip scattering events, which is clearly not the case in our regime of motional excitation. The data in Fig. 8.9 shows the tendency of even larger dephasing rates, however, the error bars are too large to make this effect significant.
The decoherence process investigated here is not be be confused with the one investigated in Ref [Tur00], where the decay of the motional coherence, due to electrical field noise during a wait time in the absence of light-matter interaction, is measured for different cat sizes. In this case, a universal decay rate proportional to the cat size $|\alpha|^2$ is found. It remains to be stated that the source of the enhancement is still unclear, possible mechanisms are i) decay on higher order sidebands for highly excited states, ii) anharmonicities of the trap potential or iii) sampling of the inhomogeneous spatial beam profile or magnetic field gradients. Further dephasing sources could be trap voltage or drive intensity fluctuations which are fast on the

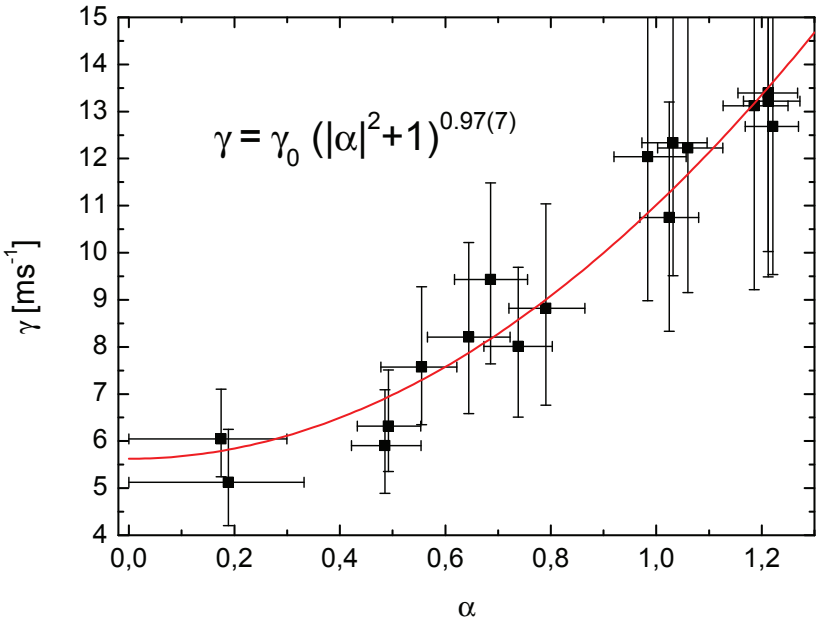

Figure 8.9.: Decoherence rate versus displacement: The plot shows the empirically introduced contrast decay rate γ from Eq. 7.11 against the extracted displacement parameters for the BSB scans pertaining to Fig. 8.7. Despite the large error bars, an increase of the decoherence rate for the maximum attained displacements by more than a factor of two is clearly observed.

BSB pulse timescale, leading to increased dephasing for excited motional states as their associated BSB Rabi frequencies are larger. This mechanism can also be excluded as the required fluctuations are quite large, furthermore enhanced dephasing rates for excited motional states were also observed on the carrier transition, were the Rabi frequencies become smaller with increasing excitation. As a conclusion, the source of the strong increase of the BSB oscillation dephasing with the motional excitation is yet unclear, and more data of better quality is required to compare the results to e.g. quantum-jump Monte Carlo simulations.

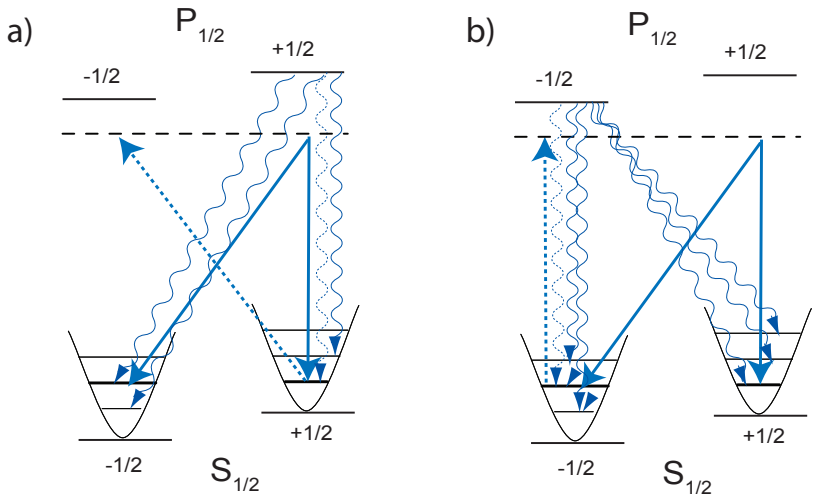

Figure 8.10.: Quantum jumps during sideband Rabi oscillations: We consider Rabi oscillations driven from $|\uparrow, 0\rangle$ to $|\downarrow, 1\rangle$. **a** indicates quantum jumps caused by a σ_- beam component, while **b)** shows the jumps for a π component. Similar pathways have to be taken into account for scattering from $|\uparrow\rangle$ by a π component and from $|\uparrow\rangle$ by a σ_+ component. The wavy arrows indicate the different types of jumps that can occur: The dashed arrow does not at all change the state and does therefore not contribute to dephasing. The vertical wavy arrows indicate changes of the motional state only and therefore contribute to the dephasing rate. The diagonal wavy arrows pertain to spin-flip transitions and therefore correspond to fast dephasing, the one ending at $|\downarrow, 0\rangle$ even removes population from the Rabi cycling as this state does not couple to the blue sideband.

8.4. The Wavepacket Beating Scheme

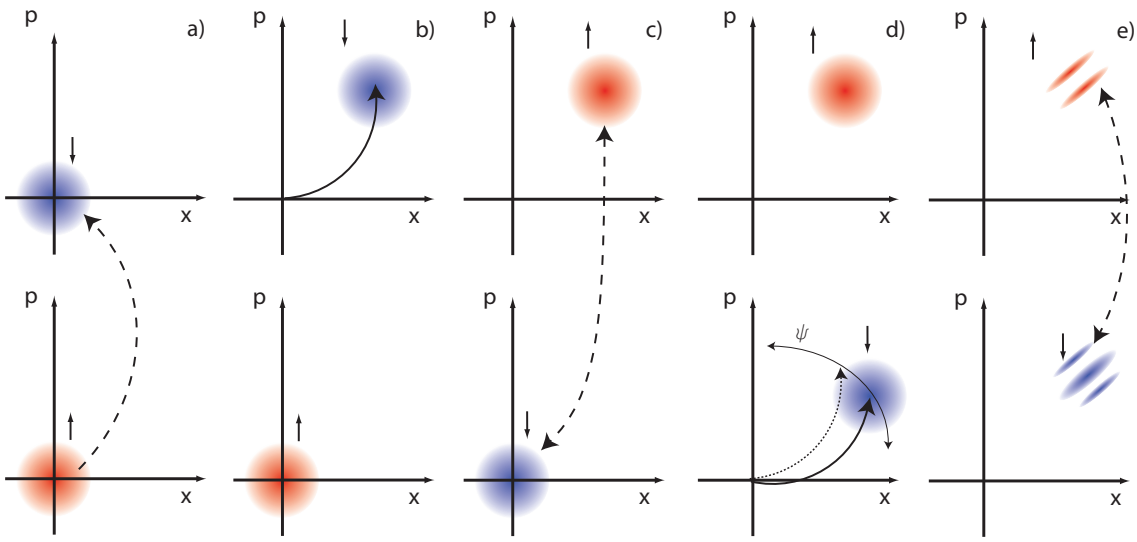

Figure 8.11.: Schematic of the wavepacket beating experiment: **a)** A resonant $\pi/2$ pulse creates an initial spin superposition (resonant driving of the spin transition is indicated by dashed arrows). **b)** The displacement force acting only on $|\downarrow\rangle$ gives rise to a displacement α of only the $|\downarrow\rangle$-part of the wavefunction. **c)** A π pulse is used to swap the populations. **d)** A second displacement pulse now displaces the part of the wavefunction which was previously not affected by the force. **e)** A concluding $\pi/2$ pulse gives rise to the final populations in $|\uparrow\rangle$ and $|\downarrow\rangle$ which are to be measured.

Two modifications of the measurement scheme presented above can be used to measure the trajectory of the ion in phase space: First, the R2 beam has to be circularly polarized such that the light force acts on one spin component only. Furthermore, a second displacement pulse of the same strength and duration but with variable phase is employed in the second branch of the spin echo sequence. Physically, one is now subsequentially displacing two different portions of the wavepacket, which yields interference if the parts are displaced such that they have a substantial overlap in the end. The scheme is illustrated in Fig. 8.11 and described in detail in the following. It has been used in Ref. [Mon96] for the first demonstration of the generation of Schrödinger cat states, however it has not been realized there that the scheme is capable of ultraprecise trajectory measurements. In contrast to Ref. [Mon96], we assume resonant driving of the spin-flip transition, such that no extra phases are accumulated during the $\pi/2$ and π pulses, but we account for off-resonant driving of the motion. The frequency difference of the driving beams during the displacement pulses is

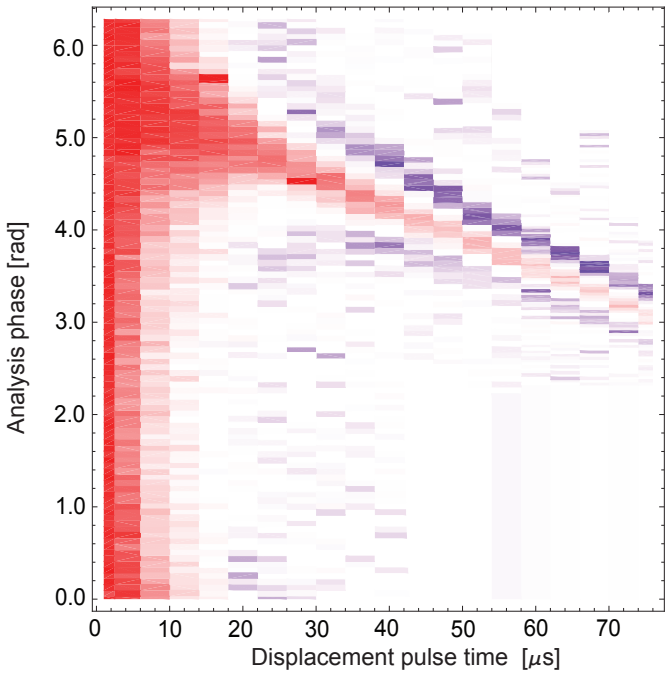

Figure 8.12.: Measurement results for the wavepacket beating scheme: The probability for finding the ion in $|\uparrow\rangle$ is plotted versus the displacement pulse time and the phase of the second displacement pulse. Red pixels indicate probabilities greater than 0.5, whereas blue pixels indicate probabilities smaller than 0.5.

given by

$$\Delta\omega = \omega_{ax} + \delta \tag{8.33}$$

After initializing to the state $|\uparrow\rangle$, the first $\pi/2$ pulse creates the state

$$|\Psi\rangle = |\uparrow, 0\rangle - i|\downarrow, 0\rangle. \tag{8.34}$$

The first displacement pulse gives rise to displacement of the $|\downarrow\rangle$ component:

$$|\Psi\rangle = |\uparrow, 0\rangle - i|\downarrow, \alpha e^{-i\frac{\delta t}{2}}\rangle. \tag{8.35}$$

The π pulse simply swaps the spin components:

$$|\Psi\rangle = |\downarrow, 0\rangle - i|\uparrow, \alpha e^{-i\frac{\delta t}{2}}\rangle. \tag{8.36}$$

The second displacement pulse now acts on the part of the wavefunction which was previously not affected:

$$|\Psi\rangle = |\downarrow, \alpha e^{-i\frac{\delta t}{2}} e^{i\phi'}\rangle - i|\uparrow, \alpha e^{-i\frac{\delta t}{2}}\rangle, \tag{8.37}$$

where the extra phase $\phi' = \phi + \delta T$ is comprised of the preset phase offset ϕ and a constant phase offset accumulated during the waiting time between the two displacement pulses. Resuperposition of the components by means of the concluding $\pi/2$ pulse creates the final state:

$$|\Psi\rangle = |\uparrow\rangle \left(|\alpha e^{-i\frac{\delta t}{2}}\rangle - |\alpha e^{-i\frac{\delta t}{2}} e^{i\phi'}\rangle \right) - i|\downarrow\rangle \left(|\alpha e^{-i\frac{\delta t}{2}}\rangle + |\alpha e^{-i\frac{\delta t}{2}} e^{i\phi'}\rangle \right). \tag{8.38}$$

As one can directly see, superposition states of the atomic motion are created *within* the individual spin components, such that the wavepacket beating scheme makes it possible to create *genuine* Schrödinger cat states. Computing the probability to find the ion in $|\uparrow\rangle$, we find

$$P_\uparrow = \frac{1}{2} \left(1 - \left(\langle \alpha e^{-i\frac{\delta t}{2}} | \alpha e^{-i\frac{\delta t}{2}} e^{i\phi'}\rangle + \text{c.c.} \right) \right). \tag{8.39}$$

With $\langle \alpha|\beta\rangle = e^{-\frac{1}{2}(|\alpha|^2+|\beta|^2-2\beta^*\alpha)}$, we find for the overlap integral:

$$\begin{aligned} \langle \alpha e^{-i\frac{\delta t}{2}} | \alpha e^{-i\frac{\delta t}{2}} e^{i\phi'}\rangle &= e^{|\alpha|^2\left(-1+(\cos\frac{\delta t}{2}+i\sin\frac{\delta t}{2})(\cos\left(\frac{\delta t}{2}+\phi'\right)-i\sin\left(\frac{\delta t}{2}+\phi'\right)\right)} \\ &= e^{|\alpha|^2(-1+\cos(\delta t+\phi')-i\sin\phi')}. \end{aligned} \tag{8.40}$$

We finally find

$$P_\uparrow = \frac{1}{2} \left(1 - e^{-|\alpha|^2(\cos(\delta t+\phi')-1)} \cos\left(|\alpha|^2 \sin\phi'\right) \right). \tag{8.41}$$

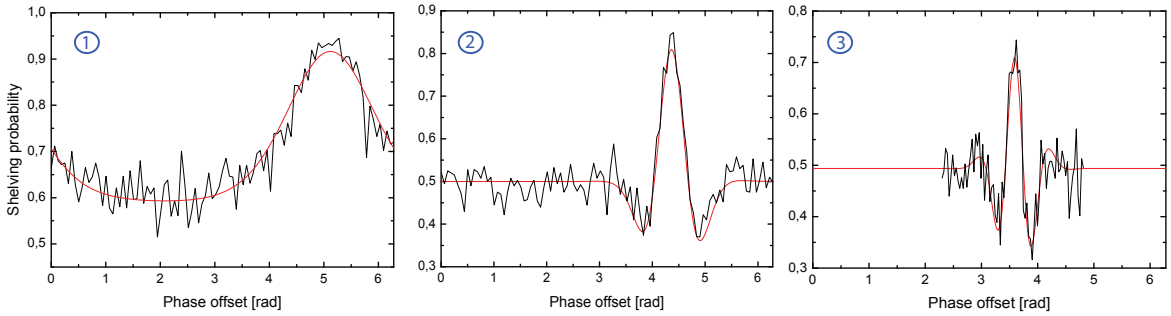

Figure 8.13.: Measured signal from the wavepacket beating scheme: The curves show the shelving probability versus the phase of the second displacement pulse relative to the first one. Each data point corresponds to 200 interrogations. The three displayed datasets pertain to displacement pulse times of 12, 36 and 60 μs.

Fig. 8.15 shows a sample of three measurements of $P_\uparrow$ versus the second displacement phase offset ϕ, along with fits to Eq. 8.41. The curves are taken for different durations of the displacement pulse. As one can clearly see, the model perfectly reproduces the measured data, except for the decreasing contrast of the interference pattern for longer displacement pulse durations. The decreasing contrast originates from the fact that one of the displacement

beams is circularly polarized and therefore exerts a strong AC Stark shift, which leads to the loss of spin coherence by intensity fluctuations, see Sec. 4.7. The contrast versus displacement time is shown in Fig. 8.14. It is also found that the accuracy of the fits to the measured data could be improved by considering a slight detuning from the spin-flip carrier transition. According to Ref. [Mon96], Eq. 8.41 only has to be modified to

$$P_{\uparrow} = \frac{1}{2}\left(1 - e^{-\gamma t} e^{-|\alpha|^2(\cos(\delta t+\phi')-1)} \cos\left(\psi + |\alpha|^2 \sin\phi'\right)\right), \tag{8.42}$$

where γ describes the contrast decay and $\psi = \delta_{\mathrm{car}} t$ describes the detuning from the carrier. The phase ψ is picked up because the experimental sequence is set up such that gaps of the spin echo sequence become longer for increasing displacement pulse durations. The AC Stark shift does not lead to an extra phase pick-up as both components of the wavefunction are subjected to same displacement pulse area. The results for the determination of δ_{car} are also shown in Fig. 8.14.

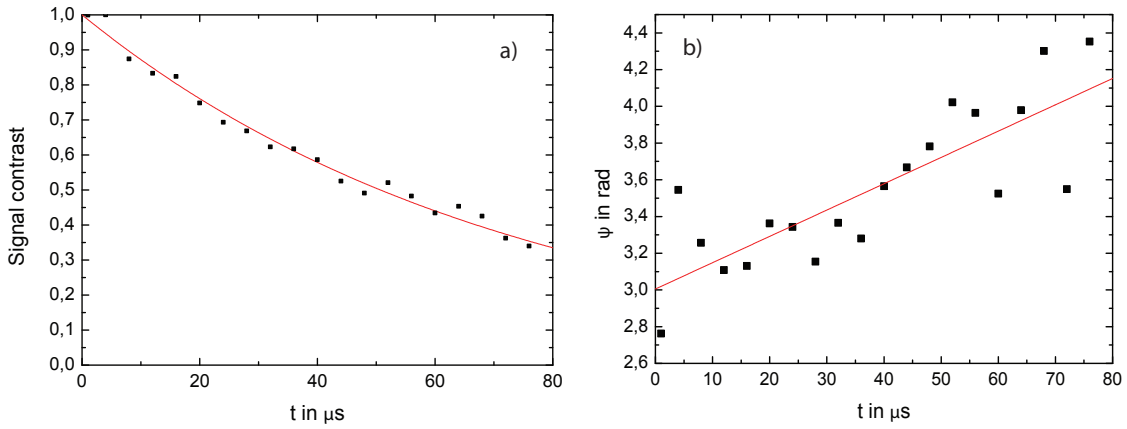

Figure 8.14.: **a)** Contrast decay due to intensity fluctuations. The $1/e$ time is found to be 73.2 μs.**b)** Correction for a slight carrier off-resonance. The detuning is determined to be δ_{car} ≈2.3 kHz.

The maximum displacement values around $\alpha \approx 3$ are already large enough for the finite Lamb-Dicke factor, i.e. the spatial inhomogeneity, to be seen in the dynamics. According to Ref. [Hom06a], this can be accounted for by replacing Eq. 8.18 by

$$\alpha(t) = -\frac{\eta\Delta_S}{2\delta}\frac{\delta}{\delta_{\mathrm{eff}}} e^{i\Delta\phi} e^{i\frac{\delta t}{2}} \sin\frac{\delta_{\mathrm{eff}} t}{2}. \tag{8.43}$$

where $\delta_{\mathrm{eff}} > \delta$, i.e. the particle returns to the origin in phase space before the phase of the force is back to its original value. As the phase of the driving force has not completed a full cycle then, further driving will lead to a cycloid-shaped trajectory, as is indicated in Fig.

8.15. Furthermore, the maximum displacement attained is reduced by a factor $\delta/\delta_{\text{eff}}$, which means that when attempting to drive ultrafast gates within a few cycles of the trap motion, the efficiency of the light force will be seriously impaired. δ_{eff} depends on δ, the Lamb-Dicke factor and the strength of the driving field. Empirical formulae are given in Ref. [Hom06a].

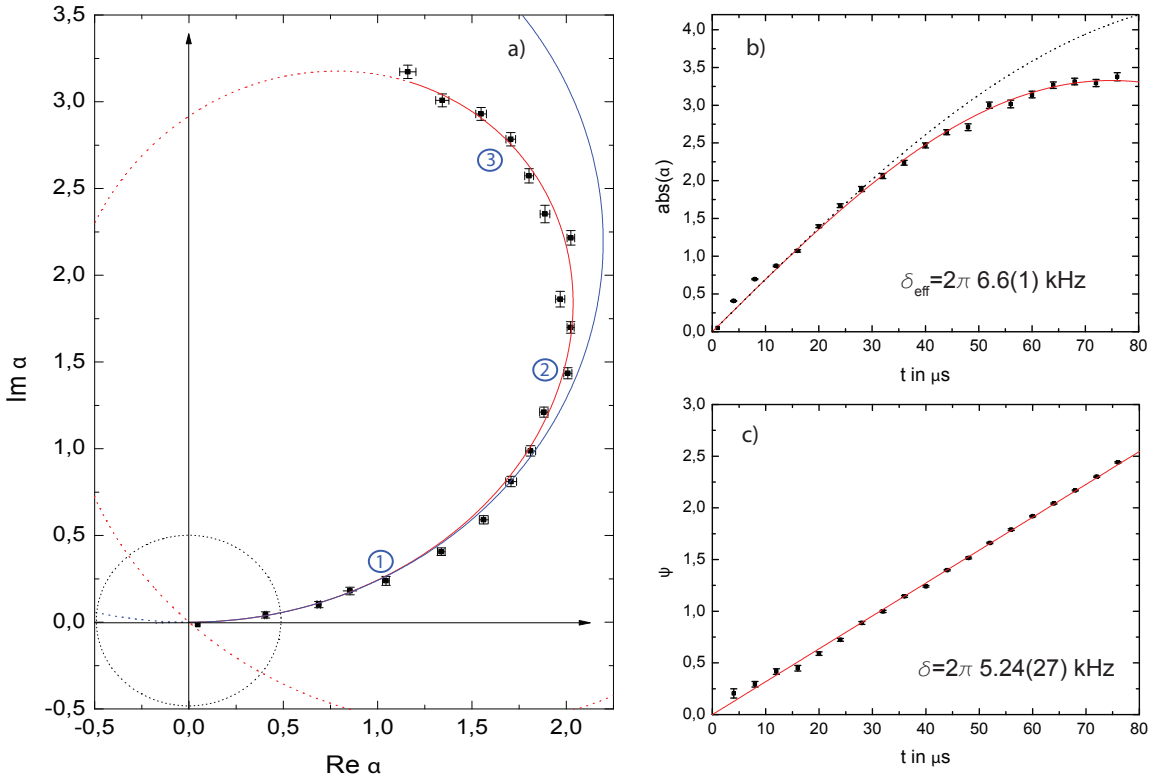

Figure 8.15.: Measured particle trajectory: **a)** The real and imaginary parts of the displacements inferred from the measured curves are shown along with the theoretical curve Eq. 8.18. For comparison with the error bars, the $1/e$ radius of the harmonic oscillator ground state wavefunction is also indicated. The red dashed line indicates how the trajectory would process beyond the measured data range. The blue curve indicates the trajectory which would be observed in the case of a spatially homogeneous force.**b)** shows a fit of the absolute values of the displacements as the are extracted from the experimental data to Eq. 8.43, from which δ_{eff} is inferred. The dashed curve shows the values that would be expected in the case of a homogeneous force. **c)** shows the motional phase ϕ where the constant phase offset δT was already removed.

As a result, the wavepacket beating scheme allows for an extremely precise measurement of the motion of the ion, where the error bars along both quadrature directions are much smaller than the corresponding scale of the ground state wavefunction. Of course this does not mean that the uncertainty principle is violated; the nature of the measurement is sta-

tistical and relies on the fact that exactly the same experimental procedure can be repeated a large number of times. However, it is a clear demonstration of entanglement as a tool for ultraprecise measurements, quite in the spirit of the emerging field of *quantum metrology*. Furthermore, it shall be elucidated that a precise measurement of the trap frequency is provided, as can be seen from Fig. 8.15 c), the trap frequency is determined with an accuracy of 27 Hz, corresponding to 0.002%. In a conventional Ramsey spectroscopy measurement, a delay time of about 40 ms would be necessary to achieve the same accuracy, which clearly lies far beyond the measured coherence time on the blue side band, see Fig. 4.34.

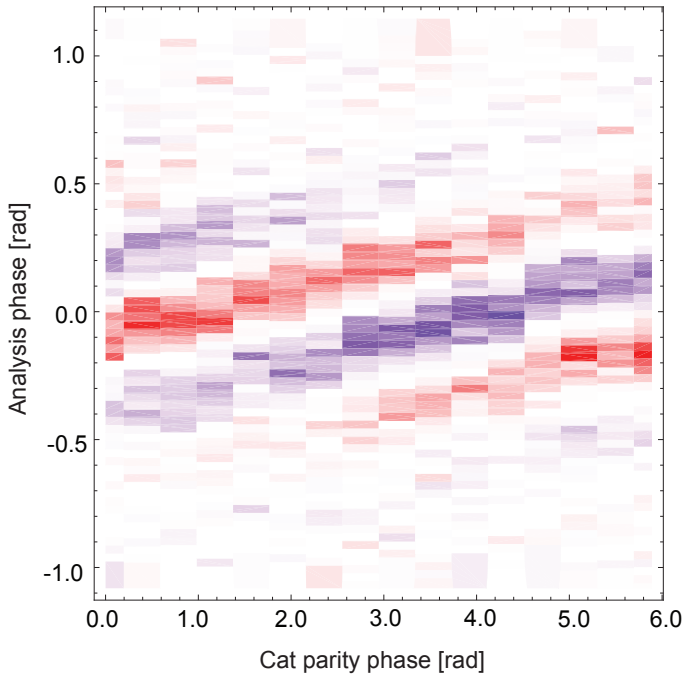

Figure 8.16.: Cat states with varying parity: The probability for finding the ion in $|\uparrow\rangle$ is plotted versus the phase of the concluding $\pi/2$ pulse and the phase of the second displacement pulse. Red pixels indicate probabilities greater than 0.5, whereas blue pixels indicate probabilities smaller than 0.5.

An interesting variation of the experiment demonstrates the full control over the final Schrödinger cat state by additionally varying the phase of the concluding $\pi/2$ pulse in the sequence. If this phase offset ψ is taken into account, the final state Eq. 8.38 is modified to be

$$|\Psi\rangle = |\uparrow\rangle \left(|\alpha e^{-i\frac{\delta t}{2}}\rangle - e^{i\psi}|\alpha e^{-i\frac{\delta t}{2}} e^{i\phi'}\rangle\right) - i|\downarrow\rangle \left(|\alpha e^{-i\frac{\delta t}{2}}\rangle + e^{i\psi}|\alpha e^{-i\frac{\delta t}{2}} e^{i\phi'}\rangle\right). \tag{8.44}$$

For the measured population in $|\uparrow\rangle$, we thus obtain

$$P_\uparrow = \frac{1}{2}\left(1 - e^{-|\alpha|^2(\cos(\delta t+\phi')-1)} \cos\left(\psi + |\alpha|^2 \sin\phi'\right)\right). \tag{8.45}$$

The results of a corresponding measurement at a fixed displacement pulse time of 65μs are shown in Fig. 8.16. It is interesting to note that the measurement principle is quite analogous to 2D spectroscopy methods in molecular science. This offers the possibility to make use of this scheme for exploring nonlinear cross-couplings between distinct vibrational modes. The basic idea would be to perform the experiment on a two ion crystal, where the ions are placed such that the COM as well as the STR mode can be excited. The modes will then be excited in a sandwich-like manner, such that the influence of an initial COM excitation on the STR mode dynamics can be investigated and vice versa. This would be analogous to the experiment performed in Ref. [Roo08], only the controlled excitation of single vibrational quanta is replaced by the controlled excitation of semiclassical vibrations. It is important to note that the wavepacket beating scheme represents a very simple method for quantum state tomography of a vibrational mode, see chapter 7. The mathematical details and possible future extensions are worked out in appendix D.

9. Measurements with Two-Ion Crystals

This chapter deals with the extension of the techniques for qubit handling developed throughout the chapters 4 and 8 to two-ion crystals, which represent the fundamental building block for our envisaged scheme for scalable quantum computing. Sec. 9.1 explains general issues on the crystal stability and shows how the read-out of two ions is performed. Measurement results on the precise alignment of crystals in the driving Raman laser field are presented in Sec. 9.2. Results from spectroscopy measurements and sideband cooling of crystals are shown in Sec. 9.3. Sec 9.4 treats the coherent manipulation of two ions and demonstrates an advanced technique for simultaneous readout, while the concluding Sec. 9.5 presents results on the generation of Schrödinger cat states with two ions, which is a crucial step towards entangling quantum gates.

9.1. Stability and Read-out

Two ion crystals represent the intended basic building block for scalable quantum information experiments in our microtrap. Two-ion crystals are only loaded in the loading region of our trap for rf-levels below 300 V peak-to-peak, corresponding to radial modes in the range between 2 MHz and 3 MHz. Sufficient stability is attained at 250 V peak-to-peak and below. This behavior is counterintuitive as normally a high aspect ratio of the trap potential is favorable for loading crystals, see Sec. 2.2. The reasons for this behavior are not entirely clear, but the following facts are known: First, parametric instabilities can occur in Paul traps if secular frequencies correspond to fractions of the rf frequency with small integer numbers in nominator and denominator, which is a well known phenomenon in classical nonlinear dynamics and is related to the Komolgoroff-Arnold-Moser (KAM) theorem. 'Canyons' of instability for such values $\beta = n/m, n, m \in \mathbb{N}$ were measured with high resolution in Ref. [Alh96]. The reason for these instabilities, which are not predicted by the (harmonic) Mathieu equations are anharmonicities, i.e. higher-order terms in the equations of motion Eqs. 2.76. These can either arise because of the trap potentials themselves or from the highly nonlinear Coulomb interaction in the case of several ions, i.e. effects beyond the linearization in Eq. 2.81. This effect was treated theoretically in [Mar03] and measurements of the energy transfer rate between different motional modes were carried out in [Roo08]. The fact that the instability of the crystal increases for higher rf-levels despite the trap parameters are still deep inside the region of stability suggests that micromotion also contributes to the instability.

However, it was found that at an rf-level of 250 V_{pp} and an axial trap frequency of $2\pi\cdot$950 kHz, a sufficient stability to perform measurements on a two-ion crystal was attained. The stability substantially decreased at axial trap frequencies below $2\pi\cdot$900 kHz and above $2\pi\cdot$1000 kHz. A fluorescence histogram of a two-ion crystal is shown in Fig. 9.1. In

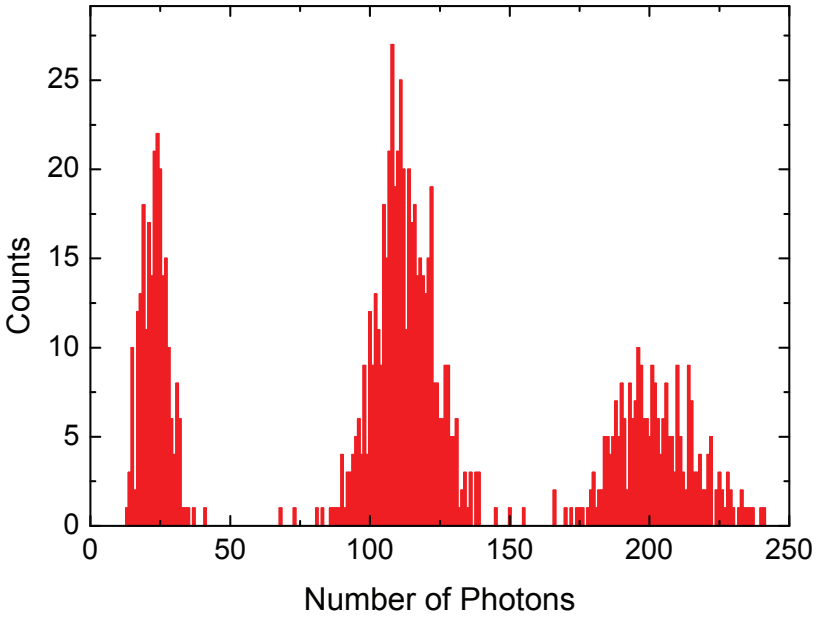

Figure 9.1.: Fluorescence histogram of two ions. In contrast to the one-ion case, the possible states can not be distinguished by means of the 866 nm repump laser. Instead, the 729 nm laser is tuned to the $m_J = +1/2 \rightarrow m_J = +5/2$ transition and irradiated onto the ions at maximum power, such that the excitation probability for each ion is about 50% and the excitation is not correlated. The peak in the middle now corresponds to the indistinguishable states $|SD\rangle$ and $|DS\rangle$ and is twice as strong as the ones for $|DD\rangle$ (left) and $|SS\rangle$ (right).

contrast to the single ion case, the possible states can not be distinguished by switching the repump laser on and off. Instead, one can make use of the quadrupole transition and transfer each of the ions with a 50% probability to the dark metastable state by strong resonant irradiation with the 729 nm beam before the fluorescence counting. One can clearly distinguish the state with no, one or two bright ions, the states $|SD\rangle$ and $|DS\rangle$, corresponding to $|\downarrow\uparrow\rangle$ and $|\uparrow\downarrow\rangle$ before shelving, therefore remain indistinguishable in the readout scheme. The drawback of working at low rf-levels is that the shelving performance is reduced because of a larger spread in the phonon distributions of the radial modes after Doppler cooling and larger Lamb-Dicke factors, both leading to a higher spread in Rabi frequencies. The adverse effect on the readout is shown in Fig. 9.2, which has to be compared to Fig. 4.19. Fig. 9.6 shows a Raman spectrum of two ions taken with the noncopropagating beam pair R1/R2. Besides the center-of-mass (COM) mode at $\omega_{\mathrm{COM}} \approx 2\pi{\cdot}950$ kHz, one finds the stretch (STR) mode at $\omega_{\mathrm{STR}} = \sqrt{3}\ \omega_{\mathrm{COM}} \approx$1645 kHz. The equilibrium distance of the two ions according to Eqs. 2.80 is given by

$$d = \sqrt[3]{\frac{e^2}{4\pi\epsilon_0}\frac{2}{m\omega^2}}, \tag{9.1}$$

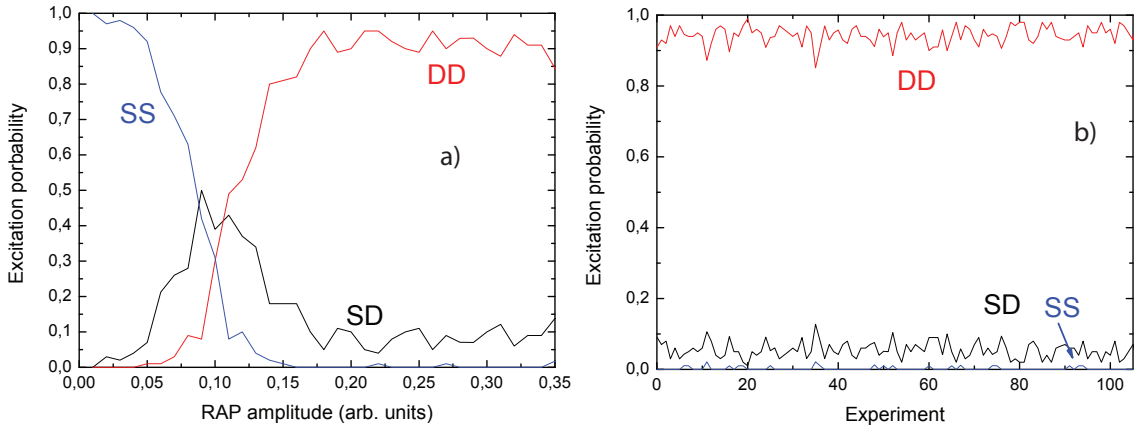

Figure 9.2.: **a)** RAP amplitude scan for a two ion crystal, where the $|S_{1/2}, m_J = +1/2\rangle \rightarrow |D_{5/2}, m_J = +5/2\rangle$ transition is used. The blue curves shows the probability for finding two bright ions, the black curve depicts the probability for finding one of the ions bright, and the red curve shows the probability for finding two dark ions. Note the emergence of a nonzero probability for only one ion being in the dark state for insufficient RAP amplitudes. **b)** shows a set of shelving runs with a double RAP at optimum amplitudes.

which is about about 4.6 μm for the conditions described above.

9.2. Localization and Alignment in a Standing Wave

The two-ion crystal is intended to be the basic building block in our future scalable quantum information processor, and one of the most advanced ingredients for its realization is the ability to perform quantum logic gates between two spin qubits comprising such a crystal. The essential prerequisites for conducting the most suitable gate for our setting, which is the geometric phase gate as is was realized in Rf. [Lei03b], are on the one hand that the spatial localization of the ions on a scale much below the wavelength of the driving laser field, which is nothing else than the statement that the ions have to be in the Lamb-Dicke regime. Effects occurring if the ions are outside this regime are discussed in Sec. 8.2 for a single ion. On the other hand, the crystal has to be aligned to the running standing wave in such a way that the relative phase of the driving field at the two different ion locations is such that the 'gate' mode on which the operation is driven couples to the field whereas the other does not. This requirement is not a strict one, however the performance of the gate deteriorates as the coupling to the gate mode becomes weaker and the off-resonant excitation of the spectator mode increases when the alignment deviates from the optimum one.

In principle, if the Lamb-Dicke factor was known with sufficient precision, the alignment of the crystal could be adjusted simply via the trap frequency. However, the angles at which the Raman beams intersect the trap axis cannot be precisely determined, and also the measurement of the Lamb-Dicke factor from the Fourier decomposition of sideband Rabi oscillations, see Sec. 4.6, is subject to a relatively high uncertainty. A measurement scheme used in Ref. [Hom06a] for the alignment quantifies the coupling strengths to the COM and STR modes with respect to the trap frequency by exerting a displacement pulse and probing the motional state. This approach is rather tedious and requires ground state cooling of both modes. We have devised a method for measuring both localization and alignment by fluorescence observation, where the alignment can be performed in real-time. The underlying idea is simple: If the frequency of the running standing wave from the R1 and R2 beams (which are necessarily vertically polarized for this measurement) is tuned close to the cycling resonance and the normal Doppler cooling laser is turned off, both cooling and fluorescence emission will be provided by the running standing wave. Therefore, the frequency component pertaining to the relative detuning δ of the beams will be visible in each ion's fluorescence level. The relative phase between these fluorescence oscillations of the two ions will be determined by the ion distance set by the trap frequency, Eq. 9.1, and information about the localization of the ions is contained in the total signal levels.

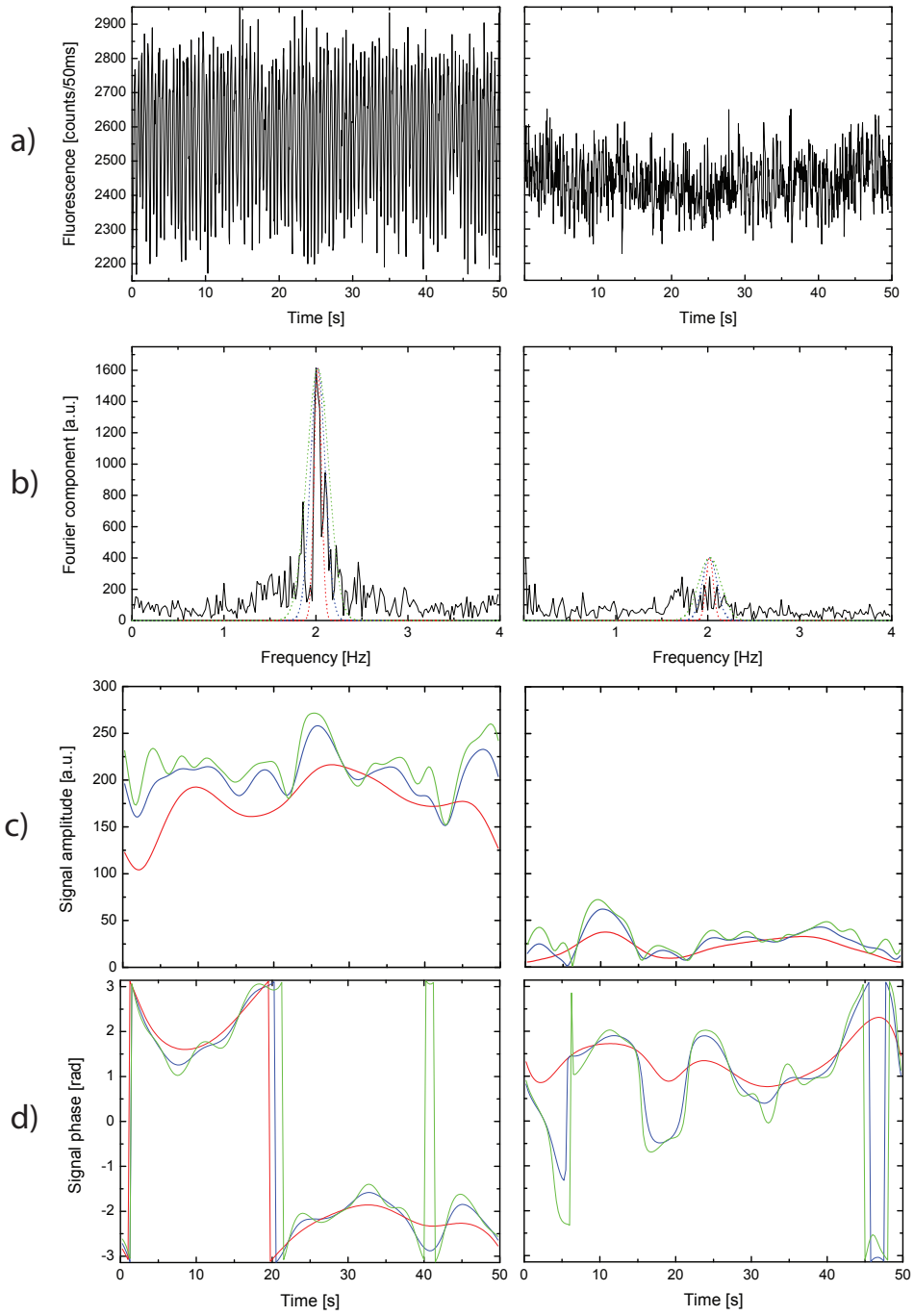

Figure 9.3.: Localization measurement samples: **a)** Measured two-ion fluorescence traces after preprocessing. **b)** Fast Fourier transform results with the Gaussian filter functions for σ=2 Hz (red), 4 Hz (blue) and 6 Hz (green). **c)** and **d)** show the resulting amplitude and phase curves after frequency shift and backward transform for the three different filter widths. The data in the left column is taken at an axial trap frequency of 1.36(1) MHz, whereas the data in the right column pertains to a trap frequency of 1.22(1) MHz

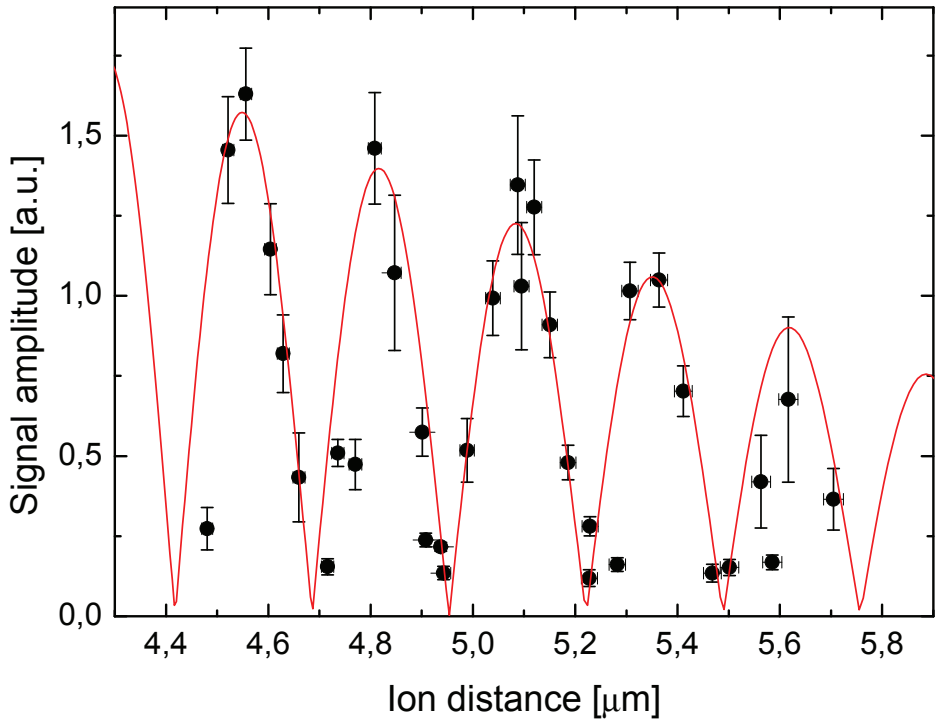

Figure 9.4.: Result of the localization measurement: The integrated signal amplitude is plotted versus the ion distance inferred from the spectroscopically measured trap frequency, along with a fit to Eq. 9.8.

The probability to find a thermal ion at position x is given by the thermal average

$$p(x) = \sum_n p_n |\psi_n(x)|^2, \tag{9.2}$$

which is a Gaussian distribution if the p_n from Eq. 2.33 are used:

$$p(x) = \frac{1}{\sqrt{2\pi\sigma^2}} e^{-\frac{x^2}{2\sigma^2}}, \tag{9.3}$$

with

$$\sigma = \sqrt{\frac{2\bar{n}+1}{2}}\sigma_0, \tag{9.4}$$

where σ_0 is the spatial extension of the ground state wavefunction $\sigma_0 = \sqrt{\hbar/2m\omega}$. If the trap frequency is lowered, the localization is decreased not only due to a larger σ_0, but also that $\bar{n}$ increases if a constant Doppler cooling temperature is assumed:

$$\bar{n} = \frac{k_B T}{\hbar\omega}. \tag{9.5}$$

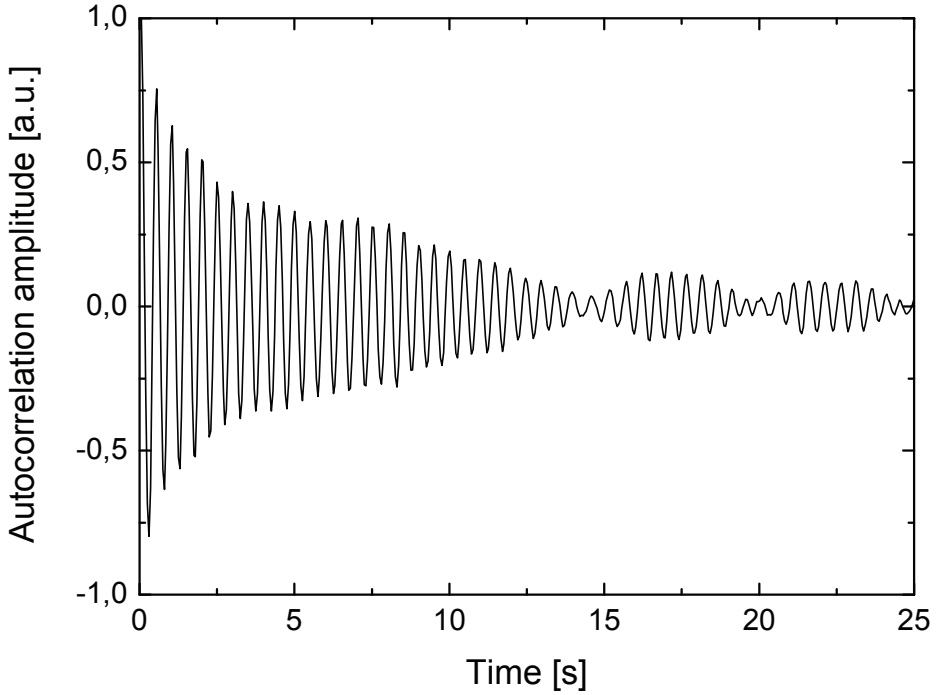

Figure 9.5.: Fluorescence autocorrelation: The autocorrelation function for the data set in the left column of Fig. 9.3 is shown. From the correlation decay it can be inferred that the timescale on which the R1/R2 interferometer drifts by a relative phase of π is in the range of 10 s.

For small saturation, the fluorescence rate of a single ion located at position x in the interference pattern will be

$$R = \frac{\Gamma}{2(1+4\Delta^2/\Gamma^2)}\left(S_1^2 + S_2^2 + 2\sqrt{S_1 S_2}\cos(\delta k x - \delta t + \Delta\phi)\right), \tag{9.6}$$

where $S_{1,2}$ are the saturation parameters of the R1 and R2 beams, δk is the difference wavevector pointing along the trap axis, $\Delta\phi$ is the relative optical phase and $\Delta \ll \delta$ is the common red-detuning from resonance. If the saturation parameters are not exactly matched or the polarization if imperfectly aligned, a fluorescence baseline occurs in the interference which decreases the signal-to-noise ratio. As we are interested only in the frequency component at δ, the baseline will be ignored in the following. For two ions, we thus obtain

$$R(x) \propto \left(\cos\left(\delta k(x_0 - l/2) - \delta t\right) + \cos\left(\delta k(x_0 + l/2) - \delta t\right)\right). \tag{9.7}$$

We now consider the case of two ions located at the sites $x_0 + x' \pm (l_0 + l')/2$. $x_0 = 0$ and l_0 are the center positions of the COM and STR wavefunctions, and x' and l' are the quantum

statistical deviations, which are to be averaged over. This yields

$$\begin{aligned} R_{\text{tot}} &\propto \int dx' p(x') \int dl' p(l') \left(e^{i\Delta k(x'-(l_0+l'/2))} + e^{i\Delta k(x'+(l_0+l')/2)} \right) \\ &\propto \cos\left(\delta k l_0/2\right) e^{-\delta k^2(\sigma_x^2/2+\sigma_l^2/2)}, \end{aligned} \tag{9.8}$$

where already only the frequency component at δ is considered and the thermal delocalization widths σ_x and σ_l for the COM and STR motion from Eq. 9.4 are used.
The experiment is carried out as follows: A two ion crystal is trapped at various axial confinement frequencies, i.e. the trapping voltage at segment #5 is changed. For each trapping voltage, spectroscopy on the quadrupole transition is performed to determine the position of the carrier and the red axial sideband. The crystal is then placed in the vertically polarized standing wave of the R1 and R2 beams, where the R2 beam is detuned from the R1 beam by exactly 2 Hz. Fluorescence is then recorded on the PMT for 50 seconds, with 50 ms binning. The resulting fluorescence displays 2 Hz oscillation if the ions are spaced exactly by an integer number of nodal distances. This 2 Hz signal component is strongly affected by shot noise, interferometer drift and spontaneous melting of the ion crystal, thus great care must be taken to obtain a valid figure of the signal strength. Two sample data sets are shown in Fig. 9.3. The data set is preprocessed to remove melting effects which would spuriously affect the resulting signal amplitude, also very large fluorescence values are present which possibly stem from cosmic ray events. The data is cleaned in such a way that fluorescence values lying outside the interval given by ± 3 standard deviations from the mean fluorescence are set to zero, the resulting corrected mean of the cleaned data then provides a valid normalization reference for the final result. The values set to zero are then set to this mean value in order to avoid artifacts in the frequency spectrum. The processed data set is Fourier transformed, the spectrum is the filtered by applying a Gaussian filer function of fixed width around 2 Hz. The filtered spectrum is then shifted such that the 2 Hz component becomes the dc one, then the backward transform is carried out, giving a smoothed information of signal amplitude and phase versus time. The amplitude is then integrated to give the final value, which is normalized on the mean of the valid fluorescence counts. For each trap voltage, 5 individual traces are taken to obtain an error estimation. Fig. 9.3 shows sample measurement results for two different trap frequencies, where also the dependence of the result on the width of the Gaussian filter function is demonstrated. For broader filter widths, the integral amplitude, which is the final quantity of interest, seems to be quite independent of this parameter.
Fig. 9.4 shows the final result, together with a fit to the model Eq. 9.8, where the data for the 6 Hz filter window was used. The floating parameters are the effective wavenumber along the trap axis, the temperature T and an amplitude scaling factor A. The effective wavelength of the beat pattern can be accurately determined due to the oscillatory structure, its value is found to be λ_{eff}=267.8(2) nm. The temperature can not be accurately determined as it is mainly given by the slope of the maxima, which is strongly correlated to A. Values around 1.5 mK, equivalent to $\bar{n}_{\text{COM}} \approx 23$ and $\bar{n}_{\text{STR}} \approx 13$ at $\omega_{\text{ax}} = 2\pi \cdot 1.35$ MHz are found, which is entirely consistent with the expected Doppler cooling result, which is also found in the thermal Schrödinger cat measurement in Sec. 8.2. In conclusion, this method is to

our knowledge to only method the determine the Lamb-Dicke factor with permil accuracy in a setting where no two-mode ground state purity of a two ion crystal, nor long enough coherence times for observing Rabi oscillations on a blue motional sideband can be attained. It provides an easy method for alignment of a two ion crystal in a standing wave and might therefore be part of the every-day routine in the future operation of the setup after beam realignment. Furthermore, it provides an easy verification that the Doppler cooling performs as expected for future traps, and is also a benchmark for the interferometic stability. Fig. 9.5 shows the autocorrelation function as it is calculated by employing the Wiener-Khinchine theorem: The power spectrum of the signal is calculated by taking the absolute squared values of an FFT of the fluorescence data, followed by the inverse transform. The resulting autocorrelation function

$$C(\tau) = \langle S(t)S(t+\tau)\rangle_t \tag{9.9}$$

is of course only an approximation as the Wiener-Khinchine theorem holds only strictly for an infinitely long acquisition period, however the correlation decay timescale is still clearly visible. [1]

[1] The finding of a 10 s timescale is consistent with a measurement where a 'mixed' Ramsey experiment is performed, where the R1/CC beam pair is used for the first $\pi/2$ pulse, and the R1/R2 beam pair for the second one. If the interferometers were perfectly stable, the fringe pattern would reveal the relative optical phase of the R2 beam with respect to the CC one. Upon scanning the concluding $\pi/2$ pulse phase, data points deviating significantly from 0.5 were measured, indicating nonvanishing correlation during the acquisition time of one data point, but no clear and reproducible fringe pattern could be observed.

9.3. Spectroscopy and Cooling

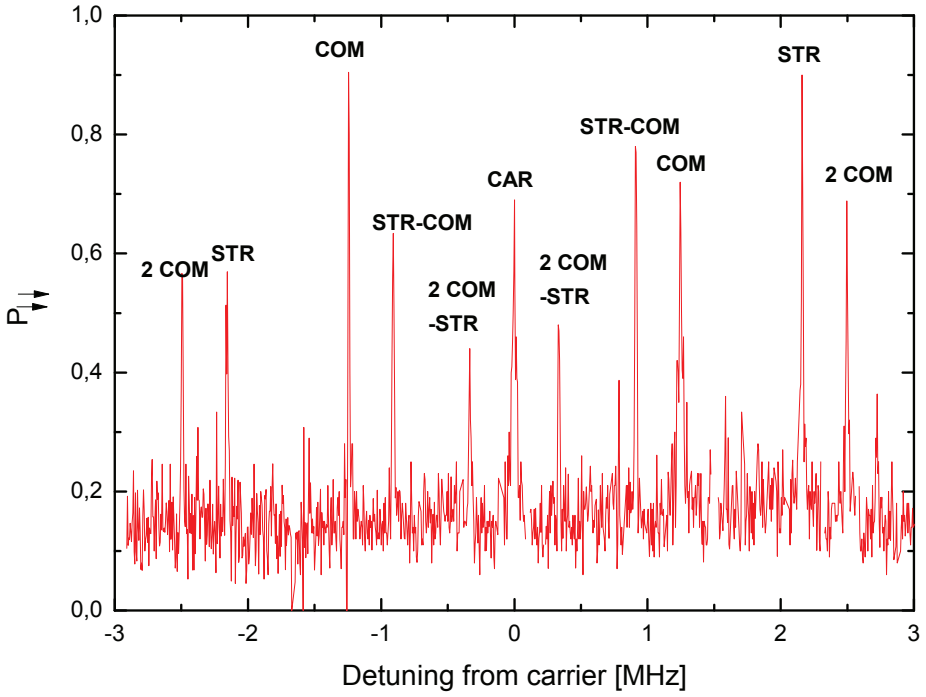

Figure 9.6.: Raman spectrum of a two ion crystal, taken with the beam pair R1/R2. The stretch mode of the ions occurs at $\sqrt{3}\nu_{\mathrm{COM}}$ as expected. Note the emergence of higher order mixed sidebands.

Fig. 9.6 shows a Raman spectrum with the orthogonal beam pair similar to Fig. 4.22. In addition to the COM mode, the stretch mode at $\nu_{\mathrm{STR}} = \sqrt{3}\nu_{\mathrm{COM}}$ occurs along with several higher order intercombination sidebands. In order to realize quantum gates, both modes have to be sufficiently cooled close to their respective ground states, as only then the ions can be sufficiently localized in the driving standing wave, irrespective of the mode on which the gate interaction is driven. We therefore employ an interleaved Raman sideband cooling scheme based on the one used in Sec. 4.6. A remarkable and yet puzzling fact is that the initial temperature of the COM mode is significantly higher in the case of two ions compared to the storage of only one ion at similar trap and laser parameters. Pulse width scans reveal mean quantum numbers in the range of $\bar{n}_{\mathrm{COM}} \approx 40..60$. The reason for this effect is still unknown, it could originate from a cooperative effect involving Coulomb nonlinearities, trap anharmonicities and micromotion.

Removal of these large phonon numbers requires a sequential cooling scheme involving higher order sidebands making use of the fact that the average Rabi frequencies on higher order sidebands is larger for higher initial temperatures and excitation on higher order sidebands leads to simultaneous removal of multiple phonons, see Fig. 4.32. The cooling sequence used in our experiments is indicated in table 9.1. From the pulse times, the cycles numbers and the repump time of 2 μs, a total cooling time of 1.66 ms results. During this time, significant radial heating of the ions takes place and also the stability of the crystal during the measurement is adversely affected.

No.	Sideband	Cooling cycles	π-time
1	3rd COM	20	6.0
2	2nd COM	30	10.0
3	1st STR	50	7.0
4	1st COM	50	11.0
5	1st STR	5	7.0

Table 9.1.: Sideband cooling sequence for two ions.

The radial temperature degrades the efficiency of both the RAP pulses and the fluorescence readout, therefore the state discrimination of $|\uparrow\uparrow\rangle, |\uparrow\downarrow\rangle$ and $|\downarrow\downarrow\rangle$ deviates strongly from the ideal one. The readout has to be described by the conditional probabilities to find the ions dark or bright (d/b) depending on their actual state before the readout. The following conditional probabilities were found when fitting the pulse width scans in Fig. 9.7:

$$\begin{aligned} p(dd|\uparrow\uparrow) &\approx 0.885 \quad p(dd|\uparrow\downarrow) \approx 0.100 \quad p(dd|\downarrow\downarrow) \approx 0.015 \\ p(db|\uparrow\uparrow) &\approx 0.250 \quad p(db|\uparrow\downarrow) \approx 0.525 \quad p(db|\downarrow\downarrow) \approx 0.050 \\ p(bb|\uparrow\uparrow) &\approx 0.015 \quad p(bb|\uparrow\downarrow) \approx 0.225 \quad p(bb|\downarrow\downarrow) \approx 0.800 \end{aligned} \tag{9.10}$$

$$\tag{9.11}$$

Note the low probability $p(db|\,|\uparrow\downarrow\rangle)$ that one ion in $|\uparrow\rangle$ actually leads to measurement of a db event. This indicates that the fluorescence rates are subject to additional fluctuations, i.e. the count statistics is strongly affected by the probabilistic heating of the ions. We extend the model for a coherently driven ion with coupling to one motional mode Eq. 4.34 to simultaneous coupling to two motional modes. The probability to find a single ion initialized in $|\uparrow\rangle$ in the $|\downarrow\rangle$ state after irradiation of a pulse of duration t is given by:

$$P_{\downarrow}^{(\Delta n_C,\Delta n_S)}(t) = \tfrac{1}{2}\sum_{n_C}\sum_{n_S} P_{n_C}^{(C)} P_{n_S}^{(S)} (\cos\left(M_{n,n+\Delta n_C}^{(C)} M_{n,n+\Delta n_S}^{(S)} \Omega_0\ t\right)\ e^{-\gamma\ t} + 1), \tag{9.12}$$

describing Rabi oscillations on the Δn_C-th, Δn_S-th sideband obtained by summation over the COM (C) and STR (S) modes with the respective phonon distributions $P_{n_C}^{(C)}$,$P_{n_S}^{(S)}$ including the matrix elements $M_{n,n+\Delta n_C}^{(C)}$ and $M_{n,n+\Delta n_S}^{(S)}$. From this, the probabilities for two

homogeneously driven ions are straightforwardly found to be

$$\begin{aligned} P_{\downarrow\downarrow}^{(\Delta n_C,\Delta n_S)}(t) &= P_{\downarrow}^{(\Delta n_C,\Delta n_S)}(t)^2 \\ P_{\downarrow\uparrow}^{(\Delta n_C,\Delta n_S)}(t) &= 2P_{\downarrow}^{(\Delta n_C,\Delta n_S)}(t)\left(1-P_{\downarrow}^{(\Delta n_C,\Delta n_S)}(t)\right) \\ P_{\uparrow\uparrow}^{(\Delta n_C,\Delta n_S)}(t) &= 1-P_{\downarrow\uparrow}^{(\Delta n_C,\Delta n_S)}(t)-P_{\downarrow\downarrow}^{(\Delta n_C,\Delta n_S)}(t). \end{aligned} \tag{9.13}$$

(9.14)

The factor of 2 in the second line is due to the indistinguishably of $|\uparrow\downarrow\rangle$ and $|\downarrow\uparrow\rangle$. Finally, the readout signals are a linear combination of these probabilities using Eq. 9.11:

$$P_{dd}^{(\Delta n_C,\Delta n_S)}(t) = p(dd|\uparrow\uparrow)P_{\downarrow\downarrow}^{(\Delta n_C,\Delta n_S)}(t) + p(dd|\uparrow\downarrow)P_{\uparrow\downarrow}^{(\Delta n_C,\Delta n_S)}(t) + p(dd|\uparrow\uparrow)P_{\uparrow\uparrow}^{(\Delta n_C,\Delta n_S)}(t), \tag{9.15}$$

and similarly for the other two signals. The fit parameters, obtained under the assumption of thermal phonon distributions on both modes, are $\bar{n}_C \approx 5.0$, $\bar{n}_S \approx 0.25$, $\eta_C \approx 0.25$, $\eta_S \approx 0.21$, $\Omega_0 \approx 2\pi\cdot 212$ kHz and $\gamma \approx 10$ ms^{-1}. The assumption of a thermal phonon distribution on the COM mode represents a rather questionable assumption, as the sideband cooling starting at a large average phonon number will supposedly transfer a considerable amount of population to the ground state while an extended hot tail is remaining in excited states. This might explain the deviations of the initial slope for the sideband scans on the COM mode in Fig. 9.7. As a conclusion, the cooling results from Fig. 9.7 were the best that could be achieved with the present apparatus, bought at a serious impairment of the readout fidelities. In order to work with ground state cooled ion strings, several technological improvements have to be made, see Chap. 10.

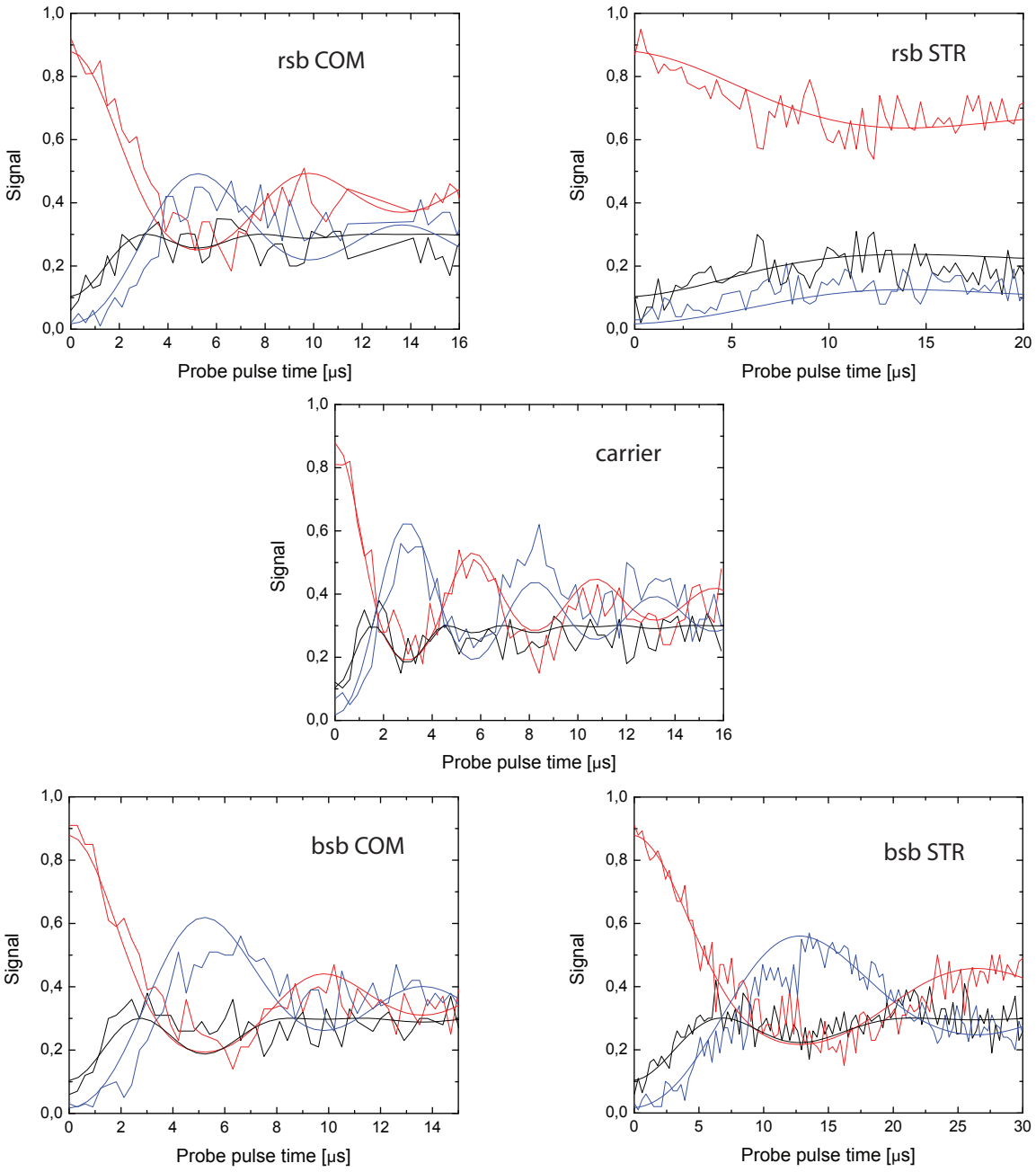

Figure 9.7.: Results for two-mode sideband cooling of two ions: The plots show pulse width scans on the R1/R2 Raman transition for two ions on the carrier and the respective red and blue sidebands of the COM and STR modes, along with fits to the model Eq. 9.15. The *dd* signal is depicted in red, the *db* signal is depicted in black and the *bb* one in blue. Note the strong difference between the rsb scans for the COM and STR mode.

9.4. Coherent Manipulations

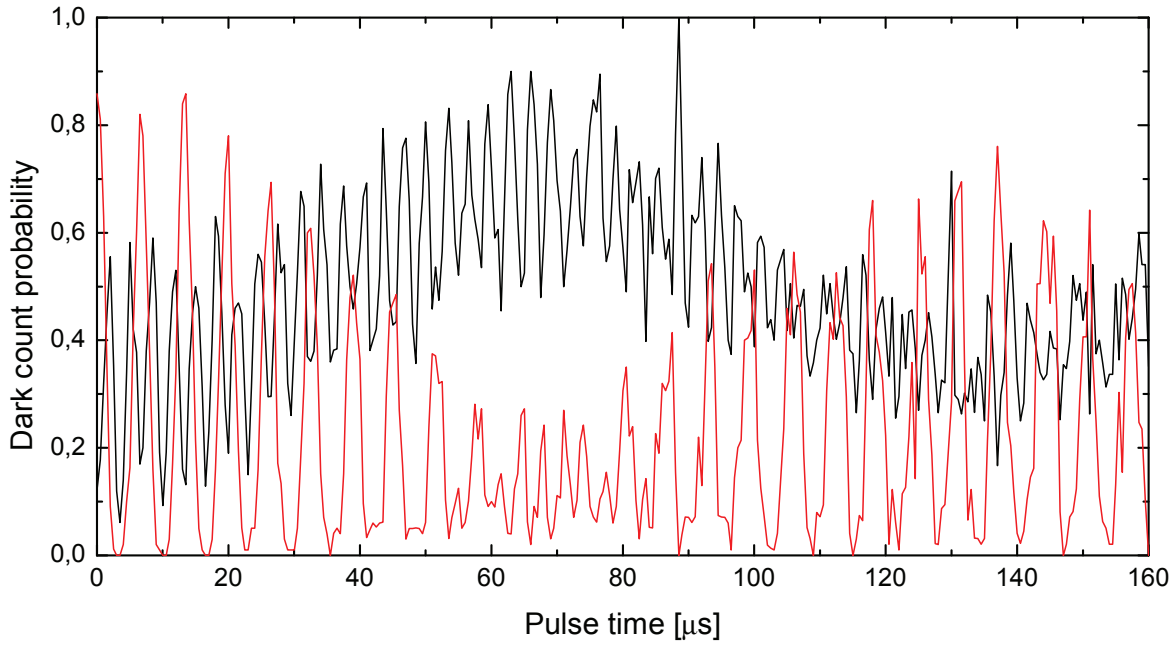

Figure 9.8.: Carrier Rabi oscillations of two ions, taken with the beam pair R1/CC, where the illumination of the two ions is inhomogeneous. The red curves shows the probability for finding the spins in $|\uparrow\uparrow\rangle$, and the black curve shows the probability for $|\downarrow\uparrow\rangle$ **or** $|\uparrow\downarrow\rangle$.

Coherent manipulations on the crystal are performed in the same way as with a single ion, namely with the copropagating beam pair R1/CC. The two-ion version of the unitary propagator Eq. 2.12 corresponding to a resonant square pulse with both beams is given by

$$\begin{aligned}\hat{U}^{(2)}(t) &= \hat{U}_1^{(1)}(t) \otimes \hat{U}_2^{(1)}(t) \\ &= \begin{pmatrix} x_1x_2 & -ie^{i\phi_2}x_1y_2 & -ie^{i\phi_1}x_2y_1 & -e^{i(\phi_1+\phi_2)}y_1y_2 \\ -ie^{-i\phi_2}x_1y_2 & x_1x_2 & -e^{i(\phi_1-\phi_2)}y_1y_2 & -ie^{i\phi_1}x_2y_1 \\ -ie^{-i\phi_1}x_2y_1 & -e^{i(-\phi_1+\phi_2)}y_1y_2 & x_1x_2 & -ie^{i\phi_2}x_1y_2 \\ -e^{i(-\phi_1-\phi_2)}y_1y_2 & -ie^{-i\phi_1}x_2y_1 & -ie^{-i\phi_2}x_1y_2 & x_1x_2 \end{pmatrix}\end{aligned} \tag{9.16}$$

with

$$\begin{aligned} x_1 &= \cos\frac{\theta_1}{2}, \qquad x_2 = \cos\frac{\theta_2}{2}, \\ y_1 &= \sin\frac{\theta_1}{2}, \qquad y_2 = \sin\frac{\theta_2}{2}, \end{aligned} \tag{9.17}$$

and the pulse areas $\theta_{1,2} = \Omega_{1,2}t$. Different Rabi frequencies $\Omega_1 \neq \Omega_2$ are found if the ions are not homogeneously illuminated by the beams, especially if the foci are of the same order of

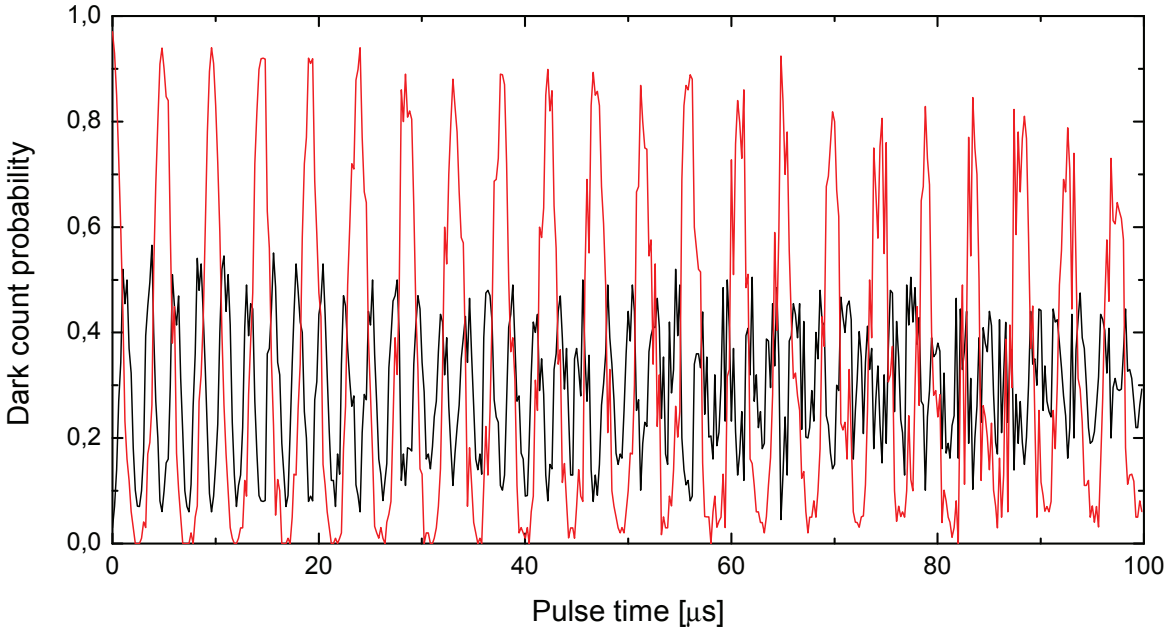

Figure 9.9.: Carrier Rabi oscillations of two ions, taken with the beam pair R1/CC, with homogeneous illumination of the two ions. The red curves shows the probability for finding the spins in $|\uparrow\uparrow\rangle$, and the black curve shows the probability for $|\downarrow\uparrow\rangle$ **or** $|\uparrow\downarrow\rangle$

magnitude or even smaller than the ion separation. The phases $\phi_{1,2}$ might be different for two reasons: First, in any case the phase fronts of the beams are in-plane with the ion crystal, such that the optical phase at one ion is delayed with respect to the other one. Second, an inhomogeneous illumination together with an imperfectly compensated Stark shift will lead to a slight off-resonance, such that the ions accumulate different phases $\phi_{1,2} \propto t$ throughout a pulse. The first phase difference does not lead to errors, as the optical phase at each ion will always stay synchronized with the first pulse. Only when attempting single ion read-out after splitting crystals, one will have to keep in mind that an addressing phase will occur. With the ion crystal initialized in $|\uparrow\uparrow\rangle$, the signals for the three distinguishable cases are found to be

$$\begin{aligned} S_{\uparrow\uparrow} &= \cos^2\frac{\theta_1}{2}\cos^2\frac{\theta_2}{2} \\ S_{\downarrow\uparrow,\uparrow\downarrow} &= \cos^2\frac{\theta_1}{2}\sin^2\frac{\theta_2}{2} + \sin^2\frac{\theta_1}{2}\cos^2\frac{\theta_2}{2} \\ S_{\downarrow\downarrow} &= 1 - S_{\uparrow\uparrow} - S_{\downarrow\uparrow,\uparrow\downarrow} = \sin^2\frac{\theta_1}{2}\sin^2\frac{\theta_2}{2} \end{aligned} \tag{9.18}$$

When Rabi oscillations are driven under inhomogeneous illumination, are beat at the difference frequency $\Omega_1 - \Omega_2$ occurs, which is shown in Fig. 9.8. Inhomogeneous Rabi frequencies

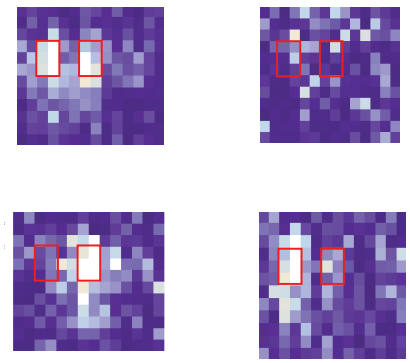

Figure 9.10.: Camera-based read-out of a two ion crystal: The four pictures show the four possible readout results of a two-ion crystal for an exposure time of 20 ms. The states can be distinguished with the bare eye. The red areas are the regions of interest from which the count level is integrated.

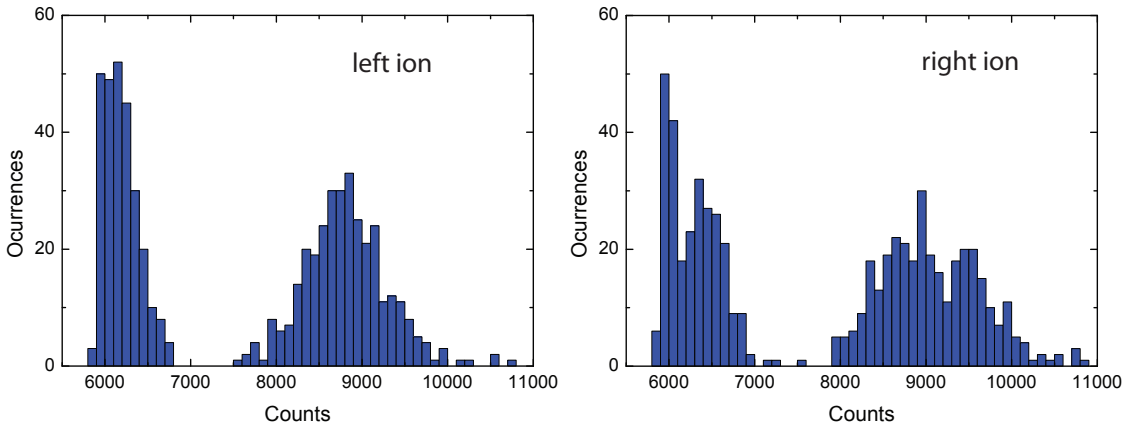

Figure 9.11.: Histograms resulting from the two-ion readout:.

were actually used to selectively address ions to produce the first deterministic entanglement of massive particles in Ref. [Tur98]. In our case, homogeneous Rabi frequencies are most often required, the corresponding signals after precise adjustment are shown in Fig. 9.9. On the long run, it is desirable to realize inhomogeneous Rabi frequencies like e.g. $\Omega_1 = 2\Omega_2$, as this

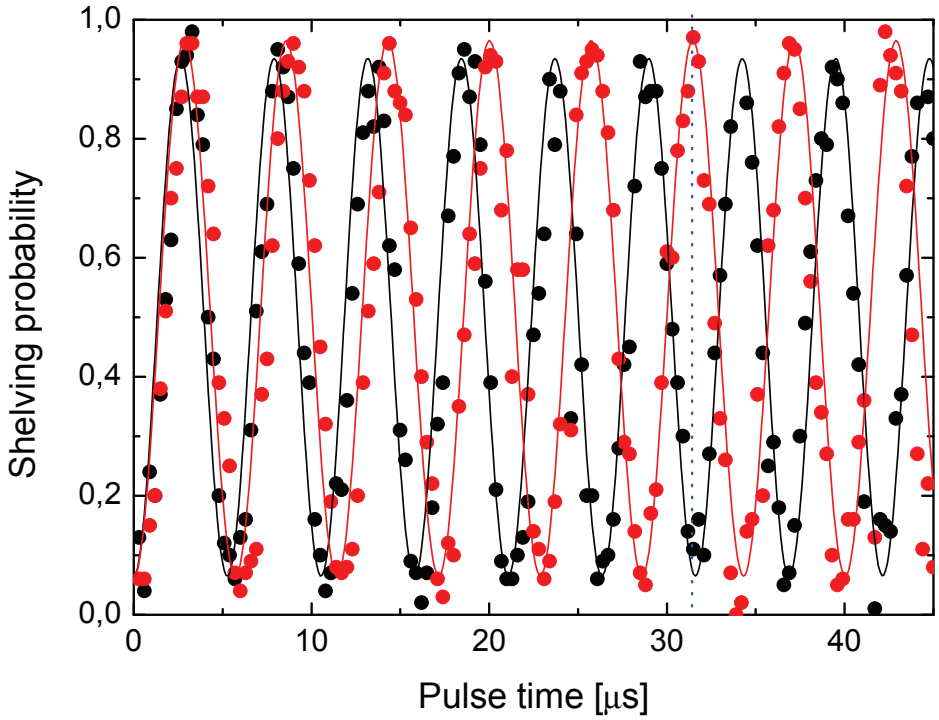

Figure 9.12.: Independent readout of two-ion Rabi oscillations: Rabi oscillations of two ions driven by R1/CC are shown, where the EMCCD camera was used for readout such that the dynamics of each individual ion can be seen. The red dots are the readout values for the left ion, the black dots are for the right one. The solid lines are fit results revealing the individual Rabi frequencies. The dashed blue line marks the pulse time for which the state $|\uparrow\downarrow\rangle$ can be deterministically prepared.

would allow for selective preparation of the computational basis states $|\uparrow\uparrow\rangle, |\uparrow\downarrow\rangle, |\downarrow\uparrow\rangle, |\downarrow\downarrow\rangle$ of two ions.

This goes along with the advantageous feature to independently read out the spin of two ions. Of course the segmentation of our trap allows for splitting of and merging of ion crystals, which is a possible approach for both independent preparation and read-out, but it requires a lot of additional overhead and is still technologically challenging, see chapter B. The second possibility for the independent readout is to use the EMCCD camera as a spatially resolving detector, which is bought at the price of less favorable signal-to-noise ratios as upon readout with the PMT [Bur10]. The realization of this independent readout scheme then allows for precise adjustment of the individual Rabi frequencies, which in turn makes the variable state preparation possible. Fig. 9.10 shows pictures for the four different bright/dark configuration of two ions. The exposure time was 20 ms in this case, which is rather long compared to the typical 2 ms for PMT readout, however it should still be possible to achieve much shorter

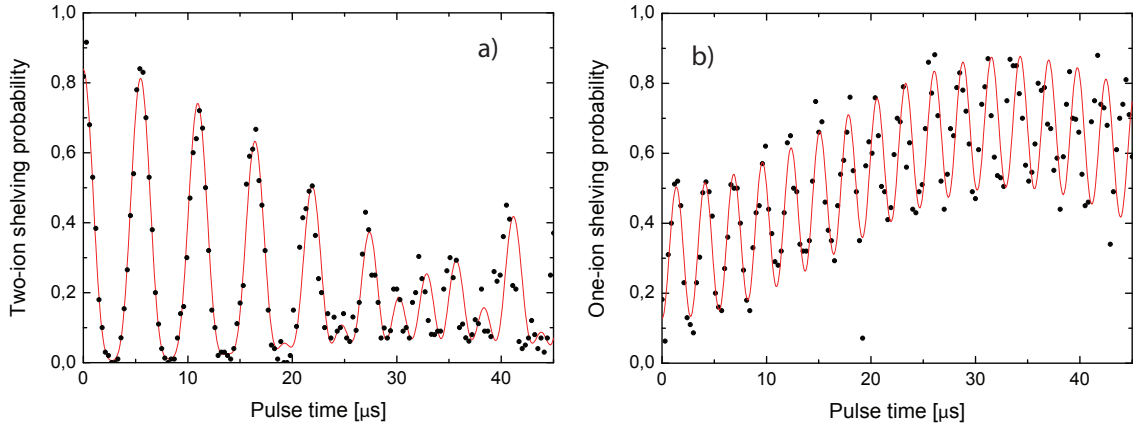

Figure 9.13.: PMT data of two-ion Rabi oscillations: PMT read-out of two-ion Rabi oscillations under the same conditions as in Fig. 9.12 are shown. **a)** shows the two-ion shelving probability $S_{\uparrow\uparrow}$, **b)** shows the single-ion shelving probability $S_{\uparrow\downarrow,\downarrow\uparrow}$ from Eq. 9.18. The solid lines are no fits, they are reconstructed with the Rabi frequencies obtained from the fits to the individual Rabi oscillations read out with camera. A slight frequency mismatch at longer pulse times is attributed to the drift of the Rabi frequency.

times upon several technical improvements like camera parameter optimization, stray light suppression and smart image processing. Fig. 9.11 shows the histograms obtained from integrating the count numbers over the regions indicated in Fig. 9.10. The count number distributions are clearly non-Poissonian, which is attributed to the nonlinear processes in the EMCCD chip. As not enough data was collected to be able to find a specific model distribution, no error estimation for the discrimination can be found, however, it can be safely stated that a clear discrimination is already possible. Fig. 9.12 shows measured Rabi oscillations driven with the R1/CC beams and read out with the camera. Rabi oscillations of the two ions at different Rabi frequencies seen, which are determined by fitting to be $2\pi\cdot189$ kHz for the right ion and $2\pi\cdot175$ kHz for the left ion. Knowing the Rabi frequencies, we can use these to predict the data obtained upon conventional PMT-based readout, according to Eqs. 9.18. The predicted curves are shown in Fig. 9.13 along with the measured data. They are found to match, although the Rabi frequencies slightly deviate for longer pulses. This can be attributed to the fact that the laser generating the Raman beams was not intensity stabilized the day the data was taken. As the structure of the curves still matches, it can be concluded that reliable readout based on the camera is possible.

9.5. A Two-Ion Schrödinger Cat

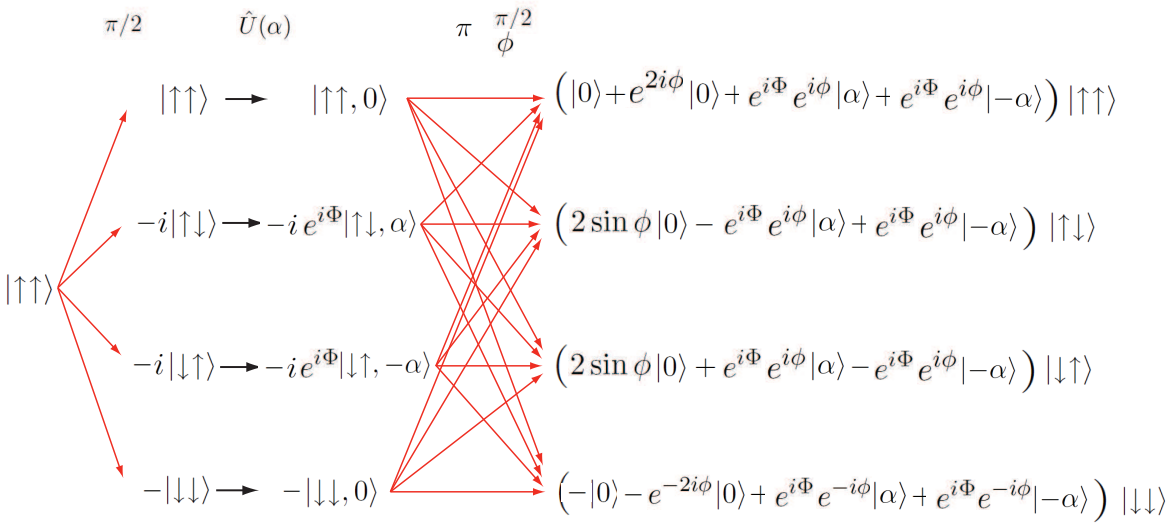

Figure 9.14.: Schrödinger cat state creation with two ions. From the rightmost column, the measured signals $S_0(t,\phi)$,$S_1(t,\phi)$ and $S_2(t,\phi)$ can be straightforwardly inferred by calculating the probabilities.

A possible mechanism for the entanglement of two spin qubits is the utilization of spin-dependent light forces as demonstrated for a single ion in chapter 8. The basic idea is to use a motional mode of the ion crystal for the creation of entanglement of the internal states of two ions analogously to the Cirac-Zoller proposal [Cir95]. The physical realization however is very different and was proposed in a more general context in [Mil09],[Sor00]. The remarkable feature of these gate schemes is that in contrast to the Cirac-Zoller scheme, no ground state cooling is strictly required, which makes the gates much more robust and easier to realize. The first experimental demonstration took place in 2003 [Lei03a] and an almost complete tomography of two spins subjected to an entangling gate operation based on this scheme was shown in [Hom06c]. Recently, a realization of a similar gate was shown even for Doppler cooled thermal ions [Kir09]. Entangling gates based on spin-dependent forces can be realized as follows: A two-ion crystal is placed in a driving Raman laser field such that only states of a given parity, i.e. *either* $|\uparrow\uparrow\rangle$ and $|\downarrow\downarrow\rangle$ *or* $|\uparrow\downarrow\rangle$ and $|\downarrow\uparrow\rangle$ are affected by the displacement force, see Fig. 8.1 for an illustration. Therefore, the geometric phase picked up during the evolution Eq. 8.21 depends on the *joint* spin state of the ion crystal, such that a controlled-phase gate is performed if the displacement is restored to zero after a complete motional cycle. The spins are then entangled, with the amount of entanglement given by the geometric phase. This phase gate can be extended to a controlled NOT gate by single qubit rotations, such

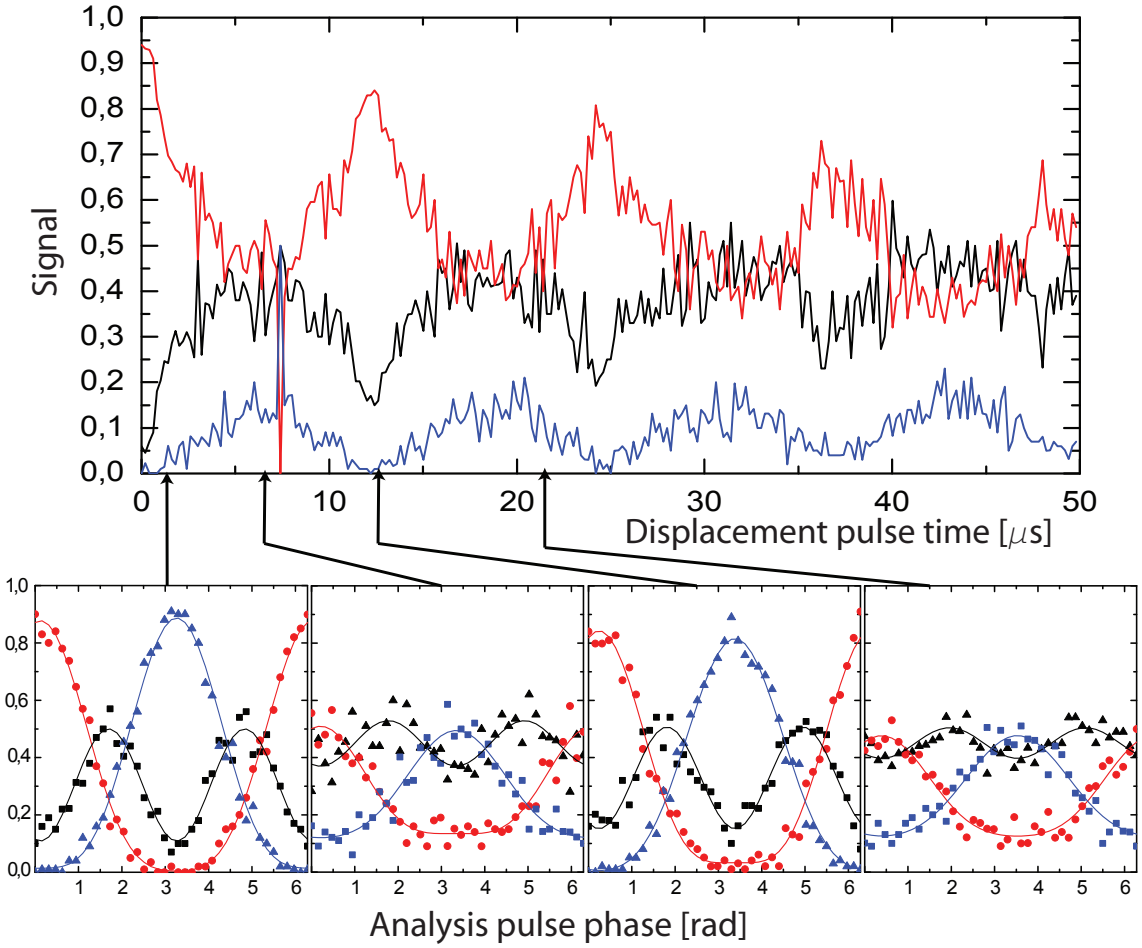

Figure 9.15.: Schrödinger cat state creation with two ions. The upper plot shows the readout signals $S_{\uparrow\uparrow}$ (red), $S_{\uparrow\downarrow,\downarrow\uparrow}$ (black) and $S_{\downarrow\downarrow}$ (blue) states versus drive pulse durations for a detuning from the STR mode of $\delta \approx 2\pi{\cdot}84$ kHz. The lower plots show scans of the analysis pulse phase for fixed displacement pulse times indicated by the arrows to the upper plot.

that an essential building block for quantum information protocols is realized. A pictorial representation of the state manipulation is shown in Fig. 9.14: A two-ion crystal initialized in $|\uparrow\uparrow\rangle$ is rotated into a balanced superposition of $|\uparrow\uparrow\rangle, |\uparrow\downarrow\rangle, |\downarrow\uparrow\rangle, |\downarrow\downarrow\rangle$. A vibrational mode of the ion crystal is displaced conditionally on the total spin state. The driving laser field is slightly detuned from the vibration frequency, such that the displacement is undone at the return time t_{ret}. If now t_{ret} and the driving amplitude are chosen such that the geometric

phase $\Phi = \pi/2$, the resulting state is can be unitarily rotated to

$$|\Psi\rangle = 2^{-1/2}\left(|\uparrow\uparrow\rangle + i|\downarrow\downarrow\rangle\right), \tag{9.19}$$

which is a maximally entangled state. The creation of entanglement can be easily deduced from the suppression of the signals pertaining to the $|\uparrow\downarrow\rangle, |\downarrow\uparrow\rangle$ signals. The ultimate proof of entanglement and measurement of the fidelity of the operation is performed by a parity oscillation measurement, see Ref. [Lei03b]. The constraint that only the spin states pertaining to a given parity are to be displaced can be relaxed to the requirement that the displacement for the different parities has to be substantially different, such that a *differential* geometric phase is picked up. Imperfect alignment will only degrade the efficiency of the gate with respect to the exploitation of the driving laser power. The important implication of this is that the gate scheme can be straightforwardly extended to a larger number of ions, most importantly to the case of four ions comprising a pair of a pair of logical qubits, encoded in a decoherence free subspace (DFS). Such a gate would have the advantage that the logical qubits would never leave the DFS at any point during the gate operation, as we have investigated in [Iva09].
The choice of the right drive amplitude is performed simply by minimizing the $S_{\uparrow\downarrow,\downarrow\uparrow}$ signal at a drive time of t_{ret}, and the placement of the ions by choice of the trap frequency is not crucial, i.e. a spin-dependent geometric phase can be picked up as long as the coupling strength to the laser field is substantially different for $|\uparrow\downarrow\rangle, |\downarrow\uparrow\rangle$ and $|\downarrow\downarrow\rangle, |\downarrow\downarrow\rangle$. However, near-perfect ground state cooling of *both* motional modes of the two-ion crystal is a critical prerequisite, as a finite temperature has several detrimental effects on the gate performance: i) Due to the temperature-induced delocalization, the coupling strength difference between $|\uparrow\downarrow\rangle, |\downarrow\uparrow\rangle$ and $|\downarrow\downarrow\rangle, |\downarrow\downarrow\rangle$ is diminished, ii) the overall coupling strength is diminished and iii) the geometric phase picked up is fluctuating, leading to a loss of phase coherence.
We have created Schrödinger cat states of two Doppler cooled ions by near resonant excitation of the STR mode. The results are shown in Fig. 9.15, where the results of a scan of the displacement pulse time at fixed analysis pulse phase are shown, along with scans of the analysis pulse phase for a set of fixed displacement pulse times. As can be seen, no signature of a geometric phase, i.e. a nonzero $S_{\downarrow\downarrow}$ signal and suppression of the $S_{\uparrow\downarrow,\downarrow\uparrow}$ signal at the return times is visible, despite the fact that a clear decay and revival of the contrast is present. The reason is the increased sensitivity of motionally excited states to displacement, see the measurements for a thermal single ion shown in Fig. 8.4 for comparison. The data from the scans of the analysis pulse phase can be used for a detailed characterization of the quantum dynamics of the two ions. We first need to generalize the simplified dynamics illustrated in Fig. 9.14 to account for imperfections: First, we include a possible displacement of the even states $|\uparrow\uparrow\rangle$ and $|\downarrow\downarrow\rangle$ by the value β, and therefore include a geometric phase $\bar{\Phi}$ for these states. Furthermore, we include a possible residual Stark shift, leading to an additional spin phase

$\theta(t)$ with respect to the pulse time t. The readout signals are then given by

$$\begin{aligned}
S_{\uparrow\uparrow} &= \tfrac{1}{8}\left(2+e^{-2|\beta|^2}\right)+\tfrac{1}{8}e^{-2|\alpha|^2}\cos 2\phi' \\
&+ \tfrac{1}{4}\cos\phi'\left(e^{-|\alpha||\beta|\cos\chi}\cos(\Delta\Phi+|\alpha||\beta|\cos\chi)+e^{|\alpha||\beta|\cos\chi}\cos(\Delta\Phi-|\alpha||\beta|\cos\chi)\right) \\
S_{\downarrow\downarrow} &= \tfrac{1}{8}\left(2+e^{-2|\beta|^2}\right)+\tfrac{1}{8}e^{-2|\alpha|^2}\cos 2\phi' \\
&- \tfrac{1}{4}\cos\phi'\left(e^{-|\alpha||\beta|\cos\chi}\cos(\Delta\Phi+|\alpha||\beta|\cos\chi)+e^{|\alpha||\beta|\cos\chi}\cos(\Delta\Phi-|\alpha||\beta|\cos\chi)\right) \\
S_{\uparrow\downarrow} &= \tfrac{1}{8}\left(2-e^{-2|\beta|^2}\right)-\tfrac{1}{8}e^{-2|\alpha|^2}\cos 2\phi' \\
&- \tfrac{1}{4}\cos\phi'\left(e^{-|\alpha||\beta|\cos\chi}\cos(\Delta\Phi+|\alpha||\beta|\cos\chi)-e^{|\alpha||\beta|\cos\chi}\cos(\Delta\Phi-|\alpha||\beta|\cos\chi)\right) \\
S_{\downarrow\uparrow} &= \tfrac{1}{8}\left(2-e^{-2|\beta|^2}\right)+\tfrac{1}{8}e^{-2|\alpha|^2}\cos 2\phi' \\
&- \tfrac{1}{4}\cos\phi'\left(e^{-|\alpha||\beta|\cos\chi}\cos(\Delta\Phi+|\alpha||\beta|\cos\chi)-e^{|\alpha||\beta|\cos\chi}\cos(\Delta\Phi-|\alpha||\beta|\cos\chi)\right),
\end{aligned} \tag{9.20}$$

where $\Delta\Phi = \Phi - \bar{\Phi}$ and $\phi' = \phi + \theta(t)$. χ is the angle in phase space between the complex displacements α and β. The signals are now modeled by

$$\begin{aligned}
S_{\uparrow\uparrow} &= a_2\cos 2\phi' + a_1\cos\phi' + b + \tfrac{1}{4} \\
S_{\downarrow\downarrow} &= a_2\cos 2\phi' - a_1\cos\phi' + b + \tfrac{1}{4} \\
S_{\uparrow\downarrow,\downarrow\uparrow} &= -2\ a_2\cos 2\phi' - 2\ b + \tfrac{1}{2},
\end{aligned} \tag{9.21}$$

with

$$\begin{aligned}
b(t) &= b^{(0)}\tfrac{1}{8}e^{-2|\beta|^2}e^{-\gamma_\beta t} \\
a_2(t) &= a_2^{(0)}\tfrac{1}{8}e^{-2|\alpha|^2}e^{-\gamma_{\alpha 2} t} \\
a_1(t) &= a_1^{(0)}\tfrac{1}{4}e^{-\frac{1}{2}\left(|\alpha|^2+|\beta|^2\right)}e^{-\gamma_{\alpha 1} t} \\
&\cdot \left(e^{-|\alpha||\beta|\cos\chi}\cos(\chi\Phi+|\alpha||\beta|\cos\chi)+e^{|\alpha||\beta|\cos\chi}\cos(\chi\Phi-|\alpha||\beta|\cos\chi)\right).
\end{aligned} \tag{9.22}$$

The empirical dephasing rates $\gamma_\beta, \gamma_{\alpha 1}$ and $\gamma_{\alpha 2}$ account mostly for the contrast loss due to the spreads of the displacements and geometric phases picked up resulting from thermal ensemble averaging. The scaling parameters $a_1^{(0)}, a_2^{(0)}$ and $b^{(0)}$ account for readout imperfections. The remarkable feature arising here is that the odd and even state displacements α and β can be read off independently from the fit results, which provides a possibility to directly align the ion in the driving laser field. Other alignment procedures as the one presented in Sec. 9.2 or the method in [Hom06a], where the sideband Rabi frequencies are measured, yield a higher experimental effort and measure the alignment in a *different* beat pattern than the one which is actually driving the displacement force. The parameters $a_1(t)$ and $a_2(t)$,

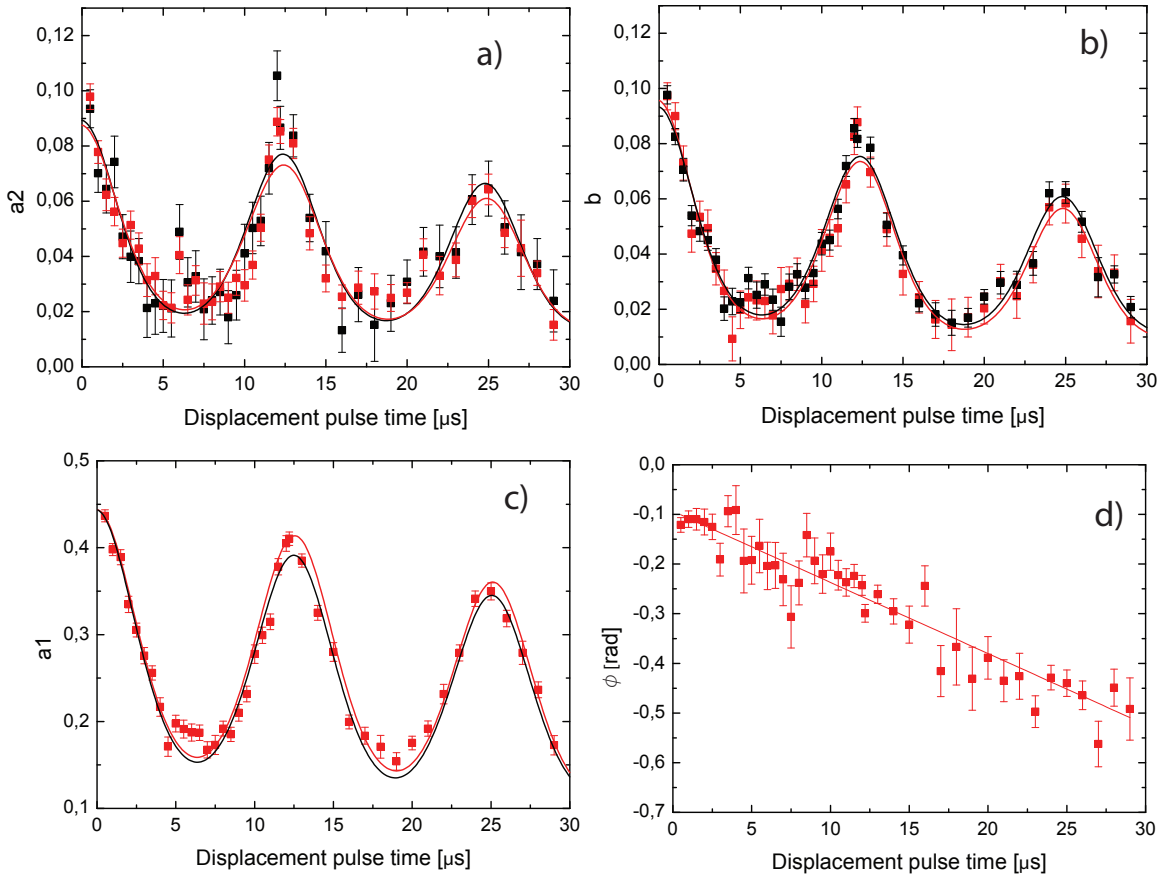

Figure 9.16.: Parameters describing the quantum dynamics of two ions: The plots show the parameters describing the state of the two ion crystal according to Eqs. 9.21, along with fits to the model Eqs. 9.22. The parameters **a)** a_2 and **b)** b can be extracted from both $S_{\uparrow\uparrow}(\phi)$ (red fit) and $S_{\uparrow\downarrow,\downarrow\uparrow}(\phi)$ (black fit), it can be seen that the fit results are consistent. The behavior of the **c)** a_1 parameter extracted from the $S_{\uparrow\uparrow}(\phi)$ can be explained by pure dephasing (black fit) or by the occurrence of a nonzero geometric phase (red fit), see text. The fitted offset phase $\theta(a)$ is shown in **d)**, which reveals a residual static Stark shift of $\Delta_S^{(0)} \approx 2\pi{\cdot}2.4$ kHz.

describing the strength of the signal oscillations with respect to ϕ' and $2\phi'$, respectively, along with the time-dependent baseline b and the Stark phase offset θ are obtained by fitting the $S_{\uparrow\uparrow}$ and $S_{\uparrow\downarrow,\downarrow\uparrow}$ signals to the model Eqs. 9.22 for the various displacement pulse times. The results are shown in Fig. 9.16.

Taking into account the time-dependent displacements according to Eq. 8.18:

$$\begin{aligned} |\alpha(t)| &= \mathcal{F}_\alpha \sin\left(\frac{\delta t}{2}\right) \\ |\beta(t)| &= \mathcal{F}_\beta \sin\left(\frac{\delta t}{2}\right), \end{aligned} \tag{9.23}$$

we obtain the dimensionless driving strengths $\mathcal{F}_\alpha$ and $\mathcal{F}_\beta$ for the odd/even states from fitting $a_1(t)$, $a_2(t)$ and $b(t)$ to Eqs. 9.22 with Eqs. 9.23. The results are shown in Table 9.2, where it can be seen that both signals yield consistent results. A significant difference between $\mathcal{F}_\alpha$ and $\mathcal{F}_\beta$ cannot be claimed.

Parameter	$a_2/S_{\uparrow\uparrow}$	a_2 from $S_{\uparrow\downarrow,\downarrow\uparrow}$	b from $S_{\uparrow\uparrow}$	$b/S_{\uparrow\downarrow,\downarrow\uparrow}$
$\mathcal{F}_\alpha$	0.41(2)	0.43(2)	-	-
$\mathcal{F}_\beta$	-	-	0.44(1)	0.45(1)
$\delta/2\pi$ [kHz]	80.1(8)	80.5(8)	80.4(5)	80.4(6)
$\gamma_{\alpha 2}$ $[\mu s^{-1}]$	0.014(4)	0.012(4)	-	-
γ_β $[\mu s^{-1}]$	-	-	0.017(5)	0.021(3)

Table 9.2.: Fit results for the parameter sets Eqs. 9.22. In order to demonstrate consistency, results from individual fits to the $S_{\uparrow\uparrow}$ and $S_{\uparrow\downarrow,\downarrow\uparrow}$ signals are compared.

For the explanation of the behavior of the a_1 values with respect to the displacement pulse time, we first assume that the differential driving strength of the odd and even states is zero, such that no differential geometric phase occurs. The result for the dephasing parameter is then $\gamma_{\alpha 1} \approx 0.008(1)\mu s^{-1}$, which is significantly smaller than the dephasing rates $\gamma_{\alpha 2}$ and γ_β. An alternative parameter set is obtained if we assume $\Delta\mathcal{F}^2$=0.011(1), consistent with the fit results for $a_2(t)$ and $b(t)$. The differential geometric phase is then given by

$$\Delta\Phi(t) = \Delta\mathcal{F}^2 \left(\sin \delta t - \delta t\right). \tag{9.24}$$

This leads to a more reduced dephasing rate of $\gamma_{\alpha 1} \approx 0.002(1)\mu s^{-1}$, , meaning that neither of the models entirely reproduces the data as can be seen in Fig. 9.16 c). As a conclusion, the data is consistent with nonzero differential geometric phase, which would amount to $\Delta\Phi \approx 0.16$ rad, but not enough precision is attained to discern between the appearance of a nonzero $\Delta\Phi$ and pure dephasing.
Cooling of both COM and STR modes close to the ground state was achieved as shown in Fig. 9.7, with the axial cooling bought at the price of a strong radial heating with a significant deterioration of the readout fidelity. A successful combination of the two-mode cooling with a displacement drive has not been possible, as the displacement drive would have required a large part of the off-resonant laser power in the CC beam, which in turn would have even increased the required total cooling time. We are however confident that improvement of the trap supply electronics and establishment of fast near-resonant cooling schemes will enable us to successfully perform geometric phase gates.

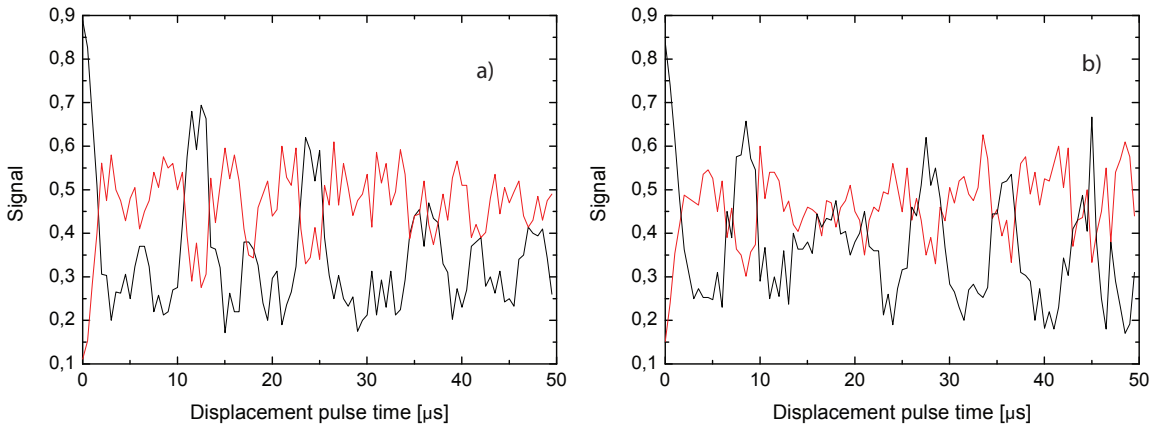

Figure 9.17.: Beat between displacement and squeezing: The plot show the signals $S_{\uparrow\uparrow}$ (black) and $S_{\uparrow\downarrow,\downarrow\uparrow}$ (red) for detuning from STR mode of about **a)** 166 kHz and **b)** 140 kHz. Beating between the displacement dynamics on STR and the squeezing dynamics on COM is clearly observed. In case a), the return time on the STR mode is about 6 μs, whereas the return time on the COM mode is about 12 μs, leading to a suppression of every second revival peak as the squeezed COM mode reduces the phase space overlap.

As a conclusion for this chapter, results on the generation of exotic multi-mode Schrödinger cat states are presented. Here, the frequency of the driving force was tuned sufficiently far to the blue side of the STR mode, such that considerable interaction on the second COM sideband occurs. This interaction is a parametric excitation at $2\omega_{\mathrm{COM}}$, i.e. squeezing. The squeezing is possible as the measurement is performed with a thermal ion crystal, where the matrix elements pertaining to the second blue sideband are sufficiently strong, or intuitively stated: large wavefunctions are much easier to squeeze as small ones. The total state of the two ion crystal after the displacment/squeezing pulse would then be:

$$\begin{aligned} |\Psi\rangle &= \sum_n p_{\mathrm{th}}(n) \sum_m p_{\mathrm{th}}(m) |\uparrow\uparrow\rangle |m, \alpha_m(t)\rangle |n, \chi_n(t)\rangle - i |\uparrow\downarrow\rangle |m, \beta_m(t)\rangle |n \xi_n(t)\rangle \\ &- i |\downarrow\uparrow\rangle |m, -\beta_m(t)\rangle |n, -\xi_n(t)\rangle - |\downarrow\downarrow\rangle |m, -\alpha_m(t)\rangle |n, -\chi_n(t)\rangle. \end{aligned} \tag{9.25}$$

With pulse-time dependent displacement parameters as in Eq. 9.23 and similar squeezing paramters $\chi(t)$ and $\xi(t)$ for the even and odd spin states, respectively. n denotes the number states of the COM mode and m denotes the number states of the STR mode. The final ket for each part of the state denotes the squeezed state of the COM mode. The results of these measurements are shown in Fig.9.17, where one can clearly observe a phase-space beating of the two motional modes.

10. Conclusion and Outlook

10.1. Conclusion

The introduction of this thesis stated that robustness and fidelity of all required qubit operations are essential foundations of any approach to achieve an experimental realization of scalable quantum information. The high fidelity is needed to attain the quantum error correction threshold and robustness is needed because the scalability inevitably implies a technological approach which will offer a less favorable environment for individual qubits. In the course of this thesis, every required operation for single qubits could be successfully realized at high fidelities, and the bottleneck limiting the fidelity could be identified in every case such that future technological improvements can be devised in order to achieve even higher fidelities. It also became clear that the robust implementations of the individual operating steps is indeed necessary, as can be seen from the measurements of the extremely high radial and intermediately high axial heating rates, see sections 4.3 and 4.6. Detailed studies of the qubit coherence were performed both in the absence and under the influence of external laser fields, with the results that the decoherence rates at the present stage allow for quantum information experiments from basic up to intermediate complexity, see Sec. 4.7. The technical and physical sources of the decoherence processes were almost completely understood, such that it is clear what the required technological improvements are. An extensive characterization and testing of the trap was performed, with the main results that ion transport throughout the whole trap structure is possible and that the actual electrostatic potential match the predicted ones with great accuracy. For the latter achievement, the microchip trap provided the testbed for our potential calculation software and for potential shaping techniques.
The methods established for single qubit operation were used for various demonstrations that complex experiments at the quantum level are indeed possible in microstructured ion traps. These experiments were of course not just carried out for demonstration purposes: The successful reconstruction of a density matrix of the state of the axial vibrational mode is the basis for future experiments on the emerging field of quantum thermodynamics. The coherent measurement method developed for the determination of atomic matrix elements is side product of the decoherence studies. It addresses a contemporary problem from atomic physics. The extensive experiments carried out on the action of spin-dependent light forces on a single ion provide the basis for future robust entangling gate operations. Furthermore, the two-ion crystal as the more complex basic building block of our experimental scheme was investigated, where individual readout and manipulation were successfully demonstrated. The stability and initial temperature of the two-ion crystal however remains to be improved.

10.2. Open Questions

This section briefly addresses the questions arising from measurement data acquired throughout this thesis which could not be entirely understood, which is done for the sake of documentation and completeness.

Stability of ion crystals: The predominant questions are associated with the rather bad stability of two-ion crystals, which is also of fundamental importance because it represents a crucial bottleneck for future progress. The bistable behavior of the crystals implies that nonlinearities are involved. In Sec. 5.2, a bistability originating from the nonlinear nature of Doppler cooling was explained, which can also be mediated by micromotion and would therefore explain the decreased stability at large trap drive rf amplitudes. However, it is not clear why two ions should be unstable at parameters where a single ion is completely stable. Furthermore, the drastically impaired Doppler cooling result of the COM mode of a two ion crystal cannot be straightforwardly explained by this mechanism. If the additional Coulomb nonlinearity present for the crystal would give rise to these effects, one would intuitively expect that the STR mode should be affected instead of the COM one.

Parasitic shelving: The incoherent excitation of population from the $|\downarrow\rangle$ level occurring during the shelving pulses could not be explained by off-resonant excitation or laser phase fluctuations. It therefore must be associated with an incoherent spectral background of the 729 nm laser. The width, strength and origin of this background remain unclear.

Enhanced laser-driven decoherence: The ratio of photon-scattering induced spin qubit decoherence and scattering rate determined experimentally in Sec. 4.7 is supported by the theoretical derivation given in Appendix A, which also predicts a set of counterintuitive effects. Future measurements are supposed to yield more precise figures for the decoherence rate and will test more sophisticated theoretical predictions.

Laser coupling fluctuations: The measurements of the Stark-shift induced decoherence rates presented at the end of Sec. 4.7 show that slow but large fluctuations of the atom-laser coupling strength are present in our system, which are not consistent with the expected beam pointing fluctuations or intensity fluctuations. A possible source of this effect might be an unstable radial behavior of the ions, which could be improved by better voltage supply electronics and better Doppler cooling.

Radial heating rates: Measurements of the fluorescence rate decrease after waiting times in the millisecond range presented in Sec. 4.3 show that the heating rates in the radial directions are tremendously larger than the one measured for the axial direction. The source of this behavior is still unknown, it can hopefully be counteracted with improved trap supply electronics.

Lower bound of the heating rates: Axial heating rate measurement have shown that the heating rate is strongly dependent on the voltage supply electronics (see Fig. B.4), it is yet unclear how low the heating can be suppressed by improvement of the circuitry.

Line broadening: Measurements of the fluorescence rates at 397 nm are inconsistent with the linewidth of about 22 MHz of that transition, see Figs. 4.4 and 5.6. Possible sources of this additional broadening are residual micromotion along the 397 nm beam or broadening

due to a large radial temperature.

10.3. Outlook

The future tasks to be solved for the demonstration of our scalable quantum information concept break down into two basic fields: First, entangling gate operations between two ions have to be accomplished, which requires a better stability of these crystals at larger trap frequencies. One therefore has to find ways to suppress noise on the DC electrodes even further and investigate the stability and noise characteristics of the trap drive RF. It might also be of great interest to investigate theoretically why the stability and initial temperature of the two ion crystal is so much different compared to the single ion case, despite the trap operation parameters are deep in the stability region. The other basic direction is the further development of the scalable voltage supply that will allow for shuttling operations much faster than qubit coherence time. This development is currently underway, however, due to the technological complexity, it might require a certain number of development iterations before the required specifications are met. If these two hurdles are taken, the methods can be combined to realize basic quantum computing tasks based on shuttling qubits in a segmented trap. For example, locally created entanglement between two qubits can be distributed by splitting the crystal and moving the ions far apart, which would allow for the realization of the largest distance ever achieved between deterministically entangled massive particles. The ability to handle three or more qubits would open the door to a rich plethora of quantum physics, addressing questions such as quantum state estimation and the characterization of higher dimensional Hilbert spaces, along with the decoherence properties of complex quantum states. In fact, the number of apparatuses worldwide which allow for deterministic operations with three or more ion-based qubits is to our knowledge limited to two at the time this thesis is written, indicating the vast unknown territory which is still open to explore.
It remains to be stated that up to now no fundamentally unsolvable problem with our experimental approach has been found, we therefore conclude with the statement that the way towards scalable quantum information still seems to be an adventurous path full of expected and unexpected obstacles, but also with many beautiful treasures at its sides and a mysterious end(?) that is yet not known.

A. Adiabatic Elimination on the Master Equation

Starting from Eq. 2.68, we make the following simplifying assumptions:

- The detuning Δ from the $S_{1/2} \rightarrow P_{1/2}$ transition is to much smaller than the fine structure splitting between the $P_{1/2}$ and $P_{3/2}$ states: $|\Delta| \ll \Delta_{FS}$, such that only the $P_{1/2}$ state is to be taken into account.
- We additionally assume that $|\Delta| \gg \Gamma$.
- We neglect the magnetic field term in Eq. 2.68 as it produces a mere energy shift which can be accounted for later on.

We can then represent the master equation Eq. 2.68 by a Liouvillian superoperator

$$\begin{aligned} \mathcal{L}(\hat{\rho}_{gg}) &\approx \left(\frac{i}{\Delta} - \frac{\Gamma}{2\Delta^2}\right)\hat{\rho}_{gg}\hat{H}_i\hat{P}_e\hat{H}_i + \text{h.c.} \\ &+ 2\frac{\Gamma}{2\Delta^2}\sum_{\sigma}\hat{A}_{1/2,\sigma}\hat{H}_i\hat{\rho}_{gg}\hat{H}_i\hat{A}^{\dagger}_{1/2,\sigma} \end{aligned} \tag{A.1}$$

If we arrange the elements of the density matrix in the form a vector,

$$\rho = (\rho_{11}, \rho_{12}, \rho_{21}, \rho_{22})^T, \tag{A.2}$$

the Liouvillian superoperator can be given in the form of a 4x4 matrix with elements containing Δ, Γ, the Clebsch-Gordon factors and the properties of the laser beams, i.e. their relative detuning, their dipolar Rabi frequencies and their polarization components.

The master equation Eq. 2.68 can be written as

$$\dot{\rho} = \left(\mathcal{L}_{\text{rabi}} + \mathcal{L}^{\dagger}_{\text{rabi}} + \mathcal{L}_{\text{stark}} + \mathcal{L}^{1\rightarrow 2}_{sc} + \mathcal{L}^{2\rightarrow 1}_{\text{sc}} + \mathcal{L}_{\text{deph}}\right)\rho, \tag{A.3}$$

where the $\mathcal{L}_{\text{rabi}}$ gives rise to coherent population transfer:

$$\mathcal{L}_{\text{rabi}} = i\frac{\Omega}{2}\begin{pmatrix} 0 & 0 & -1 & 0 \\ 1 & 0 & 0 & -1 \\ 0 & 0 & 0 & 0 \\ 0 & 0 & 1 & 0 \end{pmatrix}, \tag{A.4}$$

$\mathcal{L}_{\text{stark}}$ describes light-induced energy shifts:

$$\mathcal{L}_{\text{stark}} = i\frac{\Delta_S}{2}\begin{pmatrix} 0 & 0 & 0 & 0 \\ 0 & -1 & 0 & 0 \\ 0 & 0 & 1 & 0 \\ 0 & 0 & 0 & 0 \end{pmatrix}, \tag{A.5}$$

the $\mathcal{L}_{\text{sc}}^{i\to j}$ account for the population redistribution due to off-resonant scattering:

$$\mathcal{L}_{\text{sc}}^{1\to 2} = R_{1\to 2}\begin{pmatrix} -1 & 0 & 0 & 0 \\ 0 & 0 & 0 & 0 \\ 0 & 0 & 0 & 0 \\ 1 & 0 & 0 & 0 \end{pmatrix} \qquad \mathcal{L}_{sc}^{2\to 1} = R_{2\to 1}\begin{pmatrix} 0 & 0 & 0 & 1 \\ 0 & 0 & 0 & 0 \\ 0 & 0 & 0 & 0 \\ 0 & 0 & 0 & -1 \end{pmatrix}, \tag{A.6}$$

and finally $\mathcal{L}_{\text{deph}}$ causes dephasing, i.e. decay of the off-diagonal elements:

$$\mathcal{L}_{\text{deph}} = R_{\text{deph}}\begin{pmatrix} 0 & 0 & 0 & 0 \\ 0 & -1 & 0 & 0 \\ 0 & 0 & -1 & 0 \\ 0 & 0 & 0 & 0 \end{pmatrix}. \tag{A.7}$$

We now denote the 'bare' Liouvillian matrices without the prefactors as $\tilde{\mathcal{L}}_a$. They are mutually orthogonal and normalized such that:

$$\text{Tr}\left(\tilde{\mathcal{L}}_a\tilde{\mathcal{L}}_b^\dagger\right) = C_a\delta_{ab}, \tag{A.8}$$

with $C_{\text{rabi}} = 1$ and $C_a = 2$ otherwise. Thus the physical quantities of interest, which are the Rabi frequencies, Stark shift and the scattering and dephasing rates can be inferred by projecting them out of the total Liouvillian:

$$\begin{aligned} \Omega &= \text{Tr}\left(\tilde{\mathcal{L}}_{\text{rabi}}^\dagger\mathcal{L}\right) \\ \Omega^* &= \text{Tr}\left(\tilde{\mathcal{L}}_{\text{rabi}}\mathcal{L}\right) \\ \Delta_S &= \text{Tr}\left(\tilde{\mathcal{L}}_{\text{stark}}\mathcal{L}\right)/2 \\ R_{1\to 2} &= \text{Tr}\left(\tilde{\mathcal{L}}_{\text{sc}}^{1\to 2\dagger}\mathcal{L}\right)/2 \\ R_{2\to 1} &= \text{Tr}\left(\tilde{\mathcal{L}}_{\text{sc}}^{2\to 1\dagger}\mathcal{L}\right)/2 \\ R_{\text{deph}} &= \text{Tr}\left(\tilde{\mathcal{L}}_{\text{deph}}\mathcal{L}\right)/2 \end{aligned} \tag{A.9}$$

If we now consider two laser beams r and b, with polarization components $\vec{\epsilon}_{q,i}$ with $q = r, b$ and $i = +, 0, -$, the dipolar Rabi frequencies $\Omega_{r,b}$ and a relative detuning of $\delta = \omega_b - \omega_r$, the

quantities describing the dynamics of the effective two-level system can be given in terms of the quantities

$$\begin{aligned} M_{ij}^{bb} &= \Omega_b^2 c_i c_j \epsilon_{bi} \epsilon_{bj}^* \\ M_{ij}^{rr} &= \Omega_r^2 c_i c_j \epsilon_{ri} \epsilon_{rj}^* \\ M_{ij}^{br} &= \Omega_b \Omega_r^* c_i c_j \epsilon_{bi} \epsilon_{rj}^* e^{i(\Delta k - \delta t)} \\ M_{ij}^{qp} &= (M_{qp}^{ij})^* \end{aligned} \tag{A.10}$$

where the Clebsch-Gordan factors have been taken into account:

$$\begin{aligned} c_+ &= c_- = 1/\sqrt{3} \\ c_0 &= 1/\sqrt{6}. \end{aligned} \tag{A.11}$$

Upon using this recipe on the total Liouvillian obtained from the adiabatic elimination procedure Eq. 2.68, we finally obtain

$$\Omega = \frac{1}{2\Delta}\left(M_{0-}^{bb} + M_{+0}^{bb} + M_{0-}^{rb} + M_{+0}^{br} + M_{0-}^{br} + M_{0-}^{rr} + M_{+0}^{rb} + M_{+0}^{rr}\right) \tag{A.12}$$

$$\Delta_S = \frac{1}{4\Delta}\left(M_{--}^{bb} - M_{++}^{bb} + M_{--}^{rb} + M_{--}^{br} + M_{--}^{rr} - M_{++}^{rb} - M_{++}^{br} - M_{++}^{rr}\right) \tag{A.13}$$

$$\begin{aligned} R_{1\to 2} &= \frac{\Gamma}{4\Delta^2}\frac{1}{3}\left(M_{++}^{bb} + M_{++}^{rb} + M_{++}^{br} + M_{++}^{rr}\right) \\ &+ \frac{\Gamma}{4\Delta^2}\frac{2}{3}\left(M_{00}^{bb} + M_{00}^{rb} + M_{00}^{br} + M_{00}^{rr}\right) \end{aligned} \tag{A.14}$$

$$\begin{aligned} R_{2\to 1} &= \frac{\Gamma}{4\Delta^2}\frac{1}{3}\left(M_{--}^{bb} + M_{--}^{rb} + M_{--}^{br} + M_{--}^{rr}\right) \\ &+ \frac{\Gamma}{4\Delta^2}\frac{2}{3}\left(M_{00}^{bb} + M_{00}^{rb} + M_{00}^{br} + M_{00}^{rr}\right) \end{aligned} \tag{A.15}$$

$$\begin{aligned} R_{\mathrm{deph}} &= \frac{\Gamma}{4\Delta^2}\frac{1}{2}\left(M_{++}^{bb} + M_{++}^{rb} + M_{++}^{br} + M_{++}^{rr} + M_{--}^{bb} + M_{--}^{rb} + M_{--}^{br} + M_{--}^{rr}\right) \\ &+ \frac{\Gamma}{4\Delta}\frac{2}{3}\left(M_{00}^{bb} + M_{00}^{rb} + M_{00}^{br} + M_{00}^{rr}\right). \end{aligned} \tag{A.16}$$

In the following we give a brief interpretation of the various term occurring in the above expressions. Contributions to the Rabi frequency are only given by terms with π and a σ polarization component such as M_{0-}^{rb}. Resonant Rabi oscillations are only driven if the relative detuning δ of the two beams matches the energy splitting between $|\uparrow\rangle$ and $|\downarrow\rangle$. Terms arising from one beam only such as M_{0-}^{bb} would be resonant for zero Zeeman splitting, however the treatment then breaks down as the polarization components are not defined anymore. At a two-beam resonance, they lead to superimposed off-resonant Rabi oscillations. In the expression for the Stark shift, only terms corresponding to one polarization component occur. These can be either static homogeneous Stark shifts such as M_{--}^{bb} or spatiotemporally oscillating shifts arising from the beat between the two lasers such as M_{--}^{rb}. For the scattering rates, only the terms arising from one beam, e.g. M_{++}^{bb}, play a role as the mixed terms $M_{++}^{rb} + M_{++}^{br}$ are

real valued and oscillating around zero, such that they average out on the relevant timescales. The same statement holds for the contributions to the dephasing rate. It is important to state that these terms might still lead to enhanced decoherence effects if intensity or phase fluctuations at δ are present in the laser beams. Direct comparison between the scattering and decoherence rates reveal that the dephasing rate is not just given by half the scattering rate as it would be the case for a simple two-level system. Furthermore, an asymmetry in the ratio of dephasing to scattering rates from π and a σ polarization components arises, which is related to the amount of information about the final state carried away by the photon upon a scattering process.
If we subtract the Liouvillians pertaining to the mentioned dynamic processes, we obtain the residual Liouvillian

$$\mathcal{L}' = \mathcal{L} - \mathcal{L}_{\text{rabi}} - \mathcal{L}_{\text{stark}} - \mathcal{L}_{\text{sc}}^{1\to 2} - \mathcal{L}_{\text{sc}}^{2\to 1} - \mathcal{L}_{\text{deph}}, \tag{A.17}$$

which has the structure

$$\mathcal{L}' = \begin{pmatrix} 0 & \mathcal{L}_{12} + \tilde{\mathcal{L}}_{12} & \mathcal{L}_{12}^* + \tilde{\mathcal{L}}_{12}^* & 0 \\ -\mathcal{L}_{12}^* + 3\tilde{\mathcal{L}}_{12}^* & 0 & \mathcal{L}_{23} & -3\mathcal{L}_{12}^* + \tilde{\mathcal{L}}_{12}^* \\ -\mathcal{L}_{12} + 3\tilde{\mathcal{L}}_{12} & \mathcal{L}_{23}^* & 0 & -3\mathcal{L}_{12} + \tilde{\mathcal{L}}_{12} \\ 0 & -\mathcal{L}_{12} - \tilde{\mathcal{L}}_{12} & -\mathcal{L}_{12}^* - \tilde{\mathcal{L}}_{12}^* & 0 \end{pmatrix}, \tag{A.18}$$

with

$$\begin{aligned} \mathcal{L}_{12} &= \frac{\Gamma}{4\Delta^2}\frac{1}{6}\left(M_{0+}^{bb} + M_{0+}^{br} + M_{0+}^{rb} + M_{0+}^{rr}\right) \\ \tilde{\mathcal{L}}_{12} &= -\frac{\Gamma}{4\Delta^2}\frac{1}{6}\left(M_{-0}^{bb} + M_{-0}^{br} + M_{-0}^{rb} + M_{-0}^{rr}\right) \\ \mathcal{L}_{23} &= -\frac{\Gamma}{4\Delta^2}\frac{1}{3}\left(M_{+-}^{bb} + M_{+-}^{br} + M_{-+}^{rb} + M_{+-}^{rr}\right) \end{aligned} \tag{A.19}$$

It is unclear yet whether this remainder describes actual physical effects or if it is an artifact from the mathematical procedure. The measurement results presented in Fig. 4.38 however support an enhanced decoherence rate described by the term $\mathcal{L}_{23}$. With the experimental capability for precise decoherence measurements, this will hopefully resolved in the future by performing these measurements for various beam configurations.

B. Trap Voltage Supply Electronics

The supply electronics for dc trap voltages represents *the* crucial technological cornerstone for scalable quantum information experiments in segmented ion traps. In conventional ion trap experiments, noise reduction is accomplished by massive low-pass filtering of the supply voltages, this approach is not viable for our scheme as the ions are supposed to be moved within the trap structure on short timescales, such that voltages in the frequency range of up to 1 MHz or even more need to be admitted. Instead of relying on filtering, the development of suitable low-noise electronics is necessary. The voltage noise present on the electrodes is responsible for the heating of the ions, while the heating rate determines the suitability of a given trap for quantum information experiments. This heating process is investigated theoretically in Ref. [Lam97]. A detailed experimental study where the heating rate was investigated with respect to the ion-trap surface distance and the surface temperature resulted in heating rates that were y orders of magnitude larger than the theoretically expected ones [Des06], the reason for which remains unclear as of today. It is argued the insulting 'dirt' patches on the trap surfaces with thermally fluctuating charges give rise to the observed strong noise components, another possibility would be that residual uncompensated RF-fields lead to energy transfer to secular modes of vibrations via anharmonicities. However, that heating rate will be even larger if additional noise from the supply electronics is present. We summarize the required specifications for the required supply electronics:

- Individual supply for 64 channels.
- Voltages in the range between +10 V and -10 V.
- Extremely low noise.
- Possibility to supply individual arbitrary voltage waveforms containing frequencies in the MHz range.
- Suppression of rf pickup fed back to the output stage, or even the possibility to regulate rf-pickup on the electrodes away.

The required low noise level can only be accomplished with the use of well-shielded, battery-powered equipment. In an early stage of the experiment, we have seen tremendous improvements in the observation of coherent dynamics on the quadrupole transition upon changing the voltage supply from computer controlled analog output boards via a 9 V battery block, a battery driven buffer based on an operational amplifier to a transistor-based output stage that was finally used. This hand-made supply electronics provides only voltage supply for a single electrode pair, for this reason most experiments were conducted at a single site.

However it was used to obtain the basic knowledge on how to build a scalable voltage source, which is described later in this appendix. Figs. B.1,B.2 and B.3 show the circuit diagrams for the supply electronics that lead to the lowest observed heating rate. The trap and differential voltage are derived from a ± voltage reference and buffered, where the differential voltage is split into an inverted an a noninverted branch $V_{\mathrm{diff}-}$ and $V_{\mathrm{diff}+}$. These are then added to the trap voltage to yield the voltages

$$\begin{aligned} V_1 &= -V_{\mathrm{trap}} - V_{\mathrm{diff}+} = -V_{\mathrm{trap}} - V_{\mathrm{diff}} \\ V_2 &= -V_{\mathrm{trap}} - V_{\mathrm{diff}-} = -V_{\mathrm{trap}} + V_{\mathrm{diff}}. \end{aligned} \tag{B.1}$$

These resulting voltages are finally buffered by a push-pull transistor stage with is feed-back linearized with a fast AD817 operational amplifier.

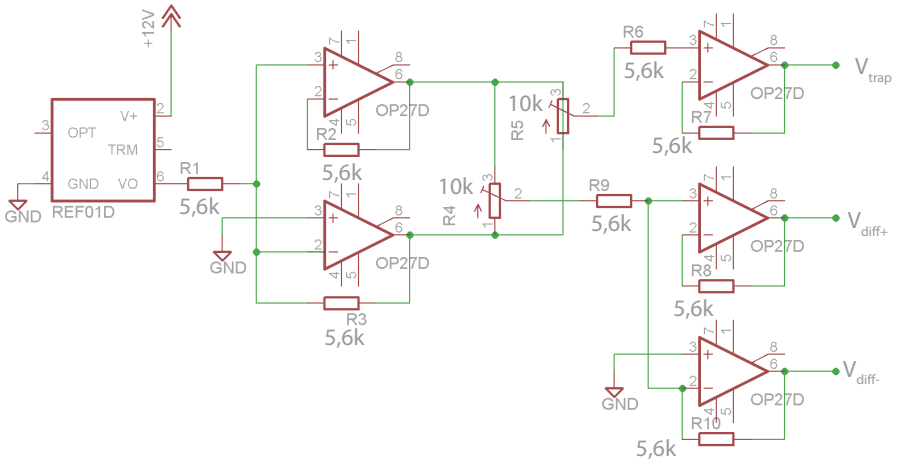

Figure B.1.: Voltage generation stage: A *REF01* and two *OP27* provide ±10 V reference leads, from which the trap offset voltage and the differential voltage are derived via 10 kΩ potentiometers. Each of theses voltages is buffered by another *OP27*, where the difference voltage is split into an inverted a noninverted branch.

Upon performing a pulse with scan on the axial red sideband of the quadrupole transition, in the thermal regime the saturation level of the excitation probability provides information on the population residing in the ground state, from which the mean phonon number of the axial mode of vibration can be inferred under assumption of a thermal phonon distribution Eq. 2.33:

$$p_0 = 1 - 2P_D^{\mathrm{sat}} = \frac{1}{\bar{n}+1}, \tag{B.2}$$

which can be rearranged to yield

$$\bar{n} = \frac{1}{1 - 2P_D^{\mathrm{sat}}} - 1. \tag{B.3}$$

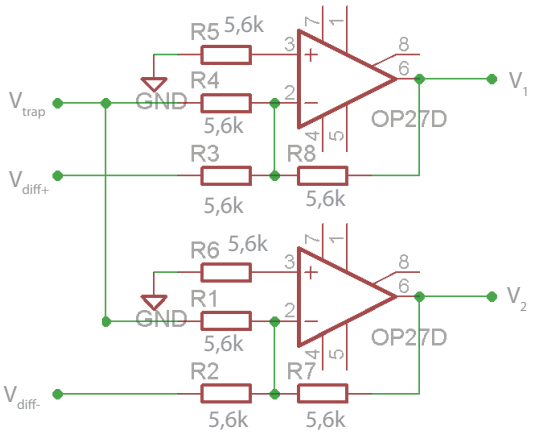

Figure B.2.: Buffer and adding stage: The trap offset voltage is added to the inverted and to the noninverted difference voltage on *OP27* adding stages.

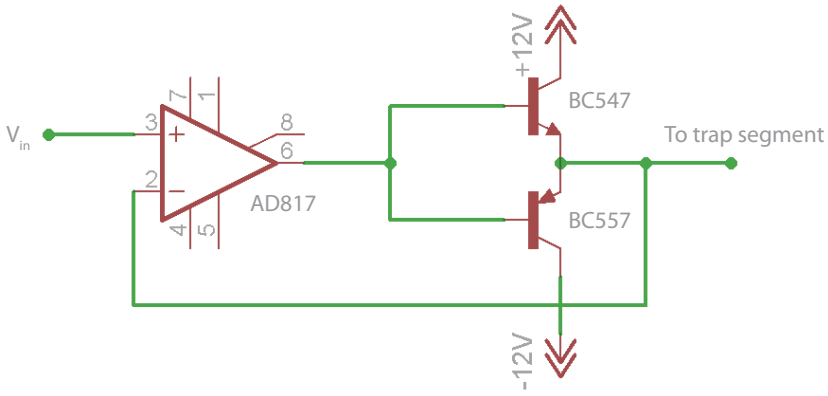

Figure B.3.: Transistor buffer stage: A fast *AD817* opamp serves as the linearizing feedback resistor for a transistor push-pull output stage.

Mean phonon numbers with respect to a delay time after ground state cooling resulting from the measurement procedures are shown in Fig. B.4. The data was taken for two different voltage supply circuits, one with an operational amplifier OP27 as output stage, the other with a transistor-based push-pull buffer stage. The output impedance of these stage were measured to be 20 Ω and 2 Ω, respectively. The data sets were taken subsequentially under the same conditions. One can clearly see that the transistor stage leads to a much

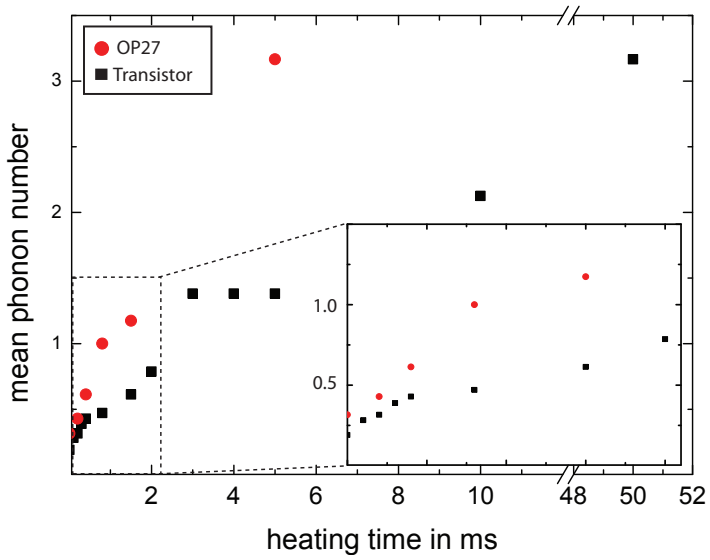

Figure B.4.: Heating rate measurements for different buffer stages: The mean phonon number obtained from Eq. B.3 are shown versus the delay between sideband cooling and probe pulse. The black dots are the values for the OP27 buffer state, and the red circles are for the transistor buffer stage. The insets shows that not even the heating rate is reduced for the transistor stage, also a smaller total temperature is attained.

better heating behavior, where the ion resides in the Lamb-Dicke regime even after a delay time of 50 ms. However it remains a puzzle why the heating behavior is not linear in time, as it was measured with a more direct method in Sec. 4.6. We argue that due to the strong radial heating rate, the laser coupling might be substantially reduced by strong radial excitations, such that the saturation timescale is much longer than the measurement time. Even if the mean phonon numbers obtained this way are not particularly trustworthy, the superiority of the transistor amplifier stage is beyond any serious doubt. Furthermore, the about 0.2 mean phonon number minimum temperature are fully consistent with the value obtained shortly after this measurement by the phonon distribution measurement presented in Sec. 4.6.

Fig. B.5 depicts the components of the present version of the computer-controlled scalable voltage supply. The work of K. Singer, G. Huber and M. Bürzele for the design and development of this complex hard- and software system is gratefully acknowledged here. The signal flow is as follows: Software routines embedded in the recent experiment control software framework *MCP* developed by Kilian Singer generate binary data from the set of analog voltage values which is to be applied to the trap electrodes. This data is sent to a Xilinx Virtex V FPGA via a Gigabit Ethernet transmission channel. This FPGA, which has an on-chip hardware PowerPC processor core, sends the data sequentially to a DAC board where the final analog output voltages are generated. As the analog electronic subsystem

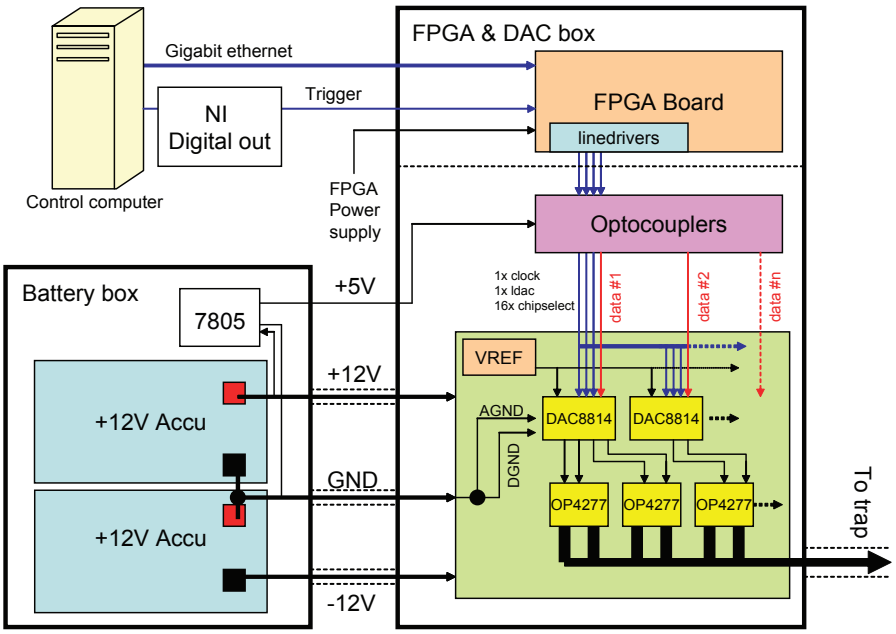

Figure B.5.: Design of the scalable trap voltage supply: The FPGA is supplied with the waveform data via Gigabit Ethernet from the control computer. The FPGA output is buffered and supplied to the DAC board via optocouplers to achieve galvanic separation. The output of the DACs is buffered by *OP4277* opamps.

is to be isolated galvanically from FPGA digital electronics to suppress digital clock noise and power line frequencies, all digital signals supplied to the DAC board are buffered by optocouplers. The quad-channel DACs 8814 are addressed by chip-select lines and serially obtain their 4x16-bit samples via a single serial data line connected to all DACs. One data sample consists of a 2-bit information selecting one of the four DACs on the chip, and the actual 16 bit voltage sample. When all DACs are supplied with their samples, an enable line (LDAC) causes them to update their output voltages simultaneously. The analog output signals are in the range between 0 V and +10 V, with respect to a +10 V precision reference supplied to all DACs. This range is mapped onto the required -10 V to +10 V range by means of two operational amplifiers, which also serve as output buffers. These OP4277 operational amplifiers come in quad packages, such that one chip can drive two analog output lines and two OP4277 chips per DAC chip are needed. The signals run via individual SMA cables to an additional output printed circuit board where they are bundled on four 25-pin Sub-D connectors. From there the voltages are supplied to the vacuum flange via shielded printer cables [1]. The power supply for the DAC board is realized with a shielded battery system

[1]LEUNIG GmbH, Sigburg, Germany

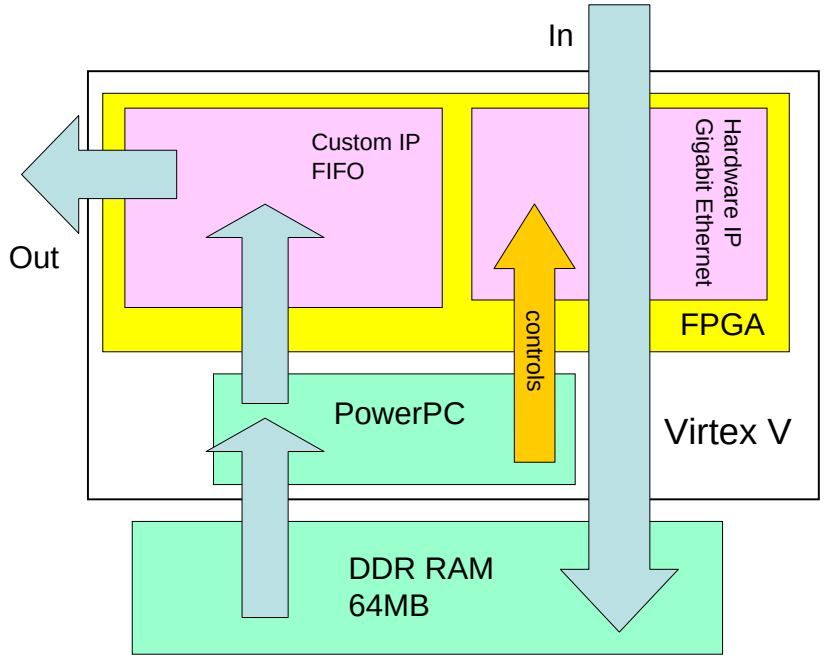

Figure B.6.: Data flow within the FPGA subsystem:.

comprised of two 12V lead-gel accumulators. The power drawn from the batteries is strongly increased due to the requirement of a +5 V supply voltage for the optocouplers, which is generated by a 7805 voltage regulator. The following problems were present with the latest version of this voltage supply:

- Strong trap-rf pickup on the dc lines of about several hundreds of mV cause transmission errors in the data supply chain, most likely on the optocoupler stage. This lead to bit-flip errors resulting in clearly visible jumps of a single trapped ion's position upon updating the electrode voltages with the same data set as was already applied before.

- Due to the large quiescent current, the lead accumulator are empty in a comparatively short time of about one hour. If the batteries are permanently connected to loading devices with switching power supplies, the motional state of trapped ions is adversely affected.

- The operational amplifier output buffer stage is not adapted to the findings from above where it was shown that a subsequent transistor stage yields a much better performance

- If damage on one specific channel occurs, it is extremely tedious to replace components, the whole DAC board will most likely have to be replaced.

The data flow on the FPGA board is depicted in Fig. B.6. The data transmitted via the ethernet line is read directly by the FPGA by means of a suitable IP (intellectual property) core. This core is controlled by a software running on the on-chip PowerPC of the Virtex IV, which transfers the data directly into an onboard 64 MB DDR RAM via DMA (direct memory access). For the output, a custom IP core utilizing a FIFO (first in, first out) buffer IP recovers data from the RAM via the PowerPC and puts the data to the output pins. For an update of all voltages, the required amount of data is 64x 18 bit for the DAC samples and 16x 1bit for the chipselect line, furthermore the clock line has to updated 32 times and finally the LDAC has to be changed. Several improvements of the protocol are envisaged, in general it will be advantageous to devise a 'smart' system instead of the passive data transfer one. As almost all the experiments are performed such that exactly the same experimental sequence is carried out a couple of hundreds of times, therefore a looping capability of the system would yield a tremendous reduction of the amount of data to be transferred. Moreover, typically only a set of electrodes is actually to be updated, therefore a protocol should be devised which contains information about the subset of channels to be updated in one step. This is possible as there is a single chip select line for each individual DAC chip, which is in principle not needed for the present protocol. An additional bottleneck is given by the fact that the data transfer from the RAM back to the FPGA is not accomplished via DMA, which represents a considerable speed reduction.
It remains as a concluding statement that the trap voltage supply represent a key technology for scalable quantum information experiments in segmented microtraps, and the challenges range over the complete data supply chain up to the final supply of the generated voltages to the electrodes.

C. Advanced Reconstruction Technique for Phonon Number Distributions

Rabi oscillations on a blue sideband are an important measurement tool to determine phonon number distributions, i.e. to characterize the (quantum) state of a given vibrational mode of trapped ions. This technique is employed in Sec. 4.6 for a precise heating rate measurement, in chapter 7 for a complete quantum state tomography and in Sec. 8.3 for monitoring the action of a light-induced displacement force. As the reconstructed occupation probabilities p_n represent physical quantities characterizing the quantum state, it is of fundamental interest to find the most accurate way to extract them from the bsb Rabi oscillation data. This task is hindered by experimental imperfections, i.e. shot noise on the data and drifting parameters as the Rabi frequency and the spin and motional preparation imperfections. The starting point is the bsb oscillation signal

$$P_{\downarrow}(t) = \frac{1}{2}\sum_n p_n(a\ e^{-\gamma\ t}\cos\left(\Omega_{n,n+1}\ t\right) + b), \tag{C.1}$$

with the Rabi frequency $\Omega_{n,n+1} = \Omega_0 M_{n,n+1}(\eta)$, the contrast a, baseline b and the decoherence rate γ. The base Rabi frequency Ω_0 is not exactly known and might be subject to drifts, the Lamb-Dicke factor η depends on the beam angles which are also not exactly known, the baseline and contrast factors depend on the spin preparation and readout, which are also subject to drifts. The decoherence rate γ depends on the impinging light intensity and also on the motional state itself, see Sec. 8.3. We also have to take into account the normalization of the p_n, thus if we consider the reconstruction as a nonlinear regression problem, we face a situation with a large number of heavily correlated and partially constrained parameters, which might also have very different ranges of values. Any standard nonlinear regression routine will therefore be condemned to fail on this problem. Two different points of view on Eq. C.1 seem to offer ways to solve this problem: First, the bsb signal can be seen as a Fourier synthesis of oscillations at different frequencies $\Omega_{n,n+1}$, the relative strength of which are directly given by the p_n. When looking at the spectrum of bsb Rabi oscillations as in Fig. 4.29, we immediately recognize two problems, namely that alias peaks appear due to the finite data acquisition time and that the peaks are rather broad and distorted, such that it is difficult to reliably read off the p_n and give figures for their accuracy. Furthermore, components beyond $n = 4$ cannot be resolved under the experimental conditions in this case. Another way would be to consider the p_n as a vector, which is multiplied by a rectangular matrix to yield the measurement values. Therefore, singular value decomposition (SVD) of this matrix can be applied to find the pseudo-inverse, which reveals the p_n when multiplied on the vector of measured data points. This was used in Ref. [Mee96], with the result that negative

probabilities appear, which have magnitudes beyond their claimed accuracy. Besides these unphysical results, the SVD method requires the other parameters to be fixed and well-known.

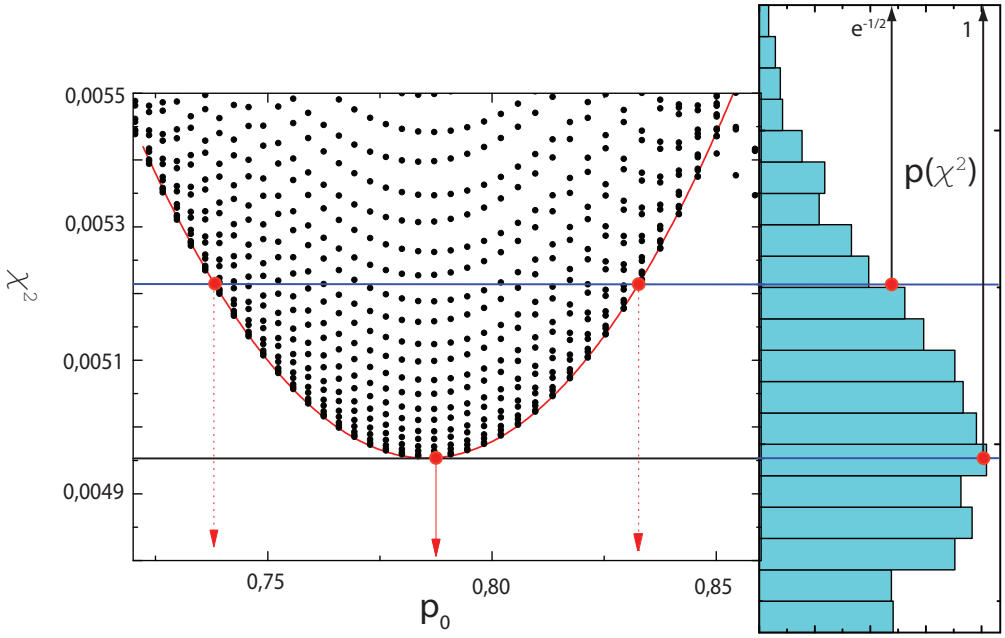

Figure C.1.: Determination of confidence interval for an occupation probability: The standard error for the ground state occupation probability p_0 for a data set similar to the one in Fig. 4.28 a) is determined as explained in the text. A set of $\overline{\chi^2}$ values with varying p_0, including first-order correlations to other varying parameters, is shown. It is bound from below by a parabola. The plot at the right shows a probability distribution of $\overline{\chi^2}$ values calculated at the best fit parameters. The $\overline{\chi^2}$ value at which the probability drops to $1/e$ sets the cutoff, which is indicated by the vertical blue line. The intersection of this cutoff line with the bounding parabola finally determine the confidence interval.

Our way for an efficient and precise phonon distribution reconstruction is to use a genetic algorithm [1]. The parameters are represented by discretized floating point numbers with a resolution of 8 bit. The range of the p_n is from 0.0 to 1.0, and they are normalized after being extracted from the genome to avoid imposing a complicated constraint on the algorithm. The other parameters are bounded to $\pm 10\%$ of a preset reasonable value. The algorithm then calculates the average rms deviation of the signal arising from the parameters of each

[1] The software for this work used the GAlib genetic algorithm package, written by Matthew Wall at the Massachusetts Institute of Technology. See *http://lancet.mit.edu/ga/Copyright.html*

individual in the population from the measured data:

$$\overline{\chi^2} = \frac{1}{N}\sum_{i=1}^{N}\left(P_{\downarrow}^{(\mathrm{meas})}(t_i) - P_{\downarrow}^{(\mathrm{calc})}(t_i)\right)^2. \tag{C.2}$$

Additional quantities are calculated to provide a guidance for the algorithm to physically reasonable phonon distributions, namely the variance of the phonon distribution

$$V = \langle (n-\bar{n})^2 \rangle_{p_n} \tag{C.3}$$

and the curvature of the distribution

$$C = \sum_{n=1}^{n_{max}-1} (p_{n-1} + p_{n+1} - 2p_n)^2 \tag{C.4}$$

The final quantity to be maximized is then

$$Q = (\alpha_\chi \chi + \alpha_V V + \alpha_C C)^{-1}, \tag{C.5}$$

where the α are positive values to be chosen such that the algorithm finds reasonable results. In other words, the algorithm is set to find parameters such that the measurement data is reproduced, and the phonon distribution should favor low n and be smooth. The last condition is related to a general aspect of tomographic maximum likelihood reconstruction of probabilistic quantities describing physical systems, where one maximizes the *entropy* additionally to the fitting in order to find the most reasonable physical state. Generally, the probability distributions with a large curvature correspond to a low entropy, as the contain more information, therefore the usage of the curvature term in Eq. C.5 is physically justified. The question is now how to obtain reliable error estimations for the resulting p_n, including their mutual correlations and correlations to the other parameters. For this, we calculate large sets of $\overline{\chi^2}$ values, where always two of the variables are slightly changed, e.g.:

$$\begin{aligned}
&\overline{\chi^2}(\Omega_0 + d\Omega_0, a, b, \gamma, p_0, ..., p_{n_{max}}) \\
&\overline{\chi^2}(\Omega_0, a, b, \gamma + d\gamma, p_0, ..., p_i + dp_i ..., p_{n_{max}}) \\
&\overline{\chi^2}(\Omega_0, a, b, \gamma, p_0, ..., p_i + dp_i, ..., p_j + dp_j, p_{n_{max}}) \\
&...
\end{aligned} \tag{C.6}$$

where the deviations are scanned across a range of 10% of the resulting value for the extra parameters and a fixed value 0.1 for the p_n. The p_n are of course to be renormalized. The set of resulting $\overline{\chi^2}$ values is plotted versus one parameter of interest, e.g. p_0, an example for which is shown in Fig. C.1. The structure of the set is always that a minimum $\overline{\chi^2}_{\mathrm{min}}$ occurs, from which the best fit parameter $p_0^{(\mathrm{best})}$ can be read off. The set is then bounded from below by a curve which is parabolic around $p_0^{(\mathrm{best})}$. The parabolic curve is obtained by reducing the set of χ values to the minimum values in a set of bins along the parameter axis. A parabolic fit can then be performed in a narrow range around $p_0^{(\mathrm{best})}$, which is also

shown in Fig. C.1. From this parabola, the desired confidence interval can then be obtained by elementary statistical reasoning. For this, we assume that for the measurement data, the projection noise error amounts to the theoretical maximum one, i.e. $\sqrt{0.5^2/M}$ for M shots, corresponding to a constant readout value of $P_\downarrow = 0.5$. For large enough M, it is then allowed to consider the shot-to-shot distribution of the $P_\downarrow$ to be Gaussian, with a standard error of $\sigma^2 = 0.5^2/M$. If a given measurement of a curve $P_\downarrow$ with N data points and M shots per point was to be repeated several times, the statistical expectation value for the shot noise deviation is given by

$$\langle\overline{\chi^2}\rangle = \sigma^2. \tag{C.7}$$

$\overline{\chi^2}$ is to be considered as a random variable as well, such that we can determine what the statistical spread of the $\overline{\chi^2}$ is. This allows to infer the confidence interval of the fit parameters from the calculated $\overline{\chi^2}$ sets by the assumption that *if $\overline{\chi^2}$ deviates by more than its own statistical spread $\sigma\left(\overline{\chi^2}\right)$ from the optimum value, the fit parameter can be considered as erroneous.* The standard deviation of $\overline{\chi^2}$ is found to be:

$$\sigma\left(\overline{\chi^2}\right) = \sqrt{\frac{2}{N}}\langle\overline{\chi^2}\rangle = \sqrt{\frac{1}{2\ N\ M}}. \tag{C.8}$$

Fig. C.1 illustrates this procedure for determination of the confidence interval for the extracted ground state population p_0 from a bsb Rabi oscillation data set similar to the one shown in Fig. 4.28 a). A probability distribution for $\overline{\chi^2}$ is calculated by drawing random measurement values according to Poissonian distributions with the calculated readout values as mean value for each probe pulse time of the data set. The $\overline{\chi^2}$ at which the probability drops to $1/e$ of the maximum value serves as a cutoff value for the determination of the confidence interval. As a general result, it can be stated that this method for the characterization of the quantum state is rather imprecise and also bounded to the Lamb-Dicke regime, therefore either the decoherence timescales have to be much improved or one has to resort to beating tomography schemes such as the one presented in Sec. 8.4 and Appendix D.

D. Tomography Method for States with Entanglement of Spin and Motion

It is of great interest to investigate the decoherence of nonclassical Schrödinger cat states by directly observing the coherent features in phase space, as it was performed on a cavity field in Ref. [Gle07]. The question arises if similar experiments could be performed with a trapped ion, as both the preparation of Schrödinger cat states (see chapter 8) and the tomography of the quantum state of a motional mode (see chapter 7) is readily achieved. It turns out that these two experiments cannot be easily combined, as the entanglement of spin and motion obscures the direct observation of the desired interference features. The Schrödinger cat state e.g. $|\uparrow,\alpha\rangle + |\downarrow,-\alpha\rangle$ cannot be unitarily transformed to $|\uparrow,\alpha\rangle + |\uparrow,-\alpha\rangle$ which would allow for the application of tomography methods such as the one presented in chapter 7. A dissipative transfer would destroy the quantum coherence of the state. A possible way to perform such an experiment is the application of the wavepacket beating scheme presented in chapter 8. If a similar experiment as in Ref. [Gle07] could be performed with a single trapped ion, the way would be paved for investigations in higher-dimensional spin Hilbert spaces, i.e. the decoherence properties of Schrödinger cat states with several ions can be measured, which is not directly possible for the cavity QED system.
First, we briefly discuss what quantity the wavepacket beating scheme measures at all and establish the connection to quantum state tomography, see chapter 7. Let us assume we could perform an arbitrary manipulation of the motional state for a single spin component only. We then generalize the scheme above such that the displacement operation in the first gap of the spin-echo sequence is replaced by a general operation leading to the quantum state of the vibrational mode $|\chi\rangle$. The reasoning leading to the measurement signal Eq. 8.41 now yields

$$P_\uparrow = \frac{1}{2}\left(1 + \Re\langle\alpha|\chi\rangle\right). \tag{D.1}$$

One realizes that besides the trivial offset and scaling factor, this partially gives the Husimi-Kano Q-function:

$$Q(\alpha) = \frac{1}{\pi}\langle\alpha|\chi\rangle\langle\chi|\alpha\rangle, \tag{D.2}$$

which contains the complete information about the quantum state $|\chi\rangle$. If the phase of the second $\pi/2$ pulse in the sequence is changed to $\phi = \pi/2$, the obtained signal is

$$\tilde{P}_\uparrow = \frac{1}{2}\left(1 - \Im\langle\alpha|\chi\rangle\right). \tag{D.3}$$

We therefore find that

$$(2P_\uparrow - 1)^2 + (2\tilde{P}_\uparrow - 1)^2 = \frac{\pi}{4}Q(\alpha), \tag{D.4}$$

which states that the value of the Q-function at a particular point in phase space can be directly measured by running two different sequences. The restriction of this tomography scheme lies in the fact that no given input state can be used, one rather has to employ spin-dependent mechanisms for the state preparation. If a general input state $|\chi\rangle$ which was created *before* the measurement sequence was to be analyzed, the resulting signal would be

$$P_\uparrow = \frac{1}{2}\left(1 + \Re\langle\chi|\hat{D}^\dagger(\alpha)|\chi\rangle\right). \tag{D.5}$$

This signal can also be used to fully determine the quantum state. The preparation step is not part of the sequence anymore, the spin-echo scheme is therefore replaced by a single displacement pulse sandwiched between the $\pi/2$ pulses. The resulting signals then read

$$\begin{aligned} P_\uparrow &= \frac{1}{2}\left(1 - \Re\langle\chi|\hat{D}(\alpha)|\chi\rangle\right) \\ \tilde{P}_\uparrow &= \frac{1}{2}\left(1 - \Im\langle\chi|\hat{D}(\alpha)|\chi\rangle\right). \end{aligned} \tag{D.6}$$

As pointed out in [Bar98], this provides a direct measurement of the *characteristic function of the Wigner function*:

$$f_W(\alpha) = \langle\chi|\hat{D}(\alpha)|\chi\rangle, \tag{D.7}$$

which can straightforwardly be extended to mixed states. The Wigner function is simply obtained by a Fourier transform:

$$W(\beta) = \frac{1}{\pi^2}\int f_W(\alpha) e^{\beta\alpha^* - \beta^*\alpha} d^2\alpha. \tag{D.8}$$

We now proceed towards the generalization to input states with possible entanglement between spin and motion, i.e.

$$|\Psi\rangle = |\uparrow, \chi_\uparrow\rangle + e^{i\psi}|\downarrow, \chi_\downarrow\rangle. \tag{D.9}$$

Normalization factors are omitted in the following and the relative phase ψ of the spin superposition is also dropped as it can be safely assumed that it can be measured and modified separately. We now consider a simple analysis sequence where a displacement drive acting only on $|\downarrow\rangle$ creates the state:

$$|\Psi\rangle = |\uparrow, \chi_\uparrow\rangle + \hat{D}(\alpha)|\downarrow, \chi_\downarrow\rangle. \tag{D.10}$$

A concluding $\pi/2$ pulse with analysis phase ϕ gives rise to

$$|\Psi\rangle = |\uparrow, \chi_\uparrow\rangle - ie^{-i\phi}|\uparrow, \chi_\downarrow\rangle + \hat{D}(\alpha)|\downarrow, \chi_\downarrow\rangle - ie^{i\phi}\hat{D}(\alpha)|\uparrow, \chi_\downarrow\rangle. \tag{D.11}$$

The resulting measured population is

$$P_\uparrow(\alpha, \phi) = \mathcal{N}\left(1 + \cos\phi\ \Im\langle\chi_\uparrow|\hat{D}(\alpha)|\chi_\downarrow\rangle + \sin\phi\ \Re\langle\chi_\uparrow|\hat{D}(\alpha)|\chi_\downarrow\rangle\right) \tag{D.12}$$

It can be seen that this leads towards the desired result: a component of the characteristic function pertaining to the motional wavefunctions associated with the adjacent spin components. More information can be extracted with a more complex scheme. Starting again from the input state Eq. D.9, we follow the sequence:

1. Shift the superposition phase by means of a Stark shift laser beam by θ_1.
2. Employ a first $\pi/2$ pulse with phase ϕ_1.
3. Drive the displacement of $|\downarrow\rangle$ by α.
4. Employ a second phase shift of θ_2.
5. Exert the concluding $\pi/2$ pulse with phase ϕ_2.

The resulting signal is then given by

$$\begin{aligned} P_\uparrow(\alpha,\phi) \;\propto\;& 2 + (\cos(\theta_1+\phi_1) - \cos(\theta_1+\phi_1-2\phi_2))\ \Im M_{\uparrow\downarrow}(0) \\ +\;& (\sin(\theta_1+\phi_1) - \sin(\theta_1+\phi_1-2\phi_2))\ \Re M_{\uparrow\downarrow}(0) \\ +\;& \cos(\theta_1+\theta_2-\phi_2)\Im M_{\uparrow\downarrow}(\alpha) + \sin(\theta_1+\theta_2-\phi_2)\Re M_{\uparrow\downarrow}(\alpha) \\ +\;& \cos(\theta_1-\theta_2+2\phi_1-\phi_2)\Im M_{\downarrow\uparrow}(\alpha) - \sin(\theta_1-\theta_2+2\phi_1-\phi_2)\Re M_{\downarrow\uparrow}(\alpha) \\ -\;& \sin(\theta_2-\phi_1-\phi_2)\Im M_{\downarrow\downarrow}(\alpha) + \cos(\theta_2-\phi_1-\phi_2)\Re M_{\downarrow\downarrow}(\alpha) \\ +\;& \sin(\theta_2-\phi_1+\phi_2)\Im M_{\uparrow\uparrow}(\alpha) - \cos(\theta_2-\phi_1+\phi_2)\Re M_{\uparrow\uparrow}(\alpha), \end{aligned} \tag{D.13}$$

with

$$M_{ij}(0) = \langle\chi_i|\chi_j\rangle \qquad \text{and} \qquad M_{ij}(\alpha) = \langle\chi_i|\hat{D}(\alpha)|\chi_j\rangle \tag{D.14}$$

Thus, by performing different measurements with appropriate choice of the phase angles $\phi_1, \phi_2, \theta_1, \theta_2$, a maximum amount of information can be obtained about the $M_{ij}^{(\alpha)}$ for a point in phase space given by α. The overlap integrals be be separately measured with a simple measurement as for the simple Schrödinger cat measurement leading to the result Eq. 8.24, the overlap integral pertaining to adjacent spin states can be measured with the simplified sequence presented above and the symmetry relation

$$M_{ij}(\alpha) = M_{ji}(-\alpha)^* \tag{D.15}$$

can be used for additional simplification. It is beyond the scope of this thesis the answer the question of the complete information about the quantum state can be obtained with this measurement scheme, but it can be stated the desired coherence measurement can already be performed with the simplified scheme.

E. Coherently Driven Ion Crystals

In this appendix, we derive a general frame work for the coherent interaction of laser beams with ion crystals aligned along the z-axis. The coupling strength for i-th ion is given by $\Omega_i = \Omega(z_i^{(0)})$ with the equilibrium position $z_i^{(0)}$ derived from Eq. 2.80. This admits both single ion addressing of the k-th ion $\Omega_i = \Omega_0 \delta_i k$ and homogeneous illumination as the limiting cases. In order to not overburden the notation, we restrict ourselves to a beam propagation along the z-axis, such that the (scalar) laser field is given by

$$E(z,t) = E_0 \cos(k_z z - \omega_l t + \phi). \tag{E.1}$$

This leads to exclusive coupling to the axial vibrational case, however, the most general case can be straightforwardly retrieved by replacing $k_z z$ with $\vec{k} \cdot \vec{r}$. For direct applicability to an experimental situation, we discern the cases for coherent driving of internal states (spin) corresponding to the situations in Secs. 2.1.4 and 9.3, and the direct driving of motional modes as in Secs. 8.1 and 9.5.

E.1. Driving the Internal State

We extend the interaction part of the Cirac-Zoller-Hamiltonian Eq. 2.45 to the case of N ions:

$$H_I = \sum_j^N \tfrac{1}{2}\hbar\Omega_j(\hat{\sigma}_j^+ + \hat{\sigma}_j^-)\left(\exp\left[i\left(k_z(z_j^{(0)} + \delta u_{zj}) - \omega_l t + \phi\right)\right] + \text{h.c.}\right). \tag{E.2}$$

Employing the generalized coordinates Eq. 2.89 leads to

$$H_I = \sum_j^N \tfrac{1}{2}\hbar\Omega_j(\hat{\sigma}_j^+ + \hat{\sigma}_j^-)\left(\exp\left[i\left(k_z(z_j^{(0)} + \sum_n M_{jn}^{(z)T} q_n^{(z)}) - \omega_l t + \phi\right)\right] + \text{h.c.}\right). \tag{E.3}$$

Writing the $q_n^{(z)}$ in second quantization

$$q_n^{(z)} = \sqrt{\frac{\hbar}{2m\omega_n}}(\hat{a}_n + \hat{a}_n^\dagger) \tag{E.4}$$

and replacing the ladder operators by their interaction picture versions

$$\begin{aligned} \hat{a}_n &\to e^{i\omega_n t}\hat{a}_n \quad , \qquad \hat{a}_n^\dagger \to e^{-i\omega_n t}\hat{a}_n^\dagger, \\ \hat{\sigma}_i^+ &\to e^{i\omega_{eg} t}\hat{\sigma}_i^+ \quad , \qquad \hat{\sigma}_i^- \to e^{-i\omega_{eg} t}\hat{\sigma}_i^-, \end{aligned} \tag{E.5}$$

we obtain the interaction picture Hamiltonian:

$$\begin{aligned} H_I^{(I)} &= \sum_j^N \tfrac{1}{2}\hbar\Omega_j(e^{i\omega_{eg}t}\hat{\sigma}_j^+ + e^{-i\omega_{eg}t}\hat{\sigma}_j^-) \\ &\cdot \left(\exp\left[i\left(k_z z_j^{(0)} + \sum_n M_{jn}^{(z)T}\eta_n(e^{i\omega_n t}\hat{a}_n + e^{-i\omega_n t}\hat{a}_n^\dagger) - \omega_l t + \phi\right)\right] + \text{h.c.}\right), \end{aligned} \tag{E.6}$$

where $\eta_n = k_k\sqrt{\frac{\hbar}{2m\omega_n}}$ is the Lamb-Dicke factor for the n-th mode. Invoking the rotating wave approximation yields

$$H_I^{(I)} = \sum_j^N \tfrac{1}{2}\hbar\Omega_j\hat{\sigma}_j^- \exp\left[i\left(k_z z_j^{(0)} + \sum_n M_{jn}^{(z)T}\eta_n(e^{i\omega_n t}\hat{a}_n + e^{-i\omega_n t}\hat{a}_n^\dagger) - \delta t + \phi\right)\right] + \text{h.c.}\,, \tag{E.7}$$

which constitutes the most general result. We now perform the Lamb-Dicke approximation assuming all δu_{zj} are much smaller than the driving wavelength and expand the exponential containing the spatial phases up to first order:

$$H_I^{(I)} = \sum_j^N \tfrac{1}{2}\hbar\Omega_j\hat{\sigma}_j^-\left(1 + i\sum_n M_{jn}^{(z)T}\eta_n(e^{i\omega_n t}\hat{a}_n + e^{-i\omega_n t}\hat{a}_n^\dagger)\right)e^{-i\left(\delta t - k_z z_j^{(0)} - \phi\right)} + \text{h.c.}\,, \tag{E.8}$$

from which we can perform a second rotating-wave-approximation under the assumption that the laser is tuned to the rsb or bsb of a specific motional mode n, $\delta = +(-)\omega_n$:

$$H_I^{(I)} = \sum_j^N \tfrac{1}{2}\hbar\Omega_j\hat{\sigma}_j^-\left(i\ M_{jn}^{(z)T}\eta_n\hat{a}_n^{(\dagger)}\right)e^{i\left(k_z z_j^{(0)} + \phi\right)} + \text{h.c.}. \tag{E.9}$$

The key difference between the driving of an ion crystal and a single ion is the occurrence of the phase factors depending on the equilibrium positions. This means that the phases of the unitary transform that is realized by the coupling to a given mode jointly depend on the total internal state, the trap frequency and the structure of the motional mode.

E.2. Driving the Motion

We start from the generalization of the coupling Hamiltonian Eq. 8.5 to N ions:

$$H_I = \sum_j^N \tfrac{1}{2}\hbar\Delta_{S,j}\hat{\sigma}_z^{(j)}\exp\left[i\left(\Delta k\hat{z}_j - \delta_R t + \Delta\phi\right)\right] + \text{h.c.}\,. \tag{E.10}$$

This is equivalent to the case of the internal state driving besides the replacement of the internal state operator $\hat{\sigma}_j^-$ and $\hat{\sigma}_j^+$ with the self-adjoint operator $\hat{\sigma}_z^{(j)}$. We can therefore

proceed along the same lines of thought as in the previous section to arrive at

$$H_I^{(I)} = \sum_j^N \tfrac{i}{2}\hbar\Delta_{S,j}\hat{\sigma}_z^{(j)}\eta_n M_{jn}^{(z)T}\left(\hat{a}_n e^{i\left(\Delta k\ z_j^{(0)}-\delta t+\Delta\phi\right)} + \text{h.c.}\right) \tag{E.11}$$

Where we admit a detuning from the motional frequency of the n-th mode of $\delta = \delta_R - \omega_n$. The equation can be rearranged to

$$H_I^{(I)} = -\sum_j^N \hbar\Delta_{S,j}\hat{\sigma}_z^{(j)} M_{jn}^{(z)T}\left(\Delta k\hat{q}_n \sin\left(\Delta k z_j^{(0)} - \delta t + \Delta\phi\right) + \frac{\Delta k}{m\omega_n}\hat{p}_n \cos\left(\Delta k z_j^{(0)} - \delta t + \Delta\phi\right)\right). \tag{E.12}$$

Assuming all motional modes to be in the ground state and denoting a total unentangled spin state with the set of spin variables $\{s_z^{(j)}\} = \pm 1/2$, we can calculate the driving force on resonance acting onto the mode using Eq. 8.14 to be

$$\mathcal{F}_n = -\sum_j^N \hbar\Delta_{S,j} s_z^{(j)} M_{jn}^{(z)T}\Delta k \sin\left(\Delta k z_j^{(0)} + \Delta\phi\right) \tag{E.13}$$

As in the case of the internal state driving, the effect of the interaction depends on the total spin state and on the oscillation mode properties. Here, even the strength of the displacement force depends on these parameters. On the one hand, this is provides a cornerstone of the geometric phase gate described in Sec. 9.5 as specific spin configurations can be selectively displaced, on the other hand this adds extra complexity especially when gates on larger, unevenly spaced ion crystals are to be performed as we investigated in detail in [Iva09].

F. Atomic Properties of Calcium

^{40}Ca ionization energy [eV]	6.11
Atomic weight [u]	40.078
$^{40}Ca^{+}$ P-state finestructure splitting [GHz]	6682.22

Table F.1.: General properties of ^{40}Ca.

$S_{1/2}$	2
$P_{1/2}$	2/3
$P_{3/2}$	4/3
$D_{3/2}$	4/5
$D_{5/2}$	6/5

Table F.2.: Landé factors of the $^{40}Ca^{+}$ states [Roo00].

Transition	Physical wavelength [nm]	Lab wavelength [nm]	Lifetime
$S_{1/2} \rightarrow P_{1/2}$	396.847	396.95916(2)	7.7(2) ns
$S_{1/2} \rightarrow P_{3/2}$	393.366	-	7.4(3) ns
$S_{1/2} \rightarrow D_{3/2}$	732.389	-	1.080 s
$S_{1/2} \rightarrow D_{5/2}$	729.147	729.34770(5)	1.045 s
$D_{3/2} \rightarrow P_{1/2}$	866.214	866.45220(5)	94.3 ns
$D_{5/2} \rightarrow P_{3/2}$	854.209	854.444(1)	101 ns
$D_{3/2} \rightarrow P_{3/2}$	849.802	-	901 ns

Table F.3.: Properties of the $^{40}Ca^{+}$ transitions [Roo00]. The *laboratory wavelength* denotes the readout value of our wavemeter at resonance.

G. Publications

G.1. Journal Publications

U. Poschinger, M. Hettrich, A. Walther, F. Ziesel, M. Deiss, K. Singer and F. Schmidt-Kaler, *High precision atomic decay rate measurement using a single trapped ion*, manuscript in preparation

Andreas Walther, **U. Poschinger**, F. Ziesel, M. Hettrich, A. Wiens and F. Schmidt-Kaler, *Using a single ion as a shot-noise limited magnetic field gradient probe*, manuscript in preparation

U. Poschinger, Andreas Walther, Kilian Singer and Ferdinand Schmidt-Kaler, *Observing the phase space trajectory of an entangled ion wave packet*, Phys. Rev. Lett. **105**, 263602 (2010)

Gerhard Huber, Frank Ziesel, **U. Poschinger**, Kilian Singer and Ferdinand Schmidt-Kaler, *A trapped-ion local field probe*, Applied Physics B 100, **725** (2010)

K. Singer, **U. Poschinger**, M. Murphy, P. Ivanov, F. Ziesel, T. Calarco, F. Schmidt-Kaler, *Experiments with atomic quantum bits - essential numerical tools*, Rev. Mod. Phys. **82**, 2609 (2010)

P. Ivanov, **U. Poschinger**, K. Singer, F. Schmidt-Kaler, *Quantum gate between logical qubits in decoherence-free subspace implemented with trapped ions*, Eur. Phys. Lett. **92**, 30006 (2010)

U. Poschinger, G. Huber, F. Ziesel, M. Deiss, M. Hettrich, S. A. Schulz, G. Poulsen, M. Drewsen, R. J. Hendricks, K. Singer and F. Schmidt-Kaler, *Coherent manipulation of a* $^{40}Ca^{+}$ *spin qubit in a micro ion trap*, J. Phys. B: At. Mol. Opt. Phys. **42**, 154013 (2009)

S. Schulz, **U. Poschinger**, F. Ziesel and F. Schmidt-Kaler, *Sideband cooling and coherent dynamics in a microchip multi-segmented ion trap*, New Journal of Physics **10**, 045007 (2008)

Stephan Schulz, **U. Poschinger**, Kilian Singer, and Ferdinand Schmidt-Kaler, *Optimization of segmented linear Paul traps and transport of stored particles*, Progress of Physics, Wiley **54**, 648 (2006)

G.2. Talks

Quantum optics experiments in a micro ion trap-towards scalable quantum logic, DPG Frühjahrstagung, Hannover 2010

A spin qubit in a segmented micro ion trap - towards scalable quantum logic under rough conditions, QIon 09, Tel Aviv, Israel 2009

A spin qubit in a segmented micro ion trap - towards scalable quantum logic under rough conditions, EMALI YR Meeting, Oxford UK 2009

A spin qubit in a segmented micro ion trap - towards scalable quantum logic under rough conditions, CCM Group Seminar, Imperial College London, UK 2009

A spin qubit in a segmented micro ion trap, DPG Frühjahrstagung, Hamburg 2009

Raman ground state cooling and coherent manipulations in the segmented micro ion trap, STR TR21 Meeting, Reisensburg, 2008

Quantenzustandsmanipulation in segmentierten Ionenfallen, DPG Frühjahrstagung, Düsseldorf 2007

Quantum state engineering in segmented ion traps, EMALI Kickoff Meeting, Zrich, CH, 2006

Optimization of transport and splitting of linear ion strings, SFB TR21 Workshop, Freudenstadt, 2006

G.3. Posters

Spin-dependent forces on trapped Ions: Entangled matter wave dynamics and decoherence, International Conference Quantum Engineering of Matter and Light, Barcelona, ES, 2010

Spin-dependent forces on trapped Ions: Entangled matter wave dynamics and decoherence, ICAP, Cairns, AUS, 2010

A spin qubit in a segmented micro-ion trap, SCALA conference, Cortina dAmpezzo, IT, 2009

Application of optimal control techniques in scalable ion trap quantum logic, Batsheva de Rothschild Seminar on Ultracold-Ultrafast Processes, Ein Gedi, Israel 2008

Application of optimal control techniques in scalable ion trap quantum logic, DPG Frühjahrstagung, Darmstadt 2008

Application of optimal control techniques in scalable ion trap quantum logic, EMALI annual meeting, Heraklion, GR, 2007

Application of optimal control techniques in scalable ion trap quantum logic, Gordon Research Conference on Quantum Control of Light and Matter, Newport, RI, USA 2007

Bibliography

[Alh96] R. Alheit, T. Gudjons, S. Kleineidam, and G. Werth, *Some observations on higher-order non-linear resonances in a Paul trap*, Rapid Commun. Mass Spectrom. **10**, 583 (1996).

[All10] D. T. C. Allcock, J. A. Sherman, D. N. Stacey, A. H. Burrell, M. J. Curtis, G.Imreh, N. M. Linke, D. J. Szwer, S. C. Webster, A. M. Steane, and D. M. Lucas, *Implementation of a symmetric surface electrode ion trap with field compensation using a modulated Raman effect*, N. J. Phys. **12** (2010).

[Alm10] M. Almendros, J. Huwer, N. Piro, F. Rohde, C. Schuck, M. Hennrich, F. Dubin, and J. Eschner, *Bandwidth-tunable single-photon source in an ion-trap quantum network*, Phys. Rev. Lett. **103**, 213601 (2010).

[Bar98] P. J. Bardroff, M. T. Fontenelle, and S. Stenholm, *Simple scheme for state measurement*, Phys. Rev. A **59**, R950 (1998).

[Bar04] M. D. Barrett, J. Chiaverini, T. Schaetz, J. Britton, W. M. Itano, J. D. Jost, E. Knill, C. Langer, D. Leibfried, R. Ozeri, and D. J. Wineland, *Deterministic quantum teleportation of atomic qubits*, Nature **429**, 737 (2004).

[Ben08] J. Benhelm, G. Kirchmair, C. F. Roos, and R. Blatt, *Experimental quantum information processing with* $^{43}Ca^{+}$ *ions*, Phys. Rev. A **77**, 062306 (2008).

[Ber98a] K. Bergmann, H. Theuer, and B. W. Shore, *Coherent population transfer among quantum states of atoms and molecules*, Rev. Mod. Phys. **70**, 1003 (1998).

[Ber98b] D. Berkeland, J. Miller, J. Bergquist, W. Itano, and D. Wineland, *Minimization of ion micromotion in a Paul trap*, J. Appl. Phys. **83**, 5025 (1998).

[Bie09] M. J. Biercuk, H. Uys, A. P. VanDevender, N. Shiga, W. M. Itano, and J. J. Bollinger, *Optimized dynamical decoupling in a model quantum memory*, Nature **458**, 996 (2009).

[Bla09] R. B. Blakestad, C. Ospelkaus, A. P. VanDevender, J. M. Amini, J. Britton, D. Leibfried, and D. J. Wineland, *High fidelity transport of trapped-ion qubits through an X-junction trap array*, Phys. Rev. Lett. **102**, 153002 (2009).

[Bru96] M. Brune, F. Schmidt-Kaler, A. Maali, J. Dreyer, E. Hagley, J. M. Raimond, and S. Haroche, *Quantum Rabi oscillation: A direct test of field quantization in a cavity*, Phys. Rev. Lett. **76**, 1800 (1996).

[Bud02] A. A. Budini, R. L. de Matos Filho, and N. Zagury, *Localization and dispersivelike decoherence in vibronic states of a trapped ion*, Phys. Rev. A **65**, 041402 (2002).

[Bur10] A. H. Burrell, D. J. Szwer, S. C. Webster, and D. M. Lucas, *Scalable simultaneous multi-qubit readout with 99.99% single-shot fidelity* (2010).

[Cah69] K. E. Cahill and R. J. Glauber, *Ordered expansions in boson operators*, Phys. Rev. **177**, 1857 (1969).

[Chi05] J. Chiaverini, J. Britton, D. Leibfried, E. Knill, M. D. Barrett, R. B. Blakestad, W. M. Itano, J. D. Jost, C. Langer, R. Ozeri, T. Schaetz, and D. J. Wineland, *Implementation of the semiclassical quantum Fourier transform in a scalable system*, Science **308**, 997 (2005).

[Cir95] I. Cirac and P. Zoller, *Quantum computations with cold trapped ions*, Phys. Rev. Lett. **74**, 4714 (1995).

[Cir97] J. I. Cirac, P. Zoller, H. J. Kimble, and H. Mabuchi, *Quantum state transfer and entanglement distribution among distant nodes in a quantum network*, Phys. Rev. Lett. **78**, 3221 (1997).

[Dan09] N. Daniilidis, T. Lee, R. Clark, S. Narayanan, and H. Häffner, *Wiring up trapped ions to study aspects of quantum information*, J. Phys. B **42**, 154012 (2009).

[DeM02] B. DeMarco, A. Ben-Kish, D. Leibfried, V. Meyer, M. Rowe, B. Jelenkovic, W. Itano, J. Britton, C. Langer, T. Rosenband, and D. J.Wineland, *Experimental demonstration of a controlled-NOT wave-packet gate*, Phys. Rev. Lett. **89**, 267901 (2002).

[Des06] L. Deslauriers, S. Olmschenk, D. Stick, W. Hensinger, and C. Monroe, *Scaling and supressions of anomalous heating in ion traps*, Phys. Rev. Lett. **97**, 103007 (2006).

[Deu00] T. W. Deuschle, *Kalte Ionenkristalle in einer segmentierten Paul-Falle*, Ph.D. thesis, Universität Ulm (2000).

[Dua04a] L.-M. Duan, *Scaling ion trap quantum computation through fast quantum gates*, Phys. Rev. Lett. **93**, 100502 (2004).

[Dua04b] L.-M. Duan, B. B. Blinov, D. L. Moehring, and C. Monroe, *Scalable trapped ion quantum computation with a probabilistic ion-photon mapping*, Quant. Inf. Comp. **4**, 165 (2004).

[Ear42] S. Earnshaw, *On the nature of the molecular forces which regulate the constitution of the luminiferous ether*, Trans. Camb. Phil. Soc. **7**, 97 (1842).

[Eks96] C. R. Ekstrom, C. Kurtsiefer, D. Voigt, O. Dross, T. Pfau, and J. Mlynek, *Coherent excitation of a He* beam observed in atomic momentum distributions*, Opt. Commun. **123**, 505 (1996).

[El-99] F. El-Orany, *Quantum statistical properties of superposition of squeezed and displaced number states*, Czech. J. Phys. (1999).

[Eps07] R. J. Epstein, S. Seidelin, D. Leibfried, J. H. Wesenberg, J. J. Bollinger, J. M. Amini, R. B. Blakestad, J. Britton, J. P. Home, W. M. Itano, J. D. Jost, E. Knill, C. Langer, R. Ozeri, N. Shiga, and D. J. Wineland, *Simplified motional heating rate measurements of trapped ions*, Phys. Rev. A **76**, 033411 (2007).

[Fid00] C. D. Fidio and W. Vogel, *Damped Rabi oscillations of a cold trapped ion*, Phys. Rev. A **62**, 031802 (2000).

[Gho95] P. Ghosh, *Ion Traps*, Clarendon Press, Oxford, 1995.

[Gle07] S. Gleyzes, S. Kuhr, C. Guerlin, J. Bernu, S. Delglise, U. B. Hoff, M. Brune, J.-M. Raimond, and S. Haroche, *Quantum jumps of light recording the birth and death of a photon in a cavity*, Nature **446**, 297 (2007).

[GR03] J. J. Garcia-Ripoll, P. Zoller, and J. I. Cirac, *Speed optimized two-qubit gates with laser coherent control techniques for ion trap quantum computing*, Phys. Rev. Lett. **91**, 157901 (2003).

[Gul03] S. Gulde, M. Riebe, G. Lancaster, C. Becher, J. Eschner, H. Häffner, F. Schmidt-Kaler, I. Chuang, and R. Blatt, *Implementing the Deutsch-Josza algorithm on an ion trap quantum computer*, Nature **421**, 48 (2003).

[Häf05] H. Häffner, W. Hänsel, C. Roos, J. Benhelm, D. C. al kar, M. Chwalla, T. Körber, U. Rapol, M. Riebe, P. Schmidt, C. Becher, O. Gühne, W. Dür, and R. Blatt, *Scalable multiparticle entanglement of trapped ions*, Nature **438**, 643 (2005).

[Hal05] P. C. Haljan, K.-A. Brickman, L. Deslauriers, P. J. Lee, and C. Monroe, *Spin-dependent forces on trapped ions for phase-stable quantum gates and entangled states of spin and motion*, Phys. Rev. Lett. **94**, 153602 (2005).

[Hay10] D. Hayes, D. N. Matsukevich, P. Maunz, D. Hucul, Q. Quraishi, S. Olmschenk, W. Campbell, and J. Mizrahi, *Entanglement of atomic qubits using an optical frequency comb*, Phys. Rev. Lett. **104**, 140501 (2010).

[Hen06] W. Hensinger, S. Olmschenk, D. Stick, D. Hucul, M. Yeo, M. Acton, L. Deslauriers, J. Rabchuk, and C. Monroe, *T-junction ion trap array for two-dimensional ion shuttling, storage and manipulation*, App. Phys. Lett. **88**, 034101 (2006).

[Hom06a] J. Home, *Entanglement of Two Trapped-Ion Spin Qubits*, Dissertation, Linacre College Oxford (2006).

[Hom06b] J. Home and A. Steane, *Electrode configuration for fast seperation of trapped ions*, Quantum Inf. and Comput. **6**, 289 (2006).

[Hom06c] J. P. Home, M. J. McDonnell, D. M. Lucas, G. Imreh, B. C. Keitch, D. J. Szwer, N. R. Thomas, S. C. Webster, D. N. Stacey, and A. M. Steane, *Deterministic entanglement and tomography of ionspin qubits*, New J. Phys. **8**, 188 (2006).

[Hom09] J. P. Home, D. Hanneke, J. D. Jost, J. M. Amini, D. Leibfried, and D. J. Wineland, *Complete Methods Set for Scalable Ion Trap Quantum Information Processing*, Science **325**, 1227 (2009).

[Hub08] G. Huber, F. Schmidt-Kaler, S. Deffner, and E. Lutz, *Employing trapped cold ions to verify the quantum Jarzynski equality*, Phys. Rev. Lett. **101**, 070403 (2008).

[Hub10a] G. Huber, *Quantum thermodynamics with trapped ions*, Ph.D. thesis, Universität Ulm (2010).

[Hub10b] G. Huber, F. Ziesel, U. G. Poschinger, K. Singer, and F. Schmidt-Kaler, *A trapped-ion local field probe*, Applied Physics B: Lasers and Optics **100**, 725 (2010).

[Ita90] W. M. Itano, D. J. Heinzen, J. J. Bollinger, and D. J. Wineland, *Quantum Zeno effect*, Phys. Rev. A **41**, 2295 (1990).

[Iva09] P. Ivanov, U. Poschinger, K. Singer, and F. Schmidt-Kaler, *Quantum gate between logical qubits in decoherence-free subspace implemented with trapped ions*, arXiv: 0909.5397 (2009).

[Jam98] D. James, *Quantum dynamics of cold trapped ions with application to quantum computation*, Appl. Phys. B **66**, 181 (1998).

[Jam01] D. F. V. James, P. G. Kwiat, W. J. Munro, and A. G. White, *Measurement of qubits*, Phys. Rev. A **64**, 052312 (2001).

[Joh09] M. Johanning, A. Braun, N. Timoney, V. Elman, W. Neuhauser, and C. Wunderlich, *Individual addressing of trapped ions and coupling of motional and spin states using rf radiation*, Phys. Rev. Lett. **102**, 073004 (2009).

[Kel04] M. Keller, B. Lange, K. Hayasaka, W. Lange, and H. Walther, *Continuous generation of single photons with controlled waveform in an ion-trap cavity system*, Nature **431**, 1075 (2004).

[Kie01] D. Kielpinski, V. Meyer, M. A. Rowe, C. A. Sackett, W. M. Itano, C. Monroe, and D. J. Wineland, *A decoherence-free quantum memory using trapped ions*, Science **291**, 1013 (2001).

[Kie02] D. Kielpinski, C. Monroe, and D. Wineland, *Architecture for a large-scale ion-trap quantum computer*, Nature **417**, 709 (2002).

[Kim09] K. Kim, M.-S. Chang, R. Islam, S. Korenblit, L.-M. Duan, and C. Monroe, *Entanglement and tunable spin-spin couplings between trapped ions using multiple transverse modes*, Phys. Rev. Lett. **103**, 120502 (2009).

[Kir09] G. Kirchmair, J. Benhelm, F. Zähringer, R. Gerritsma, C. F. Roos, and R. Blatt, *Deterministic entanglement of ions in thermal states of motion*, New. J. Phys. **11**, 023002 (2009).

[Kir10] G. Kirchmair, J. Benhelm, F. Zähringer, R. Gerritsma, C. F. Roos, and R. Blatt, *High-fidelity entanglement of ions of $^{43}Ca^{+}$ hyperfine clock states*, Phys. Rev. A **79**, 020304 (2010).

[Lab08] J. Labaziewicz, Y. Ge, P. Antohi, D. Leibrandt, K. R. Brown, and I. L. Chuang, *Suppression of heating rates in cryogenic surface-electrode ion traps*, Phys. Rev. Lett. **100**, 013001 (2008).

[Lam97] S. K. Lamoreaux, *Thermalization of trapped ions: A quantum perturbation approach*, Phys. Rev. A **56**, 4970 (1997).

[Lan03] G. Lancaster, H. Häffner, M. Wilson, C. Becher, J. Eschner, F. Schmidt-Kaler, and R. Blatt, *Doppler cooling a single Ca^{+} ion with a violet extended-cavity diode laser*, Appl. Phys. B **76**, 805 (2003).

[Lan09] C. Langer, R. Ozeri, J. D. Jost, J. Chiaverini, B. Demarco, A. Ben-Kish, R. B. Blakestad, J. Britton, D. B. Hume, W. M. Itano, D. Leibfried, R. Reichle, T. Rosenband, T. Schaetz, P. Schmidt, and D. J. Wineland, *Long-lived qubit memory using atomic ions*, Phys. Rev. Lett. **95**, 060502 (2009).

[Lei96] D. Leibfried, D. M. Meekhof, B. E. King, C. Monroe, W. M. Itano, and D. J. Wineland, *Experimental determination of the motional quantum state of a trapped atom*, Phys. Rev. Lett. **77**, 4281 (1996).

[Lei03a] D. Leibfried, R. Blatt, C. Monroe, and D. Wineland, *Quantum dynamics of single trapped ions*, Rev. Mod. Phys. **75**, 281 (2003).

[Lei03b] D. Leibfried, B. DeMarco, V. Meyer, D. Lucas, M. Barrett, J. Britton, W. M. Itano, B. Jelenkovic, C. Langer, T. Rosenband, and D. J. Wineland, *Experimental demonstration of a robust, high-fidelity geometric two ion-qubit phase gate*, Nature **422**, 412 (2003).

[Lei04] D. Leibfried, M. D. Barrett, T. Schaetz, J. Britton, J. Chiaverini, W. M. Itano, J. D. Jost, C. Langer, and D. J. Wineland, *Toward Heisenberg-limited spectroscopy with multiparticle entangled states*, Science **304**, 1476 (2004).

[Let04] V. Letchuman, P. Gill, E. Riis, and A. G. Sinclair, *Optical Ramsey spectroscopy of a single trapped $^{88}Sr^{+}$ ion*, Phys. Rev. A **70**, 033419 (2004).

[Mar94] I. Marzoli, J. I. Cirac, R. Blatt, and P. Zoller, *Laser cooling of trapped three-level ions: Designing two-level systems for sideband cooling*, Phys. Rev. A **49**, 2771 (1994).

[Mar03] C. Marquet, F. Schmidt-Kaler, and D. F. V. James, *Phonon-phonon interactions due to non-linear effects in a linear ion trap*, Appl. Phys. B **76**, 199 (2003).

[McD04] M. J. McDonnell, J.-P. Stacey, S. C. Webster, J. P. Home, A. Ramos, D. M. Lucas, D. N. Stacey, and A. M. Steane, *High-efficiency detection of a single quantum of angular momentum by suppression of optical pumping*, Phys. Rev. Lett. **93**, 153601 (2004).

[Mee96] D. M. Meekhof, C. Monroe, B. E. King, W. M. Itano, and D. J. Wineland, *Generation of nonclassical motional states of a trapped atom*, Phys. Rev. Lett. **76**, 1796 (1996).

[Mil09] G. J. Milburn, S. Schnieder, and D. F. James, *Ion trap quantum computing with warm ions*, Fortschr. d. Physik **48**, 801 (2009).

[Min01] F. Mintert and C. . Wunderlich, *Ion-Trap Quantum Logic Using Long-Wavelength Radiation*, Phys. Rev. Lett. **87**, 257904 (2001).

[Moe07] D. L. Moehring, P. Maunz, S. Olmschenk, K. C. Younge, D. N. Matsukevich, L.-M. Duan, and C. Monroe, *Entanglement of single-atom quantum bits at adistance*, Nature **449**, 68 (2007).

[Mon95] C. Monroe, D. M. Meekhof, B. E. King, W. M. Itano, and D. J. Wineland, *Demonstration of a fundamental quantum logic gate*, Phys. Rev. Lett. **75**, 4714 (1995).

[Mon96] C. Monroe, D. M. Meekhof, B. E. King, and D. J. Wineland, *A Schrödinger cat superposition state of an atom*, Science **272**, 1131 (1996).

[Mon09] T. Monz, K. Kim, A. Villar, P. Schindler, M. Chwalla, M. Riebe, C. F. Roos, H. Häffner, W. Hänsel, M. Hennrich, and R. Blatt, *Realization of universal ion-trap quantum computation with decoherence-free qubits*, Phys. Rev. Lett. **103**, 200503 (2009).

[Mya00] C. J. Myatt, B. E. King, Q. A. Turchette, C. A. Sackett, D. Kielpinski, W. M. Itano, C. Monroe, and D. J. Wineland, *Decoherence of quantum superpositions through coupling to engineered reservoirs*, Nature **403**, 269 (2000).

[Mye08] A. H. Myerson, D. J. Szwer, S. C. Webster, D. T. Allcock, M. J. Curtis, G. Imreh, J. A. Sherman, D. N. Stacey, A. M. Steane, and D. M. Lucas, *High-fidelity readout of trapped-ion qubits*, Phys. Rev. Lett. **100**, 200502 (2008).

[Näg99] H. C. Nägerl, D. Leibfried, H. Rohde, G. Thalhammer, J. Eschner, F. Schmidt-Kaler, and R. Blatt, *Laser addressing of individual ions in a linear ion trap*, Phys. Rev. A **60**, 145 (1999).

[NIS06] *National Institute of Standards and Technology (NIST) Atomic Spectra Database (ASD)*, http://physics.nist.gov/PhysRefData/ASD/index.html (2006).

[Olm07] S. Olmschenk, K. C. Younge, D. L. Moehring, D. N. Matsukevich, P. Maunz, and C. Monroe, *Manipulation and detection of a trapped Yb^+ hyperfine qubit*, Phys. Rev. A **76**, 052314 (2007).

[Oze05] R. Ozeri, C. Langer, J. D. Jost, B. DeMarco, A. Ben-Kish, B. R. Blakestad, J. Britton, J. Chiaverini, W. M. Itano, D. B. Hume, D. Leibfried, T. Rosenband, P. O. Schmidt, and D. J. Wineland, *Hyperfine coherence in the presence of spontaneous photon scattering*, Phys. Rev. Lett. **95**, 030403 (2005).

[Oze07] R. Ozeri, W. Itano, R. Blakestad, J. Britton, J. Chiaverini, J. Jost, C. Langer, D. Leibfried, R. Reichle, S. Seidelin, J. Wesenberg, , and D. Wineland, *Errors in trapped-ion quantum gates due to spontaneous photon scattering*, Phys. Rev. A. **75**, 042329 (2007).

[Pau53] W. Paul and H. Steinwedel, *Quadrupole mass filter*, Z. Naturforsch. **A8**, 448 (1953).

[Pau58] W. Paul, Q. Osberghaus, and E. Fischer, *Ein Ionenkäfig*, Forschungsberichte des Wirtschafts- und Verkehrsministeriums Nordrhein-Westfalen **415** (1958).

[Pos09] U. G. Poschinger, G. Huber, F. Ziesel, M. Deiss, M. Hettrich, S. A. Schulz, G. Poulsen, M. Drewsen, R. J. Hendricks, K. Singer, and F. Schmidt-Kaler, *Coherent Manipulation of a $^{40}Ca^+$ Spin Qubit in a Micro Ion Trap*, J. Phys. B: At. Mol. Opt. Phys. **42**, 154013 (2009).

[Raa00] C. Raab, J. Eschner, J. Bolle, H. Oberst, F. Schmidt-Kaler, and R. Blatt, *Motional sidebands and direct measurement of the cooling rate in the resonance fluorescence of a single trapped ion*, Phys. Rev. Lett. **85**, 538 (2000).

[Ram86] N. F. Ramsey, *Molecular Beams*, Clarendon Press, 1986.

[Rau01] R. Raussendorf and H. J. Briegel, *A one-way quantum computer*, Phys. Rev. Lett. **86**, 5188 (2001).

[Rie04] M. Riebe, H. Häffner, C. Roos, W. Hänsel, J. Benhelm, G. Lancaster, T. Körber, C. Becher, F. Schmidt-Kaler, D. James, and R. Blatt, *Deterministic quantum teleportation of atomic qubits*, Nature **429**, 734 (2004).

[Roo00] C. Roos, *Controlling the quantum state of trapped ions*, Ph.D. thesis, Universität Innsbruck (2000).

[Roo08] C. F. Roos, T. Monz, K. Kim, M. Riebe, H. Häffner, D. F. V. James, and R. Blatt, *Nonlinear coupling of continuous variables at the single quantum level*, Phys. Rev. A **77**, 040302 (2008).

[Rot03] D. Rotter, *Photoionisation von Kalzium*, Diplomarbeit, Universität Innsbruck (2003).

[Row02] M. Rowe, A. Ben-Kish, B. DeMarco, D. Leibfried, V. Meyer, J. Beall, J. Britton, J. Hughes, W. Itano, B. Jelenkovic, C. Langer, T. Rosenband, and D. Wineland, *Transport of quantum states and seperation of ions in a dual rf ion trap*, Quantum Inf. and Comput. **2**, 257 (2002).

[Sac00] C. A. Sackett, D. Kielpinski, B. E. King, C. Langer, V. Meyer, C. J. Myatt, M. Rowe, Q. A. Turchette, W. M. Itano, D. J. Wineland, and C. Monroe, *Experimental entanglement of four particles*, Nature **404**, 256 (2000).

[Sch06] S. Schulz, U. Poschinger, K. Singer, and F. Schmidt-Kaler, *Optimization of segmented linear Paul traps and transport of stored particles*, Fortschr. Phys. **54**, 648 (2006).

[Sch08] S. Schulz, U. Poschinger, F. Ziesel, and F. Schmidt-Kaler, *Sideband cooling and coherent dynamics in a microchip multi-segmented ion trap*, New J. Phys. **10**, 045007 (2008).

[Sch09] S. Schulz, *Scalable microchip ion traps for quantum computation*, Ph.D. thesis, Universität Ulm (2009).

[Sei06] S. Seidelin, J. Chiaverini, R. Reichle, J. Bollinger, D. Leibfried, J. Britton, J. Wesenberg, R. Blakestad, R. Epstein, D. Hume, W. Itano, J. Jost, C. Langer, R. Ozeri, N. Shiga, and D. Wineland, *Microfabricated surface-electrode ion trap for scalable quantum information processing*, Phys. Rev. Lett. **96**, 253003 (2006).

[Sin10] K. Singer, U. Poschinger, M. Murphy, P. Ivanov, F. Ziesel, T. Calarco, and F. Schmidt-Kaler, *Colloquium: Experiments with atomic quantum bits - essential numerical tools*, Rev. Mod. Phys. **82**, 2609 (2010).

[SK03a] F. Schmidt-Kaler, S. Gulde, M. Riebe, T. Deuschle, A. Kreuter, G. Lancaster, C. Becher, J. Eschner, H. Häffner, and R. Blatt, *The coherence of qubits based on single Ca^+ ions*, J. Phys. B: At. Mol. Opt. Phys. **36**, 623 (2003).

[SK03b] F. Schmidt-Kaler, H. Häffner, M. Riebe, S. Gulde, G. Lancaster, T. Deuschle, C. Becher, C. Roos, J. Eschner, and R. Blatt, *Realization of the Cirac-Zoller controlled-NOT quantum gate*, Nature **422**, 408 (2003).

[Sor00] A. Sorensen and K. Molmer, *Entanglement and quantum computation with ions in thermal motion*, Phys. Rev. A **62**, 022311 (2000).

[Sor06] J. Sorensen, D. Moller, T. Iversen, J. Thomsen, F. Jensen, P. Staanum, D. Voigt, and M. Drewsen, *Efficient coherent internal state transfer in trapped ions using stimulated Raman adiabatic passage*, N. J. Phys. **8**, 261 (2006).

[Sta04] P. Staanum, *Quantum optics with trapped calcium ions*, Ph.D. thesis, Aarhus Universitet (2004).

[Sti06] D. Stick, W. Hensinger, S. Olmschenk, M. Madsen, K. Schwab, and C. Monroe, *Ion trap in a semiconductor chip*, Nature Physics **2**, 36 (2006).

[Sto07] J. K. Stockton, *Continuous quantum measurement of cold alkali-atom spins*, Ph.D. thesis, California Institute of Technology, Pasadena, California (2007).

[Tey09] M. Tey, G. Maslennikov, T. Liew, S. Aljunid, F. Huber, B. Chng, Z. Chen, V. Scarani, and C. Kurtsiefer, *Interfacing light and single atoms with a lens*, New J. Phys. **11**, 043011 (2009).

[Tha99] G. Thalhammer, *Frequenzstabilisierung von Diodenlasern bei 850, 854 und 866nm mit Linienbreiten im Kilohertz-Bereich*, Master's thesis, Leopold-Franzens Universtät Innsbruck (1999).

[Tur98] Q. A. Turchette, C. S. Wood, B. E. King, C. J. Myatt, D. Leibfried, W. M. Itano, C. Monroe, and D. J. Wineland, *Deterministic entanglement of two trapped ions*, Phys. Rev. Lett. **81**, 3631 (1998).

[Tur00] Q. A. Turchette, C. J. Myatt, B. E. King, C. A. Sackett, D. Kielpinski, W. M. Itano, C. Monroe, and D. J. Wineland, *Decoherence and decay of motional quantum states of a trapped atom coupled to engineered reservoirs*, Phys. Rev. A **62**, 053807 (2000).

[Vah10] K. Vahala, M. Herrmann, S. Knünz, V. B. G. Saathoff, T. W. Hänsch, and T. Udem, *A phonon laser*, Nature Physics **5**, 682 (2010).

[Wes07] J. Wesenberg, R. Epstein, D. Leibfried, R. Blakestad, J. Britton, J. Home, W. Itano, J. Jost, E. Knill, C. Langer, R. Ozeri, S. Seidelin, and D. Wineland, *Fluorescence during Doppler cooling of a single trapped ion*, arXiv:quant-ph/0707.1314 (2007).

[Wil07] T. Wilk, S. C. Webster, A. Kuhn, and G. Rempe, *Single-atom single-photon quantum interface*, Science **317**, 488 (2007).

[Win98] D. Wineland, C. Monroe, W. Itano, D. Leibfried, B. King, and D. Meekhof, *Experimental issues in coherent quantum-state manipulation of trapped atomic ions*, J. Res. Natl. Inst. Stand. Technol. **103**, 259 (1998).

[Zhu06a] S.-L. Zhu, C. Monroe, and L.-M. Duan, *Arbitrary-speed quantum gates within large ion crystals through minimum control of laser beams*, Eur. Phys. Lett. **73**, 485 (2006).

[Zhu06b] S.-L. Zhu, C. Monroe, and L.-M. Duan, *Trapped ion quantum computation with transverse phonon modes*, Phys. Rev. Lett. **97**, 050505 (2006).